MICROSTRUCTURE AND STRENGTH OF CONTINUOUSLY COOLED LOW ALLOY VANADIUM AND NIOBIUM STEELS.

by

A.J. Lapointe, B. Eng. Physics

Thesis submitted to the University of Strathclyde in fulfilment of the requirements for the award of the degree of Doctor of Philosophy.

Department of Metallurgy

University of Strathclyde

November, 1975.

ACKNOWLEDGEMENTS

I am particularly indebted to Dr. T.N. Baker of the Department of Physical Metallurgy, for his constant interest in reviewing each phase of this project. I would also like to thank Professor P. Grieveson for accepting me as a post-graduate student in his Department.

A special thanks is also addressed to the technical staff of the Department of Physical Metallurgy, particularly Mr. George Coull for his assistance and advice. I would also like to mention Mr. Paul Jonquin, photographer, for his practical help and suggestions, in respect of the micrographs included in this study.

Many others have helped me in connection with the present study. I would like to mention the staff of the University Library and the Computing Department for their kind and friendly help. I am grateful also to an associate and friend, Mr. James Douglas for his careful checking of the syntax. Many thanks also to Dr. Norman MacPherson and Mr. James Irvine for the helpful discussions.

I acknowledge "La Bourse de l'Enseignement Supérieur du Gouvernement du Québec" (Canada) during the whole of this study.

Finally, I would like to mention the understanding and the practical help I have received from my wife, Murielle. I would like to say that her constant support permitted this study to be a continual rewarding experience.

TABLE OF CONTENTS

SUMMARY

The present study was concerned with the variation of strength with cooling rates in vanadium and niobium steels continuously cooled from austenite. The range of cooling rates varied from $0.05K.s^{-1}$ to $500K.s^{-1}$ approximately. It was found that a peak hardening was observed in the high vanadium steels (at $\simeq 2K.s^{-1}$), whilst the low vanadium and niobium steels produced a less definite peak. An attempt was also made to explain the variation of strength through an investigation into the strengthening mechanisms in steel. Finally, efforts were made to study changes in the microstructure in relation to cooling rates.

To gain an understanding of the effects of vanadium and niobium additions to the strength and microstructure of low carbon steels, a study of the literature particularly relevant to the present study was carried out. For instance, the relationship between structure and mechanical properties was studied. Also, the mechanism of formation of microstructural components observed in the material was reviewed. Before a study of the findings was attempted, the instruments used and the experimental methods developed in the present study, were described. Strengths and weaknesses of these methods were pointed out.

Following the observation of a peak hardening in the steels, interesting results were obtained on aspects which could explain the variation of strength with cooling rates in vanadium and niobium steels. For instance, two

distinct groups of precipitates and a near constant of 10^{10} dislocations. cm/cm^3 were found in vanadium and niobium steels.

The study of the microstructure also revealed interesting features. In particular, it was observed that the peak hardening was obtained in a ferritic matrix. It was also shown that the solution treatment influences not only the precipitation hardening but also both the macrostructure and the microstructure of steels. (In this study, microstructure refers to features observed inside the grains, whereas macrostructure is generalized to include grain structure).

The present study terminates with a discussion of the various strengthening mechanisms in the steels investigated. The strength of the materials was measured by means of hardness tests which were empirically related to the yield strength. The peak was thus ascribed to precipitation hardening. The largest increase in the height of the peak for a given amount of vanadium and niobium addition, corresponded to steels of a stoichiometric composition of (Nb, V) carbonitride. On the other hand, manganese was observed to reduce and to spread the peak evenly.

Twinning was found to be present in vanadium steels and was observed for the first time in niobium steels. The contribution to strength from microtwins was appraised, but they appcared to have negligible effect.

INTRODUCTION

There has been a great interest in recent years in the possibility of improving the mechanical properties of steels from precipitation hardening and from a better control of the rolling schedule. Generally, most of the mechanical properties are quantified following an analysis laid out by Petch.

Precipitation hardening can be obtained through the addition of vanadium, niobium or titanium. These elements have a great affinity for carbon and nitrogen present in the steels. Added even in small quantity, these elements produce precipitation of carbonitrides in steels and give rise to considerable improvement in strength. The effect is known to be sensitive to rolling condition but also has been found to be very sensitive to cooling rate alone.

In most commercial heat-treatments, the steel is heated into the austenite range, and then continuously cooled to room temperature. Tanino et al. (J. Japan Inst. Metals, 1965, 29, 734) reported an increase of hardness in vanadium steel continuously cooled at $1.4K.s^{-1}$. They associated this finding with a variety of substructural features, but no quantitative measurements could be provided. This is typical of investigations carried out in new fields.

In line with the above, the present study aims to investigate further the mechanical properties of some of the vanadium and niobium precipitation hardening steels, after continuous cooling from the austenitic solution treatment. Three objectives are thus outlined:

1- To investigate the variation of strength with cooling rates in vanadium and niobium steels of various composition.
2- To correlate the strength observed with the various strengthening mechanisms operating in these steels.
3- To study the microstructure of these steels and attempt to explain change in mechanical properties by changes in microstructure.

Chapter One. STUDY OF THE LITERATURE.

Recently, progress has been made in the development of high strength low-alloy low carbon steel. The incentive was economy and safety requirement for application in pipe-line steels, offshore structures and similar structural applications. The study of all the literature relevant to the effect of vanadium and niobium additions to the strength and microstructure of low carbon steel would be a very extensive process.

The present study of the literature aims at gaining a better understanding of (1) the relationships between structure and mechanical properties, and (2) the mechanism of formation of the microstructural components observed in the material. The present "Study of the Literature" does not pretend to be exhaustive nor comprehensive, but important studies related to steel will be reviewed and discussed.

Three subjects will be investigated: in section one, the precipitation of NaCl - type carbonitride in steel will be studied. Section two will look into another important microstructural component: twinning, whereas section three, which concludes this chapter, will be concerned about strengthening mechanismsin steel. This chapter is thus underlying the present investigation.

1.1 Precipitation of NaCl - type carbonitride in steel.

In continuous cooling experiments, the steels are solution treated in austenite and are cooled to room temperature through the allotropic transformation γ-α. Depending upon composition, changing the cooling rate from 500 $K.s^{-1}$ to 0.05$K.s^{-1}$ allows several structures: martensite, bainite, acicular ferrite and ferrite-pearlite structure.

This section reviews the following aspects: (1) precipitation in austenite, (2) precipitation during transformation from austenite to ferrite, and (3) precipitation in ferrite only.

1.1.1 Precipitation in austenite.

Precipitation can occur in the austenite during the continuous cooling depending upon the composition, the cooling rate, the γ-α transformation temperature, and the volume fraction of precipitate. The nucleation is a function of type, dispersion and density of sites, undercooling and interfacial energy of precipitate.

Solubility data collected by Aronsson [1] (Fig.1.1.1.1) would indicate that at equal solubility product NbCN would precipitate more in the austenite than VCN. A higher volume fraction of carbonitride would also increase precipitation. It was also found that the kinetics of precipitation was slow; however, after holding a Nb - steel for a sufficient length of time near the Ac_3, precipitation was observed [2,3]. Precipitation of vanadium carbonitride was positively

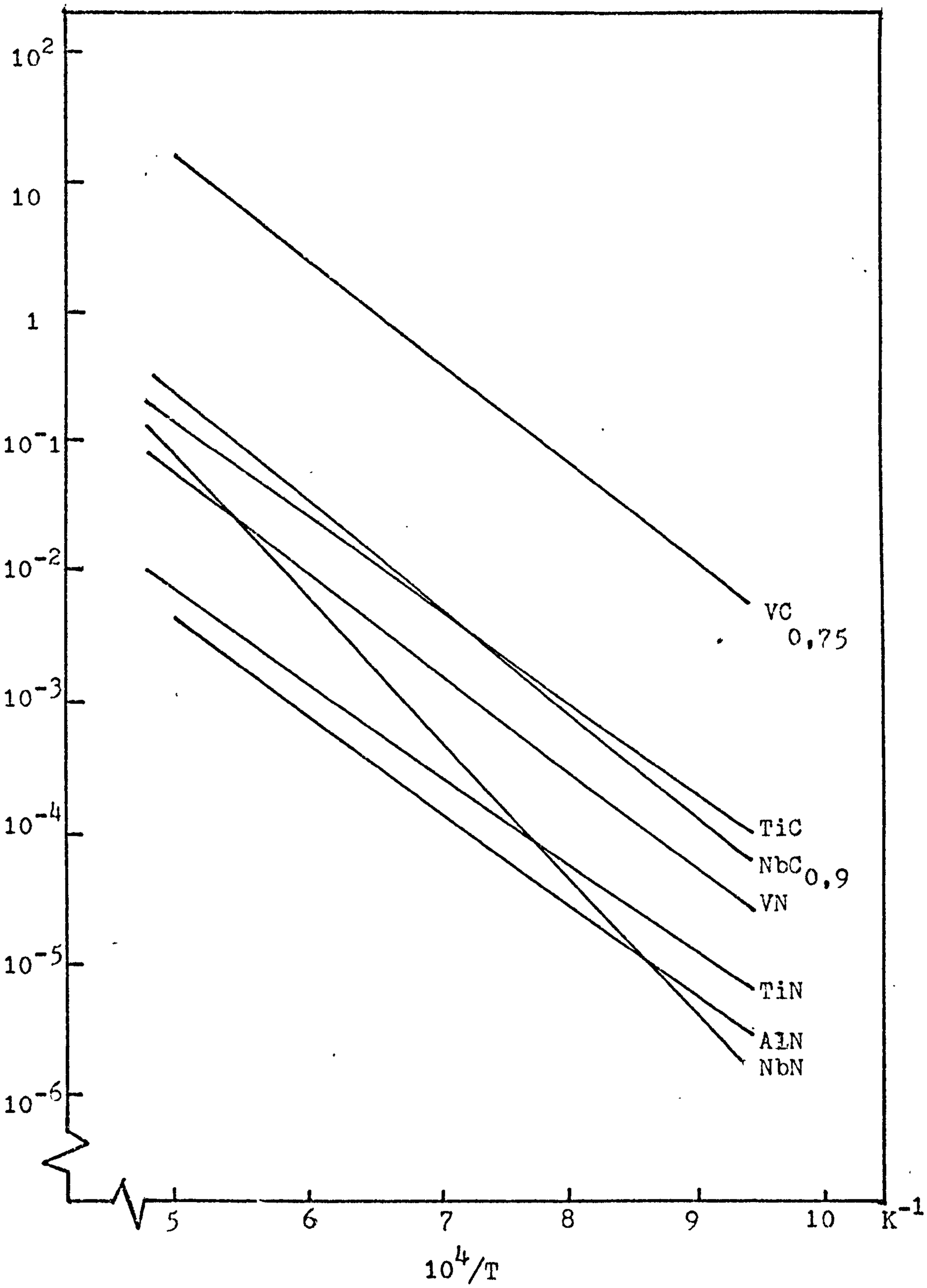

Fig.1.1.1.1 Solubility in Iron [1].

identified in austenite [4] for a Fe - 0.4% C - 2.0% V steel isothermally transformed at 1000°C for 24 hr after being solution treated at 1300°C. Consequently, it can be expected that precipitation would occur if the cooling rate is slow enough. The crystal structures of the carbonitrides are of NaCl - type for groups IV and V of the periodic table. Thus, it can be inferred that the f.c.c. carbonitrides assume the same orientation as the f.c.c. austenite matrix. In stabilized austenitic steels Silcock [10] observed that <100> NbC was parallel to <100>γ.

It is also interesting to note that deformation reduces the incubation time for NbCN precipitation to occur in austenite, as schematically described by Gray et al. [2]. However it has been measured by Le Bon et al. [5,6] that from hot torsion studies on Nb - steel, the incubation time depends directly upon the amount of deformation induced in the material. Using a rotation speed nearly as fast as the rotation speed at which dynamic recrystallisation was observed to appear, the incubation period for NbCN precipitation was reduced by about one hundred fold.[5]. The corresponding strain rate is substantially below the equivalent strain rate in industrial hot rolling processes [6]. At high strain rates, precipitation during deformation was observed to be negligible [7].

From studies on stabilized austenitic steels at room temperature, it may be possible to deduce the precipitation mechanism at high temperature in austenite before the allotropic change to ferrite. In austenitic steels,

precipitation occurs on dislocations [8,9,10], on stacking faults [10,11], on grain boundaries [9], on sub-grain boundaries [12] and probably on vacancies. In ferritic steels, prior carbonitride precipitates in austenite are generally nucleated on dislocations [9], and a slow strain rate is necessary to increase precipitation [6].

Having established the feasibility of MCN precipitation in austenite, its composition and structure will be compared to those in ferrite. The structure of the carbonitride in austenite/ferrite is of NaCl - type [13,14], whilst the hexagonal structure does not exist under normal steel composition. In respect of MCN composition, it is generally accepted [4,13-15] that V_4C_3 is misleading, whilst it is justifiable to refer to precipitation of NbCN, TiCN and to a lesser extent to VCN in ferrite. However, there is some controversy about the exact MCN composition in austenite. For instance, from free energy considerations, Roberts and Grieveson [13] predicted a $VC_{0.94}$ in austenite. However, in a comprehensive review, Hollox [14] suggested $VC_{0.89}$ as the upper limit of the VC phase. Furthermore in a study of precipitation at equilibrium in α and γ of a Fe-0.4% C-2.0% V steel, Meyzaud and Murry [4] identified $VC_{0.86}$ in austenite; they also detected no significant difference with the composition of the precipitate at equilibrium in ferrite. It should therefore be pointed out that any conclusion based on free energy, due to uncertain and unconsistent values, may lead to erroneous predictions, and should be considered with reservation [15,17].

In contrast with the above, the solubility of VCN in ferrite was reported to be a hundred fold less than in austenite [16,17]. Thus, a large amount of carbide in solution in the austenite will precipitate in ferrite, if the volume fraction of carbide present in the material allows the solution to become supersaturated in ferrite. Preferred locations for heterogeneous precipitation are at points of easy nucleation such as grain boundaries (e.g. γ-α interface).

The most suitable moment for heterogeneous precipitation to occur is at the allotropic transformation γ-α. At this point, the solubility abruptly decreases, but the temperature remains high enough to enable a fast diffusion of the elements. This assumes a sufficiently low cooling rate allowing precipitation to occur on the moving interface.

1.1.2 Precipitation during the allotropic transformation from austenite to ferrite.

Precipitation in ferrite can be inferred from solubility data. Gray et al. [3] initially described precipitation in Nb - steels as the result of two separate reactions occurring in austenite and in ferrite; no "row precipitates", later named "interphase precipitates", had been observed. In a subsequent paper, observation of interphase precipitations were made, and Gray and Yeo [2] talked about a coherent precipitation during the transformation from austenite to ferrite. They postualted that the particles are arranged as sheets parallel to the γ-α boundary interphase, each sheet corresponding to a momentary stop of the moving boundary.

A great deal of work has been done on this subject by the Cambridge School, headed by Honeycombe [18-21]. Davenport et al. [18,19] explained that the mechanism of precipitation of carbonitrides (M - CN) is controlled by the diffusion of the metal across the interphase boundary. The motion of the boundary is controlled by the rate of carbon depletion in a small zone of the austenite. When nucleation occurs, carbon is removed from that zone, reducing the stability of the austenite. The interphase boundary moves to a new site, where carbon is more abundant; and the process is repeated. The growth of the M - CN occurs only in ferrite.

The same school completed further work to obtain complementary results: particle size and inter-sheet

"spacing" increased with increasing isothermal temperature [18]; and as one would expect, decreasing volume fraction increases the inter-sheet spacing and particle size [20]; decreasing the transformation temperature by adding Mn, Cr or Ni, also increases these two parameters [20,21].

Another model to explain interphase precipitation was proposed by Morrison and Woodhead [22] and developed by Tanino et al. [23-25]. The model suggests that during the transformation γ-α, the carbonitrides nucleate on (1) dislocation dipoles to produce lined-up distribution of carbides, and on (2) dislocation loops to produce dispersed carbides.

The model proposed by Davenport et al. [18] appears to explain the characteristics of the interphase precipitation. The model of Tanino agrees less with other experimental observation [26]; the "row" is explained but not the two dimensional distribution of the precipitation. However as mentioned by Baker [27], Davenport's model produces heterogeneous precipitation and cannot explain the coherent precipitate sometimes observed. Although no positive identification of coherency was effectuated, Baker [28] suggested that the allotropic transformation γ-α gave effect to a supersaturation of V or Nb, C and N at the interface. Only when the γ-α interphase boundary has moved further in austenite, are the nuclei formed. Thus particles are formed and they grow in ferrite only; this provides an explanation of coherent particles observed in interphase precipitation. Kisman et al. [29] observed by

thermionic emission microscopy the thickening of a proeutectoid ferrite plate by a ledge mechanism. Such a mechanism could also explain the coherency of MCN particles observed in interphase precipitation. The model will be discussed later in this section with the "rod-type precipitate".

In all these models, the habit plane of M - CN carbonitrides was a {100} plane of ferrite. However, the same habit plane was also observed in tempered martensite [30,31]. In Davenport's study [18], this is explained by a greater diffusion on the <100> axis, which is the shortest path between the allotropic interface and the metal atoms; the metal atoms having lower diffusivity than the carbon or nitrogen atoms.

However, the habit plane could be explained by interatomic spacing considerations between M - CN and the ferrite. There is a similarity between the interatomic spacing of the {100} ferrite and {100} M - CN. There is an even better fit between a {110} ferrite and {100} M - CN. In the latter case, the conventional misfit is about 2% for a VC crystal with the ferrite. This results in:

M - CN	(100)	//	(100)	Ferrite
(f.c.c.)	(010)	//	(011)	(b.c.c.)
	(001)	//	(011)	

These are the well known Bain [32] orientation-relationship between face-centred cubic and body-centred cubic materials, which is better known after Baker-Nutting [33] following their study on precipitation.

Another interesting feature in steels is the fibrous or rod-type precipitate observed occasionally. In Fe - C - Mo alloys, Hall et al. [34,35] observed Widmanstätten needles and fibrous structures in thin parallel fibres. From orientation-relationship and habit direction, they concluded that the needles nucleated homogeneously in ferrite, whilst fibrous structures were formed from the austenite [36]. For vanadium steels, Edmonds [37] suggested that a mechanism of nucleation similar to the one developed by Davenport et al. [18,19] could apply. The requirements would be coherency of the fibre with the interphase boundary during its formation, and a slow motion of this boundary.

Later, Edmonds and Honeycombe [38] observed that some Mo_2C needles had a single habit plane, whilst in some other cases they had two habit planes. They suggested that a periodic precipitation at successive position of the γ-α interphase boundary could produce two needle habit planes, whereas a ledge mechanism was proposed for the formation of one needle habit plane. Mannerkoski [39] and Heikkinen [40] explained also the very fine bands of periodic precipitate parallel to the γ-α interphase boundary by a ledge mechanism. The periodicity of the precipitate was elucidated by the nature of the γ-α interphase boundary which is constituted of two parts. One part is immobile, semicoherent, and is the site of precipitation. The second part (edge) is disordered and can move because carbon nitrogen and metal atoms are depleted due to precipitation at the semicoherent

interface. This latter model can also explain the formation of interphase precipitation. The speed of the transformation, volume fraction and diffusion of elements would account for the transition from coherent or semicoherent precipitate to needle shape precipitate.

1.1.3 Precipitation in ferrite only.

At high cooling rates, hence high transformation rates, the interphase precipitation can be avoided. Jack [41] showed that, during a constant activity ageing, the nitride precipitation in a ternary alloy followed three stages; (1) mixed G.P. zones, (2) metastable precipitate, (3) equilibrium nitride phase.

The results of Masianzoni and Buzzichelli [42] on a Fe - 0.2% Nb - 0.018 % N alloy support Jack's theory of nucleation and growth. They suggested that the conditions for homogeneous nucleation may not be restricted to the case of constant nitrogen saturation. Furthermore, they concluded that the strengthening effect of G.P. zones can be higher than that produced by interphase precipitation.

This section was concerned with precipitation in steel. Chapter five, "Study of microstructure" will refer to this section. Next section will deal with another important microstructural component, twinning.

1.2 Twinning in alpha iron and other b.c.c. metals.

In this section, it is proposed to discuss some aspects of twinning in body-centered cubic (b.c.c.) metals and alloys with special emphasis on transformation twins in alpha iron. Firstly, the crystallography of b.c.c. twins is presented; secondly, the properties of the twinning phenomenon are reviewed; and thirdly follows a discussion on the theories and hypotheses of twin formation.

Recently, Mahajan and Williams [43] have reviewed the subject of deformation twinning. Fullman [44-46] studied the subject of annealing twins, whereas Baker [47] discussed transformation twins in alpha iron. Several authors have dealt with the twinning subject: Cahn [48], Hall [49], Reid [50], Reed-Hill et al. [51] and Hull [52].

1.2.1 Crystallography of b.c.c. twinning.

A twinned crystal is usually defined as a part of a crystal which is a mirror reflection of another part in a certain plane of the cystal; this plane is named the composition plane. On the other hand, Bevis and Crocker [53] expressed a wider definition of twinning; twinning shear is any shear that displaces part of the lattice into a new orientation.

There is no change in the cystal structure of a twin, only the orientation is different from the parent cystal; the deformation is then a simple shear. Fig.1.2.1.1 illustrates this concept. It is convenient to visualize a crystal sphere that undergoes a twinning shear in the n_1 direction.

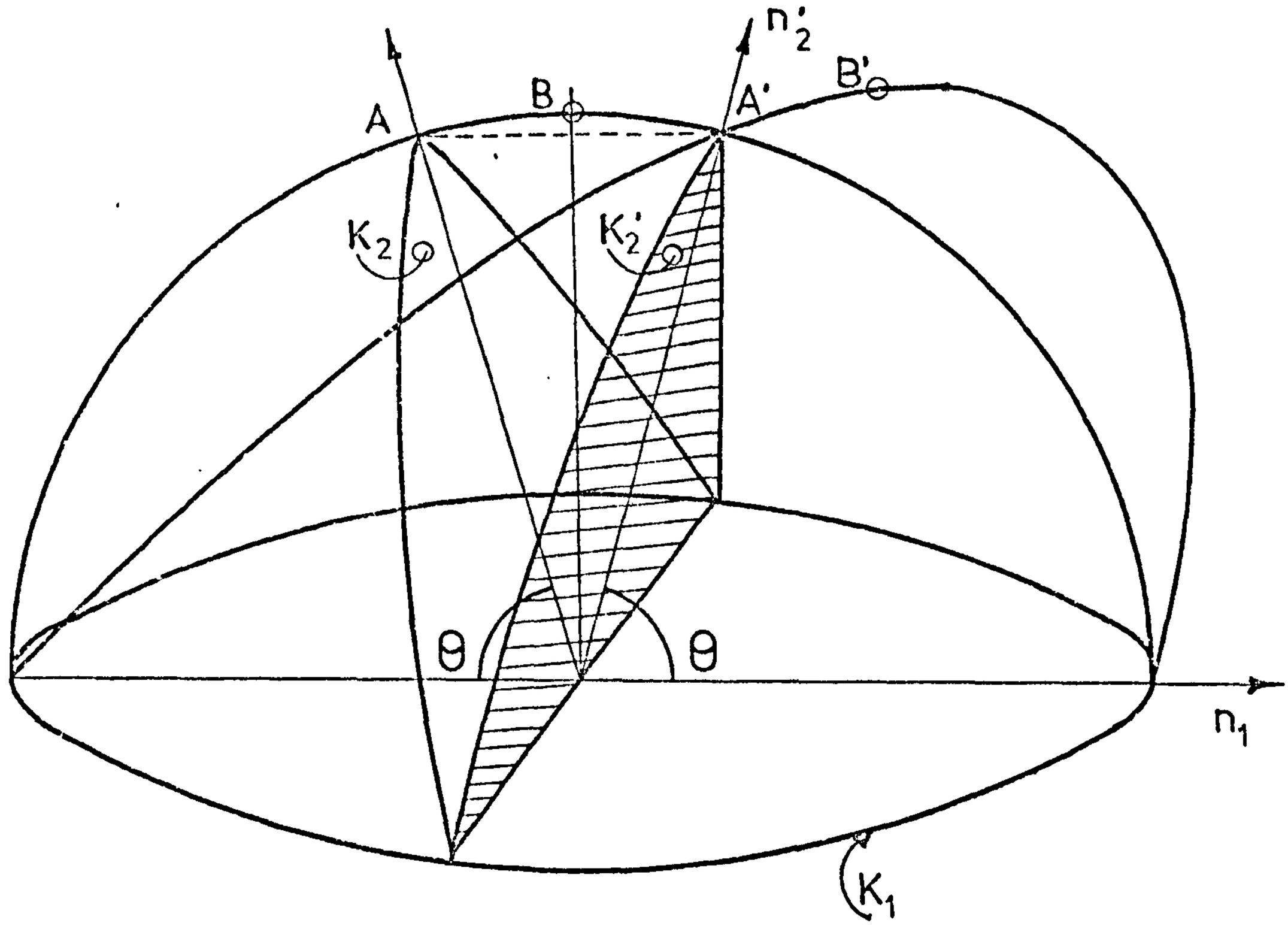

Fig.1.2.1.1 Spatial relationship between a sphere and a twinned ellipsoid. (adapted from Hall [49])

This deformation produces a twinned ellipsoid. Two planes are undistorded: these coincide with the sphere diameters intersecting with the ellipsoid. The plane K_1 has not moved and is named the "composition" plane. The other plane K_2, (of n_2 direction) is sheared in the n_1 direction into K'_2. A knowledge of either (K_1, n_2) or (K_2, n_1) enables the determination of twinning completely.

If (K_1, n_2) are rational numbers, the twin is called twin of the "first kind" or "reflection" twin [48,49]. The orientation changes can be achieved by either a rotation of π radians about the normal to (K_1), or a "reflection" into the (K_1) plane. If (K_2, n_1) are rational numbers, then the twin is one of the "second kind" or "rotation" twin [48,49]. The new orientation can be achieved by either a reflection in the plane normal to $[n_1]$ or a "rotation" of π radians about $[n_1]$. However, in crystals of high symmetry, such as metals, all four elements are found to be rational numbers, and there is no distinction between the two kinds. As a consequence, twins in b.c.c. metals are compound twins.

Following the study of Paxton [54] and Kelly [55], the Neumann bands in alpha iron were proved to be b.c.c. twins presenting a $\{112\}$ composition plane and $<11\bar{1}>$ direction. Fig.1.2.1.2 shows the shear motion as the atoms move to their new positions in the b.c.c. lattice. The associated electron diffraction pattern is shown in Fig.1.2.1.3. There are twelve different twinning systems in b.c.c. metals. Schmid and Boas [56] numbered them according to their composition plane, and this is reproduced in Fig.1.2.1.4.

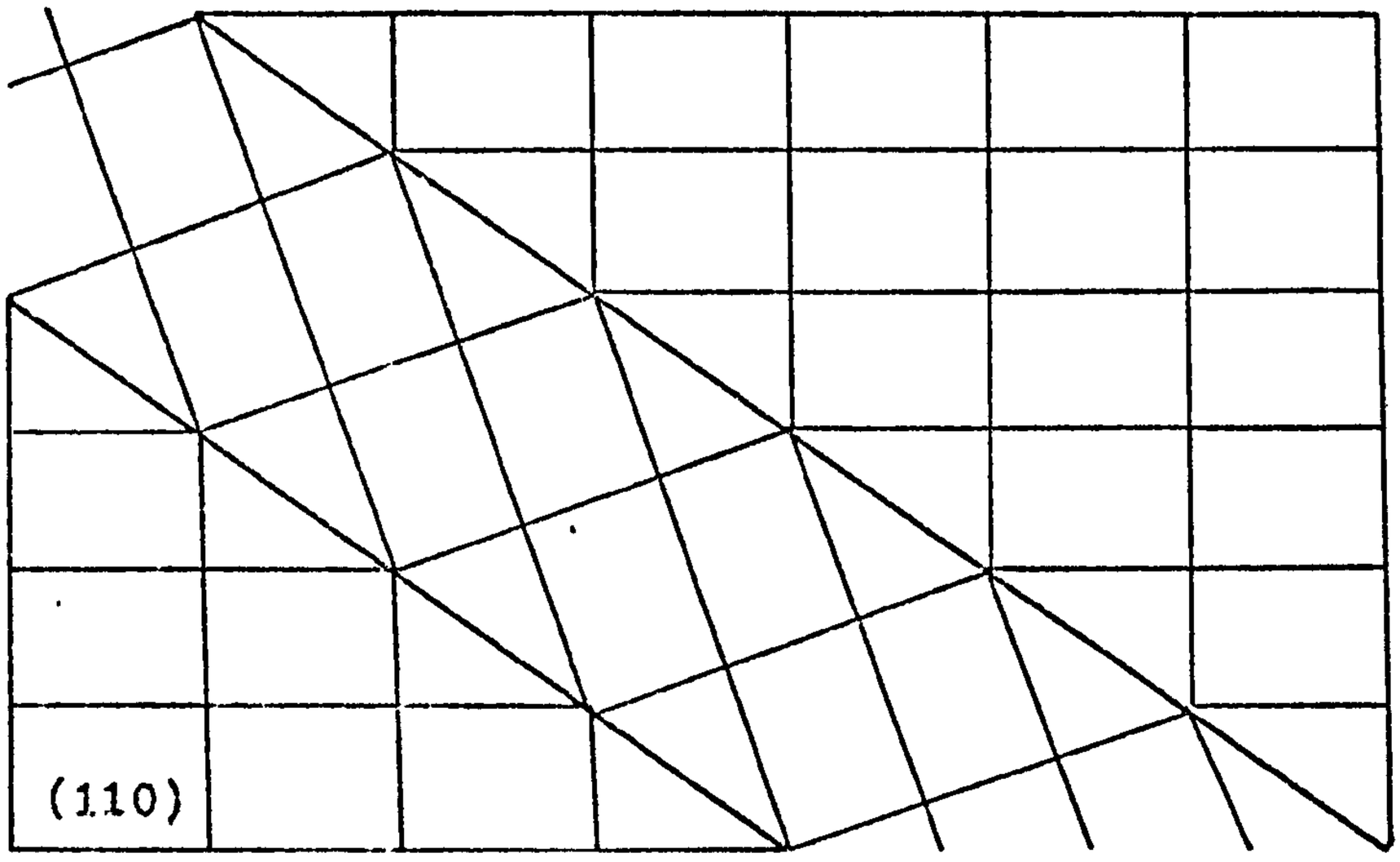

Fig.1.2.1.2 Twin layer in b.c.c. lattice.

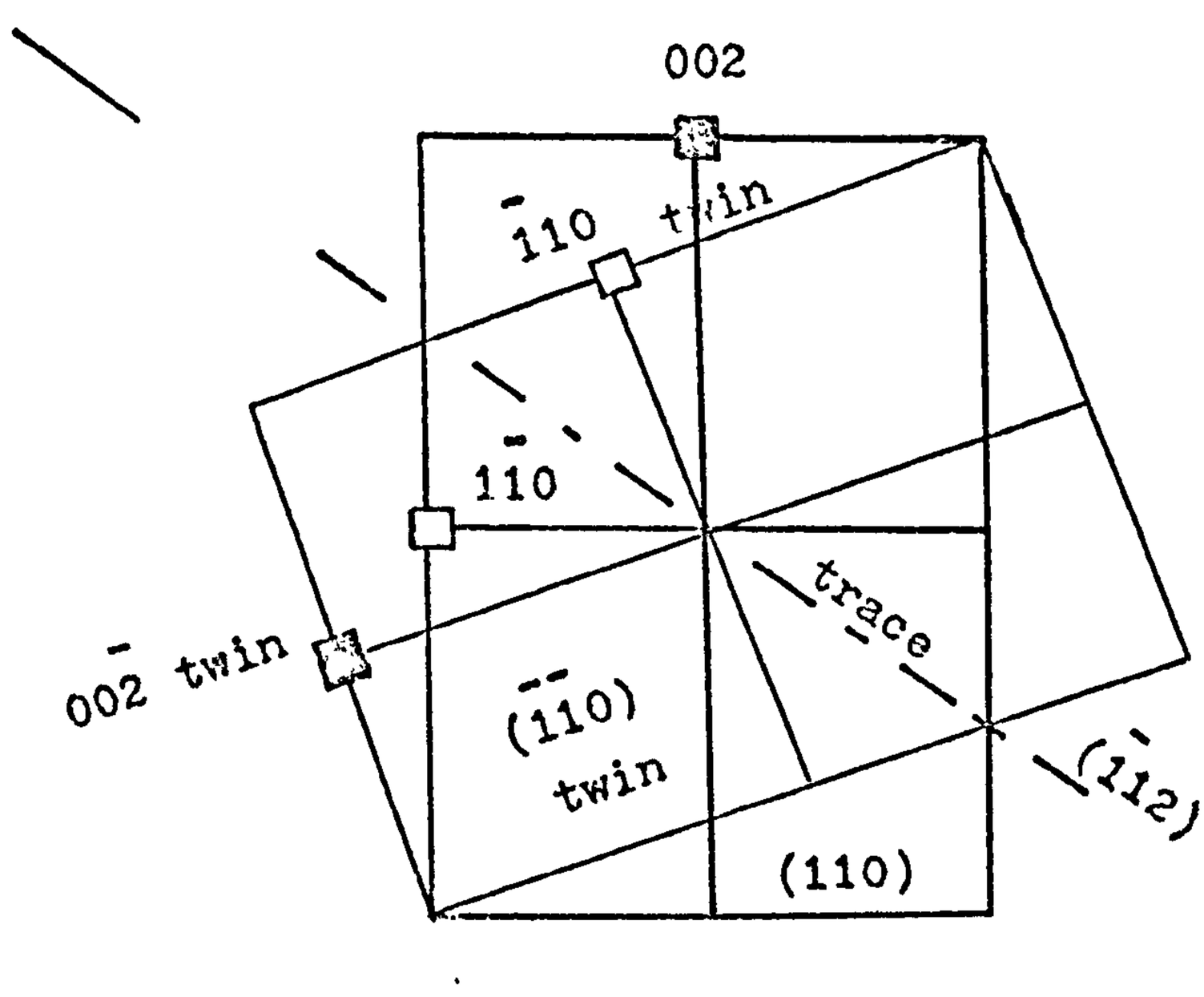

Fig.1.2.1.3 Diffraction pattern associated with the b.c.c. lattice and twin shown on Fig.1.2.1.2.

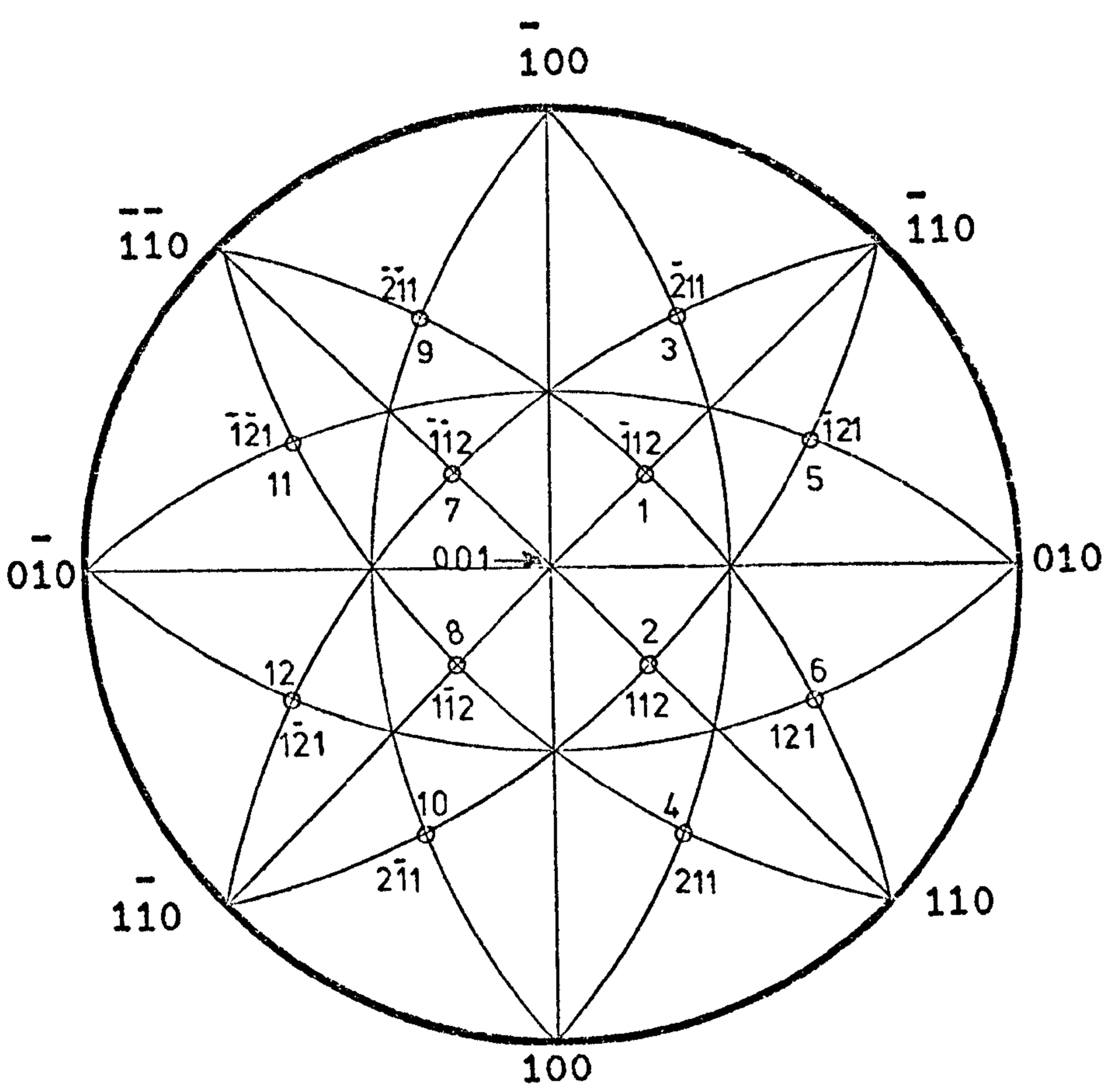

Fig.1.2.1.4 The Convention of Schmid and Boas [56] for the identification of twin systems in b.c.c. lattice.

Twinning identification from electron diffraction patterns is easily accomplished. The prediction or identification of twinned spots is readily executed, using a stereogram, by performing a reflection through the composition plane. The composition plane can be positioned on the diffraction pattern from trace analysis on the corresponding electron micrograph. The method was well illustrated by Johari and Thomas [57].

When the compositon plane has been unambigously identified by trace analysis (a {112} plane for a b.c.c. structure), the twinned reflection can also be geometrically indexed according to the relationship between the twinned crystal and the parent crystal [58-61]. Basically, the matrix reflection $(h_m k_m l_m)$ is transformed through the composition plane $(h_c k_c l_c)$ into the twinned reflection $(h_t k_t l_t)$ which is in the matrix direction $h^*_m k^*_m l^*_m$. The twinned reflection has the indices of the matrix reflection, plus a π radians rotation: $h_t k_t l_t = \bar{h}_m \bar{k}_m \bar{I}_m$. The location is on the direction and at one third of the reciprocal lattice vector:

$$\bar{g} = h^*_m k^*_m l^*_m \ ;$$

$$h_t k_t l_t = \bar{h}_m \bar{k}_m \bar{I}_m \qquad 1.2.1.1$$

in the direction of

$$h^*_m = h_m - A\, h_c$$

$$k^*_m = k_m - A\, k_c$$

$$l^*_m = l_m - A\, l_c \quad \ldots \quad 1.2.1.2$$

where $A = \dfrac{2(h_m h_c + k_m k_c + l_m l_c)}{(h_c^2 + k_c^2 + l_c^2)}$, (see Appendix A)

which for a {112} plane becomes: $A = \frac{1}{3}(h_m h_c + k_m k_c + l_m l_c)$.

1.2.2 Studied properties of the twinning phenomenon.

Twinning is qualified according to the mechanism that is thought to be causal. Twinning is very often connected with mechanical deformation, Neumann bands [54,55] for example; such twins are named "deformation twins". A second type of twin is called "annealing twins". This is a dominant feature of the microstructures of most annealed face-centered cubic metals. Another type of twin was observed by Tamura [62] inan as-cast iron and mild steel as early as 1927. This type of twin was observed in iron after the material had undergone the allotropic change γ-α; because of this association, they were given the name of "transformation twins". After the study of Paxton [54] and Kelly [55] on Neumann bands, Hutton et al. [63] using the same microbeam technique concluded: (1) that the transformation twins had $\{112\}\cdot\langle 11\bar{1}\rangle$ twinning elements, and (2) that a pair of twinned grains can share three {112} planes. These observations established that the "transformation twins" exhibit the same crystallographic elements as the "deformation twins" in b.c.c. lattice. These two categories of twins differ by their connection with one or the other mechanism.

Alloying produces various effects on twinning. Substitutional atoms decrease the stacking fault energy (SFE) in f.c.c. metals and alloys [64]. If twinning is associated with a dislocation mechanism in which a unit dislocation is dissociated into partials, a decrease in SFE

will promote twinning. The ease of twinning in the Nb - V system (b.c.c.) [65] could be explained by a decrease in SFE. In alpha iron, a theoretical SFE of 110 erg. cm^{-2} was proposed [66], hich agrees reasonably with an experimental value [67] of 140 $\pm$ 40 erg. cm^{-2}. However, a stacking fault on a {112} or even {110} plane is unstable if based on the hard sphere model for b.c.c. lattice. It was also mathematically demonstrated that whilst large single stacking faults cannot exist in the metastable configuration in the b.c.c. structure [68], three layer faults [69] on {112} are metastable and might be of some importance in twin nucleation. On the other hand, the apparent decrease in the ability to cross-slip might result from solid solution increasing the lattice friction stress, and not necessarily because solid solution decreases the SFE [70].

In V, Ti or Nb steel, the carbonitride has a greater capacity for holding interstitials. In twinning which appears to be associated with the γ-α phase transformation, Baker [47] observed that a suppression of the pearlite reaction may be essential for the phase transformation to produce a twin in α- iron. This observation can be explained from the study of Magee et al. [71]. Assuming the concept of a twinning stress, there is an increase in twinning stress due to the presence of interstitial atoms in b.c.c. metals; these interstitials are not sheared to the correct octohedral sites during twinning. The association of twinning with neighbouring carbonitrides (MCN) particles could be explained from the observation that in MCN areas, there is a depletion of C and N; the removal of interstitials (C,N) decreases the twinning

stress and allows twinning to occur more easily. This effect would be independent of the twinning nucleation mechanism.

VCN is more soluble in gamma iron than NbCN, but the solubility is very low in alpha iron. However, the depletion effect of the metal could be associated with an inhibition of cross slip due to solid solution. If slip is inhibited perhaps twinning could relieve the local stress in the matrix, where the inhibition of cross slip is sufficient to produce a stress in the matrix of the order of the stress to produce a twin.

In alpha iron, twinning stress can be related to the grain size by the Petch equation in a similar manner to the lower yield stress [66],

$$\sigma_t = \sigma_t + k_t d^{-\frac{1}{2}} \qquad 1.2.2.1$$

$$\sigma_s = \sigma_s + k_s d^{-\frac{1}{2}} \qquad 1.2.2.2$$

where σ_t, σ_s are the lower yield stresses for twinning and slip respectively. The "σ" is more dependent upon the temperature for slip than for twinning. Inversely, "k_t" has been found to be more temperature dependent than its counterpart for slip. Moiseev [66] then conlcuded that twinning has a high nucleation stress (i.e. $k_t > k_s$) but a lower frictional stress for twin propagation.

From the equation 1.2.2.1, a larger grain size would tend to promote twinning more readily; the transition from slip to twinning is occasioned by the temperature dependence of "σ" and "k". Also, an increase in strain rate promotes deformation by twinning. This again emphasizes the close relationship of slip and twinning.

1.2.3 Twin nucleation in b.c.c. metals.

There is a tendency in the literature to explain twinning nucleation by a dislocation reaction mechanism [72-77]. From twinning models in the literature, twinning is generally believed to nucleate heterogeneously. The well known pole mechanism for twin nucleation in a b.c.c. lattice was proposed by Cottrell and Bilby [72]. Under stress, a $\frac{1}{2}\langle 111\rangle$ Burgers vector lying on a $\{112\}$ plane could dissociate into two partials: $\frac{1}{2}\langle 111\rangle \rightarrow 1/6\langle 11\bar{1}\rangle + \frac{1}{3}\langle 112\rangle$. The dislocation $1/6\langle 111\rangle$ (twinning dislocation), revolves around the $\frac{1}{3}\langle 112\rangle$ (pole dislocation), and produces a twin layer on the $\{\bar{1}21\}$ plane. Unfortunately, no experimental confirmation can be found as yet in the literature.

A similar dislocation mechanism was suggested by Sleeswyk [73] to explain twinning. In this model a $\frac{1}{2}\langle 111\rangle$ screw dislocation can dissociate into three twinning partials, $1/6\langle 111\rangle$, each of them being located in one of the three $\{112\}$ planes that intersect symmetrically on the $\frac{1}{2}\langle 111\rangle$ pole dislocation. Under stress, the twin "embryo" could develop when one or two of these partials spiral around the $\frac{1}{2}\langle 111\rangle$, creating a three layer twin. The existence of these partials is postulated on the basis of energy considerations. A similar model proposed that the twin is produced by edge unit dislocations instead of screw dislocations [74]. In studies on a Mo - 35 at.% Re alloy (b.c.c.) Mahajan [75,77] supported Sleeswyk's model and concluded that slip and twinning are very closely related

phenomena; which is in good agreement with the preceding discussion.

Recently, Sleeswyk[76] proposed another nucleation mechanism described by the equation:

$$\langle 00\bar{1} \rangle = \tfrac{1}{3}\langle \bar{1}\bar{1}2 \rangle + 2 \times 1/6 \langle 11\bar{1} \rangle.$$

However, the twinning partials would not be parallel to the parent glide dislocations [77] whilst the parallelism was obeyed in the former model of Sleeswyk [73]. It is proposed that a simple dislocation reaction governs inter-relationship between slip and twinning [77].

$$\tfrac{1}{2}\langle 111 \rangle_{\text{screws}} \underset{\text{slip}}{\overset{\text{twinning}}{\rightleftharpoons}} 3 \times 1/6 \langle 111 \rangle.$$

This suggestion indeed emphasized the close relationship of slip and twinning.

The twin nucleation models previously discussed were all associated with a dislocation reaction of some kind. All these models were also concerned with deformation twinning. It is not therefore surprising that these models were studied in relation to slip. Similarly, models to explain nucleation of transformation will tend to establish some connections with the allotropic transformation and be less associated with dislocation reactions. Interphase precipitation occurs at the γ-α transformation in iron alloys. A connection between these features and the transformation twins can reasonably be postulated.

In one model [78], the nucleation of a transformation twin in vanadium steel was associated with the stress

produced at the edge of a VCN band formed at the γ-α interface. The model proposed by Heikkinen is shown on Fig.1.2.3.1. Once nucleated, the twin would grow lengthwise with the movement of the γ/α boundary. However, as mentioned by the author, the model fails to explain twins which are not observed in connection with the band colonies. The exact mode of twin nucleus formation is not yet clear. In this respect Heikkinen's model tends to support the homogenous twin nucleation of Orowan [79], in which a stable lens-shaped twin nucleus could be formed in the presence of stress concentration.

The twin nucleation mechanisms based on dislocation reactions are energetically favourable, and indeed very elegant. In all the twin nucleation models it has been emphasized that under stress the twin nucleus could develop. However none of the models explained what are the necessary conditions for twin nucleation and why twins should be formed. The ambiguity slip $\rightleftharpoons$ twinning has still to be resolved together with the connection of transformation twins with interphase precipitation.

In this section, three aspects of twinning in b.c.c. metals were discussed, namely crystallography, properties and nucleation of twins. This part of the "Study of the Literature" on twinning will be considered again in Chapter five of the present study, where discussion of some micrographs will be carried out.

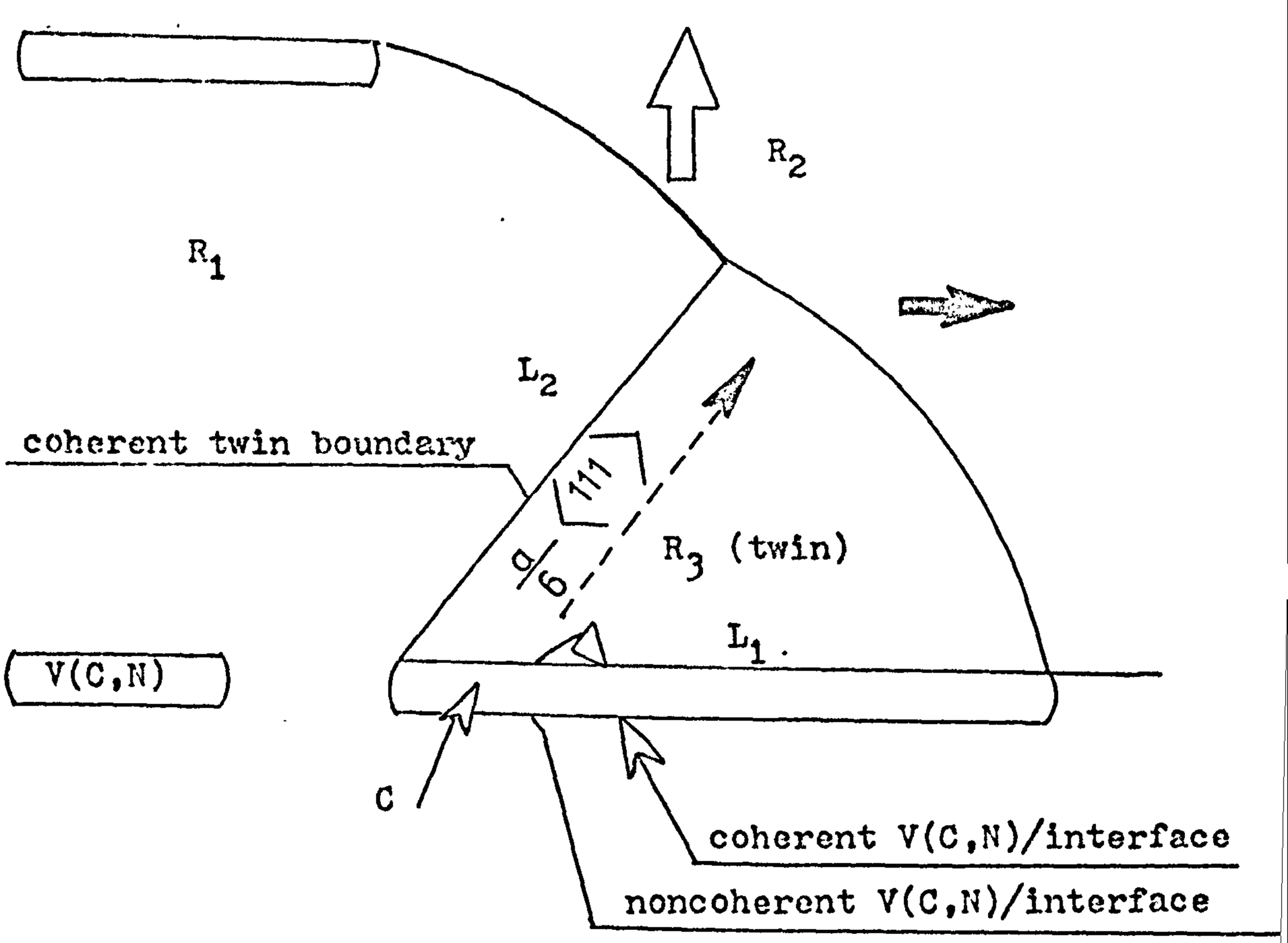

Fig.1.2.3.1 Two dimentional model for formation of transformation twins.

1.3 Strengthening mechanisms in steel.

Several contributing factors can account for the strength of steel: (1) the grain size, (2) hardening from solid solution, (3) dislocation density, and (4) precipitation hardening.

1.3.1 Strengthening effect of grain size.

Hall [80] and Petch [81] related the grain size (d) of low carbon steels to the yield stress (σ_y):

$$\sigma_y = \sigma_o + k_y d^{-\frac{1}{2}} \qquad 1.3.1.1$$

The symbol "σ_o" is the lattice friction stress, that is the resistance of the lattice crystal to the movement of dislocations. It is equal to the stress required to move dislocations during yielding; the stress is influenced [82] by both interstitials and substitutional atoms, precipitation, temperature of testing and strain rate.

The symbol "k_y" is a stress intensity factor depending upon the material. It is related to the difficulty of spreading slip across grain boundaries. The generation of fresh mobile dislocations is believed to occur probably at or near grain boundaries or sub-grain boundaries as mentioned by Kouwenhoven [82].

Improving the strength by controlling grain size appears an advantageous procedure because grain size affects both the yield strength and the fracture resistance. An indication of toughness can be obtained by measuring the ductile-brittle transition temperature (T_c)

in ferritic steels [83];

$$Tc = A - Bd^{-\frac{1}{2}} \qquad 1.3.1.2$$

where A and B are some constants.

Early attempts to control the grain size in steel were carried out by adding Al to produce AlN. Aluminium nitride and transition metal additions hinder grain growth. An alternative method is to refine grain size by use of thermomechanical treatments. This latter method can also be used with transition metal additions to restrict grain growth after mechanical treatments.

The ferritic grains are usually nucleated at the austenite grain boundaries. Small austenitic grains produce more grain boundary areas per unit volume, more ferritic nuclei and a finer grain size at the allotropic transformation. As a consequence, thermomechanical treatment in austenite is also a means of controlling the ferritic grain size. All these procedures led to "controlled" rolling of steel. Some studies on this subject were carried out at the University of Strathclyde [17,84-86]. The association of a grain boundary with an inclusion or a second phase particle results in a reduction of the total grain boundary energy. According to a current theory, reviewed by Reed-Hill [87] and Gladman [88,89], there is a critical particle size radius (r_c) above which grain coarsening occurs; r_c is a function of the product of the average matrix grain radius $\bar{R}$ and the volume fraction (f) of particlesin the microstructure.

$$r_c = \tfrac{3}{4} \bar{R} \cdot f \qquad 1.3.1.3$$

This equation is known as Zener's relationship [90]. Particle radii larger than the critical radius (r_c) can no longer restrict grain growth, therefore smaller particles more effectively hinder grain growth.

Another theory proposes that solutes impede grain boundary migration. The first quantitative treatment on the interaction between grain boundaries and solute atoms was suggested by Lücke and Detert [91]. Later, one of the authors (Lücke and Stüwe [92]) and recently Higgins [93] reviewed the subject. The drag effect of solute is caused by the motion of the boundary which breaks the symmetric distribution of solute on both sides of the boudary; the bigger the assymmetry, the larger is the resulting drag effect.

1.3.2 Strengthening by solid solution.

Contrary to the genetic phenomenon, two weak parent metals, Cu and Zn, when mixed together produce a stronger material "brass", which has been known for centuries. In f.c.c. brass, Cu atoms are replaced by slightly bigger Zn atoms, which produce a substitutional "solid solution". Pure iron can also form a substitutional solid solution. The strengthening effect of solid solution can be attributed to various factors, such as lattice distortion, electro-mechanical affinity and ordering (e.g. $CuAl_2$).

In this study, the main substitutional element in iron is manganese. Pickering and Gladman [94] adopted a modified Petch relationship to include the effect of solid solution: the latter was observed to affect the lattice friction stress only:

$$\sigma_y = \sigma_o + \sigma_{ss} + ky\, d^{-\frac{1}{2}} \qquad 1.3.2.1$$

where: σ_{ss} is the contribution of solute to friction stress. However, Kouwenhoven [82] observed that manganese had no effect on the lattice friction stress (σ_o) of alpha iron, but had an effect only on the lattice friction stress component of the pearlite contribution to yield strength. Fig.1.3.2.1 shows the contribution of solutes to the strength in polycrystalline iron.

1.3.3 Strengthening effect of dislocations.

Dislocations can contribute to strengthening, provided they are present in sufficient numbers. Keh and Weissmann [96] found an empirical relationship between dislocation density and flow stress (σ_f):

$$\sigma_f = \sigma_o + \sigma_d + kd^{-\frac{1}{2}} \qquad 1.3.3.1$$

$$\sigma_d = \alpha\, Gb \sqrt{N} \qquad 1.3.3.2$$

where: G is the shear modulus,

b is the Burgers vector,

α is a constant, 0.38 for polycrystalline iron

0.31 for single iron crystals [14,97]

σ_d is the contribution to flow stress from dislocation density.

N is the number of dislocations.cm/cm^3

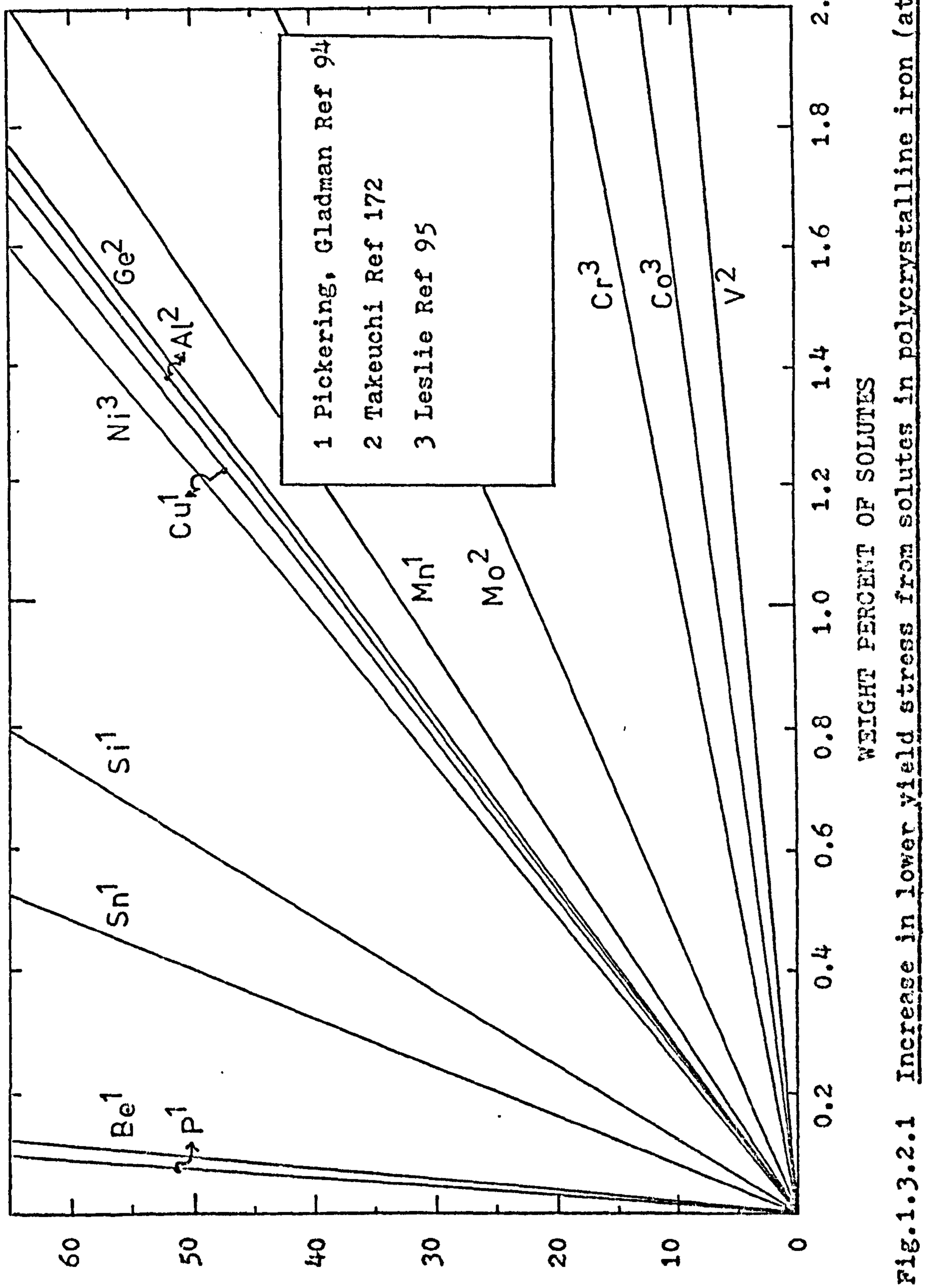
Increase in lower yield stress from solutes in polycrystalline iron (at ≃ 300K)
WEIGHT PERCENT OF SOLUTES
INCREASE IN LYS (MPa)
1 Pickering, Gladman Ref 94
2 Takeuchi Ref 172
3 Leslie Ref 95
Ni3
Ge2
Al2
Cu1
Mn1
Mo2
Cr3
Co3
V2
Si1
Sn1
Be1
P1
0
10
20
30
40
50
60
0.2
0.4
0.6
0.8
1.0
1.2
1.4
1.6
1.8
2.0

Fig.1.3.2.1

Work hardening mechanisms predict that σ_y is a function of $(G.b.\sqrt{N})$; consequently, the hardening mechanism of dislocations do not emerge clearly. However back stress effects of dislocation pile-ups, and inhibition of movement of dislocations from others could offer some explanations on how dislocations contribute to increase strength.

For polycrystalline iron, the equation 1.3.3.2 thus becomes: $(G = 8.06 \times 10^{10}$ Pa , b = 0.248 nm):

$$\sigma_{(disl.-density)} = 7.6 \times 10^{-4} \sqrt{N} \qquad 1.3.3.3$$

MPa

The modified Petch equation 1.3.2.1 thus becomes:

$$\sigma_y = \sigma_o + \sigma_{dd} + \sigma_{ss} + k_y\, d^{-\frac{1}{2}} \qquad 1.3.3.4$$

where: σ_{dd} is the contribution to the lattice friction stress from dislocation density.

1.3.4 Strengthening effect of carbonitride dispersion.

The precipitation hardening contribution to strength was found independent of the grain size, and can be related to the Petch equation through the flow stress component [94,98].

$$\sigma_y = \sigma_o + \sigma_p + \sigma_{dd} + \sigma_{ss} + k_y\, d^{-\frac{1}{2}} \qquad 1.3.4.1$$

where: σ_p is the contribution to the lattice friction stressfrom the precipitation hardening.

The effect of pearlite which is a second phase constituent, was related to the Hall-Petch equation [80,81] by Kouwenhoven [82],

$$\sigma_{yr} = f_\alpha \sigma_{y\alpha} + f_p \sigma_p \qquad 1.3.4.2$$

where σ_{yr} is the resulting lower yield strength of the material,

$f\alpha$, f_p and $\sigma_{y\alpha}$, σ_p are the volume fraction and lower yield strength of alpha iron and pearlite respectively. ($\sigma_{y\alpha}$ is σ_y in equation 1.3.4.1).

The strength of dispersion alloys is attributed to the influence of particles on dislocation movements along slip planes. Accordingly, second phase particle behaviour with dislocations could be divided into two groups, (1) particles can be impenetrable to dislocations, and on the other hand, (2) if dislocations can cut through particles, these particles are deformable or non Orowan. The former are the "non-deformable particles" (Orowan particles), which the dislocations can bypass following the Orowan [99] mechanism. The intrinsic properties of the latter particles is not important in determining the level of strength. The particles should be strong enough [100] to force the dislocations to bow between them before the dislocations bypass them. In defining the deformable particles, Kelly [101] wrote: "The second-phase particles may be cut or sheared by the glide dislocations at stresses below the Orowan stress". This suggests that less energy is required to cut through a certain particle size than to bypass the same particle size because the dislocation cannot shear it. It is therefore possible to visualize that the strengthening effect of deformable particles is less important than if it originated from undeformable particles.

It has been emphasized by Nicholson [100] that at some stage, there is a transition from deformable to undeformable particles at a critical particle size. The transition was shown tooccur before peak hardening in tempered material. A study by Papaleo and Whiteman [102] produced convincing microstructural evidence for such a transition in Fe - Si - Ti alloy. Recently, Kelly [101] discussed second phase particle strengthening.

Fig.1.3.4.1. shows a dislocation bowing out between two particles. The obstacle strength F is related to the dislocation line tension E by: $F = 2E \cos(\varphi/2)$. At the critical moment when the dislocation is unpinned: (1) If $\varphi = 0$, the particle behaves like an impenetrable obstacle (Orowan particle). (2) If $\varphi > 0$, the particle has been sheared (deformable particle). At this critical event, the shear stress necessary to cause the unpinning of the dislocation is:

$$T = \frac{F}{b\,S} = \frac{2E\cos(\varphi/2)}{b\,S} \qquad 1.3.4.3$$

where b is the Burgers vector;

S is the effective interparticle spacing.

With $\varphi = 0$, this equation becomes $T = 2E / bS$, which is the original Orowan equation [99].

It is possible to take into account the interaction between bowed dislocation branches. The effect is to lower the energy by a quantity which depends upon the separation between the two adjacent segments of the dislocation. With this correction, Ashby [103] showed that

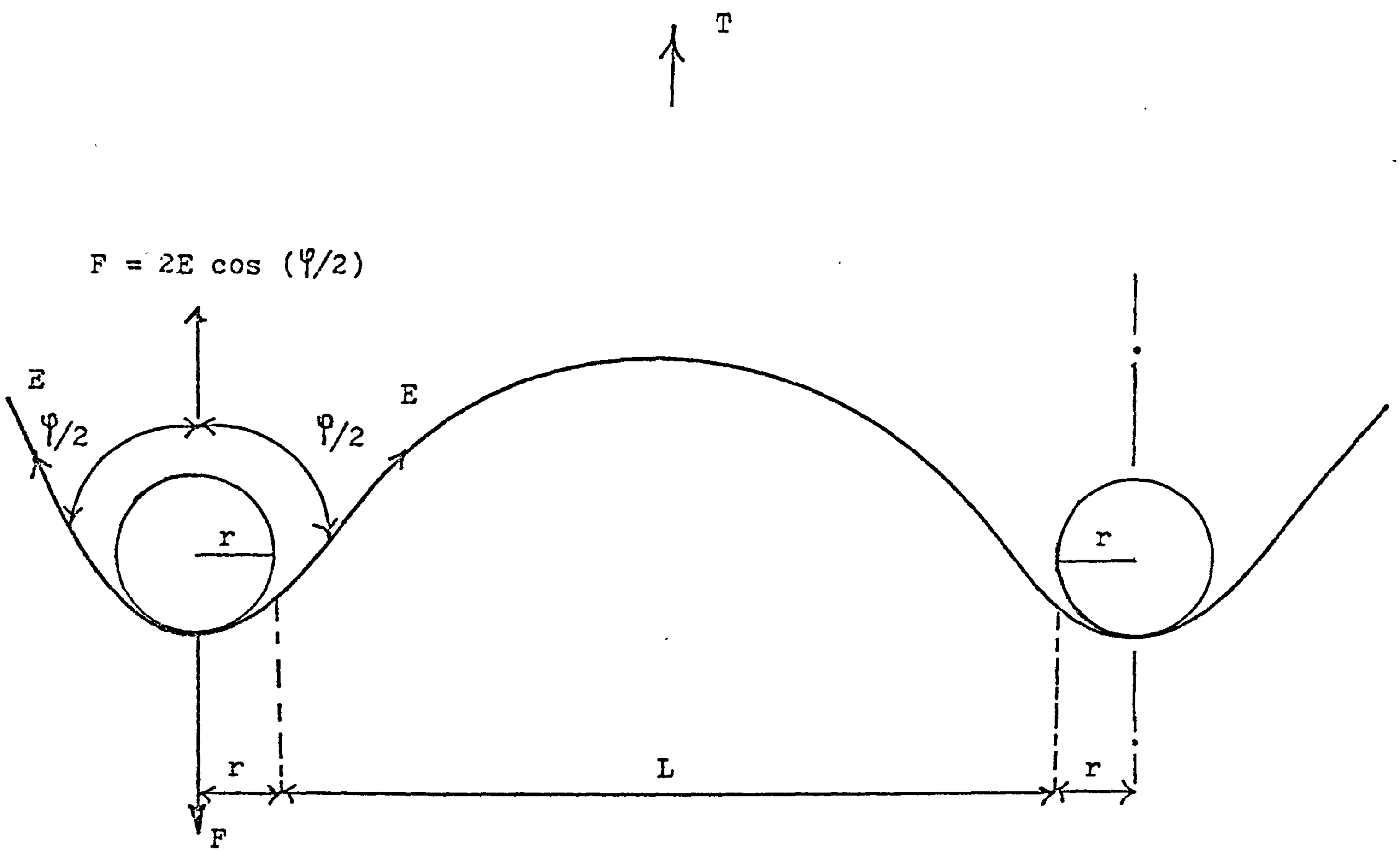

T : shear stress

E : dislocation line tension

F : obstacle strength

L : interparticle spacing

r : mean particle radius

Fig.1.3.4.1 Particle strengthening model.

the energy reaches a maximum before $\varphi = 0$. This is in line with observations of dipoles in the present study. A dipole ($\varphi = 0$) possesses less energy than a bowing dislocation at φ critical, a dipole is therefore a metastable configuration.

Bearing in mind the correction, Ashby [103] produced two equations: (assuming $\sigma_p = KT$, where K is a constant)

$$\sigma_p \text{ (edge)} = \frac{Gb}{2\pi S} \cdot K \cdot \ln (2r/r_o)$$

$$\sigma_p \text{ (screw)} = \frac{Gb}{2\pi S} \cdot \frac{1}{(1-v)} \cdot K \cdot \ln (2r/r_o)$$

the geometrical mean of these two equations being:

$$\sigma_p = \frac{Gb}{2\pi S} \cdot \frac{1}{(1-v)^{\frac{1}{2}}} \cdot K \cdot \ln (2r/r_o) \qquad 1.3.4.4$$

where σ_p is the contribution from precipitation hardening to the lattice friction stress;

G is the shear modulus;

b is the Burgers vector;

S is the effective interparticle spacing;

v is the Poisson ratio;

r is the particle radius;

r_o is the dislocation core radius ($\simeq 4b$).

Hirsch and Humphreys [104] mentioned that an equation based on the geometrical mean, provides a fair estimate of the actual friction stress. The above argument is only valid when the critical bulging ofadislocation is at $\varphi = 0$, however, the φ critical was shown to be greater than zero [103]. Although cross slip occurs in certain alloys

Ashby [103] maintained that it does not permit bypassing at a stress significantly lower than the Orowan stress. The equation 1.3.4.4 represents the currently accepted [101] Orowan equation. According to Ashby [103], this formula should be in 30% agreement with measured values. Gladman et al. [105] suggested (K = 2, σ = 2T):

$$\sigma_p = \frac{1.2\ Gb}{2.36\ \pi} \cdot n_A^{\frac{1}{2}} \cdot K \ln (r/b) \qquad 1.3.4.5$$

where n_A is the number of particles per unit area of the slip plane and $n_A^{-\frac{1}{2}}$ is the centre to centre interparticle spacing. They [105] further modified the equation to take into account the volume fraction and precipitate size only: the relationship is reproduced on Fig.1.3.4.2.

An important parameter present in equations 1.3.4.1 to 1.3.4.4 is the effective interparticle spacing (S). Corti et al. [106] have reviewed the various definitions of interparticle spacing. They are critical vis-à-vis publications that do not produce the mean particle size and volume fraction data. This would have enabled these published data to be converted to a single form for comparison purposes. Since the precipitation strengthening mechanism depends upon planar dislocation movements, the present study adopted a definition of interparticle spacing based on the average distance between particles in the slip plane. This general definition was also adopted by Kelly [101], Ashby [103] and Gladman et al. [105].

The effective interparticle spacing (S) as illustrated on Fig.1.3.4.1 is:

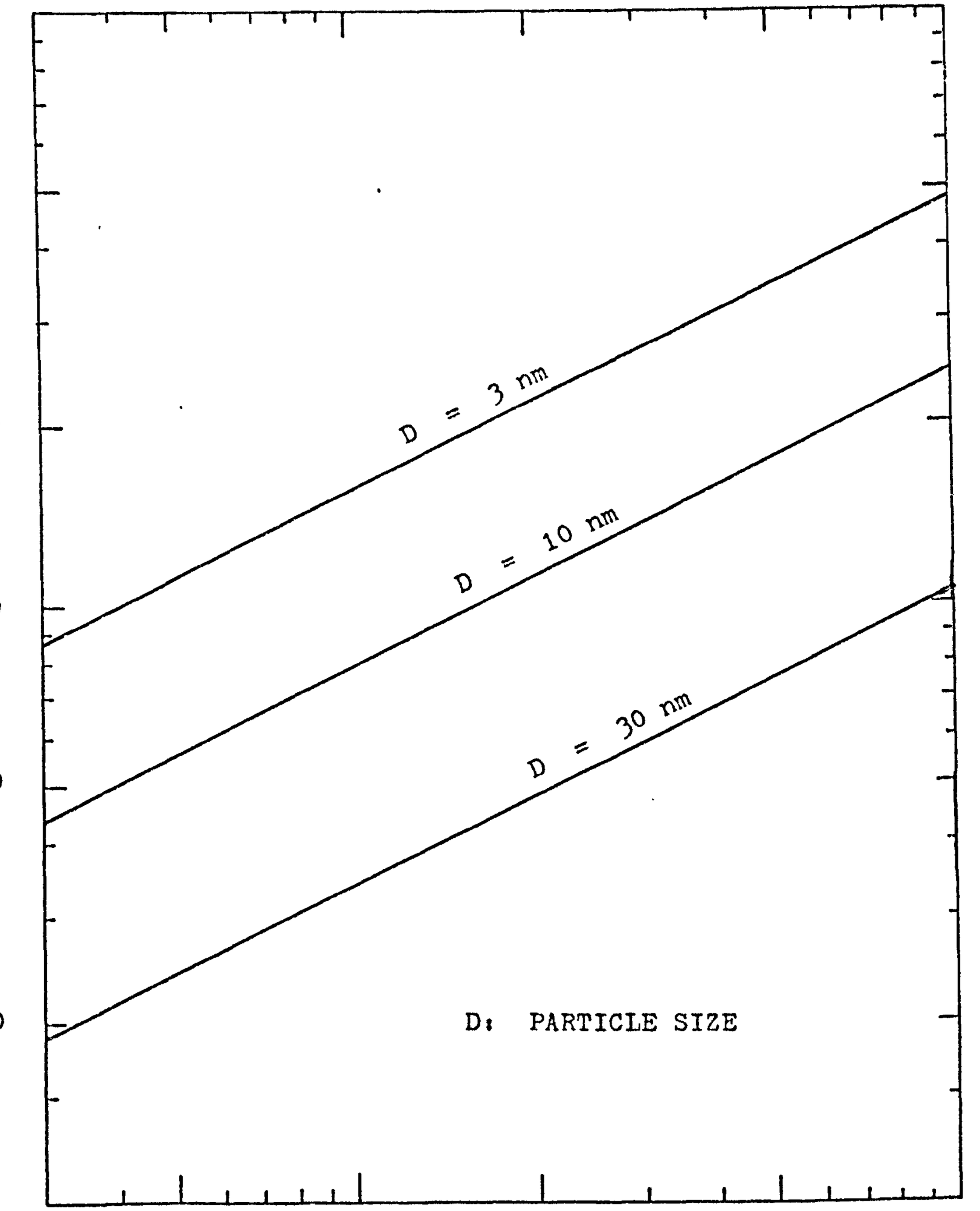

Fig.1.3.4.2 Orowan-Ashby Relationship from Gladman [105].

$$S = BL \quad , \quad \text{and } L = \frac{1}{n_A^{\frac{1}{2}}} - 2r$$

where B is a constant equal to 1.2 for a random array of impenetrable obstacles [107,108];

L is the interparticle spacing;

n_A is the number of particles intersecting the slip plane;

r is the mean particle radius.

The equation 1.3.4.4 becomes:

$$\sigma_p = \frac{Gb}{2.4\pi} \cdot \frac{1}{(1-\nu)^{\frac{1}{2}} \ (1 / n_A^{\frac{1}{2}} - 2r)} . K . \ln(2r/r_o)$$

1.3.4.6

The relationship with the volume fraction and measured particle size will be discussed in section 3.3.

When considering deformable particles, this equation should be multiplied by cos (φ / 2) and the breaking angle should be measured.

Other sources of contribution to σ_p are possible. These were recently reviewed by Kelly [101] and Brown and Ham [109] to mention only two sources. In steel, supplementary hardening can originate from: (1) difference between elastic modulus particle-matrix. This is equivalent to an increase of 3% in the effective particle radius of MCN. (2) coherency stresses; these are caused by misfit and different thermal expansion coefficients between particle and matrix. (1) and (2) produce "butterfly" shapedprecipitate when "seen" in transmission

electron microscopy. They probably cause a strengthening effect; however, Brown and Ham [109] did not find any convincing calculation of the magnitude of the strengthening effect. They suggested that a critical particle size in the order of a third for the size at which coherency was lost would produce maximum hardening.

Assuming a Baker-Nutting [33] orientation relationship for MCN, and a loss of coherency at 50% misfit, a simple calculation based on conventional misfit predits a loss of coherency at 0.2 - 0.4 nm thick to 4.0 -6.0 nm 'large' for VCN, and 0.2 - 0.4 nm thick to 1.0 - 1.5 nm 'large' for NbCN.

Other sources of strengthening, which were less relevant to the present study, include: (3) higher energy matrix-particle surface when the particle is sheared; (4) strengthening by ordered precipitate; and (5) strengthening effect from difference in stacking fault energy (SFE), for close packed particle-matrix system.

In this section, an attempt was made to describe strengthening mechanisms in steel. This section which ends the "Study of the Literature" will be used in connection with Chapter Six: "Interpretation and Discussion of results".

Chapter two: EXPERIMENTAL PROCEDURES.

In contrast to the study of the literature, which offered underlying reflections about some of the major principles or assumptions discussed in the present study, this chapter initiates the description of the experimental work carried out during the present study.

Three main aspects are presented: (1) the description of the material used, (2) the instruments developed or adapted (e.g. end quench test) and (3) the preparation of specimens for metallography and electron microscopy.

Another dimension of the experimental work, that is the experimental methods, will be discussed in the next chapter.

2.1 Materials and Analysis.

The materials used in the present investigation were vacuum melted by the British Steel Corporation, (The Corporate Laboratories - BISRA). The manufacturer also undertook a spectral analysis. Each alloy was subsequently analysed by a Quantovac in the Metallurgy Department. The analysis of the materials is shown in Table 2.1.

2.2 Heat-Treatment.

2.2.1 Fast cooling rates (>2 K.s^{-1})

Standard end-quench specimens (100 mm long by 25 mm D) gave cooling rates in the fast range. Each specimen to be solution-treated was sealed in silica glass under a low pressure of argon. An electric furnace having an actual hot zone bigger than 40 cm X 15 cm D was brought to the predetermined solution temperature. One hour at the soaking temperature was the standardized time, except that a five hour time was selected for Fe - 0.02C - 0.14Nb (material A); the solution temperatures are shown in Table 2.2. At the end of the heat-treatment, the furnace was filled with argon and the capsule was broken into pieces inside the furnace, and finally, the specimen was transferred to the end-quench tank unit. The specimen support was made of Sandanyo material to minimize heat losses. Four seconds represented a typical transfer time.

Material	C	Mn	Nb	V	N	Cr	Cu	Mo	Ni	P	S	Si	Sn
A	0.02	0.02	0.14	<0.003	0	0.01	0.01	0.02	0.01	0.004	0.004	0.01	0.002
B	0.12	0.02	<0.01	0.46	0	0.01	0.01	0.02	0.01	0.004	0.003	0.01	0.002
D	0.13	1.50	<0.01	0.45	0	0.01	0.01	0.02	0.01	0.004	0.007	0.01	0.002
F	0.03	0.06	<0.01	0.14	0.019	0.02	0.01	0.02	0.01	0.005	0.004	0.01	0.002
N	0.04	0.72	0.062	<0.003	0	0.01	0.01	0.02	0.01	0.004	0.004	0.01	0.002
V	0.10	1.53	<0.01	0.13	0.006	0.01	0.01	0.02	0.01	0.005	0.006	0.01	0.002

_____ : BISRA ANALYSIS

others: QTM ANALYSIS

P.S. The chemical composition is in weight percent. Reference is made in the text using an abbreviated form, e.g. steel A: Fe-0.02C-0.14Nb steel.

Table 2.1 Analysis of materials.

Material		Solution temperature	
		predicted*	adopted
Fe - 0.02C - 0.14Nb	(A)	1365 ± 50K	5hrs at 1525K
Fe - 0.04C - 0.06Nb	(N)	1350 K	1 hr at 1425K
Fe - 0.12C - 0.46V	(B)	1280 K	1 hr at 1325K
Fe - 0.13C - 0.45V	(D)	1285 K	1 hr at 1325K
Fe - 0.019N- 0.14V	(F)	1380 K	1 hr at 1425K
Fe - 0.006N- 0.13V	(V)	1265 K	1 hr at 1325K

* Formulae used to calculate predicted temperature for complete solution of M - X in γ-iron.

Nb C : $\log [Nb][C] = 2.96 - \frac{7510}{T} \pm 0.2$ ref. 110

V C : $\log [V]^{4/3}[C] = 7.06 - \frac{10,800}{T}$ ref. 16,17

V N : $\log [V][N] = 3.46 - \frac{8,330}{T}$ ref. 111

Table 2.2 Solution temperatures.

2.2.2 Intermediate cooling rates ($0.2\ K.s^{-1} < CR < 2\ K.s^{-1}$)

Initially, the intermediate cooling rates were obtained using various sizes of mullite tubes ($Al_6Si_2O_{13}$) filled with fused silica surrounding a round bar specimen. A thermocouple was placed in the centre of the actual specimen and the variation of temperature against time was monitored. To investigate more closely the effect of cooling rates on the transformation temperatures a Linseis dilatometer apparatus equipped with a vacuum furnace was adopted; the actual hot zone was 5 cm long X 2.4 cm D. By removing the furnace at various speeds over the 1.0 cm^3 specimen, the desired cooling rates were achieved.

2.2.3 Low cooling rates ($< 0.2\ K.s^{-1}$)

The same vacuum furnace coupled to a dilatometer apparatus provided the low cooling rates. The former was regulated by an AEI temperature controller which with thyristor action produced a very stable solution temperature. By driving the ten turn potentiometer, which set the controller, via a synchronous motor joined to interchangeable gears, it was possible to obtain different cooling rates down to $3 \times 10^{-3}\ K.s^{-1}$.

2.3 Dilatometry.

The Ar_3, Ar_1 and Bs, BF, whenever possible, were recorded by means of a Linseis differential dilatometer

operating under vacuum. The apparatus provided cooling rates between 2 $K.s^{-1}$ down to 3×10^{-3} $K.s^{-1}$. All the heated parts of the apparatus were silica glassware. Since silica glass began to collapse at 1475K, all specimens, except Fe - 0.02C - 0.14Nb (material A), were reheated in the austenitic range at the previously determined solution treatment for one hour, before cooling.

2.4 Metallography.

2.4.1 Sample preparation.

An identical technique was used to prepare samples for either metallographic examination or hardness identation. The usual practice of polishing through emery papers and ending on a one micron diamond wheel was standardized. Etching in 5% nital for ten seconds was observed to be sufficient to reveal all ferrite grain boundaries for all specimens except material A. Optical micrographs were taken on a Zeiss Ultraphot II.

2.4.2 Grain size measurement and second phase determination.

Grain sizes were measured as mean linear intercepts by counting a total of 500 grain boundaries from two right angle generated test lines. A Metals Research Quantimet (QTM) could have been used to obtain the grain size. However, this technique was not used because: (1) a bias could have been easily introduced by the

operator, (2) the QTM could also not differentiate the bainite from the ferrite, and (3) the QTM could not measure tiny grain sizes. Second phase was evaluated by a method of linear intercepts; verniers were moved alternatively over each phase.

2.5 Electron Microscopy.

2.5.1 Apparatus.

Electron microscopy examinations on carbon extraction replicas and thin foils were performed at 80 KV and 100 KV respectively in a Philips E.M. 200 fitted with a high tilt goniometer stage ($\pm$ 45°), a 360° rotation holder and a decontamination device. On a few occasions an AEI EM7 (1 Mev) equipped with a double tilt specimen holder (T $\pm$ 45°, T $\pm$ 60°) was used. This microscope was located at the Imperial College, University of London.

2.5.2 Preparation of carbon replicas.

The sample was metallographically prepared following an identical method to the one used for optical microscopy up to etching procedure. This method however, was modified as follows: (1) after the polishing with the one micron diamond polishing wheel, washing with soap under hot running water was carried out, (2) spraying with alcohol whilst still under water, (3) transferring the specimen to an alcohol bath and ultrasonically cleaning to remove any adherent particles, (4)

etching the dried specimen in 2% nital for 5-15 seconds, anf finally, (5) thoroughly washing with alcohol and drying prior to carbon coating.

Inside a Balzer's high vacuum coating unit Micro B.A.3., spectroscopically pure carbon was sprayed when the pressure gauge indicated lower than 5×10^5 mm of Hg. The change in colour produced by carbon deposition on a piece of Al previously covered with a thin gold layer (20 nm), permitted an estimate of the film thickness. The usual floating on deionised water followed the etchning in 5% nital and alcohol washing. According to the standard practice, 200 mesh copper grids supported small pieces of replica with an adjacent single crystal gold piece for calibration of the diffraction patterns.

2.5.3 Preparation of thin foils.

A suitable specimen for transmission electron microscopy should present the following characteristics: (1) the specimen must be thin enough to allow electrons to be transmitted without too much scattering, (2) it must be thick enough and sufficiently carefully prepared to be representative of the structures of the material, and (3) because iron is a magnetic material, the specimen should be small and even to reduce astigmatism produced by the interference of the specimen with the electron beam and the magnetic field of the objective lens. The useable thickness is limited to between 0.15 - 0.30 μm,

the latter figure representing the utmost limit at 100 KV.

Samples were prepared by standard techniques. A spark erosion process produced one millimiter slices which were planed to 0.25 mm. A further thinning with a solution consisting of 10% hydrofluoric acid (40% W/V) in 90% hydrogen peroxide (5 vol) reduced them to about 0.03 mm. The electropolishing terminated the preparation.

An electropolishing solution which operates at a low temperature avoids local heating of the foil during the actual reaction and reduces etching when the specimen is removed from the solution. The electrolyte used in the present study was one V/O perchloric acid (70% W/V) in methanol; an additional amount of two-butoxyethanol equivalent to 10 V/O was added to reduce the speed of the reaction. The foil was immersed between two parallel stainless steel sheet cathodes at a potential of 34 volts in the electrolyte kept at 200 K $\pm$ 3 K.

After polishing, the foil was carefully washed in methanol, ethanol and finally left in absolute alcohol ready for cutting. Whenever storage was required, the foil was kept under glycerol, in which it was possible to preserve a specimen in a viewable condition for up to three months. A small cut sample sandwiched between two 100 mesh copper grids was examined in the electron microscope. Clean specimen holders and fresh dessicating

agent (P_2O_5) in the camera chamber helped to prevent in situ oxidation of the foil.

2.5.4 Important measurements.

Dislocation density measurements were carried out from micrographs taken under two-beam conditions and with foil thicker than 0.16 micron. A line intercept method using concentric circles as test lines was utilized. The detailed method is described in section 3.2.

Precipitate was sized from carbon extraction replicas. The carbon replicas did not suffer the disadvantage of foils, that is the particle-matrix effects. A fine grain 35 mm film recorded the highly magnified particles and had the double advantages of economy and a capacity of forty exposures for a single session. The actual size determination was executed from electron micrographs enlarged to about 150 K for the 2-10 nm precipitate size range.

2.6 Mechanical testing.

2.6.1 Method for Hardness Tests.

Diamond Pyramid hardness measurements were determined by means of a Ernst Leitz Gmbh Wetzlar machine; the test was standardized using a load of one Kg. With this load a surface prepared similarly to metallographic specimens was sufficient. The rate of loading of approximately fifty $\mu m.s^{-1}$ was used to keep the transient

load as small as possible. The duration of the full load application was ten seconds. The overall experimental procedure of the ASTM E384 (1969 - Method of Microhardness of Materials) was adopted.

Ten parallel and equally spaced identations were performed at any one location on end-quench specimens, and at least fifteen measurable identations for other specimens. A Fortran program, provided the arithmetic mean with a five percent significance level on the arithmetic mean assuming a Student's t distribution for small samples.

2.6.2 Method for Tensile Tests.

Standard Hounsfield no 12 specimens were machined after heat-treatment. The average diameter of each specimen was measured at the nearest 0.01 mm. Specimens were finally tested until failure on an Instrom machine at a constant cross-head speed corresponding to a strain rate of 2×10^{-4} s^{-1}. The load cell was calibrated according to the manufacturer's recommendations and proper full scale loads were used; a zero suppression permitted expansion of any particularly interesting portion of the curve on a full scale of one KN, the most sensitive scale.

The curves were measured according to B.S. 18 (1971 - Method for Tensile Tests part two) to obtain ultimate tensile stress, upper and lower yield stress or the 0.2% offset proof stress, percentage elongation and area reduction. By unloading rapidly at the

maximum point of the strain-stress curve, and reloading, the Young's modulus was derived. Three specimens were tested for each heat-treatment investigated with this mechanical test and the mean values were recorded.

In this chapter, the experimental procedures used in the present study were reviewed. Most of the instruments were fairly standard. However, a great deal of care and patience was required in the manipulation of those instruments, which was imperative in electron microscopy.

The cooling rates obtained by end quench specimens will be evaluated in section 3.1, whereas the characteristics of the cooling curves for the various studied cooling rates will be discussed in section 4.2.

Chapter three: EXPERIMENTAL METHODS.

In relation to the "Experimental Methods", the following aspects were reviewed:

(1) Strengthening mechanisms in steel (Chapter 1.3)

(2) The instruments used in the present study (Chapter two).

The "Experimental Methods" is the part of a project which describes most of the techniques developed in relation to the parameters investigated; in the present study, these were mainly related to strength. However, before investigating the various components to strength, the cooling rate had to be determined for the end quench specimens. This will be discussed in the first section. The methods developed to measure dislocation densities, particle size and grain size are explained and discussed in sections two, three and four respectively.

This chapter is one of the major divisions in this study with respect to the handling of results (Chapter four), because they depend upon the methods used. The next chapter will present the findings.

3.1 Cooling rates for end quench specimens.

This section is concerned with the derivation of cooling curves for end quench specimens. Standard [112] end quench specimens were used to provide cooling rates in the 2-500 $K.s^{-1}$ range. The cooling curves could have been produced solely from empirical data, but in addition a mathematical treatment was considered for matching with available data from the literature. During cooling, heat was lost from specimens through: (1) the air surrounding the specimen and the radiation emitted from the specimen, (2) the water from the quenched end.

The heat lost through air and radiation alone was measured by inserting a thermocouple in the centre of the specimen and monitoring temperature changes against time. This data was plotted as dimensionless temperature against time, and used for any value of the initial temperature (solution temperature) of the specimen.

To evaluate the heat lost through the quenched end, the standard end quench specimen was considered to be a half portion of a solid bounded by two parallel planes (a finite slab). A solution to this problem was proposed by Carslaw and Jaeger [113].

The solution found its origin from the well known Fourier equation for an unsteady heat flow:

$$\rho \cdot c_p \frac{\partial T}{\partial t} = (\nabla \cdot k \nabla T) \qquad 3.1.1$$

where: ρ is the density of the solid

C_p is the specific heat at constant pressure

T is the temperature

k is the thermal conductivity

t is the time

If the thermal conductivity is independent of the temperature and position, equation 3.1.1 becomes:

$$\frac{\partial \theta}{\partial \tau} = \frac{\partial^2 \theta}{\partial n^2} \qquad 3.1.2$$

where: $\theta = \dfrac{(T - T_f)}{(To - T_f)}$ is the dimensionless temperature

and To, T_f are the initial and final temperature respectively.

$n = y/b$: dimensionless length, at y mm opposite to quenched end over the total length b.

$\tau = \alpha t/b^2$: dimensionless time at t seconds

$\alpha = k/(\rho . C_p)$: thermal diffusivity of the solid

for the initial condition of $\tau = 0$, $\theta = 1$, and for the boundary conditions of $n = \pm 1$, $\theta = 0$.

The solution is then expressed in the form of an infinite series:

$$\theta = 2 \sum_{i=0}^{\infty} \left[\frac{(-1)^i}{(i + \frac{1}{2})\pi} \right] \cdot \left[\cos (i + \tfrac{1}{2})\pi n \right] \cdot \left[e^{-(i+\frac{1}{2})^2 \pi^2 \tau} \right] \qquad 3.1.3$$

This model requires modifications because it is assumed that the thermal diffusivity (α) is a constant independent of the temperature and position. The algorithm used for correction is represented as follows:

(1) To permit exact calculation of the thermal diffusivity

(α), the dimensionless temperature (θ) of equation 3.1.3 was fixed. Consequently, a trial and error method was used to determine the dimensionless ($\mathcal{T}$).

(2) At a certain selected distance "h" from the quenched end and for $\theta_s > 0$, there is a variation of temperature from $\theta = 0$ at the quenched end to $\theta = \theta_s$ at the distance "h". As α is temperature dependent, an average value of thermal diffusivity had to be found.

(3) The detailed procedures involved the following:

(i) The specimen was divided into a multitude of small segments. For a particular temperature, α was considered constant in the whole segment. Consequently, at any time during quenching, the values of α and thus τ varied as discrete quantities along the bar.

(ii) For the first segment near the quenched end, the equation 3.1.3 was calculated for τ with α as a function of θ only.

(iii) At a distance "h" from the quenched end, α is given the value corresponding to the selected θ_s. The value of τ_s is thus found by solving equation 3.1.3. Values of θ corresponding to τ_s can be found for each segment between the quenched end and the segment at a distance "h" from this end. Corresponding values of α were assigned to each segment, and an average $\bar{\alpha}$ was obtained. The equation 3.1.3 can thus be recalculated using this "new" value of α .

(iv) The process in (iii) was repeated until the difference between the "old" α value and the "new" α value caused

the value of t (time) to change less than 0.001 second in the dimensionless τ.

Thermal diffusivity (α) data used in the present model was that for pure iron [114]. However, the effect of impurities (I) and quench efficiency (Qe) reduced the thermal diffusivity (α):

$$\alpha' = Qe\ (I.\alpha) \text{ or } \alpha' = Eff.\alpha \qquad 3.1.4$$

This situation was considered by replacing α by α' in equation 3.1.3.

The modified equation 3.1.3 was written in Fortran computer language and processed by an IBM 370/158. A run time of 300 s (CPU)was needed for every combination of initial temperature (To) and efficiency (Eff). The flowchart in Fig.3.1.1 illustrates the overall pattern.

After values of time (t) were obtained for water quench only, the effect of air and radiation losses were added:

$$\frac{1}{\Delta t'} = \frac{1}{\Delta t_{water}} + \frac{1}{\Delta t_{air\ +\ rad.}}$$

(eq.3.1.3) (empirical)

The cooling rate at 975K was calculated as an average cooling rate between 985K and 965K. A comparison with an empirical cooling curve for end quench specimens was necessary to assign a proper value to the "Eff".

Russell and Williamson [115] produced empirical values of cooling rates for end quench specimens, using steels containing approximately the same amount of impurities as the steels used in the present work. The values

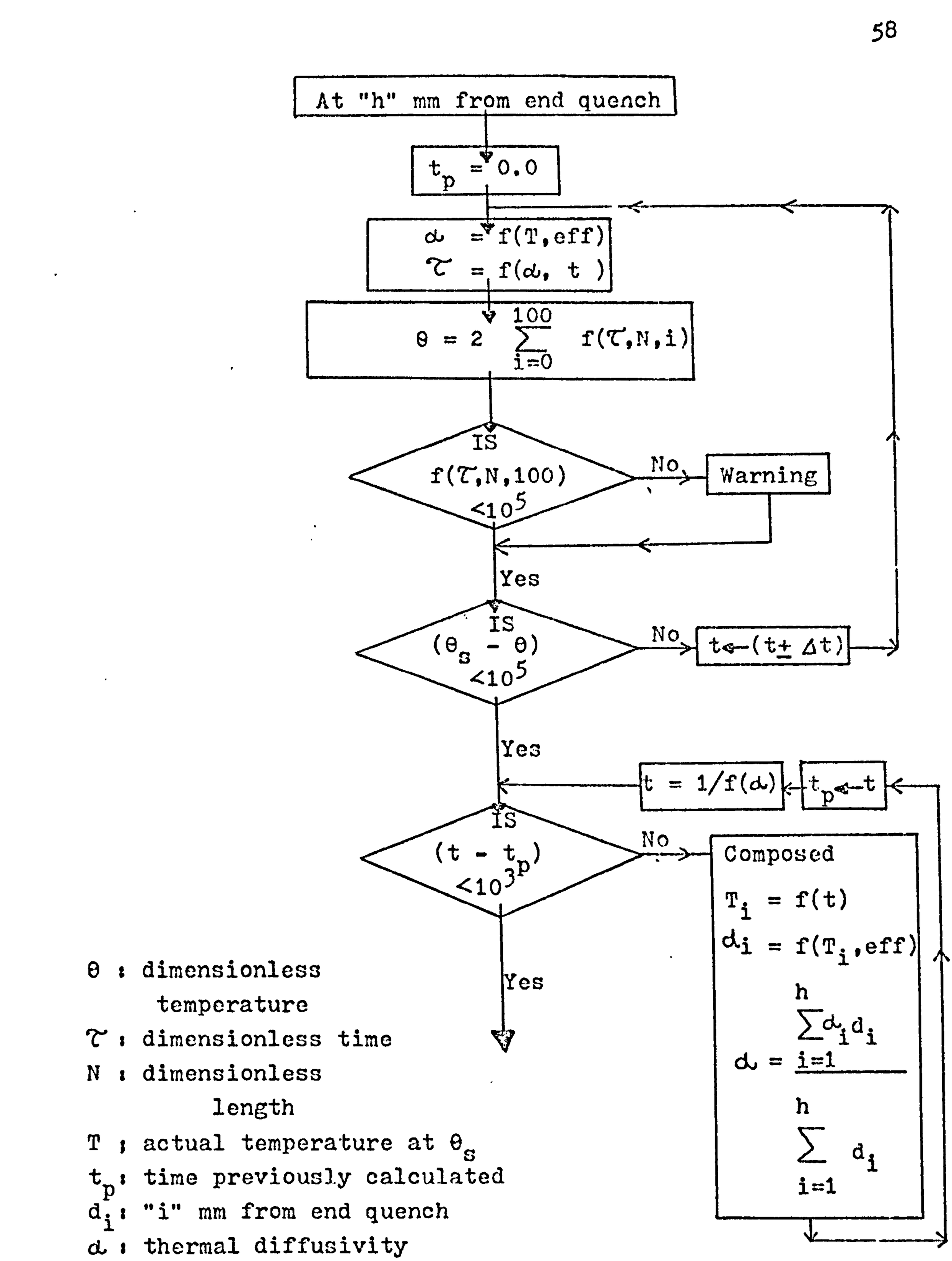

θ : dimensionless temperature

τ : dimensionless time

N : dimensionless length

T : actual temperature at θ_s

t_p : time previously calculated

d_i : "i" mm from end quench

α : thermal diffusivity

Fig.3.1.1 Flowchart of the end quench algorithm.

"Time (t) to cool from initial temperature to a selected dimensionless temperature θ_s."

obtained from the model are shown in Fig.3.1.2, whereas comparison with Russell can be seen in Fig.3.1.3. At 1125K, the combination of impurities and quench efficiency produced an "Eff" of 27%. Near the quenched end, the cooling rates predicted after computation were higher than those found by Russell et al.[115]. An explanation for this difference might be that whilst the efficiency of the quench was approximately constant during the whole quenching, it was not constant at the earliest stage, when the water was vaporized at the quenched end, thus reducing the efficiency.

The end quench test is generally described as a test in which a 25 mm bar undergoes water quenching at one end whilst the other end is air cooled only. From a solution treatment at 1125K, a 25 mm D bar would produce a cooling rate of $1.75K.s^{-1}$ at 975K if air cooled. In Fig.3.1.3 is reproduced the ASTM curve: "approximate cooling rates for an end quench specimen" [6]. From the maximum austenitising temperature recommended by the ASTM method (1195K) and from comparison of the ASTM curve with Russell's curve, both the ASTM and Russell's curves can be assumed to have originated from a similar initial temperature.

However, at a distance of 40 mm from the quenched end, the ASTM departs from Russell et al. to reach the equivalent air cooling rate of 25 mm D bar ($1.75K.s^{-1}$) at 63 mm. The knowledge of the cooling rate produced by water quenching only at 63 mm from the quenched end

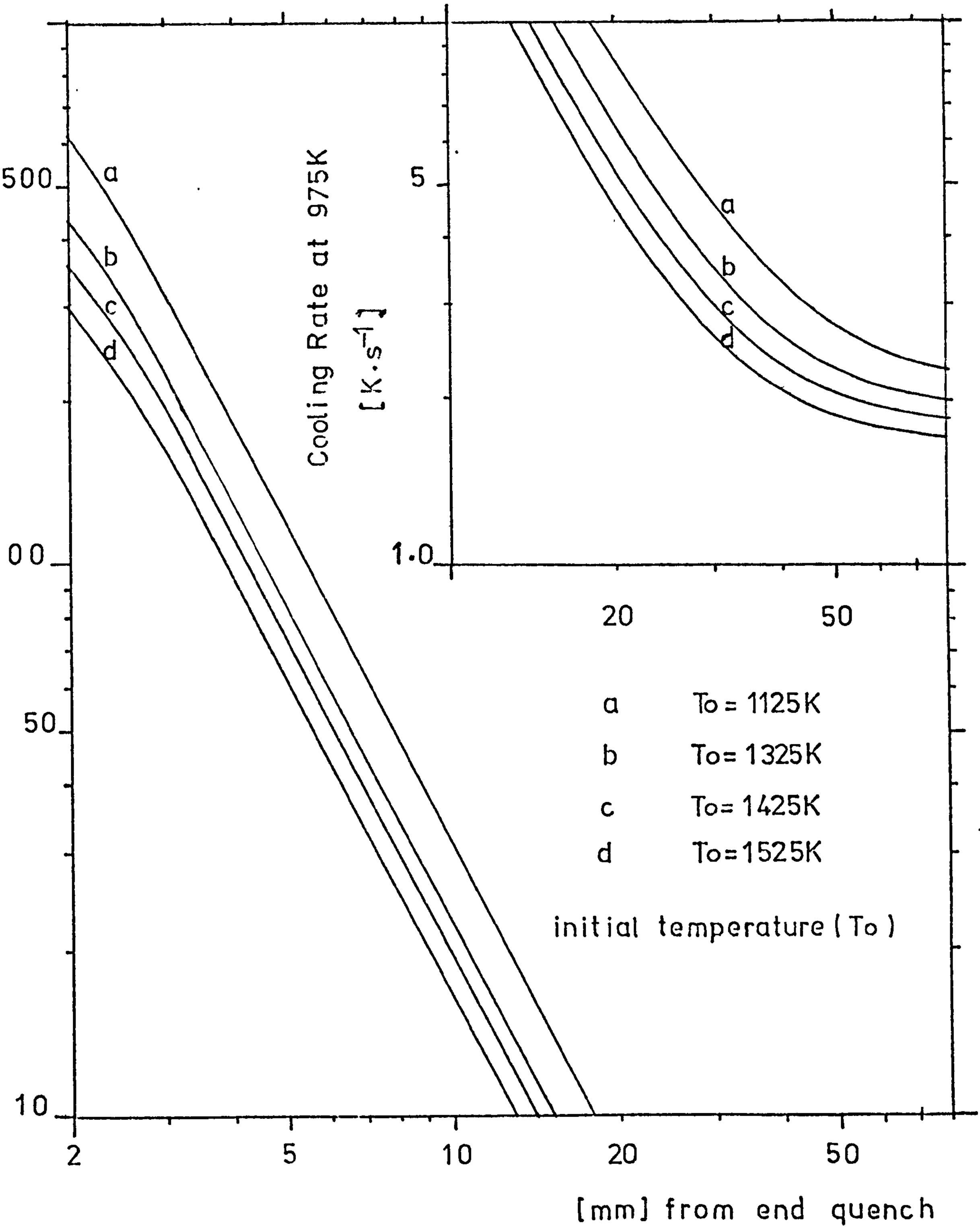

Fig.3.1.2 Cooling rate as a function of distance from end quench (computed from modified equation 1.2.3)

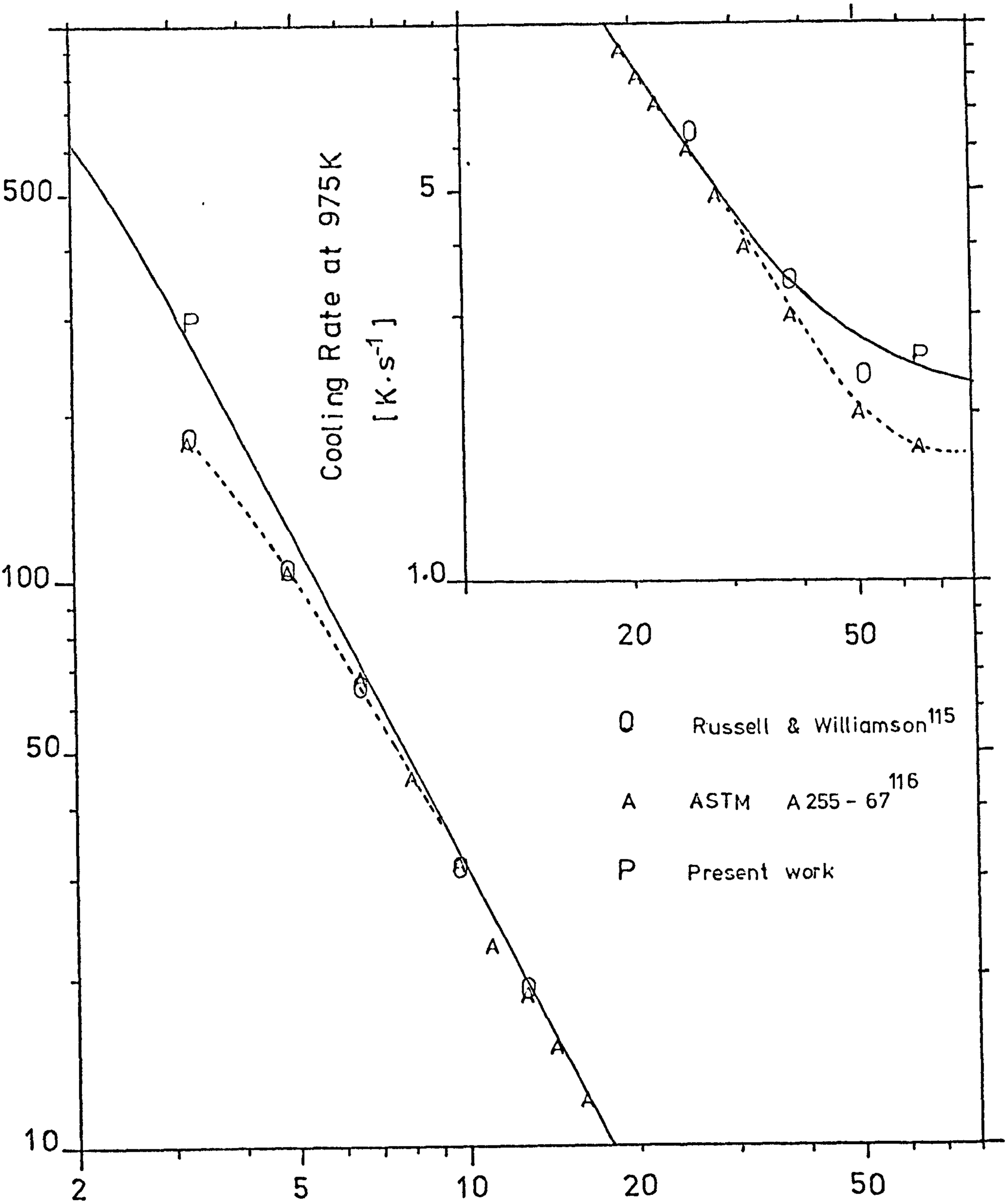

Fig.3.1.3 Cooling rate against distance from end quench from an initial temperature of 1125 K.

can indicate if the water quench effect is negligible vis-à-vis the air cooled effect. The axial cooling rate of a 200 mm D water quench bar was calculated to be 1 $K.s^{-1}$ according to Atkins and Andrews data [117]. Although the 1 $K.s^{-1}$ cooling rate for a 200 mm D is faster than a 200 mm thick slab (equivalent to an end quench specimen), it indicates that the cooling rate produced by water only is of the same order as the one produced by air cooled only (at 63 mm from the quenched end).

The present model thus predicts faster cooling rates compared to the ASTM results. A possible explanation of the discrepancy between this finding and those of the ASTM is that the latter perhaps wanted to emphasize the accepted definition of an end quench specimen acting as a 25 mm air cooled bar at the opposite end to its quenched end.

Consequently, whilst the predicted cooling rates near the quenched end are possibly too high, the faster cooling rates on its opposite end are thought to be of greater accuracy than those proposed by the ASTM results.

3.2 Determination of dislocation densities.

In this section, the method for determining dislocation densities will be described. Previous studies [118,119] showed that it is possible to determine the density of dislocations by counting the number of dislocation intercepts with a test line of known length. For instance, Hirsch [118] mentioned that a series of concentric circles used for test lines might overcome the effect of a possible anisotropic distribution of dislocations in the plane of the foil. Moreover, the requirements of randomness [120] are better met with a circular test line.

In the present study, dislocation densities were measured by counting dislocation intersections with a test line of two concentric circles. The same procedure was used by Stacker and Holt [121]. However, the present test line had an outside radius of 5 cm and an inside radius of $5/\sqrt{10}$ cm. The choice of the outside radius $R_{out} = \sqrt{10}\ R_{inner}$ intended to produce an inner area ten times smaller than the area encompassed by the larger one; this produced a pseudo-magnification (10X) of the former.

For random dislocations, the density (ρ) in cm length per unit volume (cm^3) is:

$$\rho = \frac{2\ P_L}{t\ V_b} \qquad 3.2.1$$

where: P_L : number of dislocation intercepts with the test line per unit length of test line. (P_L is a symbol largely used in Stereology [120])

t : thickness of the foil

V_b : proportion of visible Burgers vector for a particular low two-beam operating reflections (see Fig.3.2.1)

Also, images of dislocations are not mathematically thin, but they possess a finite width. When a dislocation appeared to be tangential to a test line, a count of $\frac{1}{2}$ was registered. The number of tangent touches should indicate the magnitude of the experimental error [120].

In the present study, a "sample" refers to the result of one measurement made with the test line (equation 3.2.1). In any one sample, therewere at least fifty intercepts counted with a circular test line (R_{outer} = 5 cm); fifty intercepts were considered to be sufficient [119]. The dislocations were counted from the projected image of the electron micrograph on a white sheet containing the circular test lines. The magnification was adjusted in order to produce between fifty to one hundred intercepts with the present test line; thus it was a compromise between counting a sufficient number of dislocations per test line and the tedious work of counting very many per test line.

At intermediate cooling rates ($\simeq$ 1 $K.s^{-1}$), the electron micrographs were taken at magnifications of 9 K to 20 K times, whilst the projected images were about 45 K times. Two to three " samples " were obtained from different areas of each micrograph. A number of thirty samples was considered to be statistically sufficient to represent the population [122] (dislocations) according to

$\bar{g}.\bar{b}$

$\bar{b}$ \ $\bar{g}$	<110>	<200>	<211>
	$\bar{g}.\bar{b}$	$\bar{g}.\bar{b}$	$\bar{g}.\bar{b}$
$\frac{1}{2}<\bar{1}11>$	0	$\bar{1}$	0
$\frac{1}{2}<1\bar{1}1>$	0	1	1
$\frac{1}{2}<11\bar{1}>$	1	1	1
$\frac{1}{2}<111>$	1	1	2

V_b	0.5	1	0.75

Fig.3.2.1 Fraction of visible dislocations (V_b) under different two-beam operating reflections.

the normal curve; this represented about ten different areas of foil. Sampling was avoided in regions where sub-boundaries or recovery structures were present. Counting in these regions can result in dislocation densities ten times higher than the surrounding matrix. No dislocation determination was carried out in areas where grains intercepted the specimen edge.

The electron micrographs were taken under two-beam operating reflections to take into account the exact proportion of missing Burgers vectors of dislocations as shown in Fig.3.2.1. Imaging in such a condition avoided also multiple images of the same dislocation, thus improving the quality of the micrograph. In an attempt to find out the type of Burgers vector present in b.c.c. iron, Hale and Dingley[127] used numerous low and high order two-beam operating reflections to identify separately each type of Burgers vector. However, France and Loretto [124] pointed out that two-beam high order reflections produced images of dislocations from "missing" Burgers vectors. In a subsequent paper, Hale and Brown [123] accepted that the majority of dislocations present in iron were of $\frac{1}{2}$ a<111> type. In the present study, the dislocations present in iron were all considered to be $\frac{1}{2}$ a<111> type, in order to calculate the proportion of visible dislocations under a particular low order two-beam condition (Fig.3.2.1).

Another important quantity used in the determination of dislocation densities (eq.3.2.1) is the foil thickness. The thickness of the foil was measured on occasions by

stereo-pair micrographs, but mainly by counting grain boundary fringes. The stereo method seemed interesting; however, the greatest difficulty occurred when measuring the length of dislocations. For instance, in an illustration [125] of the method in Al - Cu, a thickness of 212 nm $\pm$ 100 nm was obtained with a tilt of 20^{o} at 100 KV. Whilst an error of 100 nm is acceptable when viewing a thicker specimen at One Mev, the stereo-pair method does not seem more accurate for measuring foil thickness in iron than the grain boundary fringes method.

The thickness of the foil is obtained by counting grain boundary fringes in the latter method. In bright field, usually white fringes [118] are counted. However, Fig.3.2.2 shows that when black fringes are counted instead of white fringes, the thickness is given by: $t = n\xi^{w}_{g} \pm \frac{1}{2}\xi^{w}_{g}$, where ξ is the extinction distance depending upon two-beam reflections; the error can be further reduced due to different values of $n\,\xi^{w}_{g}$.

Studies [126] on the HVEM showed that the representativeness of the bulk material is preserved when the thickness is greater than 100 nm. However, in the present study, it was found that in foil thickness between 100 to 150 nm, the measured dislocation density (ρ) had a lower value than ρ measured in areas thicker than 150 nm. Therefore, micrographs used for dislocation density determination always had a foil thickness greater than 150 nm (about 6 ξ_{110}) and were typically between 200 and 270 nm.

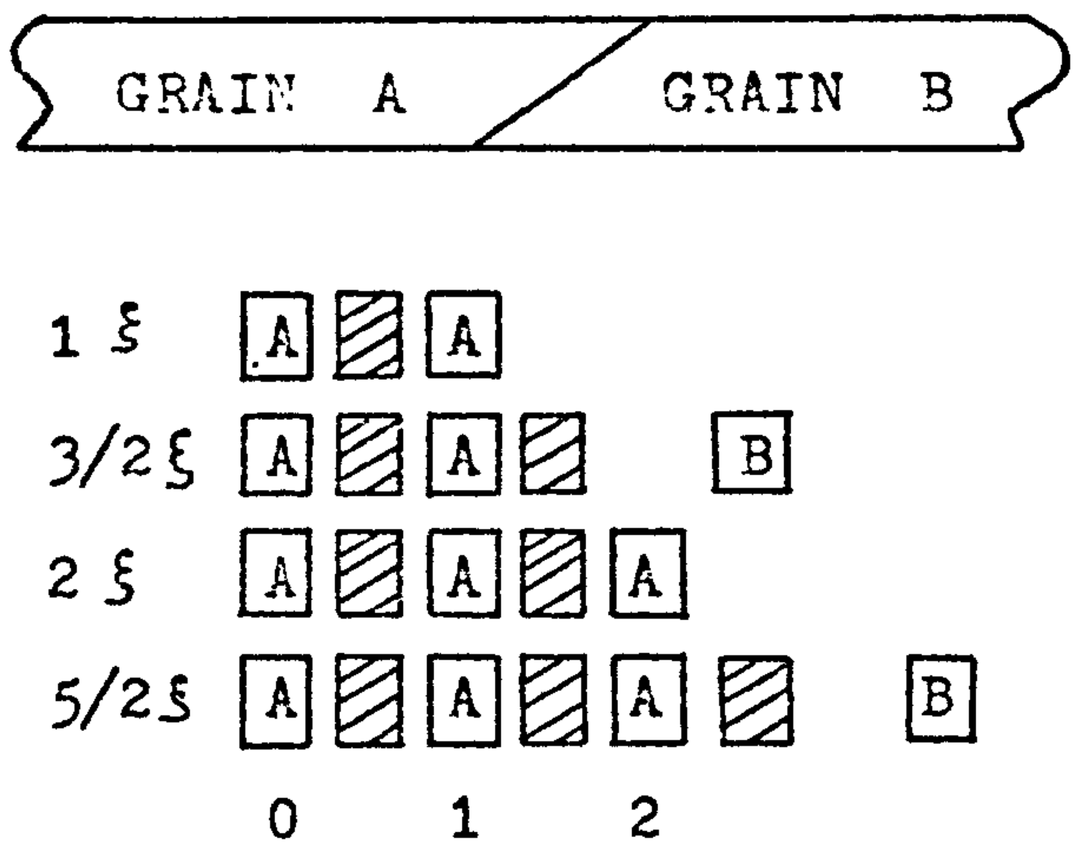

$n_b = 1$

$n_b = 2$

$n_b = 2$

$n_b = 3$

$$t = n_b \, \xi_g^w$$

where: $\xi_g^w = \xi_g / (1 + w^2)^{\frac{1}{2}}$

$t \rightarrow$ foil thickness

$n_b \rightarrow$ number of black fringes

$\xi \rightarrow$ extinction distance

$g \rightarrow$ two-beam operating reflection

$w \rightarrow \dfrac{a \, g \, \xi_g}{L}$

where a is the distance of the Kikuchi line from the g operating reflection

L is the camera constant.

Fig.3.2.2 Foil thickness measurement at grain boundary.

3.3 Analysis of MCN particle size distributions in metallic materials using carbon replicas.

The technique for preparing a clean carbon replica was described in section 2.5.2. The MCN particles were assumed to be small and hard, and therefore they were not sectioned when the specimen was sectioned, polished and replicated. Ashby and Ebeling [128] mentioned that a carbon replica is suitable for measuring particles in the 10 - 1000 nm range; carbon replicas are not however, suitable for determining the volume fraction of particles. When the volume fraction was known, the method was believed to enable the determination of the number of particles per unit area (n_A) and the spacing between them [128,129]. In previous studies [128,129] an insistence was placed upon: (1) the care in preparing carbon replicas and (2) the systematic error in the determination of n_A.

In those studies [128,129] the particle analysis was based on a surface distribution of particles. Although it seems an acceptable treatment for large particle sizes, it is important to ascertain what thickness of material the carbon replica extracts, as shown in Fig.3.3.1. Consequently, the distribution of a small particle size in carbon replicas is more likely to be a volumetric distribution as opposed to a surface distribution.

The use of direct carbon replicas from metal surfaces was preferred to thin metal foils to perform the measurement of particle size in the range 2 - 10 nm. The main

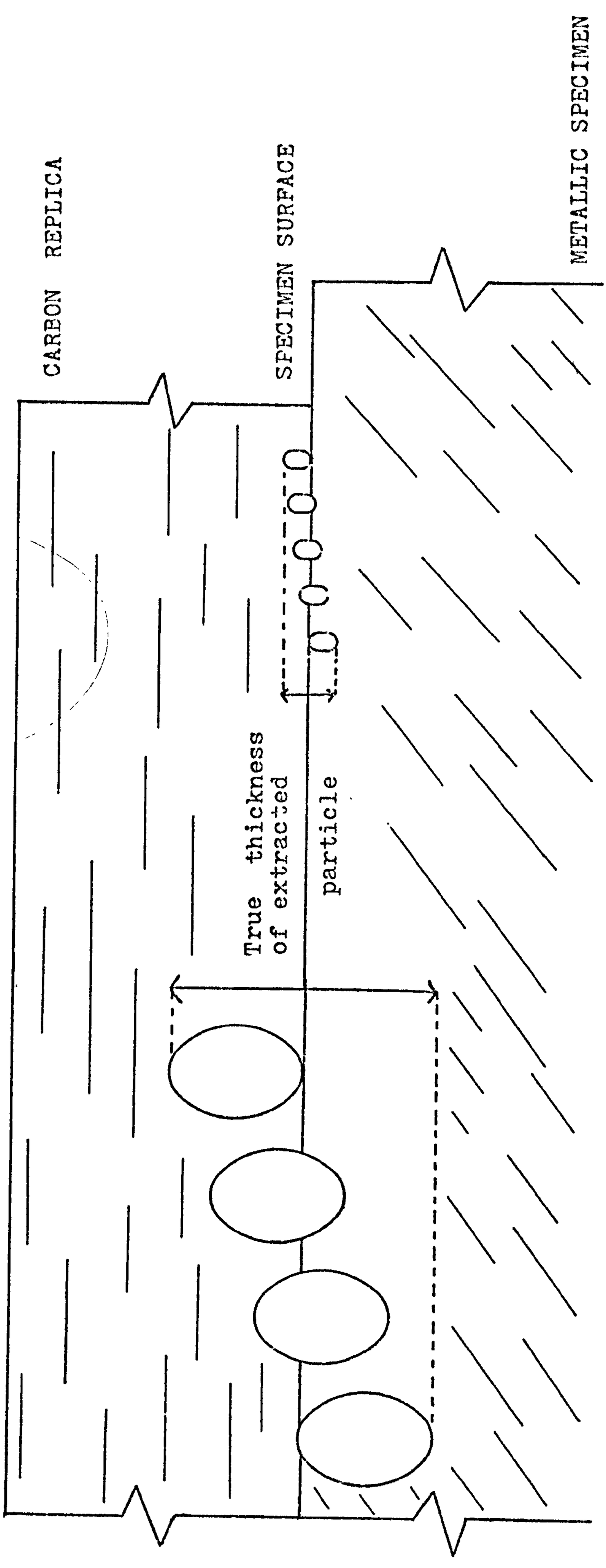

Volumetric distribution of particles in carbon replica.

Fig.3.3.1

restrictions for particle size determination in thin foils are: (1) the particle-matrix interactions (e.g. strain fields and dislocation loops around particles), (2) sampling (several samples are needed for one measurement) and (3) overlaps of particles which should be mathematically corrected. It has been mentioned that the correction method for overlapping particles is very tedious, and also that the determination of particle size and volume fraction in thin foil is somewhat pedantic [130].

The limiting factors for a replica are its thickness and its self structure. There is little self structure for a carbon replica as compared to a plastic replica, and it is easy to prepare a carbon replica as thin as 15 - 20 nm. The resolution obtainable in the electron image of inherent details in a carbonaceous specimen (e.g. biological specimens, plain carbon replicas) is in the order of a tenth its thickness [131]. Practically a difference of 2 nm in the thickness of a carbon replica can be detected. The failure to attain high resolution in carbonaceous specimens was ascribed to lack ofcontrast [131]. However, the maximum resolution of inherent details in the carbon replica was less important since the measurement of individual extracted metallic particles was the main parameter investigated. The scattering factor of VC is four times the scattering factor of Carbon, and it certainly improves the contrast. This could explain why high resolution was claimed in carbon extraction replicas [132,133]. It is thought that the resolution achieved was of the order

of the resolving power of the instrument, which is about 1.0 - 1.5 nm when fitted with a goniometer stage. The direct carbon extraction replica was mentioned earlier on to produce a volumetric distribution of particles as opposed to a surface distribution. It is assumed that all particles in Fig.3.3.1 are captured. These particles are embedded to different depths in the surface of the specimen and are touching or intersecting the specimen surface. The component "T" is the effective thickness of the volume of precipitate, and it is dependent upon the precipitate size. To assume a surface distribution would lead to an erroneous result in the volume fraction and the mean particle size.

When the determination of particle size is effectuated through the sizing of particles into different class intervals, there is a specific volume for every interval. The different "volume" of precipitate can be normalized and a corrected mean is therefore obtained. However, the result is a corrected mean; the uncorrected mean and standard deviation are presented in Chapter four: RESULTS for comparisons with other studies.

Different quantities of MCN will precipitate at different cooling rates; the measured volume fractions obtained from carbon replicas were mathematically normalized with respect to the cooling rate producing the highest volume fraction measured. Following this treatment, other measured volume fractions at different cooling rates were adjusted according the the calculated theoretical

volume fraction.

Small MCN particles were observed to be disc shaped, and the latter can be approximated to an oblate ellipsoid (ellipse rotated around the minor axis). The ratio, major axis to minor axis was determined by the ratio of the conventional misfit in the Baker-Nutting orientation relationship with alpha iron. This ratio was considered constant (VCN$\simeq$15) over the whole range of particle size. This aspect will be discussed further in section 4.5. The three dimensional parameters of a particle are then completely defined when the major axis of the two-dimensional projected image is measured.

An attempt was also made to measure the effective thickness (T). If the ratio major axis ($\frac{D}{2}$) to thickness (t) of the particle is large, as it is for VCN, the value of T is dependent upon only D and the angle φ that the major axis of the particle makes with the surface. Fig.3.3.2 illustrates this concept; therefore $\cos(\varphi) = \frac{D\ min}{D\ max}$,

where D max is D measured, and $T = 2D \sin(\varphi)$. However, the particles can be misoriented during the extraction. A value T = 2D produced better results from volume fractions, and this relationship was adopted throughout the present study.

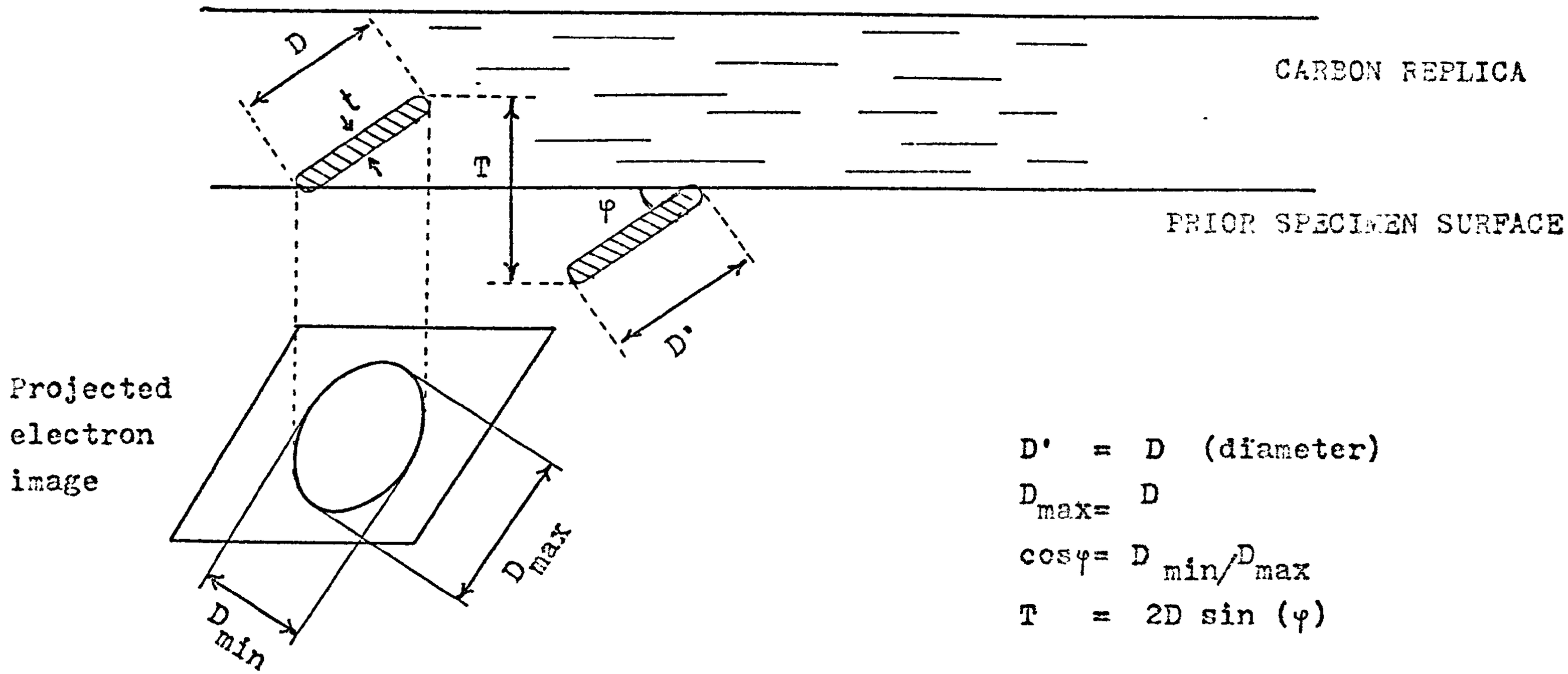

$D' = D$ (diameter)

$D_{max} = D$

$\cos\varphi = D_{min}/D_{max}$

$T = 2D \sin(\varphi)$

Fig.3.3.2 Measurement of the effective thickness (T)

3.4 Estimation of the error on grain size measured by the linear intercept method.

Grain size is often expressed as the mean intercept length [94,134,135]. This method implies counting grain boundaries intercepting a test line of known length. The method is simple but offers no way of finding a statistical error, except by measuring several times the same specimen with either the same number of counts each time or the same length of test line. This section discusses a method of evaluating the error made when measuring grain size by linear intercept method. The error was related to the number of grain boundary intercepts counted.

In the present study, the scheme adopted was to generate test lines at right angles to each other, and to record the number of intersections as the specimen moves under the crosshairs of the microscope. This scheme had the double advantage of being able to establish the degree of preferred orientation and was easily adaptable to record the percentage of second phase.

In the intercept method, the intercept length over a grain varies from zero to a maximum dimension for every grain measured in a particular cross section of the material investigated. Another important consideration is that the cross section plane cuts only a few grains at their maximum size. The conversion of mean intercept length to true volume diameter requires the assumption of an arbitrary

grain shape; this subject has been reviewed by Thompson [136]. However, the important quantity to consider is some average distance across randomly orientated grains, rather than a maximum dimension [137]. Following the above approach, the mean intercept method, being such an average, was adopted to evaluate grain size throughout this study.

To estimate the statistical error in evaluating the mean intercept, the standard deviation had to be derived. This was achieved by measuring each individual grain on the test line. This was extensive time consuming work. An average value was sought for application to each specimen in the present study. All the materials, on which grain size determination was carried out, had been previously solution treated in austenite and continuously cooled. There was, also, no sign of preferred orientation in these materials. Therefore this suggested that the distribution of grains from one sample to another should be alike. Following this assumption, the ratio: standard deviation (s) to arithmetical mean ($\bar{X}$) should be almost constant. This occurred for a few investigated samples of various compositions and grain size. The ratio $S/\bar{X}$ was a constant equal to 2/3. Consequently, the 95% confidence limit ($\Delta\bar{X}$) was expressed as a function of $\bar{X}$ only:

$$\Delta\bar{X} = 1.96\ S/\sqrt{N}\ ,\Delta\bar{X} = 1.3\ \bar{X}/\sqrt{N} \qquad 3.4.1$$

where: $\bar{X}$ is the arithmetical mean (the mean intercept) for N grains.

Data collected on a test line intercepting 250 grains would produce an $\Delta\bar{X}/\bar{X}$ = 8.2% for 95% confidence limit on

the mean. There is good agreement with the 8% value quoted by Pickering and Gladman [99] for similar conditions. In the present study, it was usual practice to evaluate the mean intercept after counting at least 500 grains. Therefore, less than 6% of the error ($\Delta\bar{X}$ / $\bar{X}$) might be attribuable to this process.

With this section, the main experimental methods developed and used in the present study have been discussed. Strengths and weaknesses of these methods were pointed out, but these aspects will be re-appraised in detail in the next chapter: THE RESULTS.

Chapter four: RESULTS.

This chapter, the results, is concerned with the findings gathered, from the instruments used, or from the experimental methods developed, in the present study. An attempt will be made to answer two of the objectives set out at the beginning of this study, namely:

(1) How does the strength vary with cooling rate in vanadium and niobium steels?

(2) How can this variation be explained (i.e. an investigation into the strengthening mechanisms in steel).

The third objective, which was concerned with the changes in the microstructure in relation to cooling rate, will be studied in the next chapter: STUDY OF MICROSTRUCTURE.

Before commenting upon the results, a word should be said about the use of SI units [138,139]. A special effort was made in the present study to use SI units whenever possible. The SI units system is a coherent system with only one unit for each physical quantity, well defined symbols and decimal prefixes. "Le système international d'unités" (SI) is not a new idea and found its origins in the 16^{th} century. However, the year 1790 could be regarded as an official date; that is when the "Assemblé nationale française" requested l'Académie des Sciences" to work out a system of units for world wide adoption. It is believed that the use of an international system of units will permit greater cooperation and better universal understanding.

4.1 Hardness ($Kg.mm^{-2}$) against cooling rate ($K.s^{-1}$).

Hardness ($1HV = 1Kg.mm^{-2}$) using a one Kg load was plotted against cooling rate ($K.s^{-1}$) for each material investigated. Two groups of steels were selected: (1) three steels with vanadium additions, and (2) two steels with niobium additions. In the vanadium steel group, the carbon content was approximately 0.1C weight percent (w.%) for all the three steels. The first material (Fig.4.1.1) had a vanadium content (0.46 w.% V) adjusted to produce a stoichiometric composition of VC; 1.5 w.% manganese was added to the second steel (Fig.4.1.2). The third steel was modified to the typical of a commercial composition (Fig.4.1.3); this required the vanadium to be reduced to a maximum of 0.15 w.% approximately.

In the niobium steel group, one steel had a composition chosen to produce a stoichiometric composition of NbC (Fig.4.1.4). The volume of additions was limited by the maximum temperature attainable by the furnaces used in order to achieve complete solution of NbC. The second Nb steel (Fig.4.1.5) was typical of a commercial niobium addition (i.e. 0.6 - 0.7 w.% maximum).

In the figures, the length of the bar at each location on the cooling curve represents the error of hardness measurement; its value represents the 95% confidence limit on either side of the calculated mean. Fast cooling rates ($> 2K.s^{-1}$) were measured on end quench specimens; the conversion from measured distance on end quench specimens

to cooling rates were previously described in section 3.1. Although the conversion model contains limitations, it is believed that the experience gained in locating the distance on end quench specimens (therefore the equivalent cooling rate), has reduced the error to a minimum. The lower cooling rates were read directly from the recorded time-temperature curves of continuoulsy cooled specimens.

All the curves were traced by free hand and it can be noted that a peak hardness is present in every figure. For niobium steels, these peaks are magnified due to a change of hardness scale on the ordinate axis. In Fig.4.1.1, it was possible to measure independently both the hardness of the bainite and the ferrite; in this Fe - 0.1C - 0.46V steel, the rise in hardness follows the appearance of the first ferritic grains in the material. In Fig.4.1.2, the addition of manganese seemed to have caused the peak to appear at a lower rate than in the material without a manganese addition.

The effect of the decrease in vanadium content seems to have produced more of a plateau than a definite peak (Fig.4.1.3). In Fe - 0.02C - 0.14Nb steel, the hardness started to increase even at very high cooling rates ($80K.s^{-1}$) corresponding to the presence of a low carbon martensitic structure (Fig.4.1.4). Where the curve is showing a sharp decrease in hardness ($\triangleq 2K.s^{-1}$), the structure was observed to have changed from bainite to almost all ferrite. The Fig.4.1.5

shows a typical commercial composition of a niobium steel. The addition of manganese produces a plateau instead of a peak. The same effect was observed in vanadium steels.

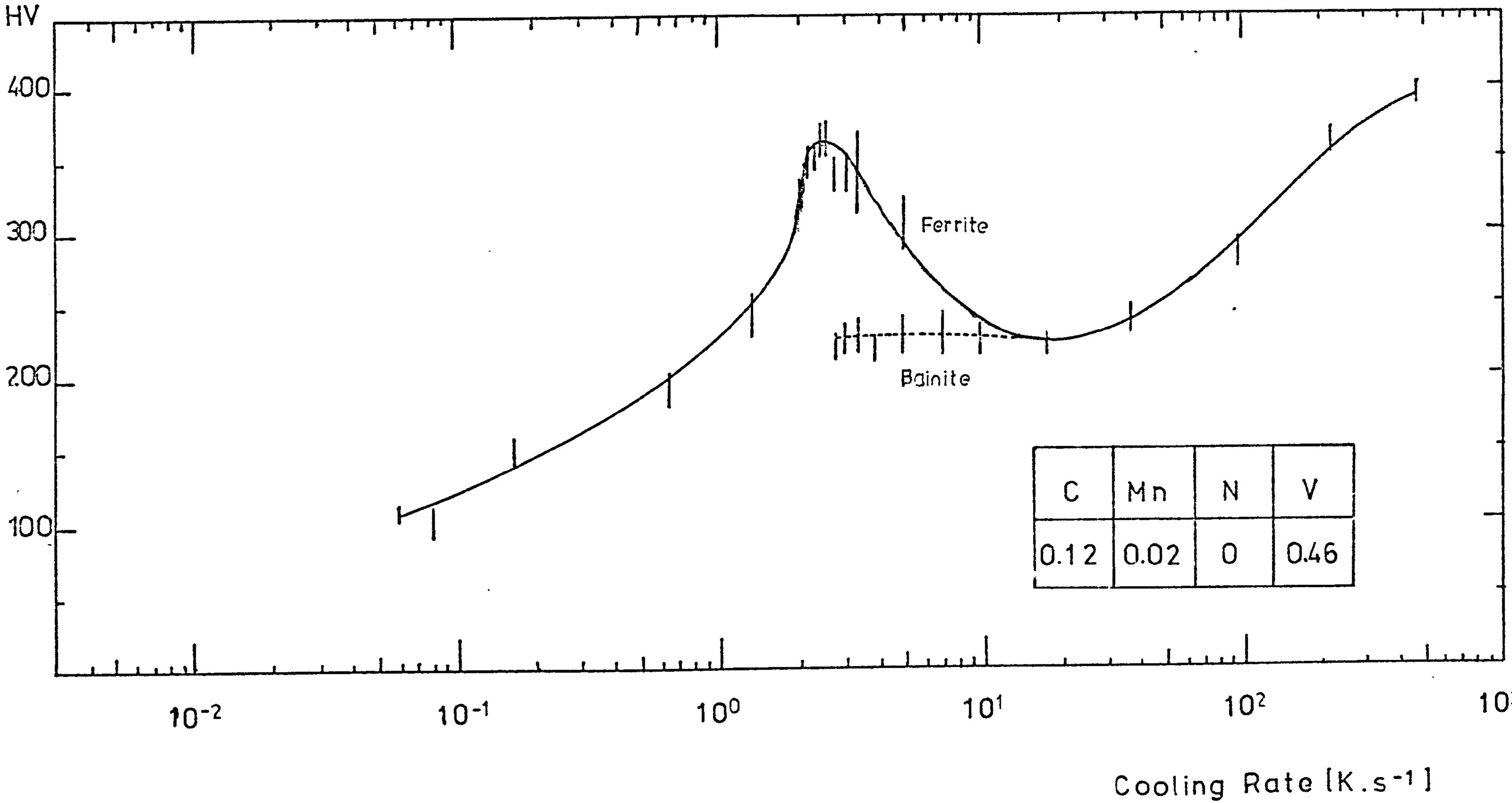

Fig.4.1.1 Graph of hardness against cooling rate in high vanadium steel.

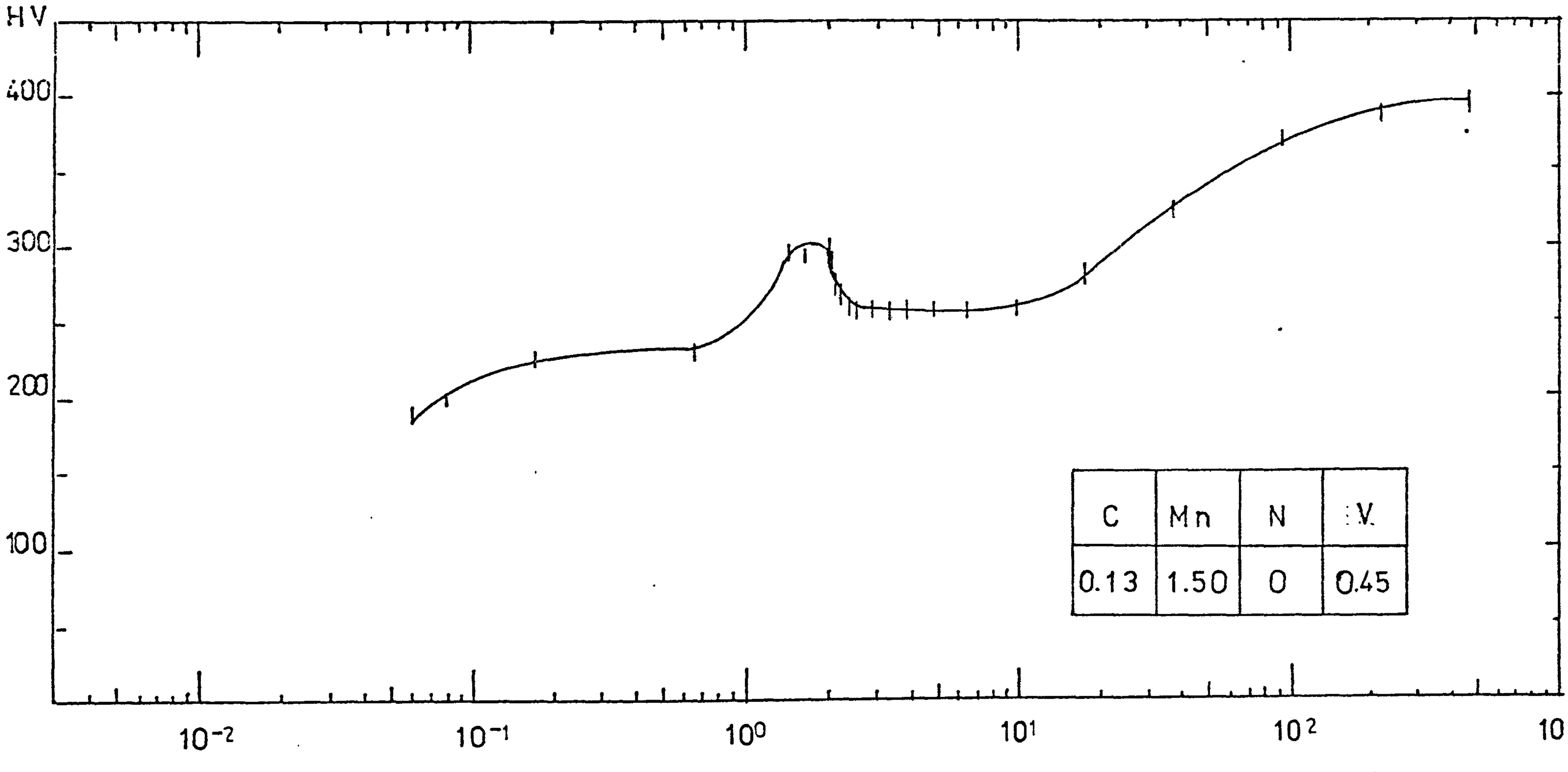

Fig.4.1.2 Graph of hardness against cooling rate in high vanadium-manganese steel.

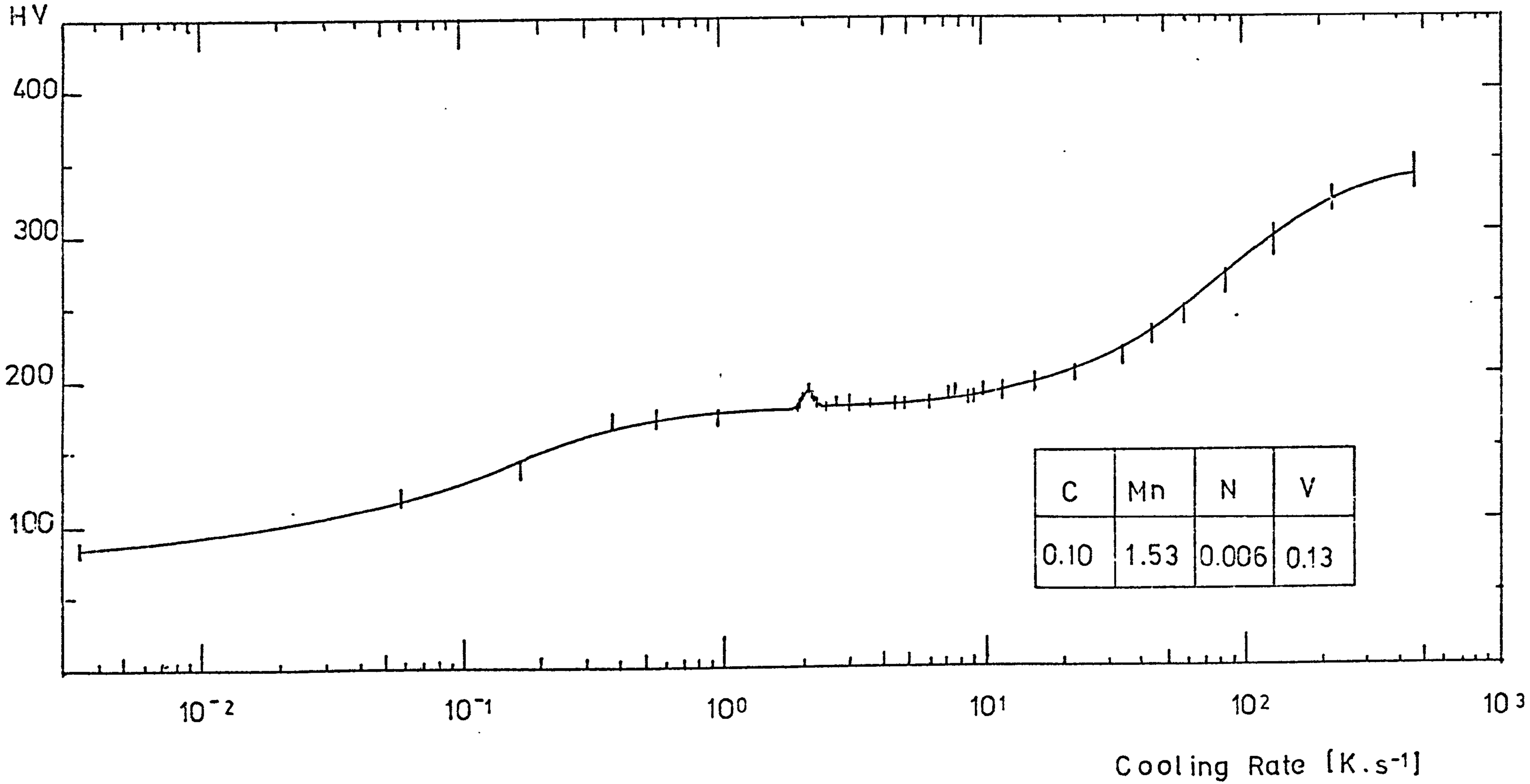

Fig.4.1.3 Graph of hardness against cooling rate in low vanadium steel.

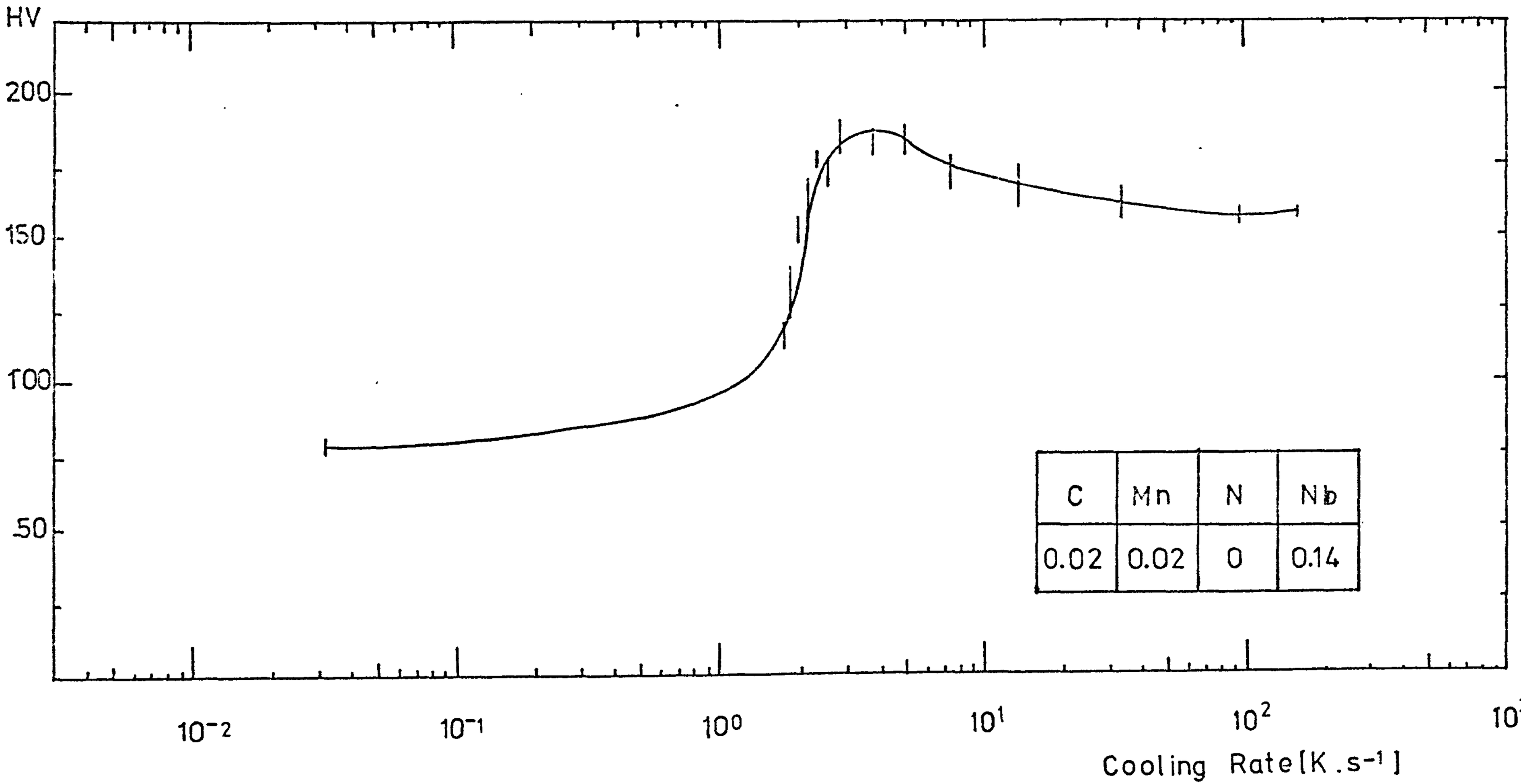

Fig.4.1.4 Graph of hardness against cooling rate in niobium steel.

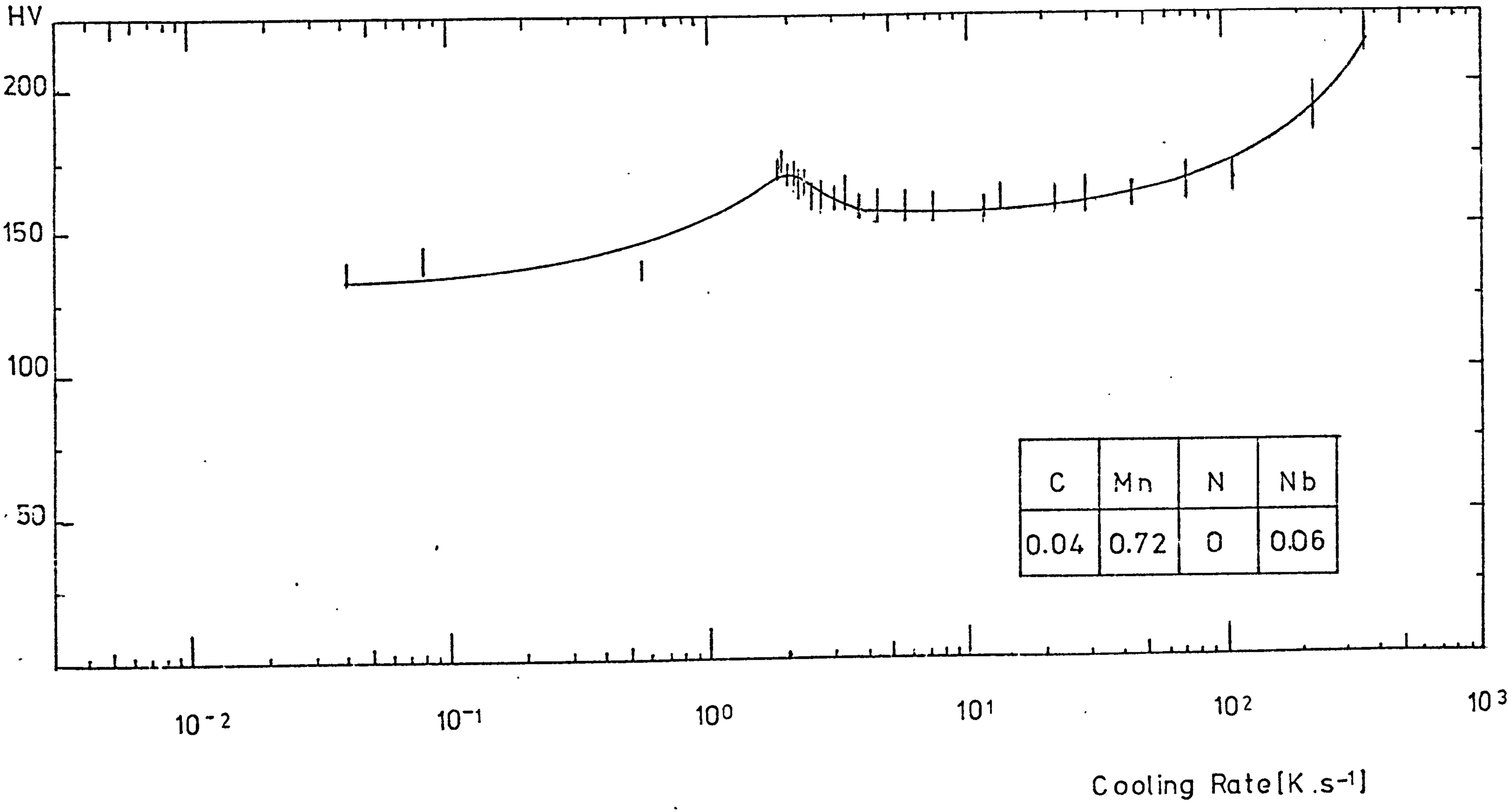

Fig.4.1.5 Graph of hardness against cooling rate in low niobium manganese steel.

4.2 Cooling curves.

In the present study, the material was investigated over a large range of cooling rates. Two means of obtaining the necessary cooling rates were adopted: namely: a modified end quench test in the high cooling range, (this is explained in section 3.1) and a controlled vacuum furnace in the low cooling range (see section 2.2). Typical cooling curves produced by the two techniques are shown in Fig.4.2.1.

In the present investigation, a wide range of cooling rates was used. The shape of the cooling curves was not as important as the congruence of the curves in order to allow comparisons between different cooling rates. For example, precipitation is very dependent upon the characteristics of heat-treatment, and the shape of a cooling curve illustrates the characteristics of the heat-treatment in continuously cooled specimens. However, when precipitation is studied as a function of the cooling rates, the curves should be congruent to allow a comparison to be made.

It can be seen in Fig.4.2.1 that the shape of the curves changes progressively and regularly from a high cooling rate to a very low cooling rate. At the cooling rate of $2K.s^{-1}$, two curves can be seen in Fig.4.2.1. These curves represented the common boundary between the cooling rates obtained from

end quench specimens and from the vacuum furnace described in section 2.2. The two curves almost coincided, thus indicating the reliability of the two methods at 2 $K.s^{-1}$.

It was therefore felt that comparisons between different observations at different cooling rates could be effected using the cooling rate as a criterion.

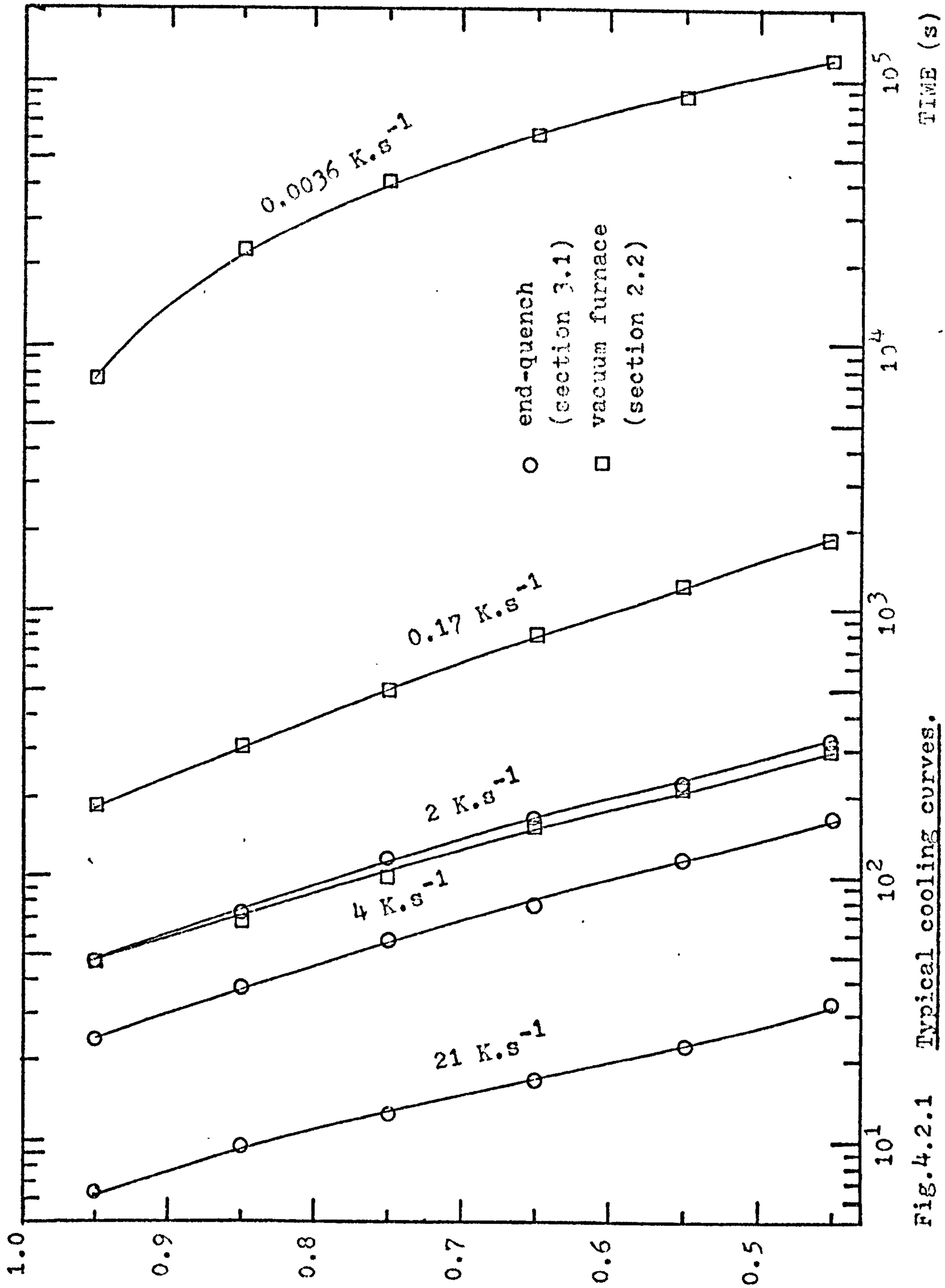

Fig.4.2.1 Typical cooling curves.

4.3 Mechanical testing results.

This section is concerned with the mechanical properties of the studied alloys. These tests were carried out in order to find a basis for comparison between the tensile properties of the alloys and the hardness values. The increase in the hardness of the alloys (see section 4.1) seemed to be associated with a reaction in ferrite. Consequently, the alloys received a heat-treatment to insure that the structure was all ferrite, or at least that no bainite was present in the structure. This made possible an equivalence between ferritic hardness and some tensile values; this will be discussed further in Chapter six.

The mechanical properties are shown in Table 4.3.1. The mechanical tensile test figures represent the average values from three specimens of each material, except for VT1 and VT3, where two specimens only were tested (more material was not available). The corresponding hardness tests were carried out initially on one of the tensile heads for every tensile specimen of steel "B" (Fe - 0.1C - 0.46V). Fig.4.3.2 illustrates selected mechanical values for the three specimens BT2. The hardness values represent the arithmetic mean of at least fifteen measurable identations on any one tensile head. Each "error" ΔH on hardness values was calculated at the 95% confidence level on the arithmetic mean, assuming Student's t distribution for small samples. The three tensile specimens

(BT2) were cut out of the same piece of material. The hardness results in Fig.4.3.2 thus indicate that the hardness tests can be reproduced. Therefore, three statements can be inferredfrom Fig.4.3.2:

(1) the material is homogenous,

(2) the hardness test is reproducible within the error limit, (reliability of the measurement)

(3) the variation of hardness values in the three BT2 specimens is not intrinsic to the material, but is due to statistical fluctuations.

The above considerations made it possible to carry out further hardness tests in other materials using only one tensile head instead of three. This procedure was also applied to the grain size determination and pearlite content.

An example of hardness distribution can be observed in Fig.4.3.3. This distribution was obtained by combining all the hardness measurements carried out in the BT2 specimen, using one standard deviation unit (z) for the class size. It can be observed that the distribution is slightly positively skewed, but the skeweness $\left[\,3(\text{median} - \text{mean})\,/\text{standard deviation}\,\right]$ is less than 0.2. It is therefore justifiable to use the Student's t distribution for small samples, which should be used whenever the distribution is approximately normal, but the sampling contains fewer than thirty elements.

Other dimensions could have also been studied, e.g. the influence of alloying elements on the ductility.

It can be seen in Table 4.3.1 that the material DT2 (0.45V) had a 0.2% proof stress value which was 45% higher than in material VT1 (0.13V). At the same cooling rate, both materials had the same grain size and a similar composition except for the vanadium content. Generally, an increase in strength corresponds to a decrease in ductility; however, in the present study, these materials exhibited a similar ductility at room temperature.

Another relevant aspect to investigate would be to compare a niobium steel with a vanadium steel. The steel NT2 (Fe - 0.04C - 0.06Nb - 0.7Mn) had similar mechanical properties to the steel VT1 (0.1C - 0.13V - 1.5Mn), although it contained only half the alloying additions. A more complete study of the influence of alloying elements on the ductility would have been interesting, but this was beyond the scope of the present study.

Material*	C.R $K.s^{-1}$	UTS MPa	UYS MPa	LYS MPa	0.2%P MPa	Young's modulus GPa	% L/Lo measured on spec.	on graph	A/Ao %	Hardness $kg.mm^{-2}$	G.S. α-Fe μm	Pearlite %	size μm
A T1	0.03	235	-	-	125	189	52	48	80	77 ± 2	295	-	-
A T2**	0.03	223	-	-	119	218	51	47	85	69.5± 1	248	-	-
B T1	0.06	385	-	-	216	201	35	31	73	120 ± 3	87	-	-
B T2	0.08	363	231	221	-	201	34	33	74	111 ± 3	49	-	-
D T1	0.06	587	-	-	400	206	31	25	68	187 ± 4	34	3.8	8
D T2	0.08	608	-	-	434	221	25	26	65	198 ± 3	23	5.8	11
N T1	0.04	463	303	302	-	203	34	31	66	135 ± 3	24	14.1	19
N T2	0.08	482	319	317	-	210	34	30	68	147 ± 2	21	19.0	21
V T1	0.08	461	302	298	-	195	32	29	63	130 ± 3	23	15.5	20
V T2	0.06	301	205	197	-	222	51	48	81	88 ± 1	24	-	-
V T3***	0.06	314	-	-	185	213	42	35	75	95 ±	51	trace	

* The material: composition was reproduced in table 2.1

** A T2: different heat-treatment than A T1

*** V T3: heat-treated 6 hrs at solution temperature instead of 1 hr (V T2)

Table 4.3.1 Mechanical testing results.

Material	UTS MPa	UYS MPa	LYS MPa	0.2%P MPa	Hardness $Kg.mm^{-2}$
B T2 a	364	233	227	220	109.3 ± 1.5
B T2 b	362	228	217	227	110.9 ± 2.0
B T2 c	362	232	220	225	113.5 ± 2.7
B T2 av.	363	231	221	224	111.0 ± 3.0

Fig. 4.3.2 Selected mechanical properties in Fe - 0.1C - 0.46 V steel continuously cooled at 0.08 $K.s^{-1}$.

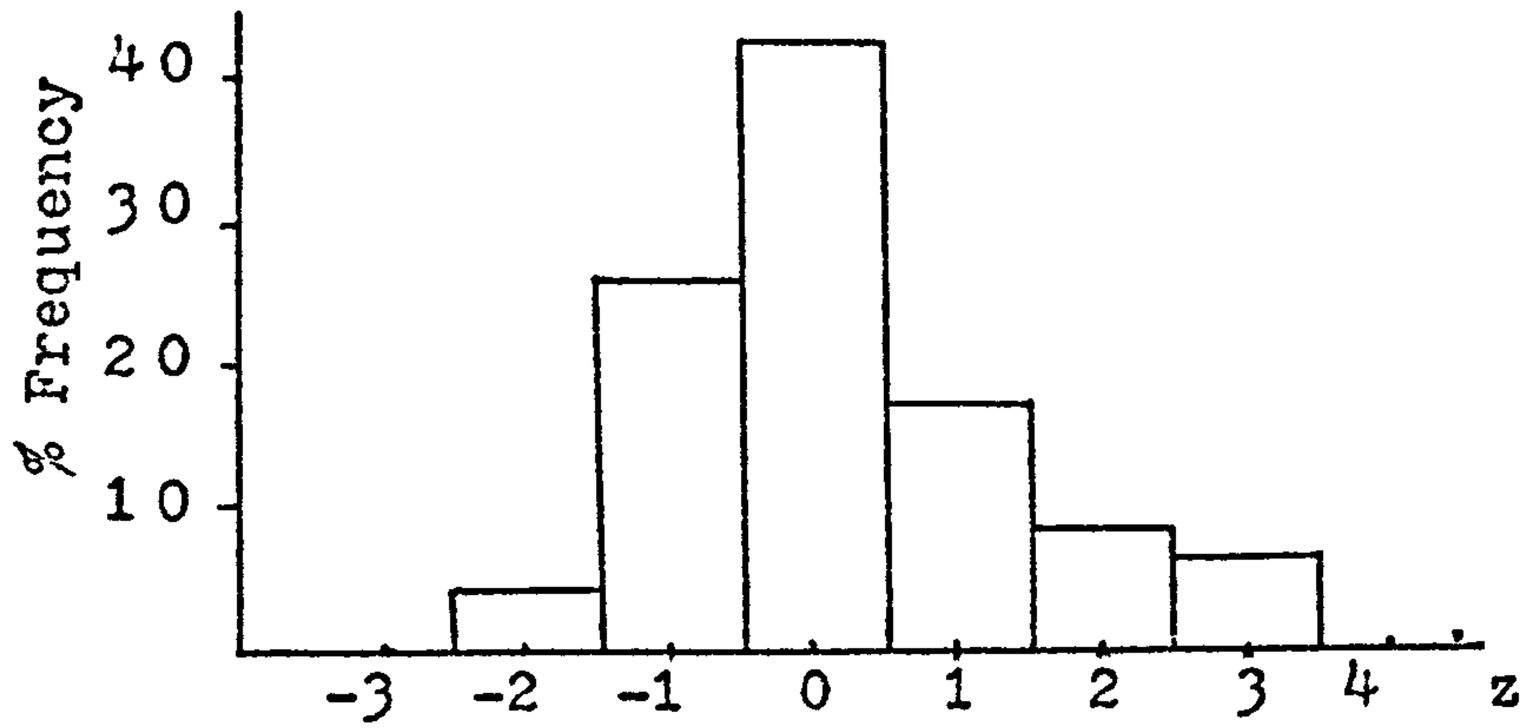

$\bar{X}$ = 111 $Kg.mm^{-2}$

S = 5 $Kg.mm^{-2}$

ΔX = 3 $Kg.mm^{-2}$

Fig.4.3.3 Hardness distribution in Fe - 0.1C - 0.46V steel continuously cooled at 0.08 $K.s^{-1}$.

4.4 Grain size measurements.

Grain boundaries interfere with slip in polycrystalline metals and grain size strongly influences the strength of metals. An empirical relationship between the yield strength and the square root of the grain size was originally proposed by Hall and by Petch independently [80,81] (see equation 1.3.1.1). This equation has been successively modified to take into account other strengthening mechanisms in steels. Similarly, in the present study, the contribution of grain size to strength was taken into consideration through a modified Hall-Petch equation.

The ferritic grain sizes were measured by a linear intercept method and the accuracy of the method was discussed in section 3.4. The ferritic grain size values are presented in Tables 4.4.1 to 4.4.3.

The usual method to reveal prior austenitic grain boundaries is to etch the specimen in a solution of picric acid and a wetting agent. The solution etches the region where impurities segregated during the austenitic heat treatment; this region corresponds to the prior austenite boundaries. It was not possible to reveal austenitic grain boundaries with this method in the present investigation. The failure could be explained by the very high degree of purity of the alloys used in this study.

However, the ferritic grains were observed to nucleate at the prior austenitic grain boundaries as shown in

Fig.5.1 and Fig.5.2 ($\simeq 6.5K.s^{-1}$). Consequently, selecting a sample corresponding to the cooling rate where the ferritic grains started to appear, enabled the determination of the austenitic grain sizes to be made. Table 4.4.4 shows an estimation of the austenitic grain sizes.

In one material (Steel "D"), individual austenite grains were measured to verify if the relationship established between the arithmetic mean ($\bar{X}$)and the standard deviation (S) were still valid (see section 3.4), that is $S \simeq 2/3\ \bar{X}$. The relationship found was $S = 0.58\ \bar{X}$ which agrees reasonably well with the empirical relationship. The distribution of the austenitic grain sizes in the steel "D" is shown in Fig.4.4.5.

As can be observed, the distribution is skewed positively and cannot be approximated to a normal distribution. A similar shape in the distribution was obtained from ferritic grain sizes. Such a distribution was expected because the linear intercept method was used, which entails that the probability of cutting a grain at its maximum dimension is less than the probability of cutting it at any smaller dimension. However, the intercept method is widely used to estimate grain sizes, because the method produces an average dimension of the grains instead of a maximum dimension. This is the important quantity used to describe the bulk properties [137].

Fe - 0.1C - 0.46V steel

Cooling rate $K.s^{-1}$	Grain size μm	Bainite %	Bainite Region size μm	Pearlite %	Pearlite size μm
18.0	--	100	---	--	--
4.0	14	63	220	--	--
2.5	14	13	75	--	--
2.0	17	0	0	--	--
0.17	45	--	--	--	--
0.06	87	--	--	--	--

Fe - 0.1C - 0.45V - 1.5Mn steel

Cooling rate $K.s^{-1}$	Grain size μm	Bainite %	Bainite Region size μm	Pearlite %	Pearlite size μm
4.0	--	100	---	--	--
1.6	16	19	27	--	--
1.4	17	16	28	--	--
0.65	21	1	--	--	--
0.17	23	--	--	2.9	10
0.08	24	--	--	3.7	--
0.06	34	--	--	5.8	11

Table 4.4.1 Ferritic grain size measurements in high Vanadium steels.

Fe - 0.1C - 0.13V - 1.5Mn steel

Cooling rate $K.s^{-1}$	Grain size μm	Bainite %	Bainite Region size μm	Pearlite %	Pearlite size μm
18.0	--	100	---	--	--
4.0	9.4	60	---	--	--
2.0	10.0	53	29	--	--
1.9	11.0	45	27	--	--
0.6	15.0	14	---	--	--
0.37	16.0	9	---	--	--
0.31	18.0	7	---	--	--
0.17	21.0	--	---	9.4	--
0.08	23.0	--	---	15.0	20
0.06	24.0	--	---	.2	--
0.003	59.0	--	---	.2	--

Fe - 0.03C - 0.14V steel

Cooling rate $K.s^{-1}$	Grain size μm	Bainite %	Bainite Region size μm	Pearlite %	Pearlite size μm
0.17	69	0	0	0	0

Table 4.4.2 Ferrite grain size measurements in low Vanadium steels.

Fe - 0.02C- 0.14Nb steel

Cooling rate $K.s^{-1}$	Grain size μm	Bainite %	Bainite Region size μm	Pearlite %	Pearlite size μm
3.3	45	83	540	0	--
1.75	145	0	---	0	--
0.03	248	0	---	0	--

Fe - 0.04C - 0.06Nb - 0.7Mn steel

Cooling rate $K.s^{-1}$	Grain size μm	Bainite %	Bainite Region size μm	Pearlite %	Pearlite size μm
3.3	12	60	145	--	--
1.9	21	30	180	--	--
0.08	21	0	---	19	21
0.04	24	0	---	14	19

Table 4.4.3 Grain size measurements in niobium steels.

MATERIAL		GRAIN SIZE
Fe - 0.02C - 0.14Nb	(A)	650 μm
Fe - 0.04C - 0.06Nb - 0.7Mn	(N)	230 μm
Fe - 0.1 C - 0.46 V	(B)	220 μm
Fe - 0.1 C - 0.45 V - 1.5Mn	(D)	50 μm
Fe - 0.1 C - 0.13 V - 1.5Mn	(V)	60 μm

Table 4.4.4 Estimation of the austenitic grain sizes.

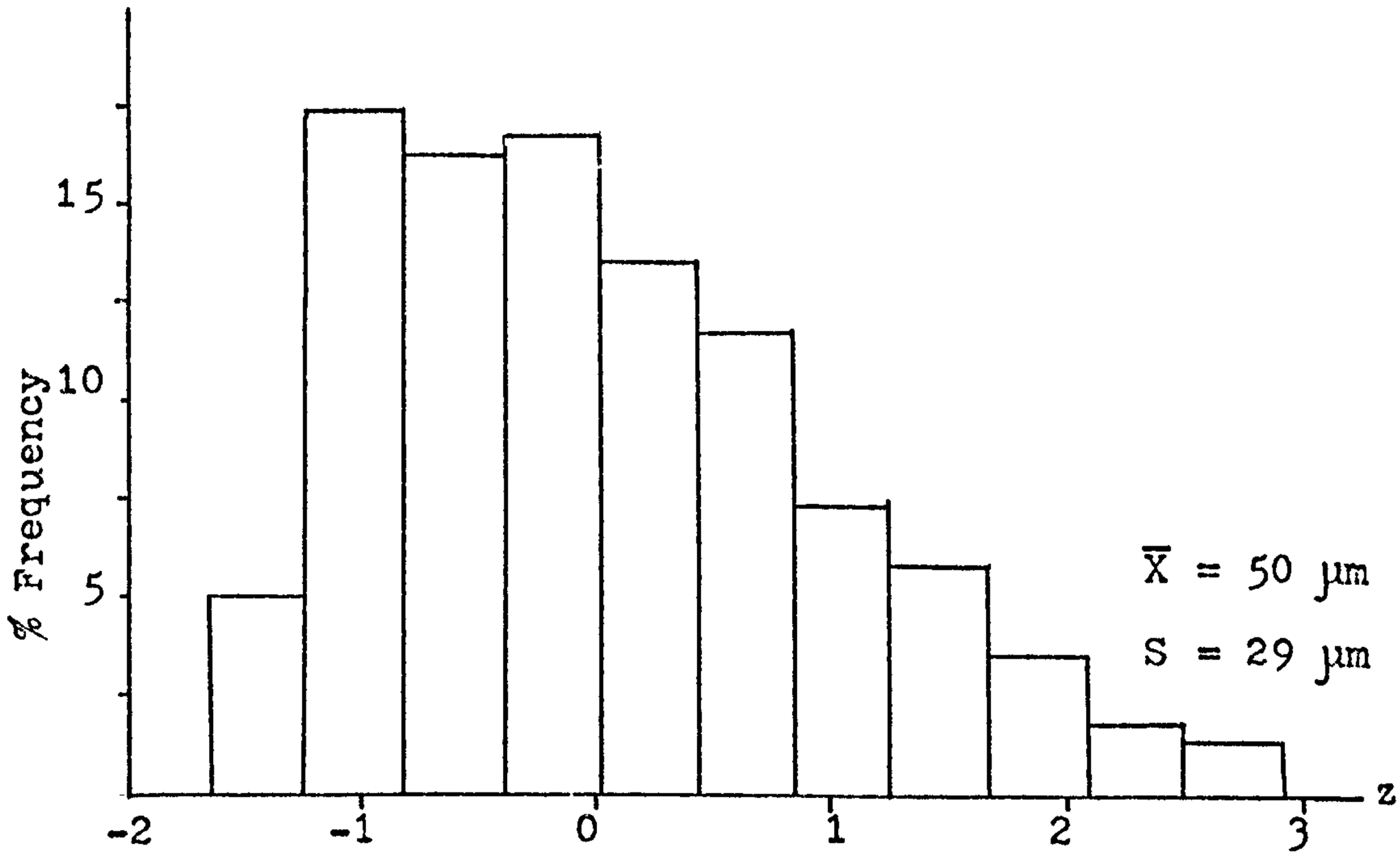

Fig.4.4.5 Austenite grain size distribution in Fe - 0.1C - 0.45V - 1.5Mn steel by the linear intercept method.

4.5 Particle size and volume fraction.

It is necessary to know the particle size and the volume fraction in order to evaluate the theoretical contribution from precipitation hardening to the strength of a material.

The vanadium and niobium steels are usually considered as precipitation hardened steels. In the present study, the strengthening effect of the carbonitride particles (MCN) was evaluated by means of measuring their size and volume fraction direct from carbon replicas. The method was described in detail in section 3.3.

The particle sizes and volume fractions are presented in Fig.4.5.1 to 4.5.3. Two distinct groups of particle size can be distinguished in every steel. Two methods of calculating the volume fraction were used; a preliminary calculation was carried out assuming a surface distribution of hard and unsectioned particles, following Ashby and Ebeling [127]. A successive calculation used a volumetric distribution which considered that the carbon replicas produced a thick film containing the particles. The MCN particles were observed to be disc shape and some fixed ratios of diameter to particle thickness were assumed. These ratios were calculated from the conventional misfit of the MCN particles with the alpha iron matrix. These ratios were 16 for VCN and 4.5 for NbCN. Although the ratios were calculated for lost coherency only, they were taken as constant

over the complete range of particles sizes. The volume fraction was normalized over the maximum volume fraction obtained at any particular cooling rate. Generally, the maximum volume fraction was found by adding successively the volume fraction of small and large particle size distributions at low cooling rates.

Before moving on to the subject of the validity of the volume fraction measurements (i.e. the extent to which the measurements are dealing with what they are supposed to measure), the reliability of particle size measurements will be appraised (i.e. the extent to which repeated measurements produce the same results).

4.5.1 Validity and reliability of particle size measurements.

The mean particle size ($\bar{X}$) presented in Fig.4.5.1 to 4.5.4 was the arithmetic mean of sized particle distributions. An average of five hundred particles was measured in each case in several areas ($\simeq 6$) of carbon replicas. The reliability of a test carried out following the above conditions has to be assessed.

When the test was repeated in the areas of material previously investigated, the arithmetic mean was found to vary by a factor of less than 2% compared with the original value. Similarly, when the test was repeated in new areas of the micrographs, the new arithmetic mean showed a typical variation of 5%. Furthermore, when a new carbon replica was prepared and the entire test

repeated as shown in Fig.4.5.4, the new arithmetic mean showed again a 5% variation. If one takes into consideration that the magnification calibration of the electron microscope is of similar accuracy, the agreement between the two results shown in Fig.4.5.4 was exceptionally high. In line with the above, the 95% confidence limit on the arithmetic mean was about 0.1nm; therefore, both results are surprisingly in complete agreement within the statistical error.

An example of the distribution of particle sizes is presented in Fig.4.5.5. It can be seen that the distribution shape is skewed positively and cannot approximate to a normal distribution. Furthermore, all the distributions exhibit approxi mately the same degree of skewness and this was found to be independent of the average particle size. This was also observed when the two distinct groups of particle sizes were compared in any material at a selected cooling rate. An example of this observation is presented in Fig.4.5.6, together with an illustration of particle size measured in carbon replicas and in foils. The latter comparison illustrates the validity of the test: both the shape of the distribution and the statistical values are in reasonable agreement. Consequently, because (1) the reliability of the test can be reasonably ensured, (2) similar shapes of the distribution of different particle sizes are observed and (3) because comparison of particle distributions in carbon replicas with particle distributions

in thin foils can be achieved, the distributions shown in Fig.4.5.1 to 4.5.3 are thought to be a fair representation of the particle distribution present in the steels investigated in this study.

4.5.2 Validity and reliability of volume fraction measurements.

In order to evaluate the validity and reliability of the volume fraction measurements, the following comments must be considered. Concern was expressed about the volume fraction estimated from carbon replicas (see section 3.3), because the volume fraction is an important quantity used in the calculation of strength from precipitation hardening. The study of Ashby and Ebeling [127] and the present experimental work raise doubts about the reliability and the validity of volume fraction values.

Leaving aside temporarily the validity of the volume fraction values, a few tests were carried out to assess the reliability of volume fractions measured. In the high vanadium steel "B", the measurements on the specimens cooled at $4.0K.s^{-1}$ showed a scatter of $\pm$ 8% about the mean value. In niobium steels, an example is shown in Fig.4.5.4. This figure illustrates the best agreement obtained: $\pm$ 4% between different carbon extractions. These tests in vanadium and niobium steels were performed from different extractions. However, these results cannot be conclusive as the following discussion will

demonstrate.

One of the main problems appeared to be how many particles should be counted, or similarly, how many areas of the material should be investigated. This question poses the problem of the representativeness of the areas examined in the material under study. Moreover, doubts about representativeness of sampling raise further doubts about the evaluation of the error involved in carrying out a test. Therefore, the problem is how to ascertain the representativeness of samples.

Briefly, in the present study, the method used was: (1) a two millimeter square of carbon replica was examined thoroughly under the microscope to ascertain the suitability of the replica (i.e. MCN rings on diffraction pattern, clean and very thin replica,...), (2) familiarization by the operator with the structure and (3) thereafter, at least ten micrographs of so-called representative areas were taken for every distinct group of particle sizes observed to be present in the replica. After this process was completed, the micrographs were re-examined to find out smaller areas where the particle size distribution and the volume fraction determination could be carried out. The representativeness is thus limited by the operator himself. The experience gained was an important asset; however, the limiting factors present in the operator made it impossible to assess quantitatively the error encountered during the whole process of the investigation.

One solution to the problem would be to use a sampling technique based on the linear intercept method. One can think of a very thin region bounded by two parallel lines traversing a large portion of the specimen as with the intercept method. But it would be ludicrous to expect a determination of the particle sizes. A solution to the problem of representativeness will only be found when a method is developed which ascertain that particular areas could represent the material under study. Consequently, the measured volume fraction and particle sizes have some unsatisfactory characteristics, but they may well be as good as any others at present obtainable.

To evaluate the validity of the volume fraction measurements, two criteria will be discussed: (1) agreement between the measured volume fraction and the predicted volume fraction, and (2) the variation of the measured volume fraction with cooling rate.

Volume fractions calculated assuming a surface distribution (% f, Ashby) can be seen in Fig.4.5.1 to 4.5.3. Consistently, they produced higher values than the volume fraction calculated from composition. However, the carbon extraction replicas produced a volumetric distribution instead of a surface distribution, and the particles were thin disc shapes rather than spheres. Volume fractions calculated using a thick MCN film concept (% f, t-film) are also included in Fig.4.5.1 to 4.5.3. In high vanadium steels (Fig.4.5.1), the volume fractions were lower than the calculated volume fraction

from composition (f_c). In Fig.4.5.2 disagreement between measured volume fraction (t.-film) and f_c started to appear, whilst the volume fractions calculated in Fig. 4.5.3 (Nb steels) were ten times larger than f_c. This observation raises doubts about the validity of the volume fraction measurements.

However, if the measured volume fractions were normalized and plotted against cooling rates, the volume fractions can be seen to change systematically with cooling rate. A comparable pattern was obtained for every material as shown in Fig.4.5.7 to 4.5.11. These graphs illustrate also the existence of two distinct groups of precipitates.

Some comments may be made about the validity of the volume fraction measurements. It can be observed from Fig.4.5.7 to 4.5.11 that a genuine variation in the volume fraction of precipitate is present as a function of cooling rate. The value of the measured volume fractions may be connected with the predicted volume fraction (f_c) although the measured values appeared inaccurate to begin with. If a relationship exists between measured volume fraction and predicted volume fraction, it is possible that the relationship is sufficiently linear to enable a comparison between the different volume fractions measured; but this would require further study for confirmation.

In résumé, the validity and reliability of particle

size determination from carbon replicas were confirmed. However, in respect of volume fraction determination, both the validity and reliability were appraised, and the uncontrollable limitations of the techniques were considered. This section will have a bearing on the discussion of the calculated contribution from precipitation hardening.

Fe - 0.1C - 0.46V steel (From composition f = 0.785%)

Cooling rate $K.s^{-1}$	$\bar{X}$ nm	S nm	% f Ashby	% f t.-film	% f norm.
4.0	3.9	1.7	7.0	0.22	25
2.0	4.2	1.5	5.9	0.19	21
2.0	12.0	3.8	2.7	0.08	9
0.17	50.0	17.0	15.0	0.46	52
0.06	18.0	6.4	16.0	0.49	56
0.06	66.0	36.0	13.0	0.39	44

Fe - 0.1C - 0.45V - 1.5Mn steel (From composition f = 0.762%)

Cooling rate $K.s^{-1}$	$\bar{X}$ nm	S nm	% f Ashby	% f t.-film	% f norm.
4.0	4.2	1.7	5.7	0.18	14
1.4	4.4	1.3	2.9	0.09	7
1.4	18.0	9.3	37.0	1.20	93
0.17	5.1	1.9	4.6	0.14	11
0.17	20.0	9.6	7.6	0.24	19
0.06	17.0	7.2	15.0	0.45	36
0.06	64.0	23.0	22.0	0.68	55

Fig.4.5.1 Particle size ($\bar{X}$) and volume fraction (f) measured in high vanadium steels.

Fe - 0.1C - 0.13V - 1.5Mn steel (From composition fc= 0.213%)

Cooling rate $K.s^{-1}$	$\bar{X}$ nm	S nm	% f Ashby	% f t.-film	% f norm.
4.0	3.1	0.7	14.0	0.39	90
2.0	3.3	0.8	15.0	0.42	99
0.37	6.3	2.1	10.0	0.29	68
0.37	17.0	5.0	5.0	0.14	32
0.17	4.1	1.1	6.6	0.18	43
0.06	4.0	0.9	8.1	0.23	53
0.06	34.0	14.0	2.4	0.07	15

Fe - 0.03C - 0.14V steel (fc = 0.23%)

Cooling rate $K.s^{-1}$	$\bar{X}$ nm	S nm	% f Ashby	% f t.-film	% f norm.
0.17	74	22	5.5	0.15	52
0.17	300	95	5.2	0.14	48

Fig.4.5.2 Particle size ($\bar{X}$) and volume fraction (f) measured in low vanadium steels.

Fe - 0.02C - 0.14Nb steel (From composition fc = 0.16%)

Cooling rate $K.s^{-1}$	$\bar{X}$ nm	S nm	% f Ashby	% f t.-film	% f norm
3.3	6.7	2.2	9.5	1.0	100
1.7	6.7	2.2	5.1	0.56	56
1.7	32.0	9.2	1.4	0.16	16
0.03	4.5	1.4	3.3	0.37	37
0.03	54.0	22.0	5.0	0.56	56

Fe - 0.04C - 0.06Nb - 0.72 Mn steel (From composition fc=0.054%)

Cooling rate $K.s^{-1}$	$\bar{X}$ nm	S nm	% f Ashby	% f t.-film	% f norm
3.3	3.2	0.8	3.5	0.39	39
1.9	4.5	1.3	7.0	0.79	79
0.6	4.7	1.0	5.5	0.62	62
0.6	7.9	1.3	3.4	0.38	38
0.06	4.5	1.1	5.9	0.66	66
0.06	22.0	12.0	2.5	0.28	28

Fig.4.5.3 Particle size ($\bar{X}$) and volume fraction (f) measured in niobium steels.

Cooling rate $K.s^{-1}$	$\bar{X}$ nm	S nm	% f Ashby	% f t.-film
0.06	4.46	1.15	5.9	0.66
0.06	4.66	1.04	6.4	0.71

Fig.4.5.4 Three month interval test in Fe - 0.04C - 0.06Nb - 0.7Mn steel.

Material: Fe - 0.1C - 0.45V - 1.5 Mn steel

Sample: Carbon replica

Relative frequency (F%) against standard deviation unit (z)

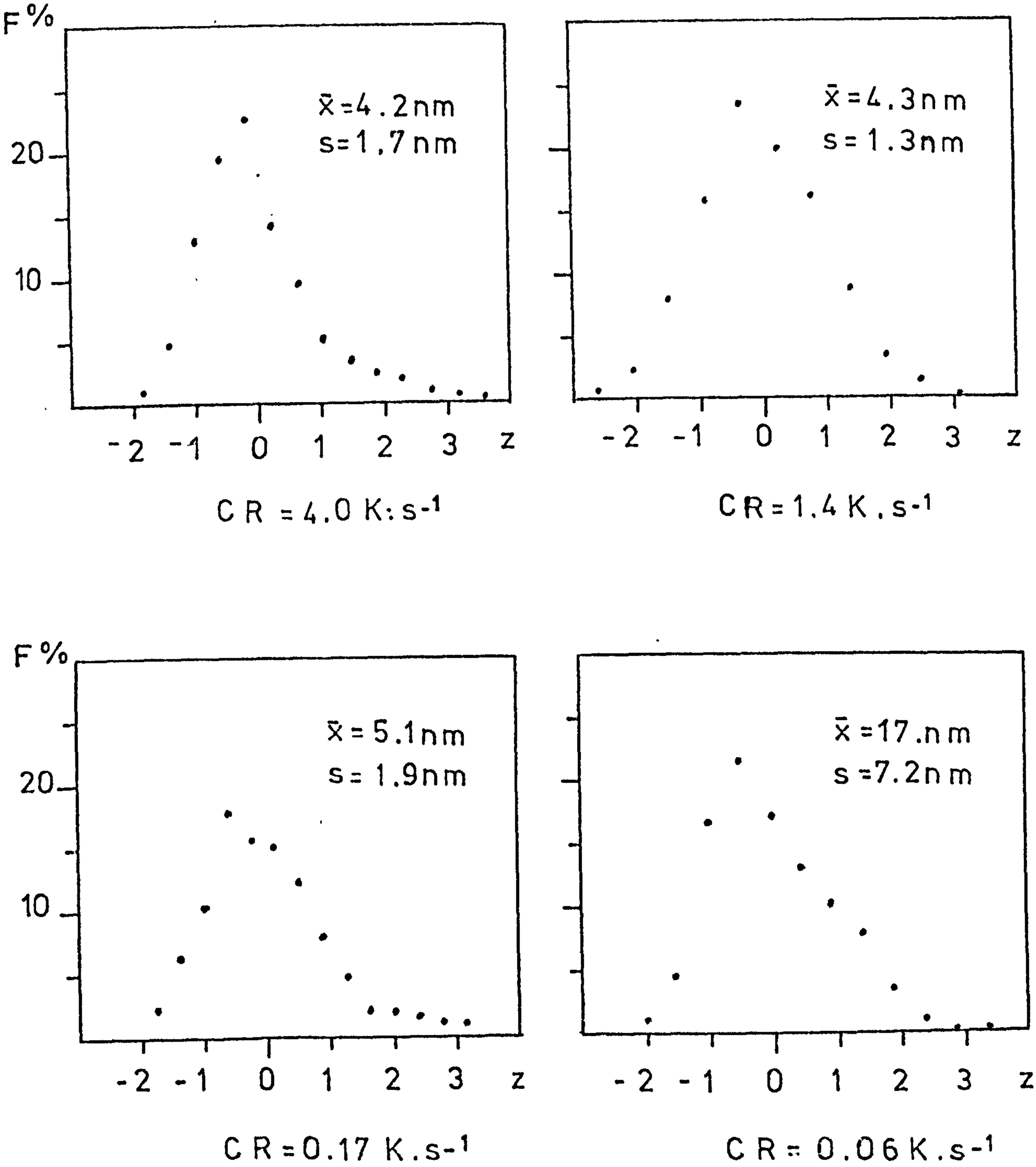

Fig.4.5.5 Distribution of small particle sizes in vanadium steel.

Material A: Fe - 0.02C - 0.14Nb steel

N: Fe - 0.04C - 0.06Nb - 1.5Mn steel

Relative frequency (F%) against standard deviation unit (z).

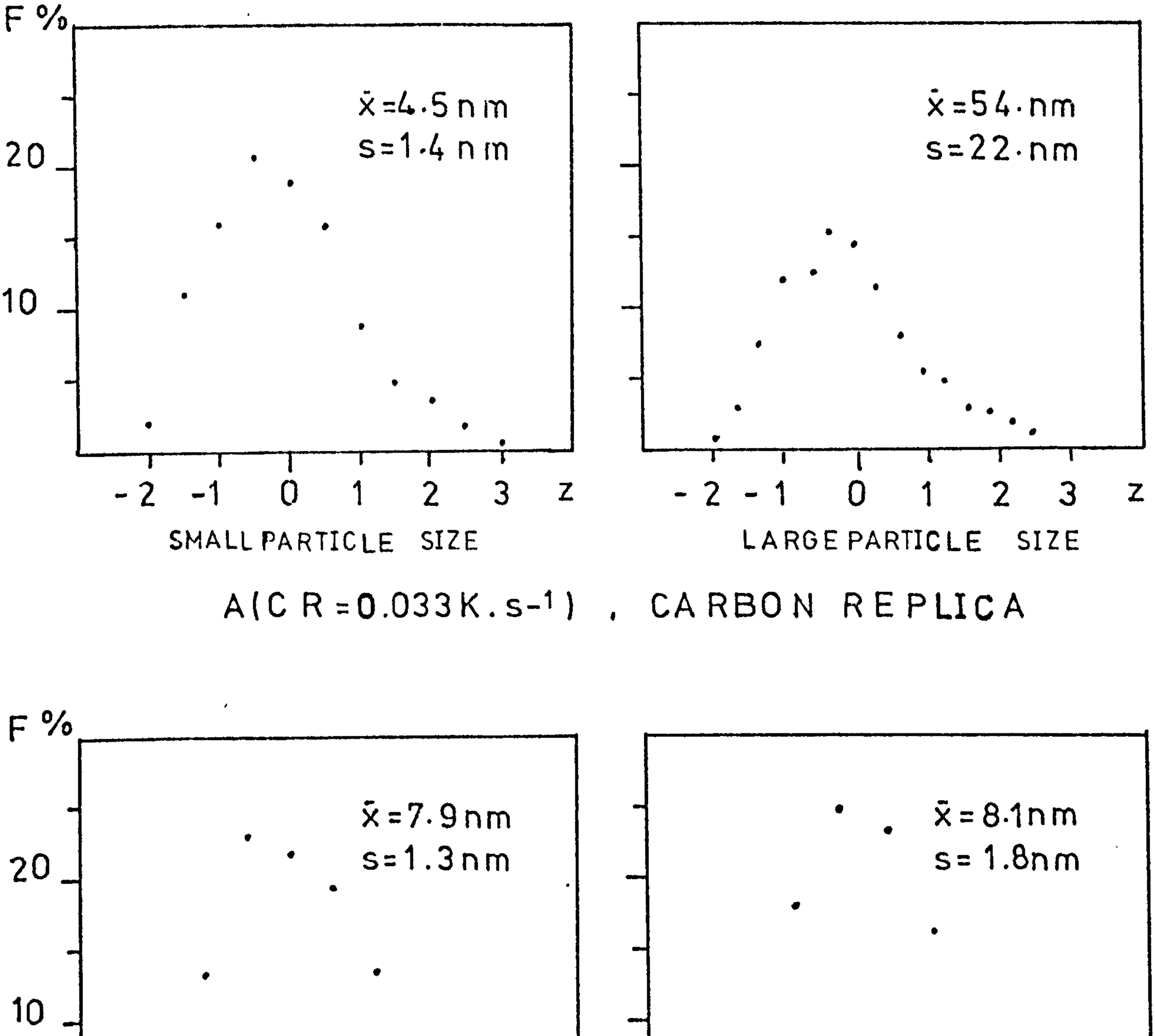

Fig.4.5.6 Distribution of particle sizes in niobium steel.

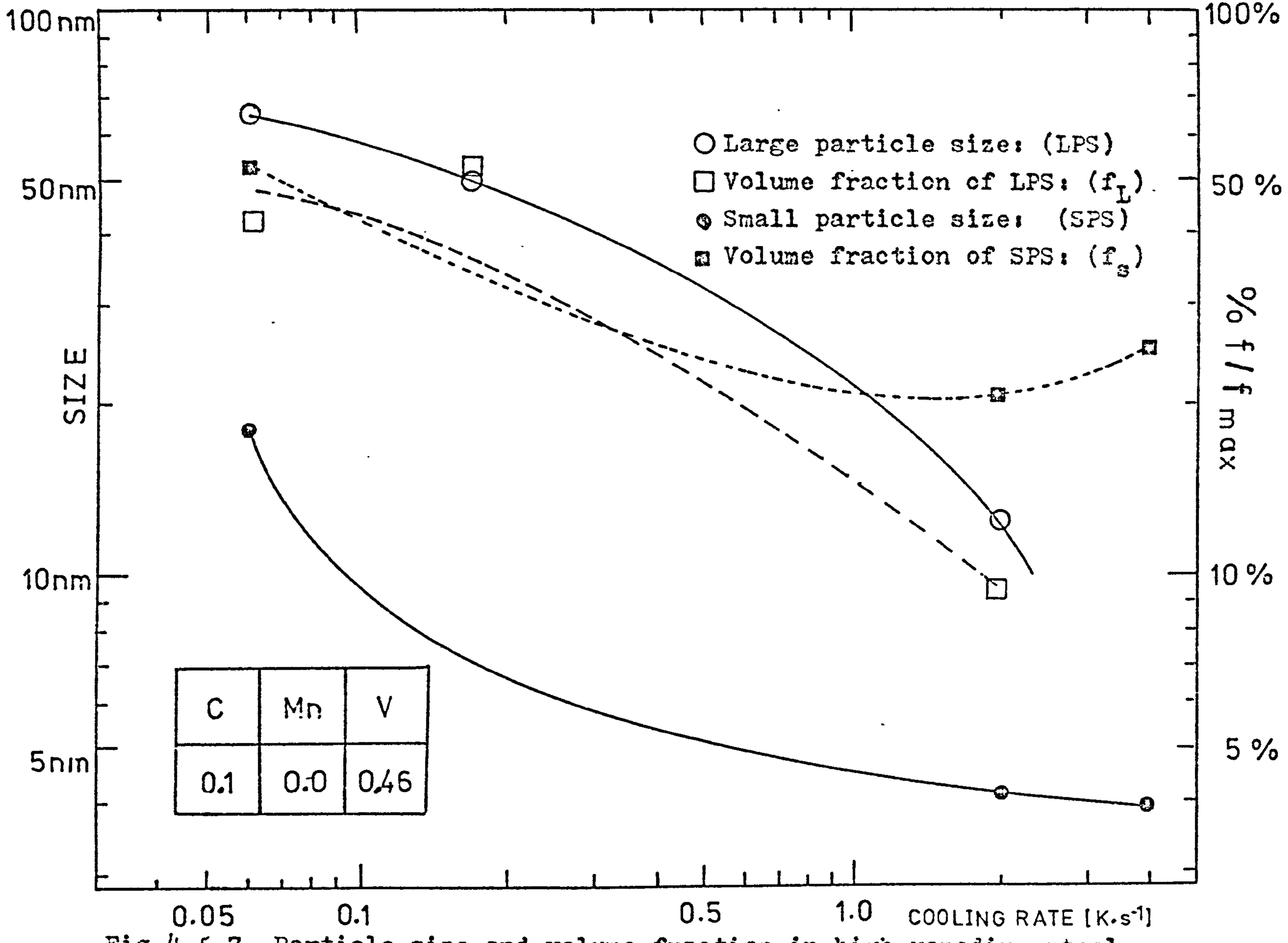

Fig.4.5.7 Particle size and volume fraction in high vanadium steel.

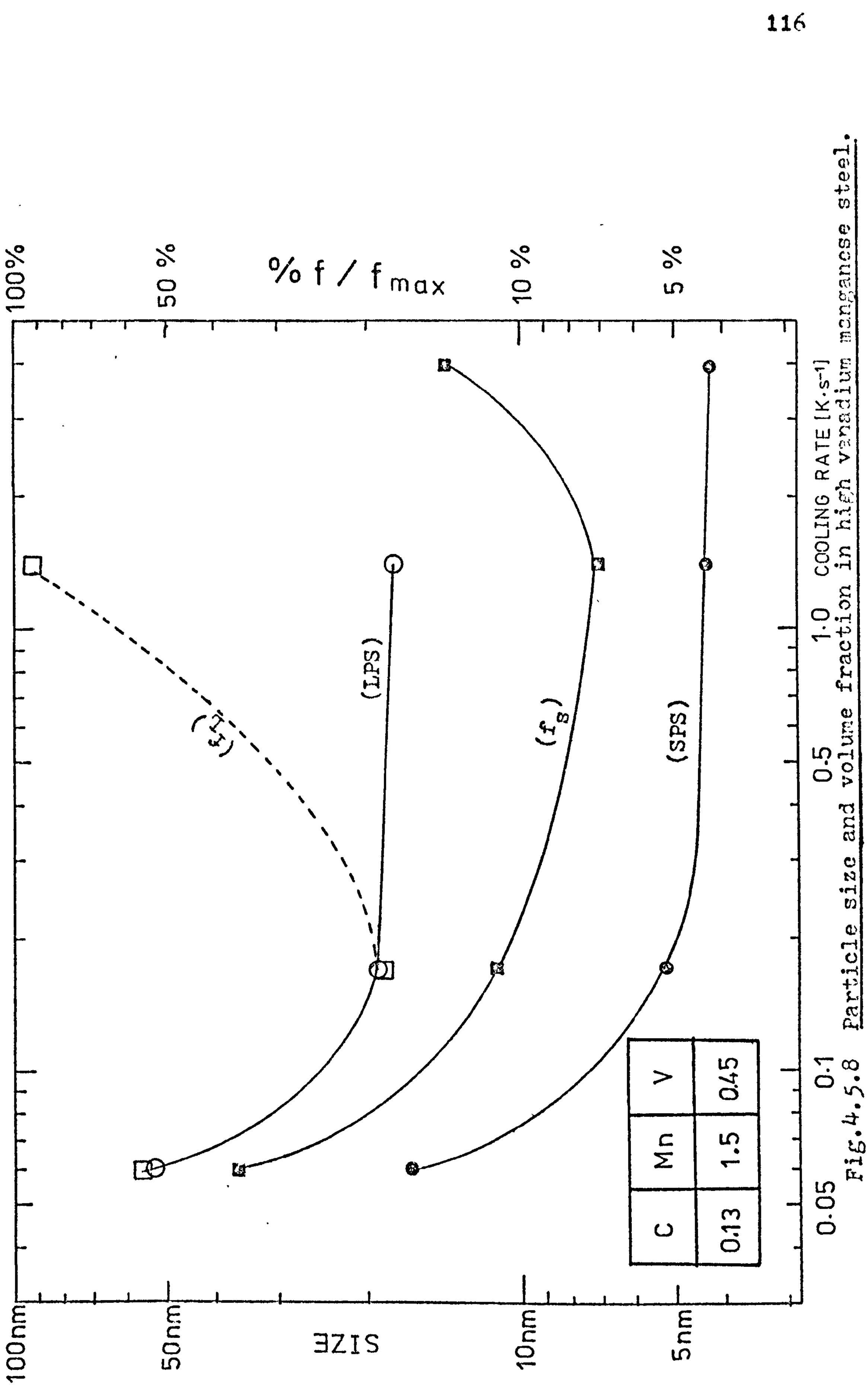

Fig.4.5.8 Particle size and volume fraction in high vanadium manganese steel.

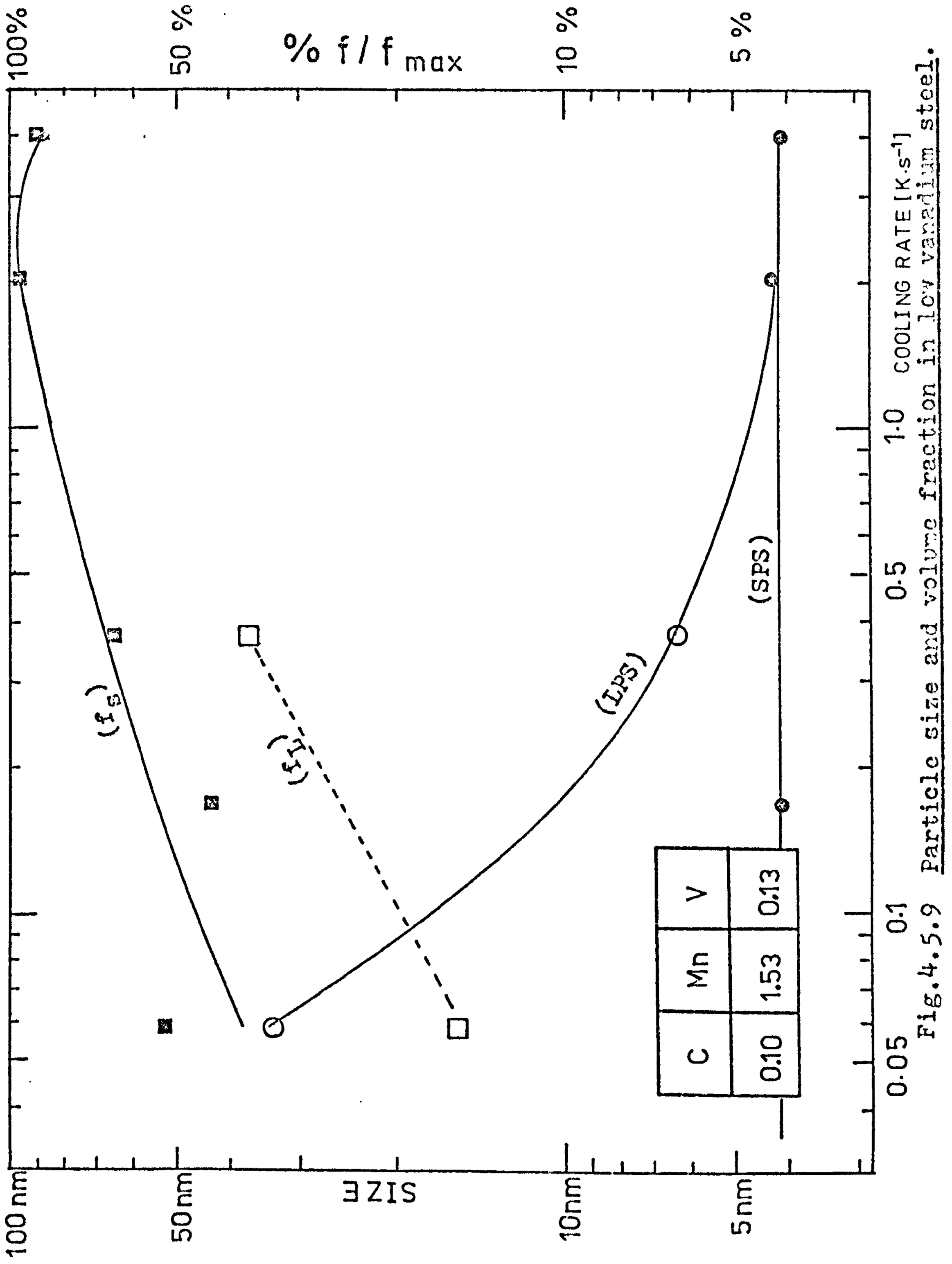

Fig.4.5.9 Particle size and volume fraction in low vanadium steel.

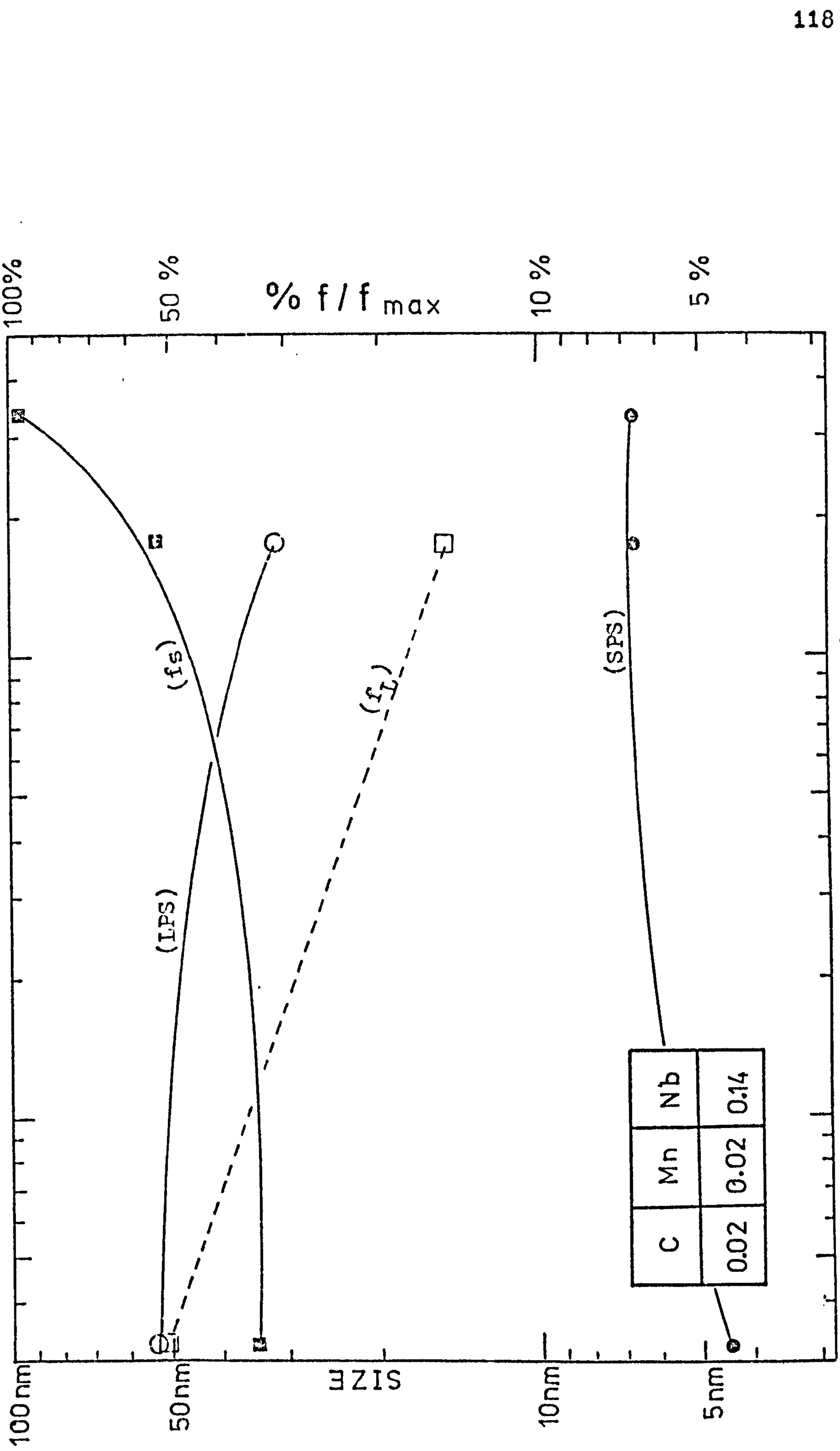

Fig.4,5.10 Particle size and volume fraction in niobium steel.

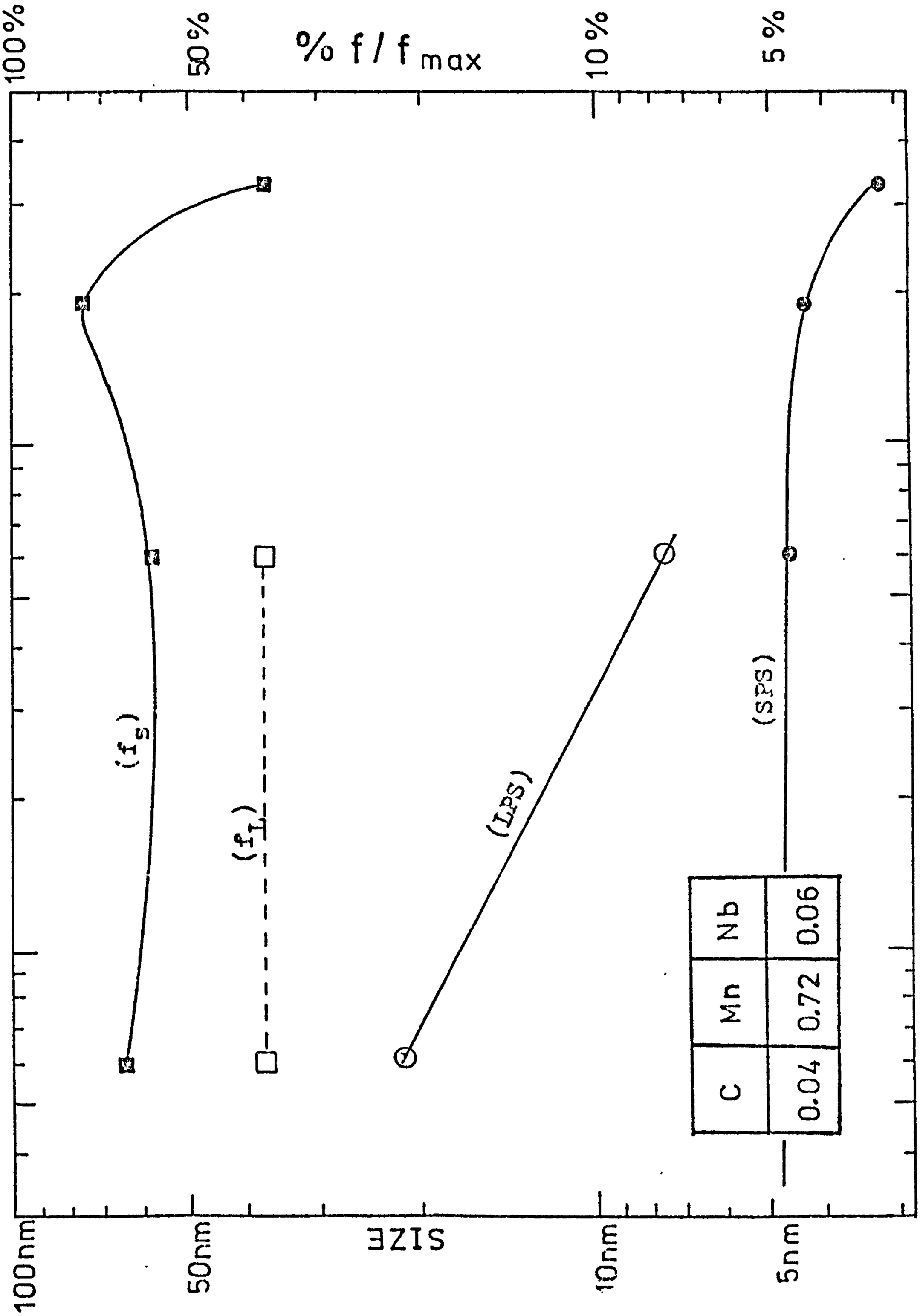

Fig. 4.5.11 Particle size and volume fraction in niobium manganese steel.

4.6 Estimation of dislocation densities.

Dislocation densities were investigated in order to take into consideration their contribution to strength. The materials studied were those of low vanadium and low niobium steels which were of a typical commercial composition.

In the present study, the dislocation densities were measured by counting the dislocation intersections with a test of two concentric circles. The method was described in detail in section 3.2. In brief, the method consisted of taking electron micrographs of areas of known thickness in the material, and to cover each area with the test line. Areas were sufficiently large to often allow space for two or three test lines; correspondingly two or three samples were obtained per area.

The density of dislocations was evaluated for each sample. Thus, from an average of ten micrographs per material investigated, twenty to twenty five samples were obtained. The arithmetic mean and the standard deviation of these samples were calculated. The "error" $\bar{X}$ was defined as the 95% confidence level on the arithmetic mean, assuming Student's t distribution for small samples.

The results are shown in Fig.4.6.1. An example of the distribution of the dislocation density for a Fe - 0.1C - 0.13V - 1.5Mn steel is shown in Fig.4.6.2, using one standard deviation unit (z) for the class size. All the values were contained between the $z = \pm 3$ boundaries.

As can be seen in Fig.4.6.1, the dislocation densities decrease with decreasing cooling rates. However, from the peak hardening ($\simeq 2K.s^{-1}$) to a cooling rate ten times slower than at the peak, the dislocation densities were approximately a constant of 10^{10} dislocations. cm per cubic cm. Also, the majority of results are contained within the 10% error limit. To reduce this error by a factor of <u>two</u>, it would be required to increase by <u>four</u> the number of micrographs; $\Delta \bar{X}$ is a function of the inverse of the square root of the number of micrographs, following the requirements of statistics. This would have probably led to a better representation of the dislocations present in the materials. However, it was felt that a reduction of the 10% error would be unjustified when the accuracy of every evaluation for each sample is taken into consideration. The limiting factor, as stressed in section 3.2, was the measurement of the foil which at the moment does not permit more than about 90% accuracy. Furthermore, the error on the magnification should also be considered. For example, the error on material V ($0.37\ K.s^{-1}$) is a good illustration of the error that is present in the process of evaluating dislocation density. It is thus felt that the results presented in Fig.4.6.1 are acceptable considering the techniques used.

Cooling rate $K.s^{-1}$	Number of micrographs used	Number of samples obtained	arith. mean ($\bar{X}$) (giga dislocations - cm/cm^3)	standard dev. (S)	$\Delta\bar{X}$	$\%\Delta\bar{X}$
(V steel) Fe-0.1C-0.13V-1.5Mn						
0.37	10	19	8.7	3.3	1.6	18.0
0.06	9	33	13.7	2.7	1.0	7.0
0.003	8	19	2.2	0.6	0.3	13.0
(Nb steel) Fe-0.04C-0.06Nb-0.7Mn						
1.9	13	25	9.4	2.1	0.9	9.5
0.6	10	21	10.6	1.5	0.7	6.6
0.06	7	18	3.4	0.6	0.3	8.6

Fig.4.6.1 Estimation of dislocation densities.

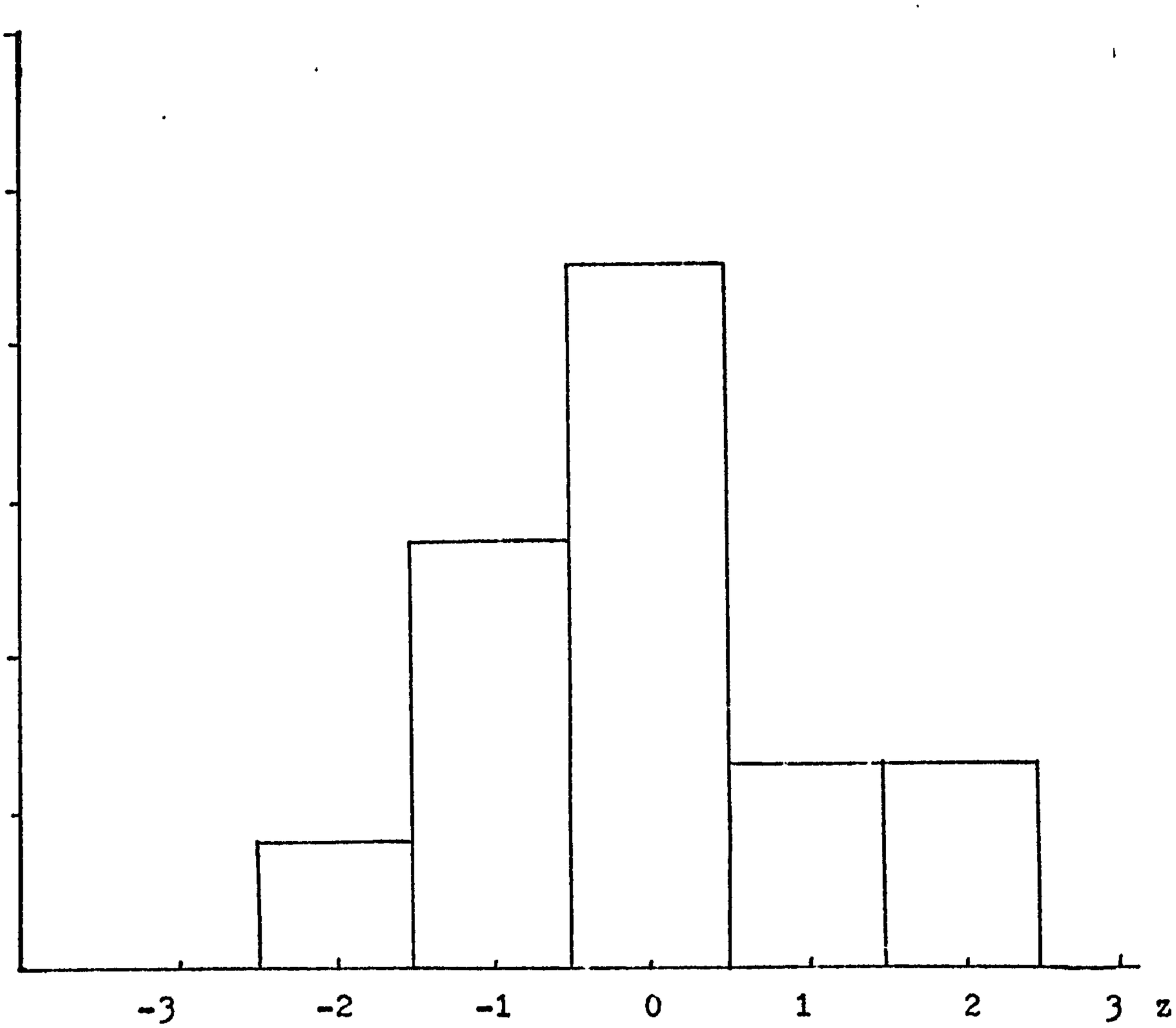

$\bar{X}$ = 1.37 * 10^{10} dislocations.cm/cm^3

σ = 0.27

Fig.4.6.2 Frequency distribution of dislocation densities in Fe - 0.1C - 0.13V - 1.5Mn steel continuously cooled at 0.06 $K.s^{-1}$.

4.7 Estimation of the allotropic transformation temperatures.

The determination of the allotropic transformation temperature is important in view of its association with some microstructural features of alloy steels, particularly interphase precipitation and twinning (see Fig.5.16 for examples). The experimental procedures used to estimate the allotropic transformation temperatures were described in section 2.3. Cooling rates had a very marked effect on the allotropic transformation as can be seen in Fig.4.7.1. This variation was taken into consideration in the design of quenching experiments during continuous cooling.

It was noted in the literature that the Ar_3 and Ar_1 values often were obtained from rod specimens placed in a vacuum furnace fitted with a standardized differential dilatometer. The fastest cooling rates obtained from such equipment were generally of the order of 0.1 - 0.2K.s^{-1}. However, the Ar_1 and Ar_3 values obtained were sometimes used as a basis for the design of experiments such as a rolling schedule. This procedure could lead to misinterpretations of the real conditions of the experiments carried out. In the present study, a 25 mm air cooled round bar corresponded to a cooling rate of approximately 2K.s^{-1}. Therefore, if the Ar_1 and Ar_3 readings at 0.17K.s^{-1} (see Fig.4.7.1) had been used to design any experiments based on the allotropic transformation temperatures, the

design of the experiment would have been erroneous because the real transformation temperature at $2K.s^{-1}$ would have been lower by as much as 70K depending upon composition.

Finally, the effect of the various alloying elements on the allotropic transformation can be assessed from Fig.4.7.2. As expected, manganese depressed the Ar_3 and Ar_1 temperatures, as did niobium whereas vanadium raised them.

Fe - 0.12C - 0.46V

Cooling rate $K.s^{-1}$	γ to α transformation			Bainite		sol. treat.
	Ar_3 K	50% K	Ar_1 K	B_s K	B_f K	K
2.0	1070	991	928	543	532	1325
0.55	1126	1042	969			1325
0.17	1148	1068	1008			1325
0.17	1148	1068	1013			1475
0.08	1163	1094	1011	491	451	1325

Fe - 0.13C - 0.45V - 1.5Mn

Cooling rate $K.s^{-1}$	γ to α transformation			Bainite		sol. treat.
	Ar_3 K	50% K	Ar_1 K	B_s K	B_f K	K
1.6	995	893	773	513	484	1325
1.4	1010	890	770			1325
0.65	1015	910	851	513	482	1325
0.17	1069	989	921	510	477	1325

Fe - 0.10C - 0.13V - 1.53Mn

Cooling rate $K.s^{-1}$	γ to α transformation			Bainite		sol. treat.
	Ar_3 K	50% K	Ar_1 K	B_s K	B_f K	K
2.0	1015	956	866			1325
0.17	1036	981	878			1325
0.06	1060	993	912			1325
0.003	1076	1031	960			1325

Fig.4.7.1 Effect of cooling rates on the allotropic transformation in vanadium steels.

MATERIAL	γ to α transformation			sol. treat.
	Ar_3 K	50% K	Ar_1 K	K
Fe - electrolytic iron	1177	1175	1156	1325
Fe - 0.12C - 0.46V	1148	1068	1008	1325
Fe - 0.13C - 0.45V - 1.5Mn	1069	989	921	1325
Fe - 0.10C - 0.13V - 1.53Mn- 0.006N	1036	981	878	1325
Fe - 0.10C - 0.15V - 1.58Mn- 0.021N	1047	957	854	1500
Fe - 0.04C - 0.13V - 1.47Mn- 0.004N	1106	1055	986	1425
Fe - 0.03C - 0.14V - 1.5Mn - 0.023N	1070	1034	970	1500
Fe - 0.03C - 0.14V - 0.019N	1165	1126	1084	1425
Fe - 0.04C - 0.06Nb - 0.72Mn	1044	982	901	1425
Fe - 0.02C - 0.14Nb	1167	1167	1026	1425

Fig.4.7.2 Effects of alloying elements on the allotropic transformation at $0.17K.s^{-1}$.

In this chapter, following the objectives outlined at the beginning of this study, an attempt was made to present and describe the findings which were gathered from various instruments and methods.

One of the objectives was concerned with the variation of strength with cooling rates in vanadium and niobium steels. In brief, a peak hardening was observed in the high vanadium steels whilst the low vanadium and niobium steels produced a less definite peak (plateau). The reliability and the validity of these results were considered and were found to be satisfactory.

In order to explain the results, which was the second objective outlined in this study, several aspects were considered (e.g. dislocation densities, precipitation sizes). These aspects will be correlated with the variation of strength with cooling rates in steels, in Chapter six: INTERPRETATION AND DISCUSSION OF RESULTS.

Chapter five: STUDY OF MICROSTRUCTURE.

This chapter, as a complement to Chapter four, discusses the third objective of the present study which is to compare the structure of the material investigated at various cooling rates. The vanadium and niobium steels will therefore be compared in detail. This chapter will serve two purposes: (1) to complement the results presented in the last chapter by means of illustrations and (2) to examine the structure in depth.

Microscopical metallography found its origins in the nineteenth century, that is when Professor H.C. Sorby of Sheffield initiated the systematic practice of microscopical examination of metals [140,141]. From then on, the structure of material was divided into two main groups: the term microstructure was reserved for the structure as seen with an optical microscope, whilst the term macrostructure was only used in connection with the structure seen by the naked-eye, or with a low power magnifying glass. The event of the electron microscope did not change the terminology. However, in this study, the term microstructure was restricted to structure observed inside grains whilst macrostructure was extended to describe groups of grains.

This chapter will therefore attempt to tackle four aspects of the study of micrographs. The first section will be concerned with the comparison between the macrostructure of vanadium and niobium steels at various

cooling rates. The second section will give an account on the MCN solubility experiments carried out to ascertain the validity of the equations for solubility. These equations were used to calculate the solution temperature of steels (see Fig.1.1.1.1 and Table 2.2). The last two sections of this chapter will be concerned with the microstructure as seen by transmission electron microscopy. This study will be restricted to the vanadium and niobium steels of commercial composition. Thus, the third section will discuss precipitation morphology and precipitation/dislocation interactions in the steels. A brief comment will be added about the indexation of the micrographs. Finally, the fourth section will deal with twinning and its nucleation mechanism.

5.1 Effect of cooling rate on the macrostructure of steels.

This section compares the macrostructure of vanadium and niobium steels at different cooling rates. The hardness of these steels was observed to change as a function of cooling rate, and a peak hardness was obtained at a critical cooling rate ($\simeq 2K.s^{-1}$),(see Fig.4.1.1 to 4.1.5).

Typical macrostructures of vanadium and niobium steels continuously cooled from the austenite are shown in Fig.5.1 to 5.3. The variation of cooling rates caused the usual macrostructures in low alloy steels to appear: for example in Fe - 0.1C - 0.13V - 1.5Mn (Fig.5.1), martensite ($450K.s^{-1}$), bainite ($6.5K.s^{-1}$) and ferrite-pearlite ($0.06K.s^{-1}$). The formation of these structures was a function of cooling rate (Fig.5.1) and a function of the composition of the steels (Fig.5.2 and 5.3).

In order to gain an understanding of the macrostructures studied in the steels, a detailed explanation of the structures found in Fe - 0.1C - 0.13V - 1.5Mn steel as a function of cooling rate is presented (see Fig.5.1). In this steel, martensite was observed from $500K.s^{-1}$ down to approximately $85K.s^{-1}$. Martensite has a body-centered tetragonal crystal structure, for which the lattice parameters were found to vary linearly with carbon content [142]. Due to this specific crystal structure, martensite is a well defined phase in steel as are austenite (f.c.c.) and ferrite (b.c.c.). The martensite is nucleated from the austenite. The habit plane

and orientation relationship of martensite with the austenite varies according to the carbon content [143]. This happens because the parent austenite and the martensite change their lattice parameter by different amounts depending upon the carbon content. Consequently, the martensite is expected to show different characteristics in the five alloys investigated.

At a lower cooling rates ($< 85 K.s^{-1}$), the structure of 0.13% vanadium steel.(see Fig.5.1) was composed of a mixture of carbide and ferrite as revealed by the electron microscope using carbon replicas. This needlelike shape structure was identified as bainite. At the cooling rate of $6.5 K.s^{-1}$ the prior austenitic grain boundaries appeared to be outlined by small ferrite grains. This observation made it possible to carry out an estimation of the austenitic grain size for which a value of 60 μm was found (see section 4.4). The ferrite grains were found to be relatively free of large carbides compared to their adjacent bainite areas. These particular ferrite grains were probably formed in the γ tod transformation range of temperatures because, in this hypoeutectoid steel, only ferrite could have been formed before the eutectoid temperature was reached during continuous cooling.

On the other hand, in this 0.13% vanadium steel, it is at a cooling rate of $2.1 K.s^{-1}$ that a peak hardening was observed (see Fig.4.1.3). The structure was composed of a mixture of 45% ferrite grains ($\bar{X}$ = 10 μm) and 55% bainite (see Fig.5.1). Like the 0.45% vanadium steel,

an attempt was made for this 0.13% vanadium steel to determine with certainty the hardness value of the ferrite ($HV_f \pm \Delta_f$) and of the bainite ($HV_b \pm \Delta_b$). This however could not be achieved for the 0.13% vanadium steel because the hardness of the ferrite and the bainite were too closely related (i.e. $|HV_f - HV_b| < |\Delta_f + \Delta_b|$).

However, from the cooling rate of $2.1K.s^{-1}$ down to $0.06K.s^{-1}$, the bainitic structure was progressively replaced by a pearlite-ferrite structure as illustrated in Fig.5.1. At a cooling rate of $0.003K.s^{-1}$, it can be seen also in Fig.5.1 that all the pearlite had disappeared. The pearlite was replaced by spherodized cementite as revealed by the electron microscope.

A similar morphology of structures discussed for the low vanadium steels (Fig.5.1) can be observed in high vanadium steels(Fig.5.2) and in niobium steels (Fig.5.3). In Fig.5.2, the two high vanadium steels were compared with respect to their manganese content. It can be seen that the manganese promoted the formation of bainite at lower cooling rates. A similar effect was found in the niobium steels (see Fig.5.3); (it should be noted that there has been a change of scale for magnification in order to take into account the larger grain sizes of the 0.02C - 0.14Nb steel, as compared to the 0.04C - 0.06Nb steel). The manganese was observed to lower the $\gamma \rightarrow \alpha$ allotropic transformation in steel (see section 4.7) and is known to displace to a longer time the "pearlite nose" of a plain carbon steel in a time-temperature-transformation (TTT diagram).

Thus, for an equivalent cooling rate in the manganese steel of Fig.5.2, (1) less ferrite will be formed in the γ-α range, because the nucleation rate is at a lower equilibrium temperature, and (2) the curve might not have penetrated sufficiently into the austenite to pearlite transformation area, to allow pearlite to form, whilst the cooling rate was yet sufficiently slow to penetrate into the austenite to bainitic transformation area, thus allowing a bainitic structure to be formed.

Fig.5.4 illustrates the mixed structure of bainite and ferrite for the low vanadium and low niobium steels studied in the present investigation. In the bainitic areas, the dislocation densities were approximately estimated to be 10 times higher (10^{11} dislocations.cm/cm^3) than in the ferritic areas. At peak hardening, the vanadium steel contained 55% bainite compared to the 30% found in the niobium steel. It can also be deduced from Fig.5.4 that many specimens were required to determine the dislocation density in ferrite. The study of ferritic areas in both materials was important because the peak hardening appeared to be associated with the presence of ferrite in the macrostructure of the steels. Consequently, the bainite and martensite were not studied further and the work was concentrated at the cooling rate where ferrite could be formed.

In résumé, the effect of the variation of cooling rates on the macrostructure in vanadium and niobium steels was studied. For instance, it was shown that the peak hardening observed previously (see section 4.1) corresponded to the appearance of small ferrite grains in the macrostructure.

5.2 Solution treatments of the steels.

This section presents an account of the experiments carried out to determine the temperature at which complete solution of MCN was achieved in γiron, bearing in mind that a predicted temperature was available from solubility equations. The effect on the macrostructure of a partial solution treatment is also illustrated.

The solubility equations used in the present study are shown in Table 2.2, whilst these equations and others collected by Aronsson [1] are shown in Fig.1.1.1.1. Large undissolved particles were sometimes observed in specimens quenched in iced brine after one hour heat-treatment at the solution temperature predicted from solubility equations. However, this observation was largely confined to the niobium steels (see Fig.5.5 and 5.6), whereas the vanadium steels were relatively free of such particles.

In Fe - 0.03C - 0.19N - 0.14V steel, the predicted temperature for complete solution of VN in γiron was 1380K (see Table 2.2). To investigate the effect of a partial solution of VCN compared to a complete solution of VCN in the microstructure and in the macrostructure, two heat-treatments were selected at a temperature below and above the predicted temperature for complete solution. Two samples underwent solution treatment at 1325K and 1425K before being quenched in iced brine after one hour heat-treatment. Carbon replicas were prepared from the two samples and examined in the electron microscope. The

material heat-treated at 1425K showed a very small volume of small precipitates which were detected at high magnification (using electronic gun tilt dark field). The specimen heat-treated at 1325K, 55K below the predicted temperature for complete solution, showed areas where precipitate had grown to 50 nm in size. Such an area can be seen in Fig.5.7. The ring diffraction pattern obtained from the above area corresponded to a VCN crystal structure and lattice parameter. In the three other vanadium steels used in the present study, the same procedure was repeated at a selected temperature (1325K, which was above the predicted temperature for complete solution). In all these steels (see Table 2.2), no such areas as those seen in Fig.5.7 were observed. The selected temperature was therefore adopted for further solution treatments to achieve complete VCN solution in those steels.

In Fe - 0. 04C - 0.06Nb - 0.7Mn steel, complete solution of NbC was expected to occur at 1350K $\pm$ 50K (see Table 2.2). However, the same procedure used for Fe - 0.03C - 0.14V steel was repeated with two niobium steel samples heat-treated at 1425K and 1475K respectively for one hour. The results are shown in Fig.5.5. Whilst no area was observed where precipitate had grown (such as shown in Fig.5.7), large undissolved particles were revealed, as can be seen in Fig.5.5. The 1425K solution treatment was adopted for this material because: (1) no area was observed where precipitate had grown, and (2) a smaller austenitic grain size was found at 1425K.

The problem of large undissolved particles was met also in the Fe - 0.02C - 0.14Nb steel. The composition of the steel was adjusted to produce a stoichiometric composition of NbC. From the NbC solubility equation (see Table 2.2), it was predicted that the NbC would be completely dissolved at 1365K $\pm$ 50K. The procedure described for Fe - 0.03C - 0.14V steel was used on samples heat-treated one hour at 1425K, 1475K and 1525K. In all samples, areas such as those shown in Fig.5.7 were observed as illustrated in Fig.5.6 (NbC rings in the electron diffraction pattern), whereas after a three hour heat-treatment at 1525K, areas similar to those shown in Fig.5.6 were seldom seen.

However, large undissolved particles were still present in the structure after the above heat-treatment. These large undissolved particles were found to contain niobium as revealed by X-ray scans for NbKα. It should not, however be concluded that they were NbC particles, but in any event, complete solution implies that niobium atoms would be substituted for iron atoms and vice versa. Nevertheless, it can be postulated that the reaction occurred at the particle-matrix interface and that a long time might be necessary to dissolve a large particle such as is shown in Fig.5.6 as well as to replace it with iron. Considering the above observation, a five hour solution treatment at 1525K was adopted.

The importance of a solution treatment producing complete or incomplete solution can be considered in terms

of its effect on the macrostructure and the microstructure. This effect is illustrated in Fig.5.7. As mentioned earlier, the predicted temperature for complete solution was 1380K. In the two specimens continuously cooled from the austenite, twinning was not seen in the microstructure of the specimen heat-treated at 1325K (55K below predicted temperature for full solution) whilst it was seen in the other specimen (1425K). The macrostructure of the latter was a regular grained structure compared to a mixture of small and large grains in the former. This last observation can be explained by applying the Zener relationship [90] (see section 1.3.1). The maximum volume fraction of VCN at 1325K was calculated from a solubility equation shown in Table 2.2. This value corresponded to 40% of the total volume fraction of VCN in the Fe - 0.03C - 0.019N - 0.14V steel. The average particle size was 50 nm. According to the Zener relationship [90] with these values of particle size and volume fraction, grain size up to 70 μm should have a restricted growth from the pinning action of the particles, whereas larger grains should grow at the expense of smaller ones.

Another experiment, cycling through the γ-α transformation, was designed to investigate if twinning could be observed again when the solution temperature was too low to dissolve all the VCN. Samples were heat-treated at 1325K for one hour before being cycled 50 times between two temperatures (cooling rate $\simeq 2K.s^{-1}$, heating rate $\simeq 1K.s^{-1}$). An illustration of this experiment can be seen in Fig.5.8. It was thought that the same structure could be repeated

at every cycle towards the end of the cycling test, if a sufficient number of cycles were completed. At the end of the cycling experiment, the samples were cooled at 0.17K.s^{-1} from their maximum temperature to enable comparisons to be established with the "one cycle" macrostructure of Fig.5.7. For this Fe - 0.03C - 0.019N - 0.14V steel, the Ar_3, 50% γ-α and Ar_1 were 1165K, 1126K and 1084K respectively. It can be seen in Fig.5.8 that twinning is not present in the microstructure. According to Moiseev [66], a larger grain size should promote twinning more easily. In line with this, the 1225K - 925K sample was examined under the electron microscope (see Fig.5.8). The microstructure showed recovery networks but no sign of twinning.

The macrostructure of the 1325K - 925K sample (see Fig.5.8) exhibited irregular grain boundaries which resulted from pinning by particles. The 1225K - 925K sample showed large grains with regular grain boundaries which arose from unrestricted growth. The particles were assumed too large to pin the boundaries. However, in the 1125K - 925K sample, the grains were much smaller (50% γ-α at 1126K). It is possible to explain this grain refinement in terms of small grains of austenite formed during reheating from α to γ iron. The nucleation sites for γ iron and then for α iron were probably increased (in number) by the presence of large particles in the matrix, and more so by the large particles at the grain boundaries.

In résumé, it has been shown in this section, that complete solution is not only important to obtain the full benefit of precipitation hardening, but it also has an influence on the microstructure as well as on the macrostructure obtained.

5.3 Precipitation morphology in vanadium and niobium steels.

This section will give an account of the features observed in the steels mainly by transmission electron microscopy. The present description is restricted to the vanadium and niobium steels of commercial composition. Precipitation and dislocation/interactionsare illustrated and commented upon.

Before commenting upon the subject of precipitation, a note should be included about the indexation of micrographs. The information obtained from an electron micrograph is limited unless the corresponding electron diffraction pattern could be indexed. It is necessary to associate structural features with crystallographic planes and directions in order to identify them with confidence. The electron penetration is maximized when the crystal is orientated slightly positively to the first order Bragg position in 100 KV electron microscopy [144]. The electron transmission is very poor at the position of symmetry and consequently, the two-beam approximation was used throughout the present study. Each diffraction pattern was indexed according to the standard practice and was subsequently drawn on the micrograph, taking into account the rotation of the image relative to the diffraction pattern.

On the subject of precipitation, interphase precipitation was found in the ferrite of every material investigated in the present study. An example is shown in Fig.5.9. The subject of interphase precipitation was reviewed in

section 1.1.2. Similar patterns of interphase precipitation were observed: occasionally, the rows followed the general contour of the grain boundaries, whilst at other times they formed acute angles with the grain boundaries. Their wavy nature (see Fig.5.10, 0.17K.s^{-1}) indicates that the rows did not follow any particular crystallographic direction and did not possess any definite habit plane. An illustration of the large particle size found in the high vanadium steels at 0.06K.s^{-1} is shown in Fig.5.10. At this particular cooling rate the mean particle diameter was 66 nm with a standard deviation of 36 nm. The particles had a thin platelet shape.

Precipitates exhibiting strain fields were found in Fe - 0.1C - 0.13V - 1.5Mn steel from 2K.s^{-1} down to 0.003K.s^{-1}. Such precipitate can be seen in Fig.5.11 for a steel cooled at 0.003K.s^{-1}. There is no displacement fringe contrast inside the precipitate and there is a line of no contrast perpendicular to the direction of the reciprocal lattice vector ($\bar{g}$). Such precipitates were seldom seen in appreciable numbers and size at higher cooling rates, and a partial analysis was thus carried out.

First, it was attempted to explain these features as a result of a thermal strain. Assuming the particles formed at high temperature in alpha iron, during cooling to room temperature, the precipitate would be progressively stressed from the combined thermal contraction of the iron matrix and of its own structure (other factors, such as MCN diffusion were omitted in this consideration).

A strain value of 3.5×10^{-2} was calculated from thermal equations for carbides and matrices [145]. There is a relation between the state of strain in the matrix surrounding spherical particles and the image width measured on micrograph under a particular $\bar{g}$ vector [146]. Assuming a thermal strain from a spherical particle, it was calculated that such a spherical particle would have a diameter of 17 nm. However, such a particle size could easily be seen in vanadium steel (e.g. in Fig.5.9) by contrast of the particle alone. Such a particle size cannot be seen in Fig.5.11, and consequently, this explanation must be rejected.

Secondly, the strain field observed in Fig.5.11 can have originated from strain due to coherency of the particle with the matrix. Assuming that coherency would be lost after 50% misfit between the particle and the matrix, it was calculated that this would correspond to a spherical particle of 7 nm in diameter. However, such a particle size can be observed in vanadium steel by contrast of the particle alone, and as previously stated, this explanation has to be rejected.

Finally, a similar relationship between the state of strain and image width measured on micrographs was found for disc shape particles [146]. Two assumptions were thus made: (1) the ratio, thickness to particle diameter, was assumed to be related to the Baker-Nutting orientation relationship [33] for f.c.c. particles in a b.c.c. matrix. (2) the normal to the disc plane was

assumed to be in the [020] direction as shown in Fig.5.11 (i.e. the edge of the disc was perpendicular to the beam direction). Following these assumptions the particle parameters were 1 nm thick and 16 nm diameter. One nanometer is the upper limit of resolution of the microscope fitted with a goniometer stage. The last finding appeared to be the only plausible one and, clearly, other studies are required to elucidate this particular problem.

A possible mode of formation of lined-up precipitate is illustrated in Fig.5.12. Edmonds [37] explained these fibrous structures by a similar mechanism to the Davenport model [18]; that is, under conditions of coherency of the fibre with the interphase boundary, the fibre could form with a slow motion of the γ-α interface (see section 1.1.2 for a discussion of the mechanisms). In the $(\bar{1}11)$ plane (see Fig.5.12), the usual characteristics of the interphase precipitation are absent. Although there are rows of aligned precipitate, these rows do not formed genuine interphase precipitation, but are thought to be the first stage of the formation of "rod" type precipitate. It is possible to understand the reasons that have made some earlier workers [23-25] postulated the formation of interphase precipitation from the lining up of precipitate on dislocations (see at point A; Fig.5.12). However, this latter model does not explain the "rows" seen in the (001) plane (see Fig.5.12).

The rod type of precipitate is thought to form as follows: (1) dislocations are generated at $\pi/2$ radians

to the interface boundary in alpha iron, (2) according to Davenport et al. [18] or the Baker [27] model for the formation of interphase precipitation, the growth of the precipitate in the row occurs in ferrite only, (3) if the MCN supersaturation is sufficiently high in ferrite for homogeneous precipitation to occur, the incubation time required for heterogeneous precipitation is less than the time required for the former. Consequently, the MCN precipitate will tend to form on the site of the dislocations (see point B, Fig.5.12), and also on the small nuclei, (4) however, the dislocations allow pipe diffusion and according to the Gibbs-Thomson effect (Ostwald ripening) [147], large precipitates grow at the expense of small ones (small closely arranged precipitates can be regarded as a large particle by the surrounding area), (5) the lines of precipitates are progressively filled up (see point C, Fig.5.12) until there is no more material available due to the establishment of a depletion zone and insufficient time and temperature (in continuously cooled material) for more growth.

The pinning effect on the dislocations by the precipitates can probably account for the relatively high dislocation densities (10^{10} dislocations.cm/cm^3) found in continuously cooled materials (see Fig.4.6.1). There is a change in volume of one percent due to the allotropic transformation of gamma iron to alpha iron, which probably causes the generation of dislocations, to accommodate the internal strain. An illustration of these dislocations

is presented in Fig.5.13 and 5.14.

In Fig.5.14, it was possible to image both the dislocations and the interphase precipitation by using an objective aperture to cover the $[01\bar{1}]$Fe and $[020]$ VCN simultaneously. This shows the importance of considering that under special conditions, the reciprocal lattice vector ($\bar{g}$) of the oxide, MCN precipitate and alpha iron could be nearly equivalent in terms of dimension and orientation. Assuming that the Baker-Nutting [33] orientation relationship is obeyed for both iron oxide (Fe_3O_4) and MCN with respect to α iron, all three reflections will appear closely related in the diffraction pattern [17,148].

(e.g. d_{110} α-Fe = 0.203nm, d_{200} MCN = 0.207nm, d_{400} Fe_3O_4 = 0.210nm).

Finally, in Fe - 0.1C - 0.13V - 1.5Mn steel, precipitates surrounded by loops were observed at low cooling rates ($0.17K.s^{-1}$). These loops were larger in the Fe - 0.03C - 0.14V steel and seemed also to be associated with precipitate exhibiting strain field. However, the determination of strain is difficult (see Fig.5.11 and text) and so is the characterization [149] of associated loops. The execution of these techniques was complicated further because there is only one particular magnification (9K) where both the bright field image and the diffraction pattern can be in focus (with an EM 200). However, Burgers vector determination carried out (as in Fig.5.15) suggested that the loops could be of $\frac{1}{2}\langle 111 \rangle$. Further work is needed to clarify these interesting features.

5.4 Twinning in vanadium and niobium steels.

A fascinating feature was noted in the steels examined in the microscope: twinning. The investigation was carried out with regard to the effect of cooling rate in continuously cooled vanadium and niobium steels of commercial composition. The effect of twinning on strength will be appraised in section 6.4.

Every time that twinning was revealed by the electron microscope, the material exhibited an optical microstructure with features similar to "slip bands" also observed in deformed material. This observation is illustrated in Fig.5.16. It can be seen that all the bands are parallel to each other and that their common direction changes from grain to grain (e.g. in 0.13%V - 1.5%Mn steel). The dimensions of the bands decrease also with the addition of manganese, which is known to reduce the temperature at which the allotropic transformation begins in steel. In the 0.13%V - 1.5%Mn steel, each band probably corresponded to an entire twin colony (see Fig.5.20) whilst in 0.14%V - 0.0%Mn steel, small grain (few μm in size) were observed to be in a $(112)\langle 11\bar{1} \rangle$ twin orientation relationship with respect to the α iron matrix.

Twinning was identified by trace analysis. Using a stereogram, the trace of the composition plane {112} was determined. The indexing of the twin reflections was made easier by the use of equations predicting the position of a twin reflection with respect to a matrix reflection

and known composition plane (see equations 1.2.1.2 and test). These equations were computed (Fortran computer language) for several reflections with respect to the twelve possible (112) composition planes, and the results are presented in Appendix A.

Twinning has been reported [23,27,47,78] in vanadium steels, but has been said to be absent in niobium steels [23,27,47,78]. However, twinning was identified in Fe - 0.04%C - 0.06%Nb - 0.72%Mn steel from the peak hardening ($\simeq 2K.s^{-1}$) down to $0.06K.s^{-1}$. In Fig.5.17, twins were imaged under different reflecting conditions. Displacement fringes at the twin matrix interface can be seen in bright field contrast and in dark field contrast under a [200] matrix two-beam condition. In this dark field micrograph, the twin crystals were completely dark (not imaged) whilst they were all imaged when using a $[0\bar{1}1]$ twin reflection, which did not image the matrix.

In Fig.5.18, twinning is observed at a cooling rate of $0.5K.s^{-1}$. A small grain is observed to be in a twin orientation relationship with the iron matrix. It is possible for twinning to play a role in recrystallisation. This small grain grew from a small twinned crystal. A high dislocation density (10^{10} dislocations. cm/cm^3, see Fig.4.6.1) and a slow cooling rate may favour this phenomenon. However, the effect of manganese on the γ-α transformation temperatures could be the essence of the difference between the band features observed in the manganese and in the non-manganese niobium and vanadium steels (see Fig.5.16).

This last finding leads to the postulate that the mechanism of twin formation can be related to the γ-α transformation. In Fig.5.19, twins are observed near a grain boundary. One twin located at the point "A" is sited on this unusual ragged grain boundary. The small grain at the point "B" can be seen to grow along one of the coherent twin-matrix interfaces. One could interpret these findings as leading to twin growth and not necessarily to twin nucleation. If the grain boundary was moving to the twin, because the grain G1 was growing at the expense of the grain G2, the twin could have acted as a particle (e.g. at point A) and would have impeded the grain boundary motion. Under suitable conditions, these twins could have grown (e.g. at point B) when the boundary tried to advance further into grain G2. Because the material is continuously cooled this process is slowed down and finally ceases, due to a lack of thermal activation.

The size of the twins in niobium steel did not appear to changesignificantly with the cooling rate; if any change occurred, their size seemed to be reduced with cooling rate (see Fig.5.17 to Fig.5.19). The same consideration applies to the twins found in the vanadium steels of Fig.5.20.

The twin colony in vanadium steel was observed to contain more members than its counterpart in niobium steels. The smaller dimensions of the twins in vanadium steel can be explained by the higher manganese content in this steel. The finding that manganese seemed to reduce the size of individual twins was shown in Fig.5.16.

An attempt was also made to calculate the volume percent and number of twins per unit volume in vanadium steel (see Fig.5.20). Each individual twin is assumed to have the shape of an ellipsoid. This assumption was considered to apply so long as the apparent length of the twin was large vis-à-vis the apparent width and apparent thickness of the twin (i.e. only uninterrupted thickness fringes could be seen in the interior of the twin observed in Fig. 5.20, but not in Fig.5.17). An illustration of the method used appears in Appendix B. However, it can be seen in Table 5.4.1 that the volume occupied by one twin and the volume fraction of twins corresponding to their numbers, decreased with decreasing cooling rate. At a cooling rate of $0.003K.s^{-1}$, examination carried out at 100KV and 1000KV did not reveal twinning in this material.

Aligned precipitate (or "rod" type precipitate) was occasionally observed in the neighbourhood of small twins in vanadium steel. Similar findings were reported by Heikkinen [78] who inferred that the twin nucleation could be related to a mechanism involving VCN precipitate. An illustration of this mechanism is shown in Fig.5.21. It can also be seen that one of the twins is completely wrapped by spiralling dislocations imaged under different reflecting conditions. This can be interpreted as the twin acting as a hard particle and interacting with dislocations.

The bright field image shown in Fig.5.22 seems to support Heikkinen's idea that the twin nucleations are associated with precipitate-like features. However, a

Cooling rate ($K.s^{-1}$)	$2.0K.s^{-1}$ (peak)	$0.06K.s^{-1}$
Average volume occupied by one twin	$1.7X10^{-4}$ μm^3	$1.4X10^{-4}$ μm^3
Number of twins in the immediate area ($twins.m^{-3}$)	$3.1X10^{20}$	$2.5X10^{20}$
Grain size	10 μm	24 μm
*Approximate volume % of twins	$3.8X10^{-5}\%$	$6.9X10^{-6}\%$
*Approximate number of twin ($twins.m^{-3}$)	$2.6X10^{15}$	$4.2X10^{14}$
Dislocation density ($dislocations.m/m^3$)	******	$1.4X10^{14}$
Equivalent sphere diameter	69 nm	64 nm
Mean surface to surface inter-twin spacing	74 μm	190 μm

* The volume of one grain was calculated using the assumption that grains are equivalent to a distribution of spheres, for which the average volume can be deduced from Fulman [150];
volume = $(\pi^4/48).D^3$. One grain in evey ten contained twins.

Fig.5.4.1 Variation of twin frequency as a function of cooling rate in Fe-0.1C-0.13V-1.5Mn steel.

closer examination reveals that dislocations can be seen bowing between the particles.

Furthermore, in a bright field image presented by Hèikkinen as evidence of twin nucleation, the electron image of the "precipitate" (Fig. 6 of ref. 78) exhibited oscillatory effects which were similar to the oscillatory effects at images of inclined dislocations near the foil surfaces [146a].

In Fig.5.23, it can be seen that the particles associated with the twin (upper part of the twins with respect to the page) are all associated with a dipole (D). Although not every dipole nucleated a twin, evey twin is associated with these features. This leads to the suggestion that twin nucleation may occur when another dislocation attempts to by-pass a pinned dipole [151].

In brief, twinning was found in niobium and vanadium steels. The effect of a manganese addition to these steels was to reduce the individual size of the twins. The dimensions, volume and frequency of the twins appeared to decrease with decreasing cooling rates.

This chapter has attempted to complement the results described in Chapter four. From the micrographs discussed and many others not included in the presentation, it can be concluded that no texture was developed. Also, the macro and the microstructure were related to cooling rates. It was found that the peak hardenings observed in section 4.1 were obtained from a ferritic matrix. The solution treatment has been shown to influence not only the precipitation hardening but also both the macro and the microstructure (e.g. presence of twins) in steels.

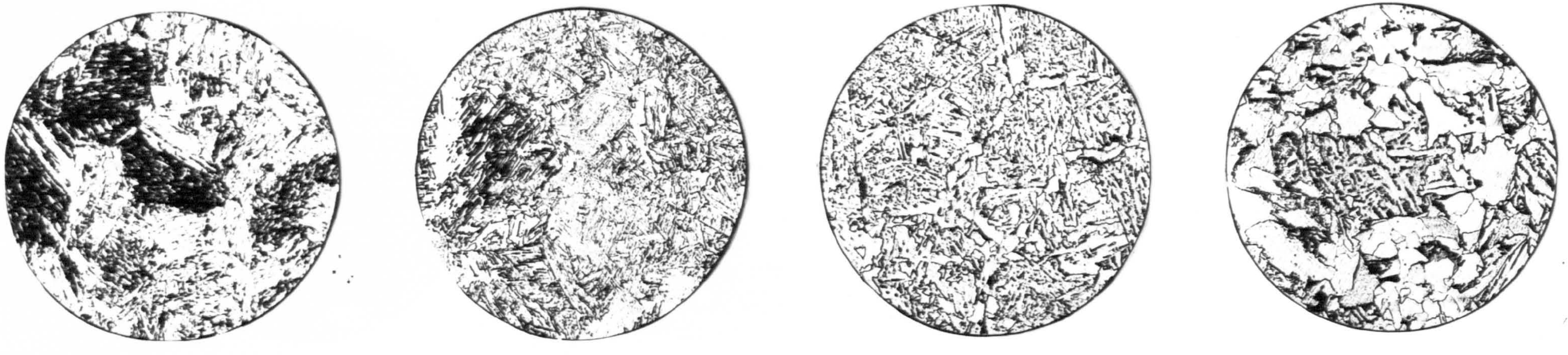

Fig. 5.1 Effect of cooling rates on the macrostructure of 0.1C-0.13V-1.5Mn steel.

No Mn

450 K.s^{-1}

85 K.s^{-1}

6.5 K.s^{-1}

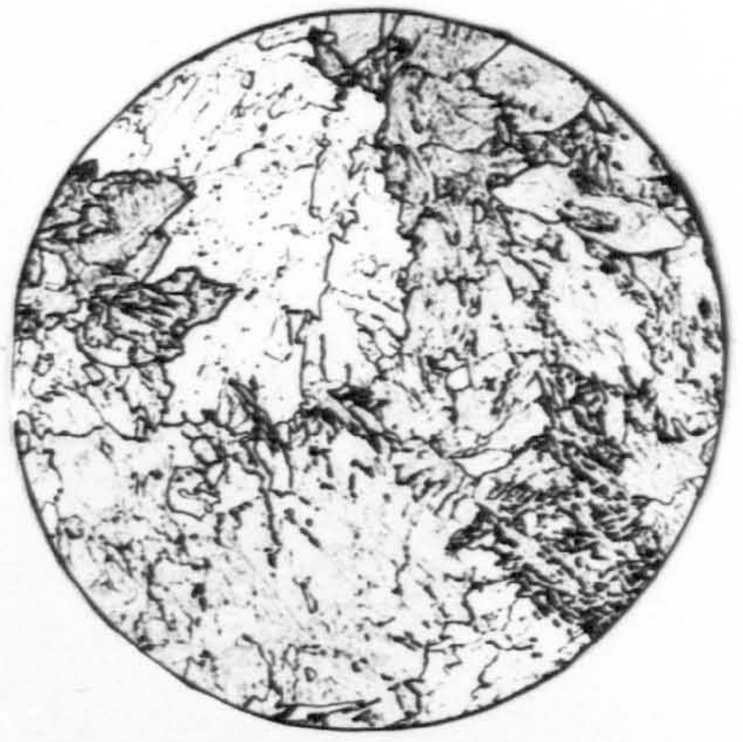

2.3 K.s^{-1}.

100 μm

1.5 Mn

Fig. 5.2 Effect of cooling rates and Mn content on the macrostructure of 0.1C - 0.45V steels.

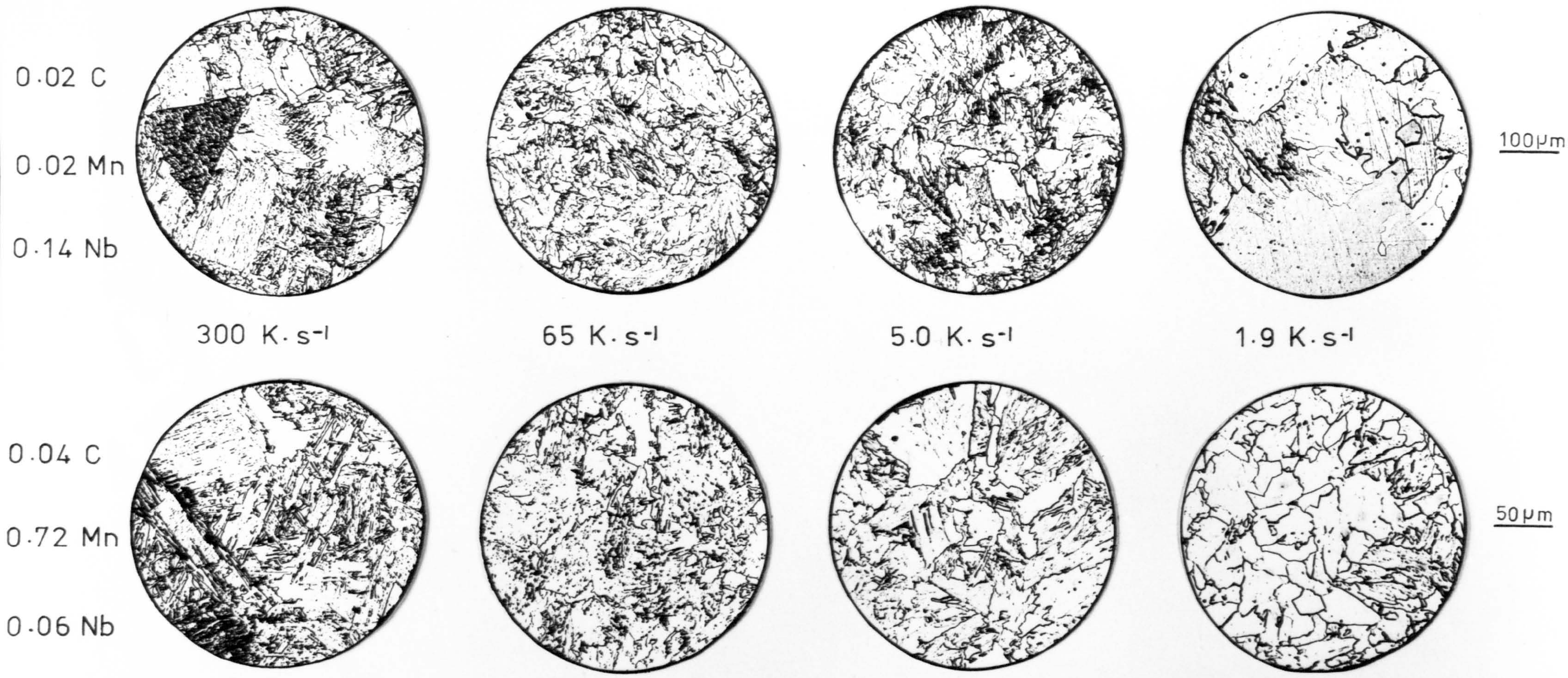

Fig. 5.3 Effect of cooling rates on the macrostructure of Nb steels.

Fe - 0.04 C - 0.06 Nb - 0.72 Mn

Fe-0.1 C-0.13 V-1 5 Mn

Fig. 5.4 Structures at peak hardening.

1.0 μm

50μm

Quenching from 1425 K

Quenching from 1475 K

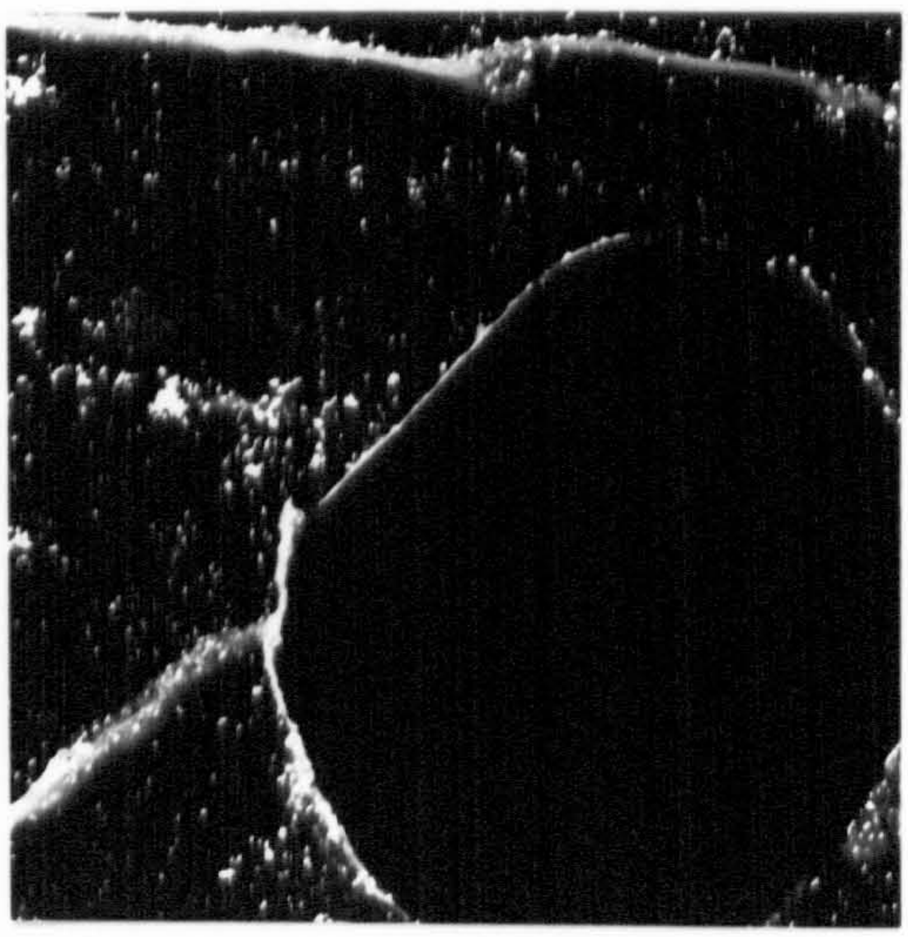

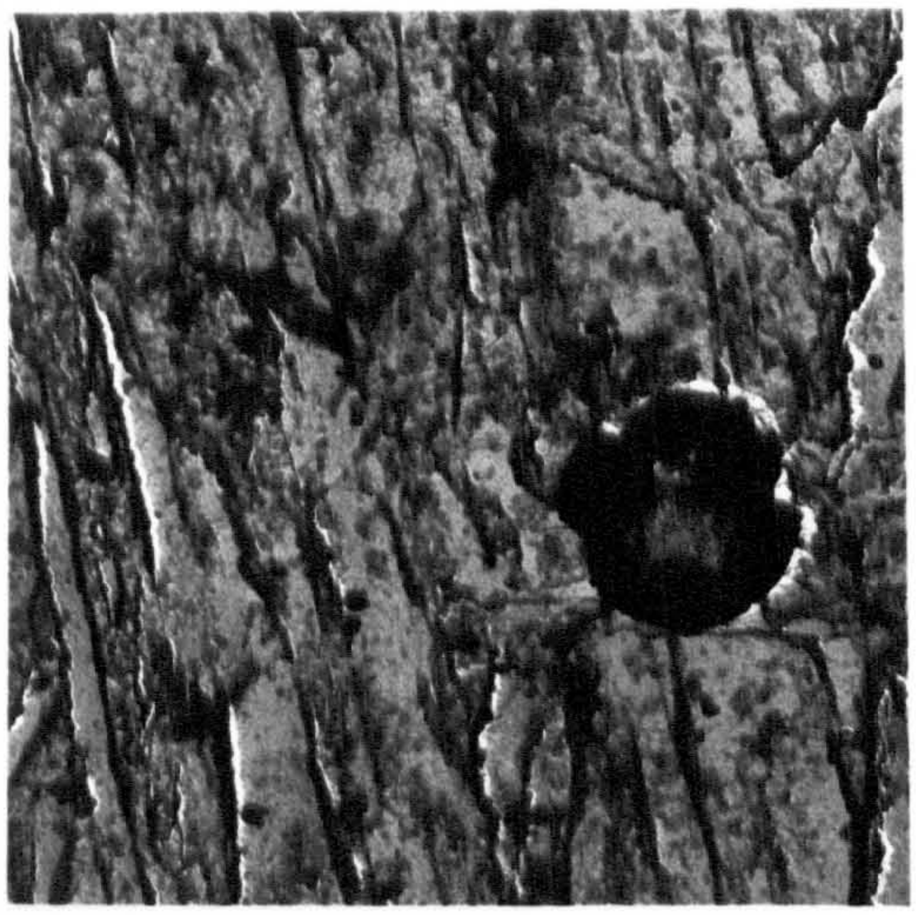

1.0 μm

Quenching from 1425 K

Quenching from 1475 K

Fig. 5.5 Quenching from solution temperature in 0.04 C - 0.06 Nb - 0.72 Mn steel.

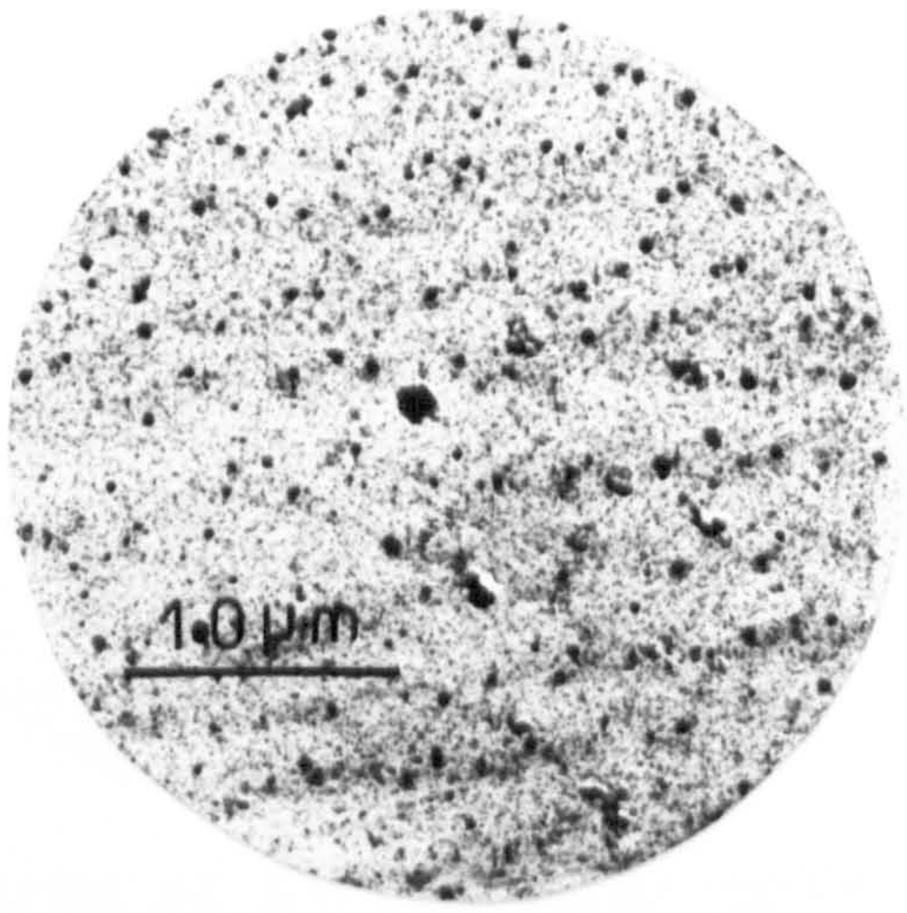

QUENCHING from 1425 K

CARBON REPLICA

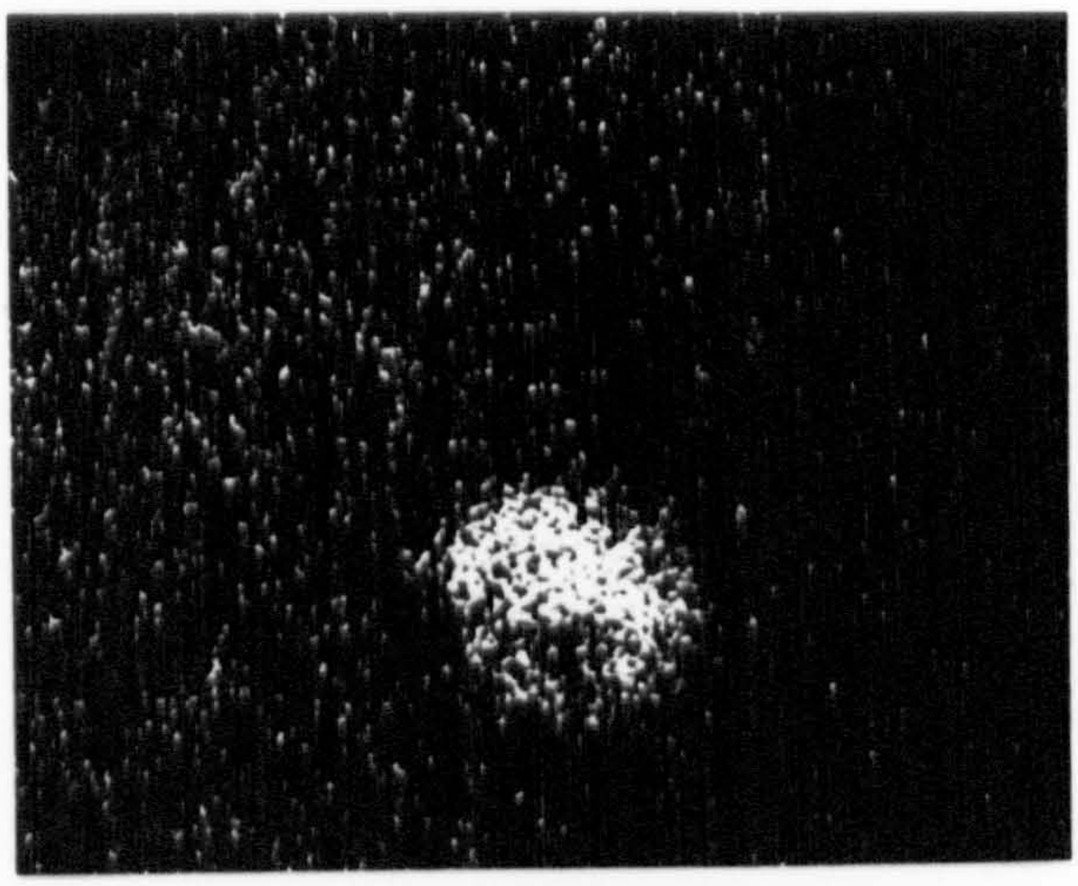

30 μm

QUENCHING from 1525 K

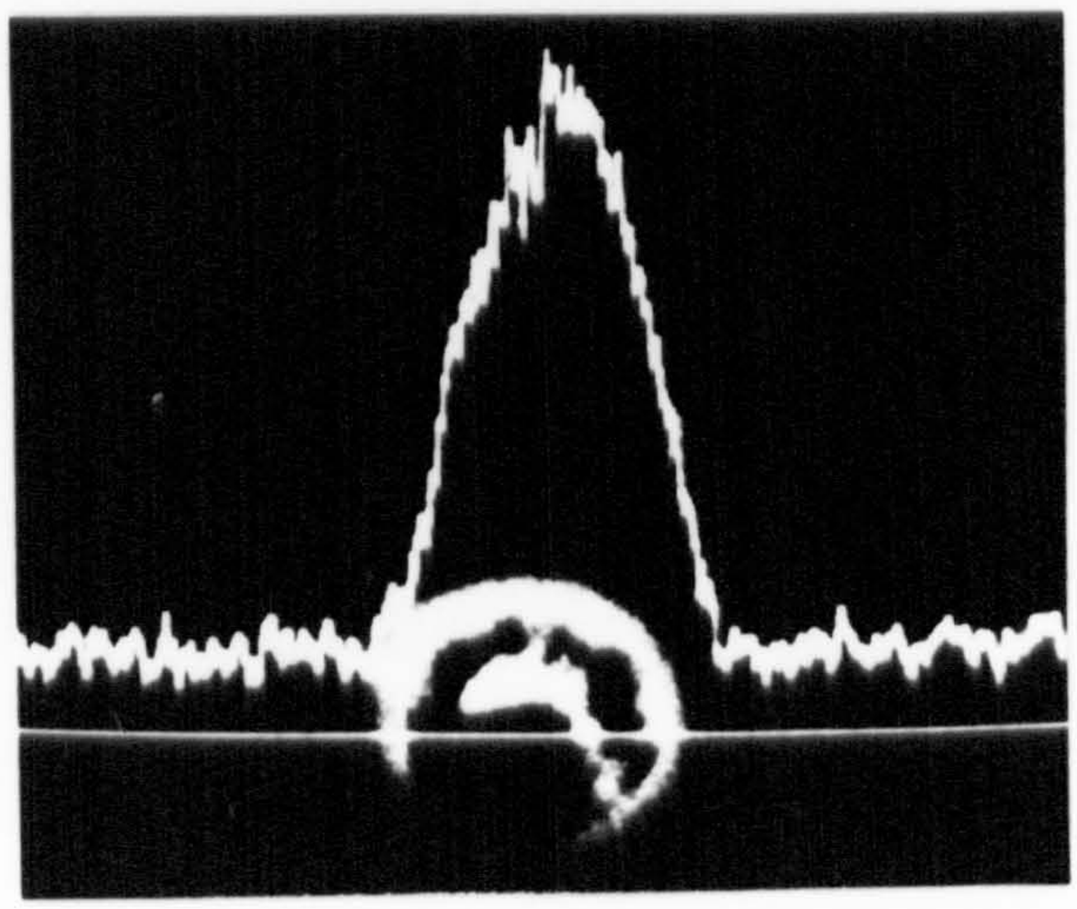

Fig. 5.6 X-Ray scans for Nb Ka in Fe-0.02C-0.14 Nb.

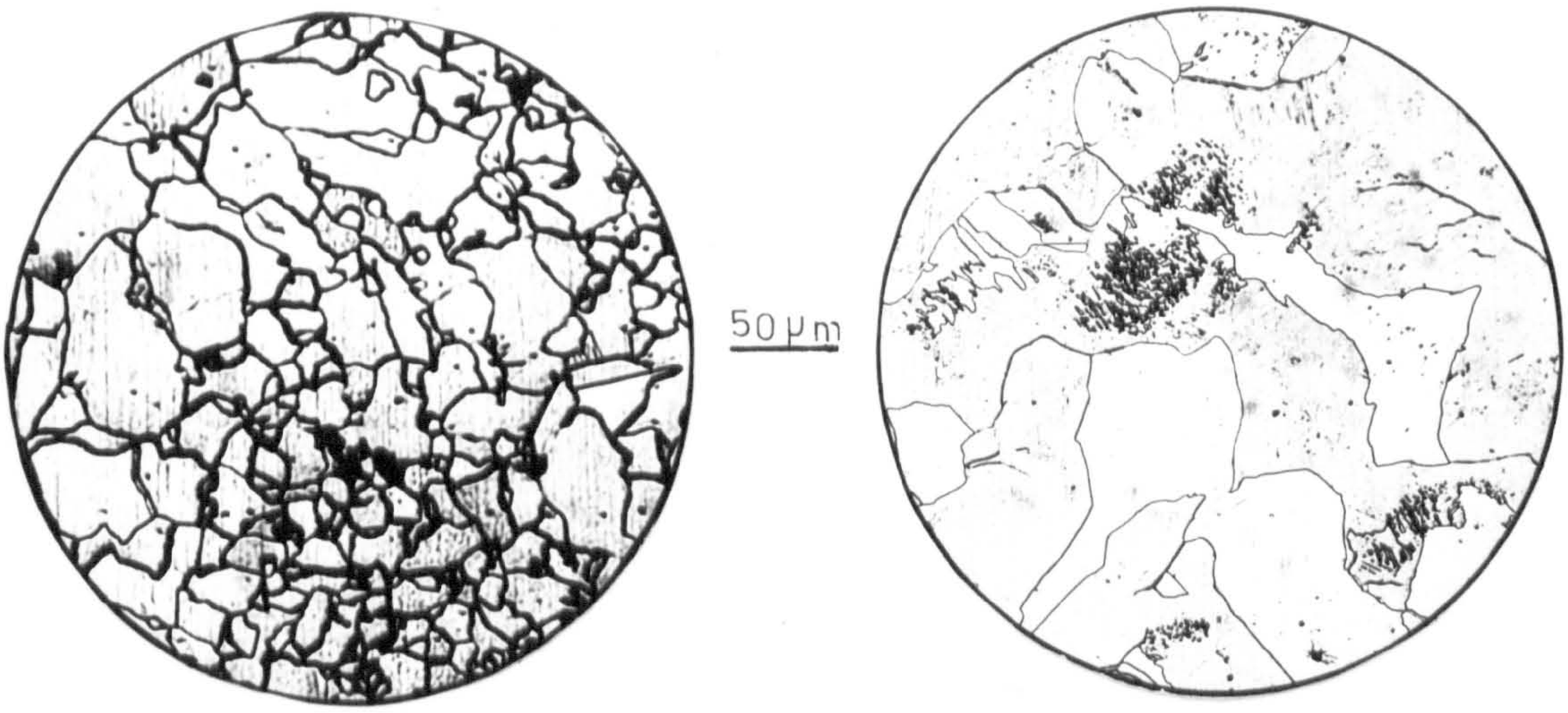

Effect of partial VCN solution on the structure of Fe-0.03C - 0.14V

Fig. 5.7

50 μm

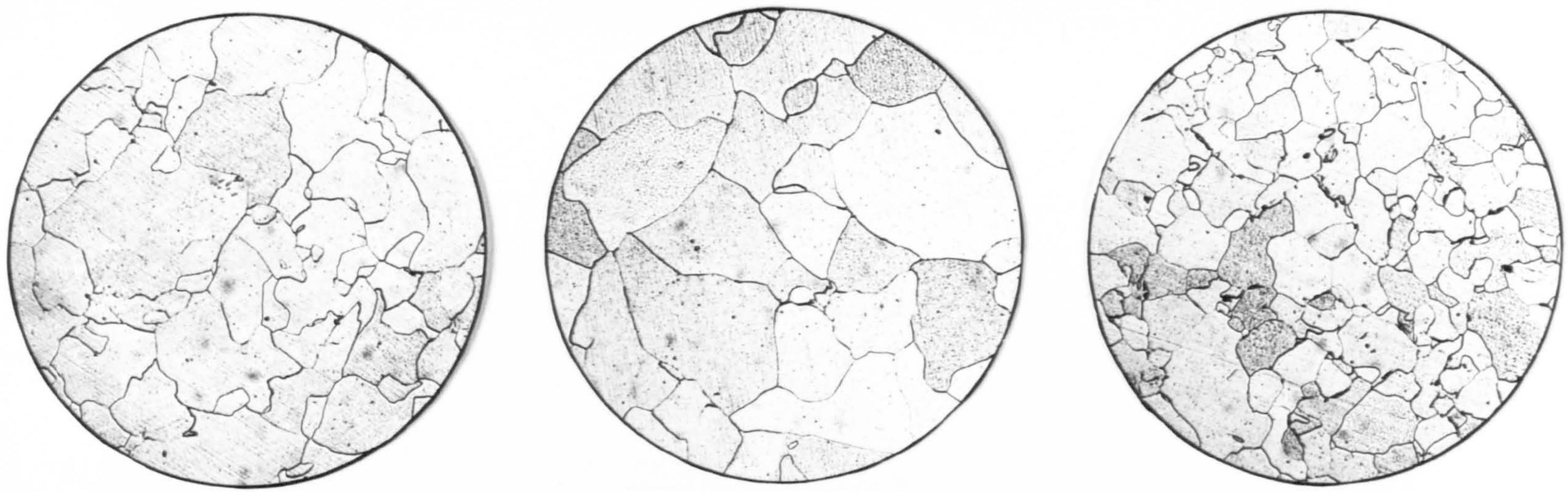

between 1325 K to 925 K 1225 K to 925 K 1125 K to 925 K

Fig. 5.8 Change in the macrostructure with multiple cyclings through the allotropic transformation of Fe - 0.03C - 0.14 V

Fig.5.9 Interphase precipitation in

0.1C - 0.13V - 1.5Mn steel.

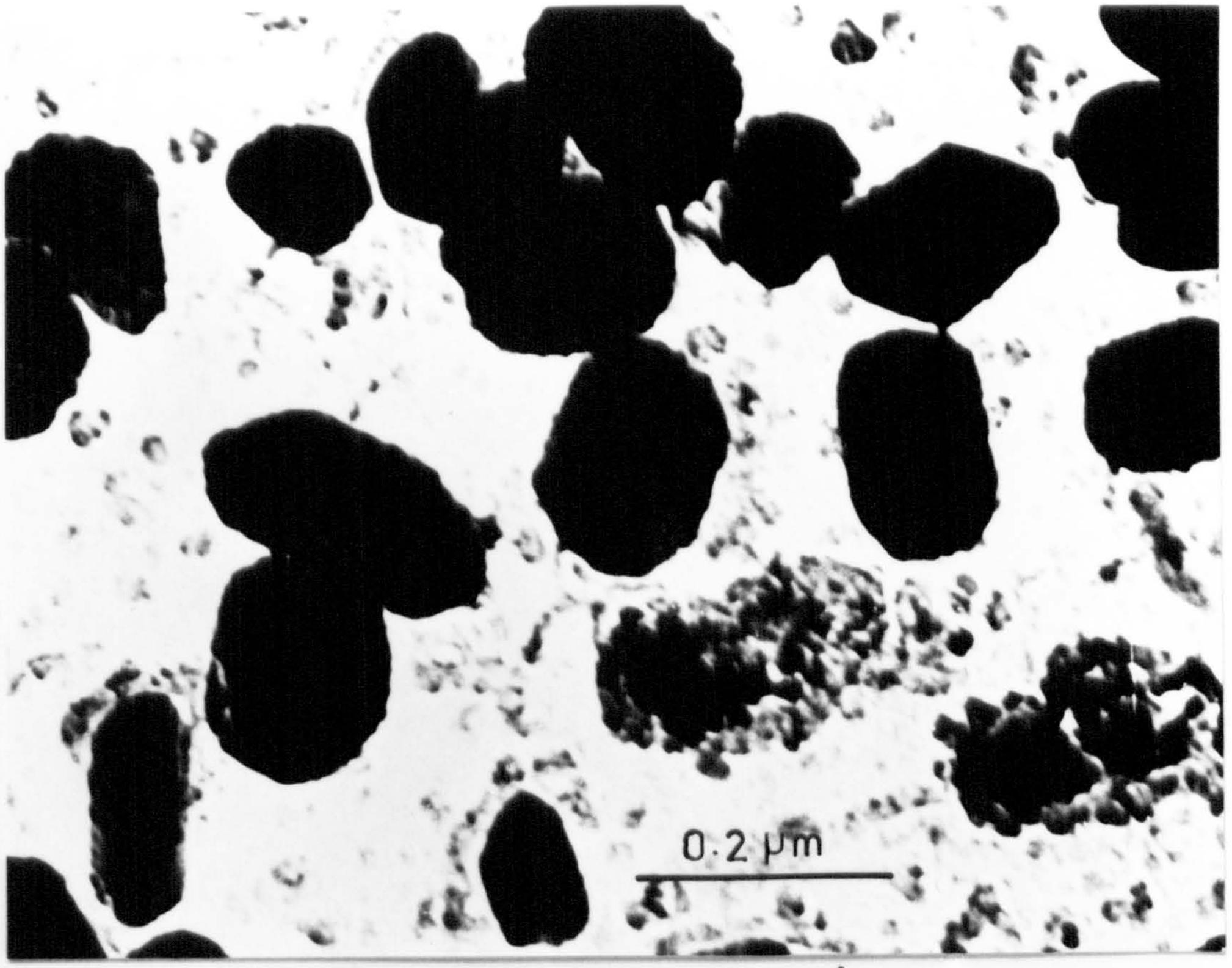

CR = 0.17 K .s^{-1}

CR = 0.06 K.s^{-1}

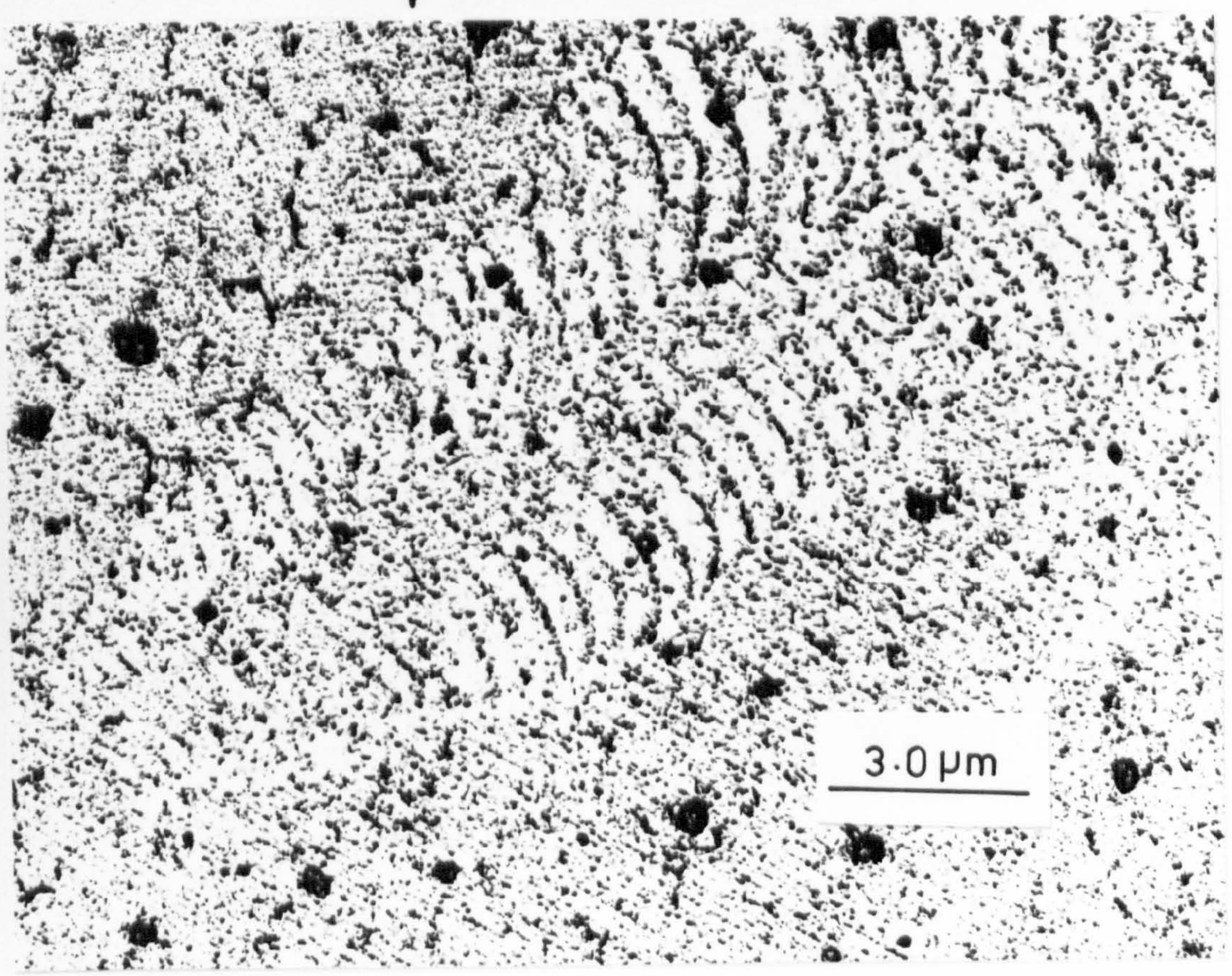

Fig. 5.10 Precipitation in 0.1C - 0.45V steel.

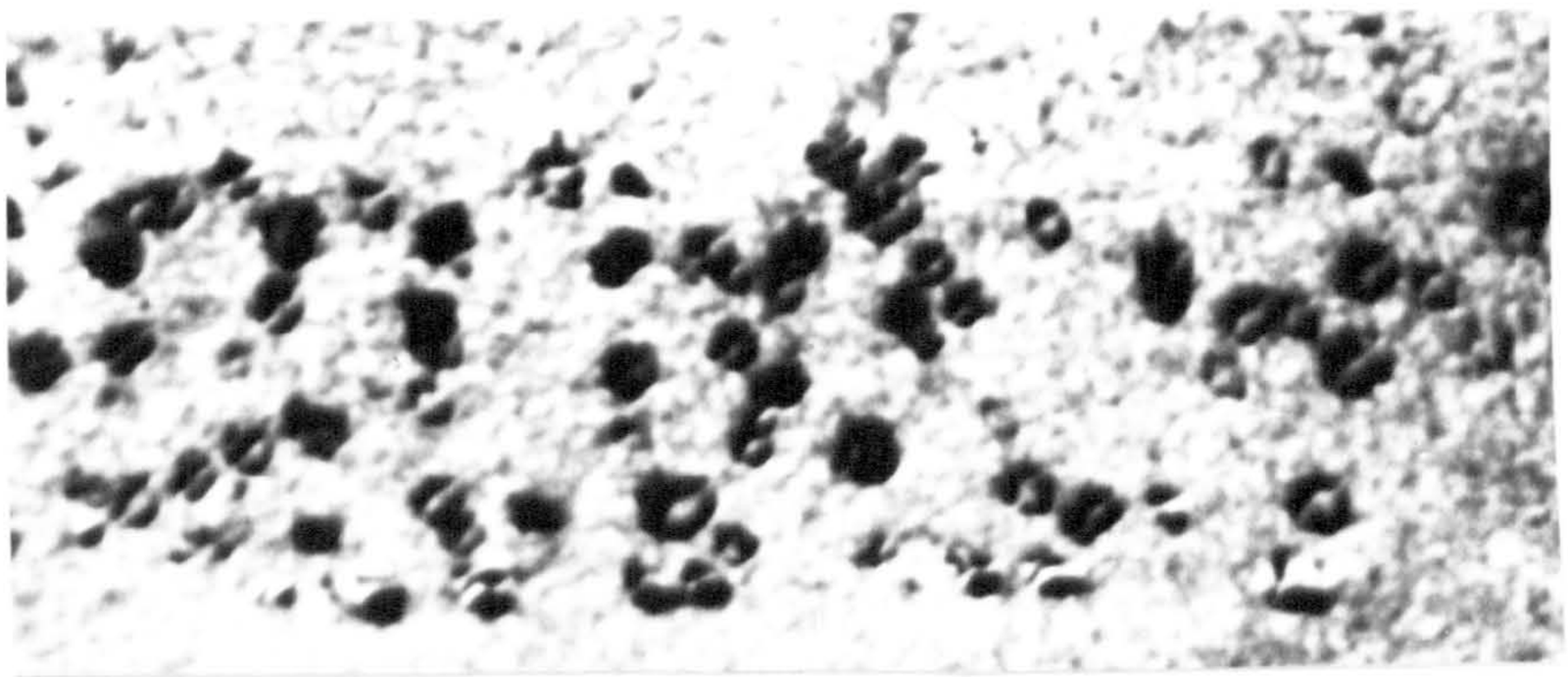

Two - beam $\bar{1}\bar{1}0$

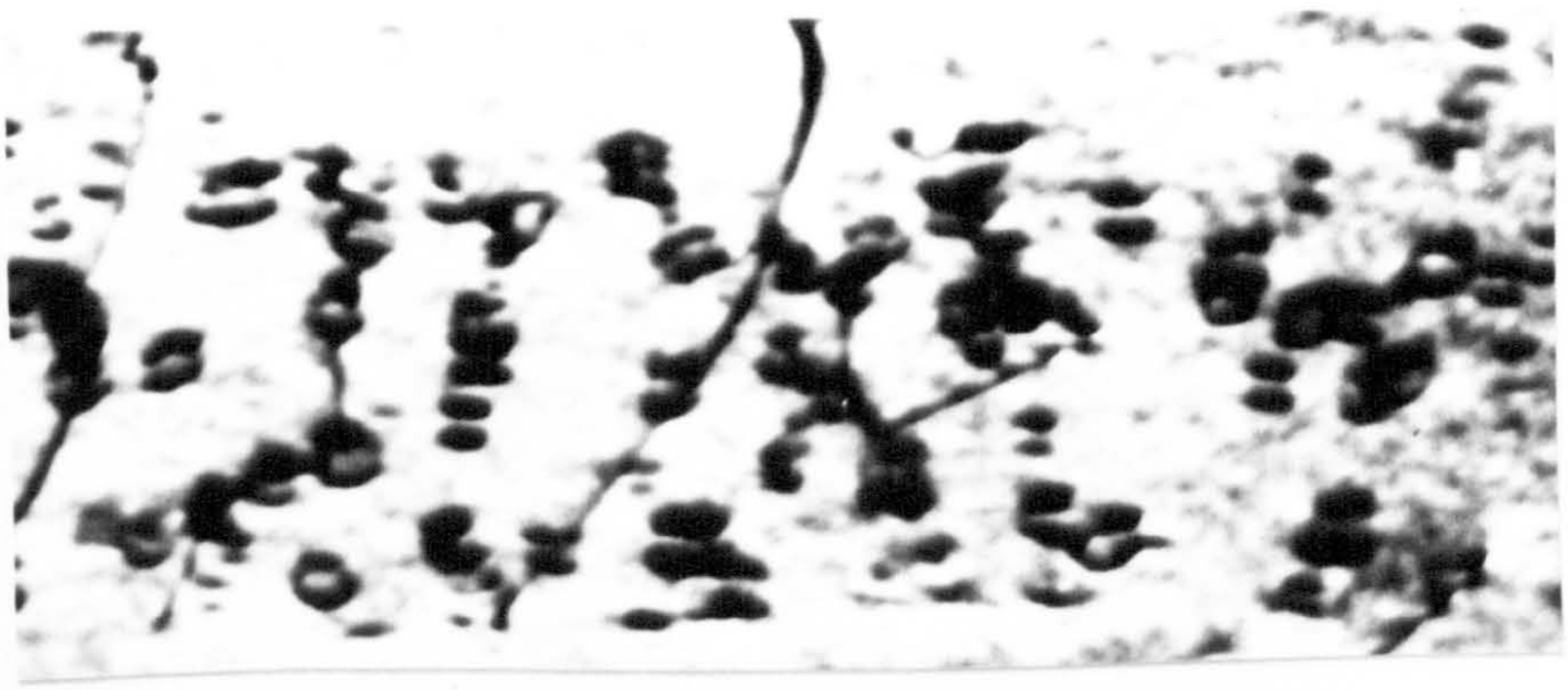

Two - beam 020

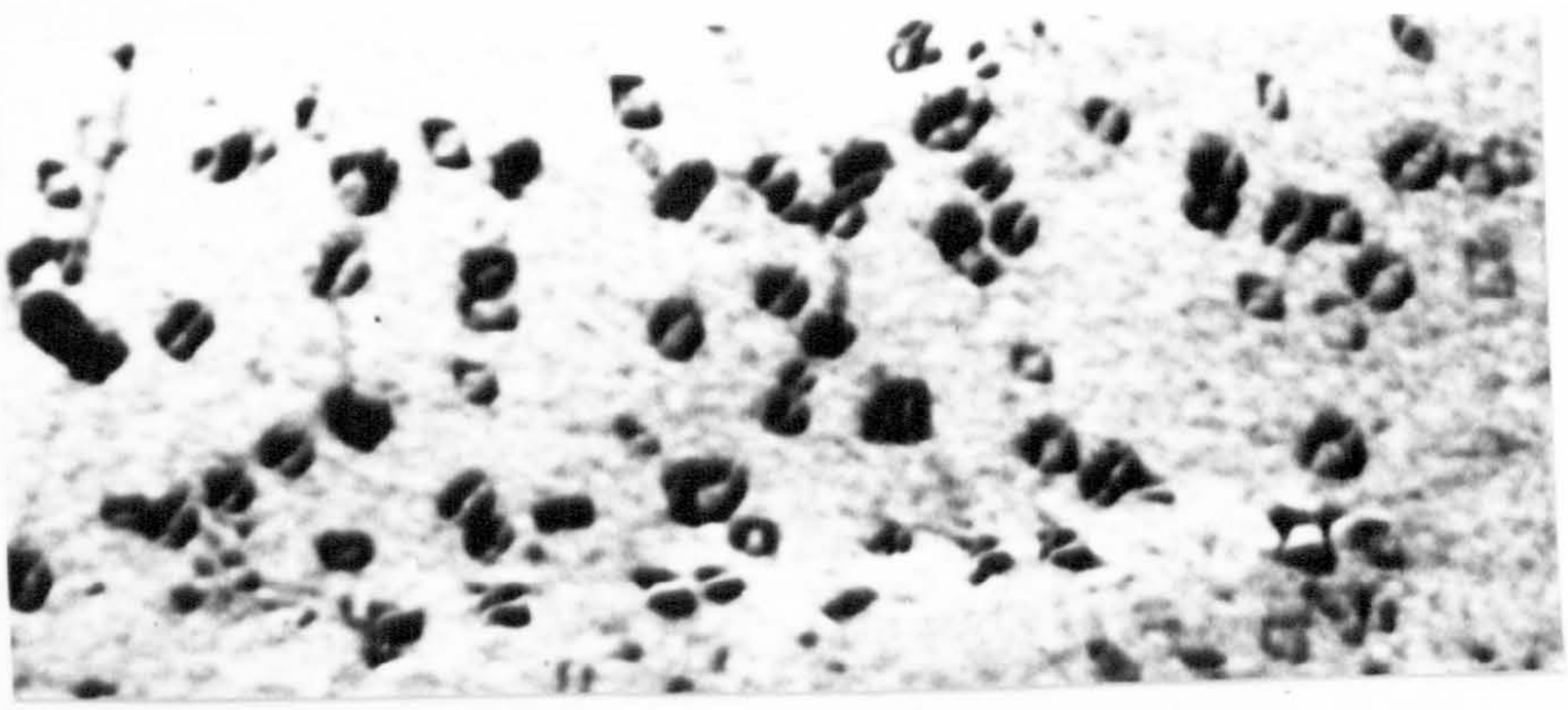

Two - beam 110

Fig. 5.11 Precipitation exhibiting strain-field in Fe - 0.1C - 0.13V - 1.5 Mn

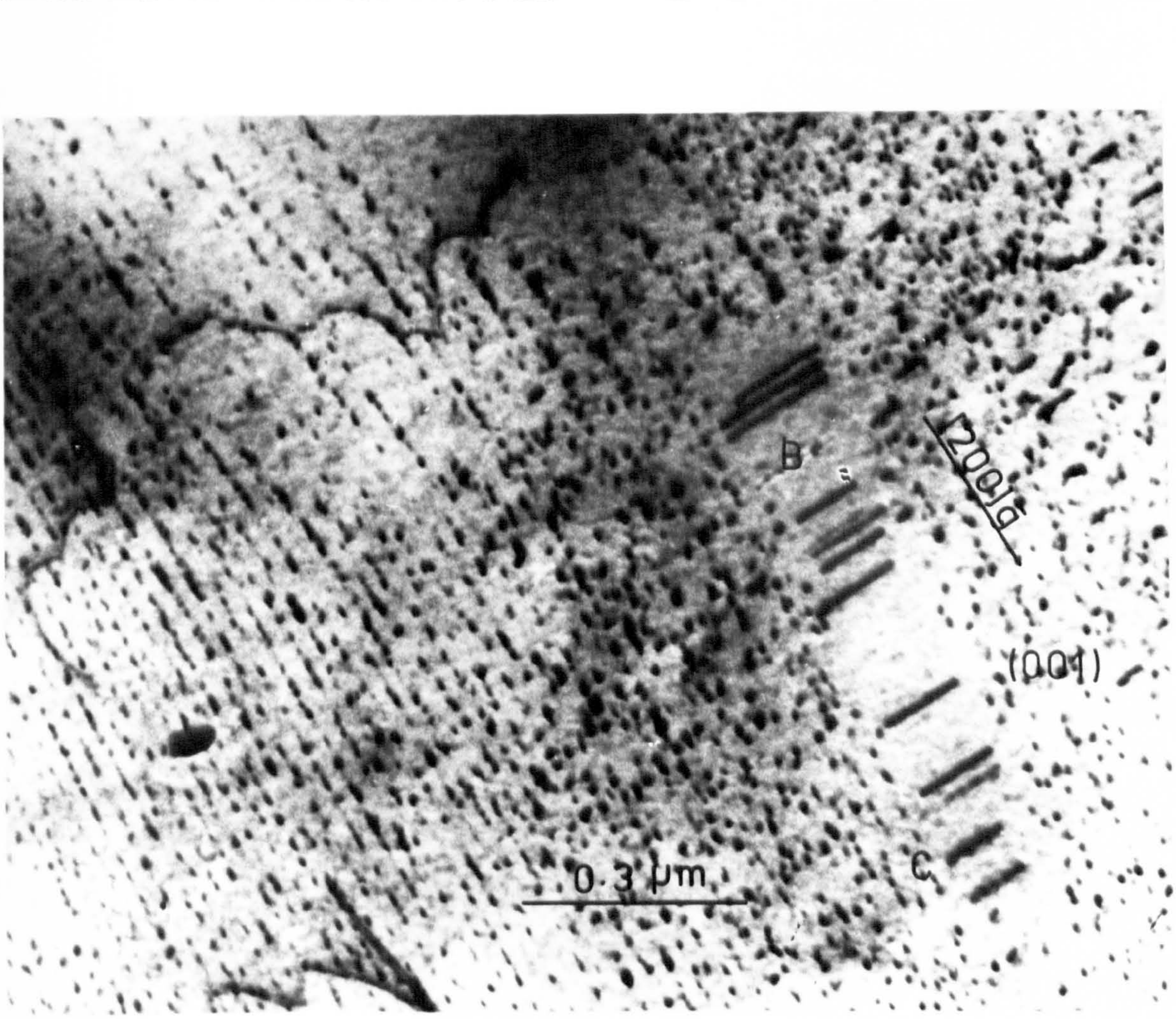

Fig. 5.12 Aligned precipitates in Fe-0.1C-0.13V-1.5Mn

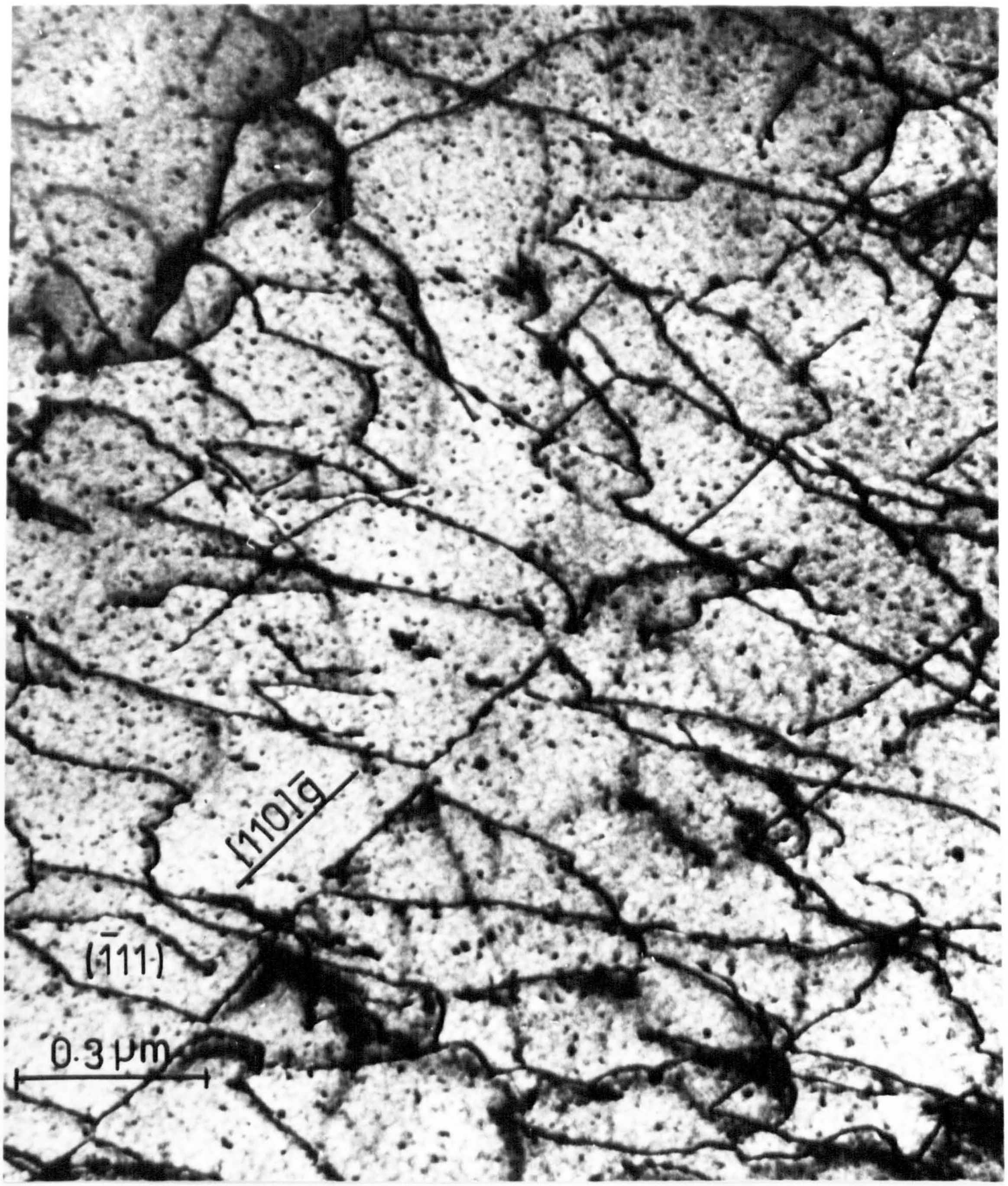

Typical area where dislocation densities were determined.

Fig. 5.13 Dislocations in Fe • 0.1C - 0.13V - 1.5Mn

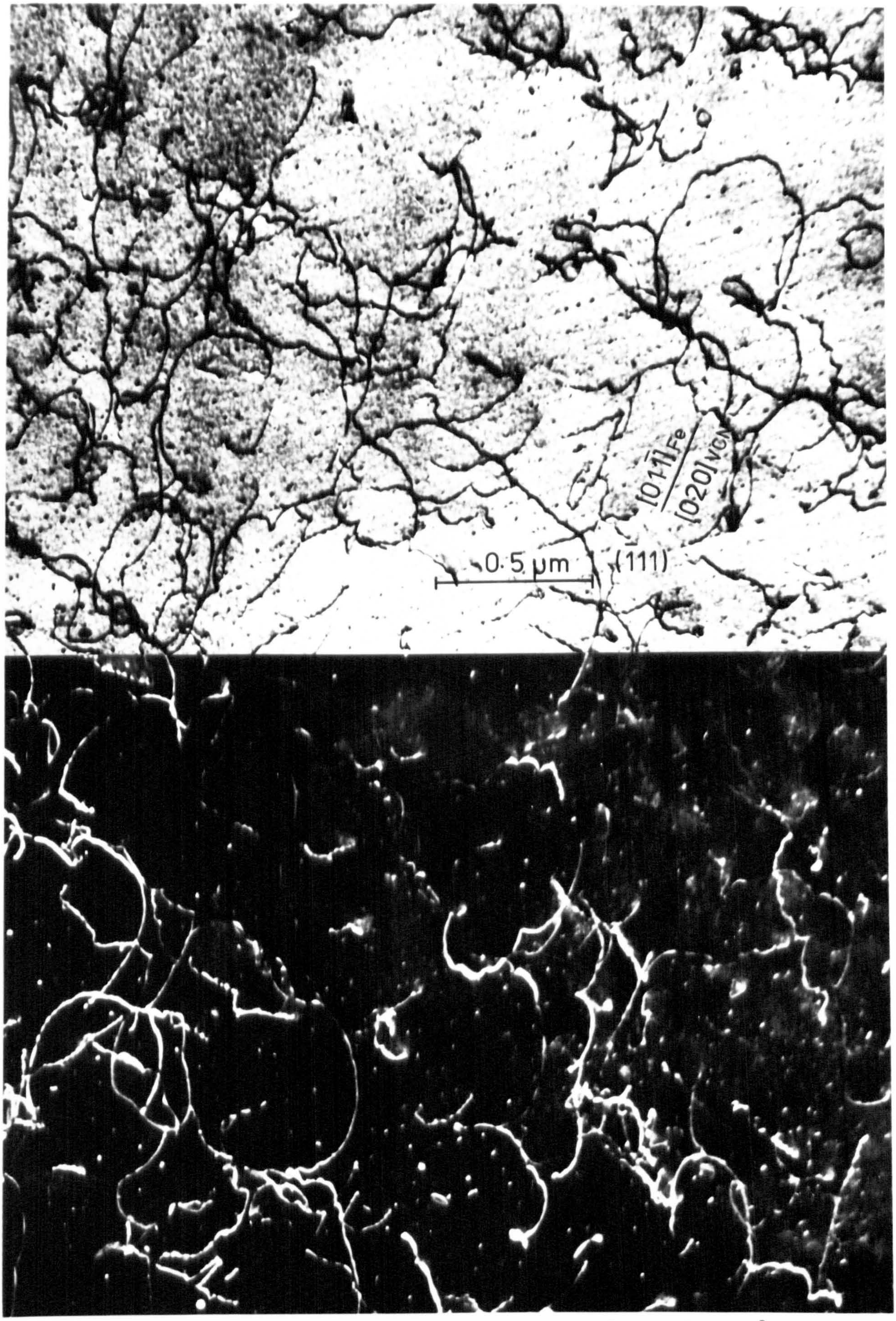

Dark-field $01\bar{1}$

Fig.5.14 Interphase precipitate and dislocations in Fe-0.1C-0.13V-1.5Mn

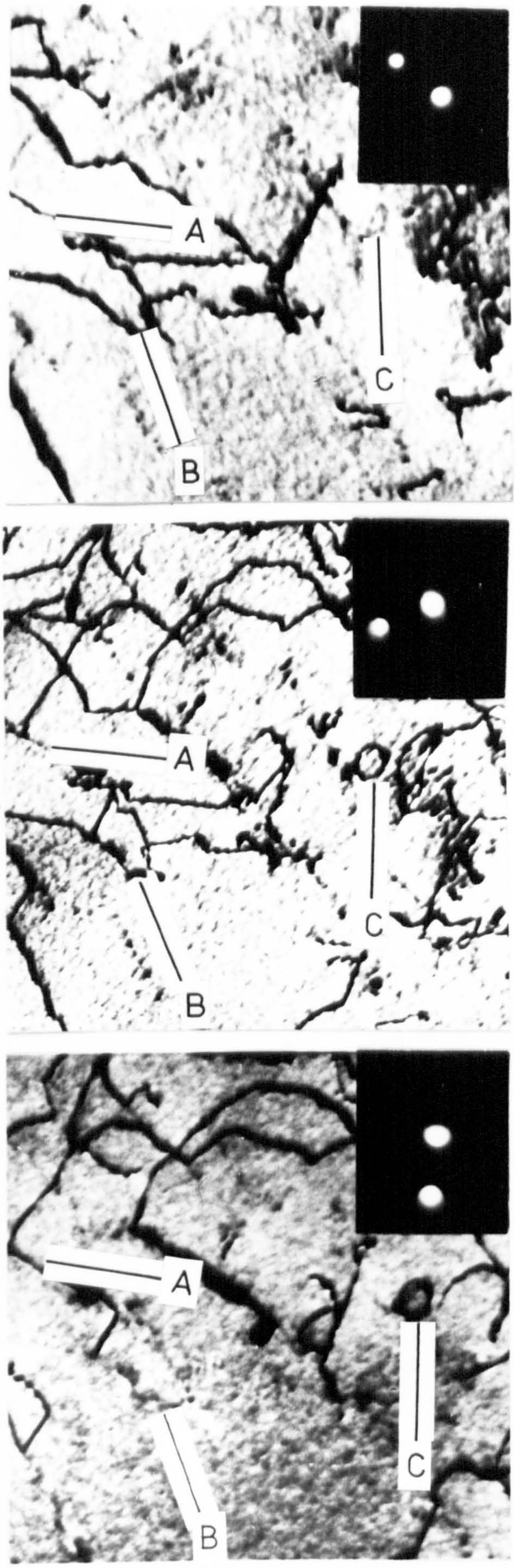

0.3μm

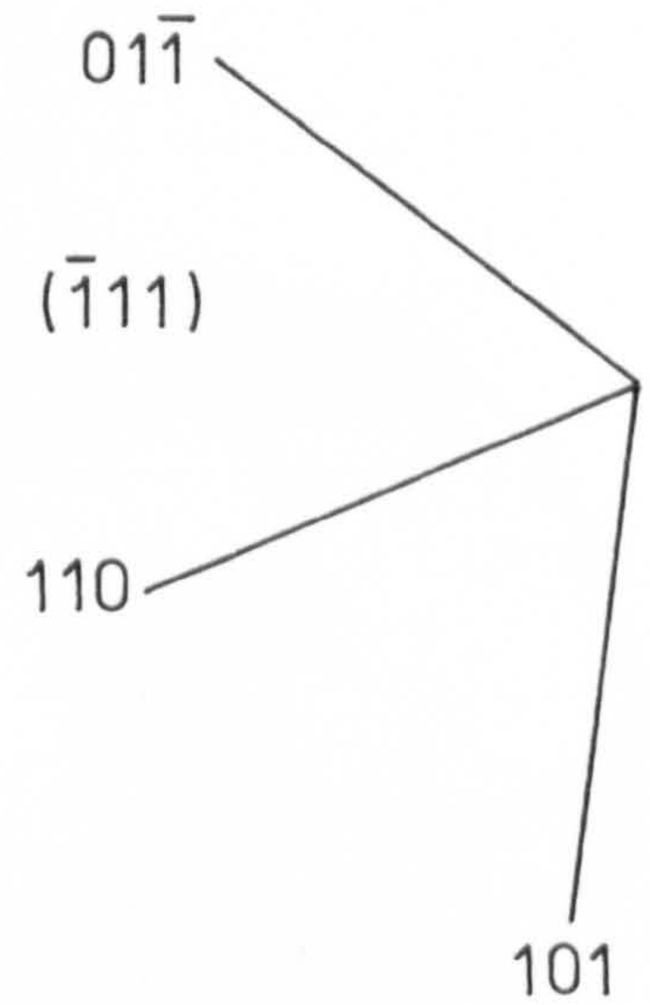

$\bar{b}$ / $\bar{g}$	$\bar{g}\cdot\bar{b}$			e.g.
	01$\bar{1}$	110	101	
0.5[$\bar{1}$11]	0	0	0	
0.5[1$\bar{1}$1]	$\bar{1}$	0	1	A
0.5[11$\bar{1}$]	1	1	0	B
0.5[111]	0	1	1	C

Fig.5.15 Burgers vector determination in Fe-0.1C-0.13V-1.5Mr

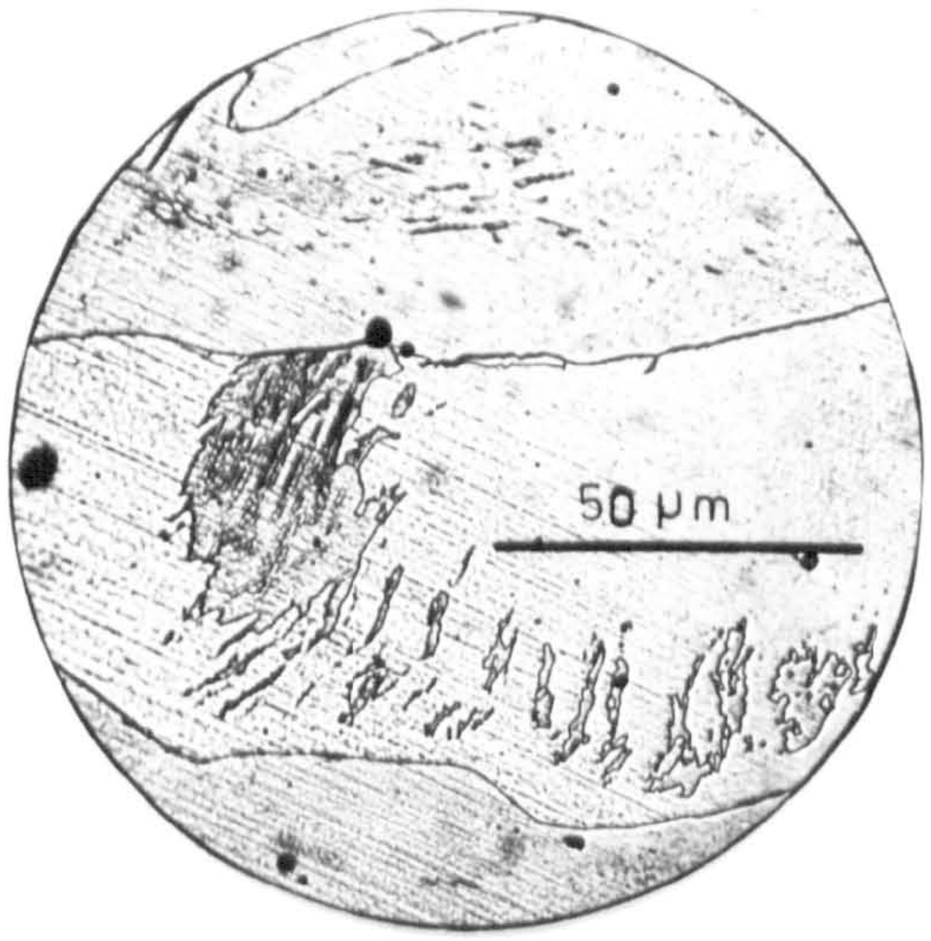

0.14 V 0.0 Mn

CR = 0.17 K.s^{-1}

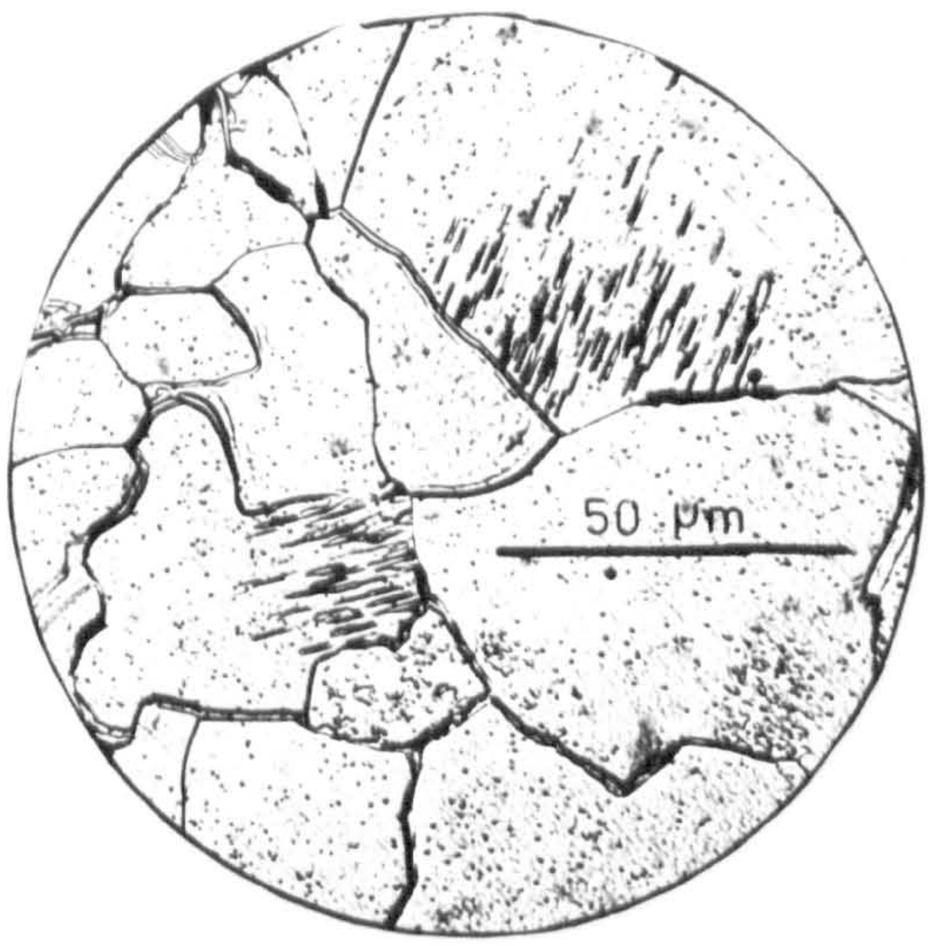

0.13 V 1.5 Mn

CR = 0.17 K.s^{-1}

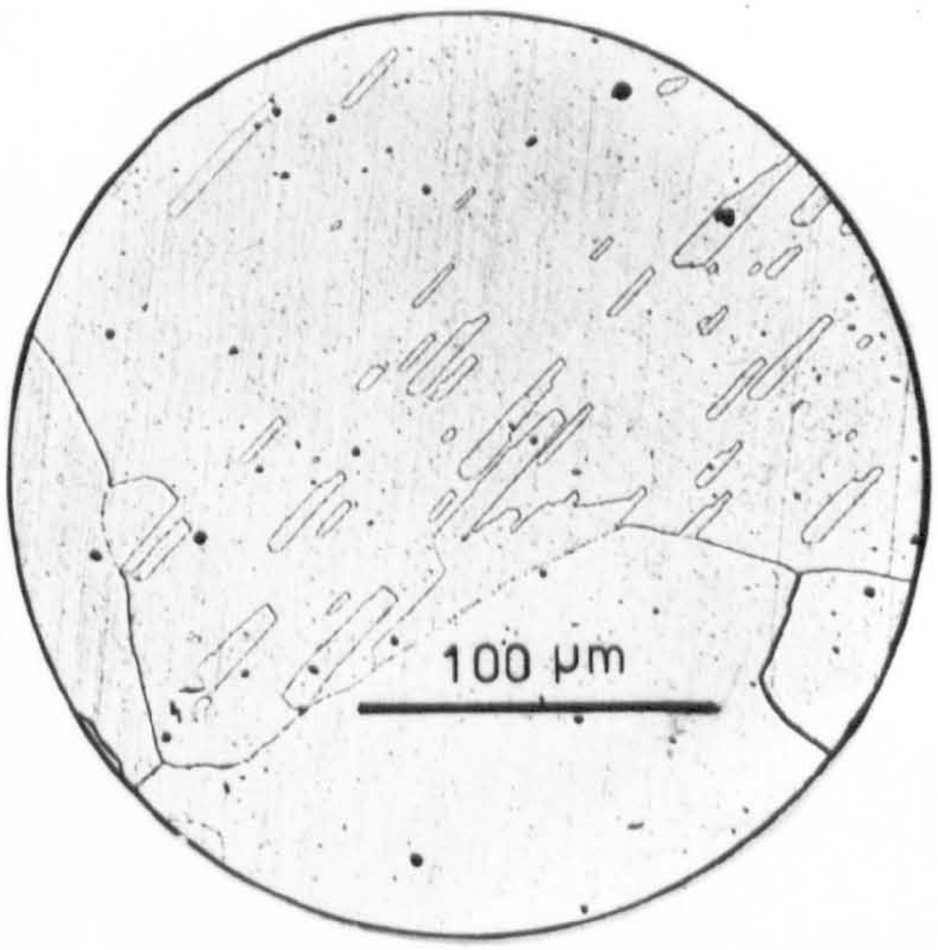

0.14 Nb 0.0 Mn

CR = 0.03 K.s^{-1}

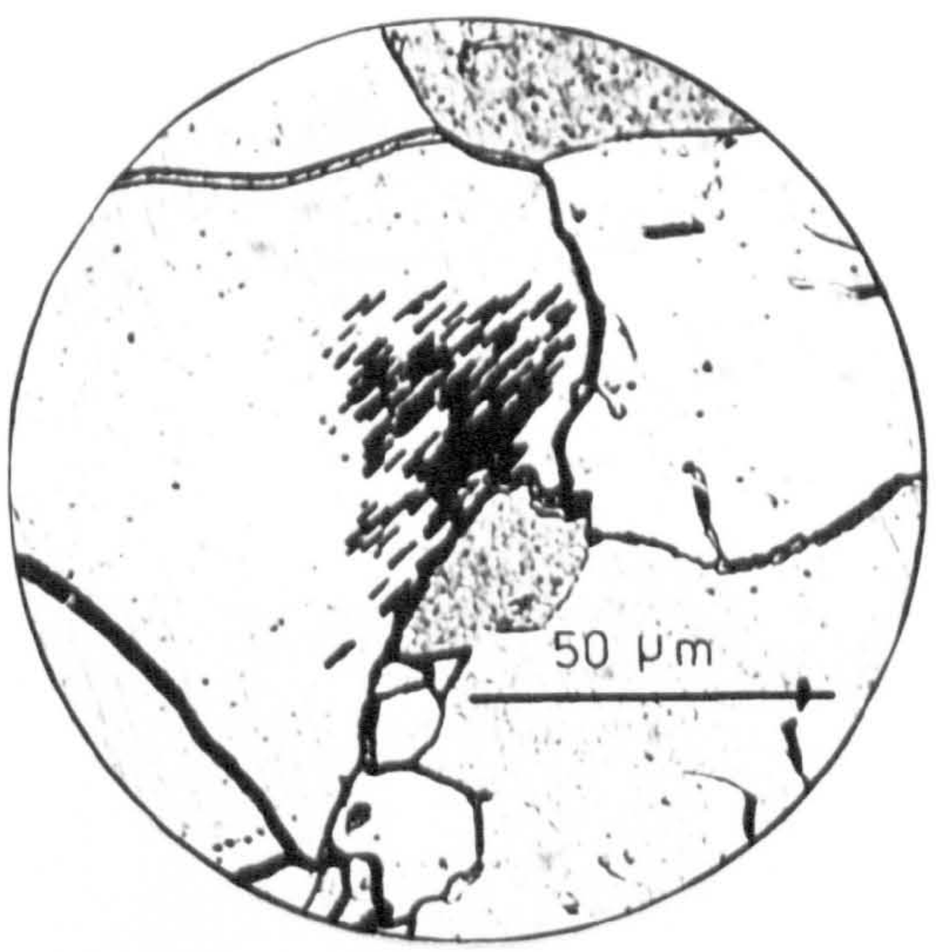

0.06 Nb 0.7 Mn

CR = 0.35 K.s^{-1}

Fig.5.16 Effect of Mn on twinning in low carbon steels.

(011)

0.5μm B.F.

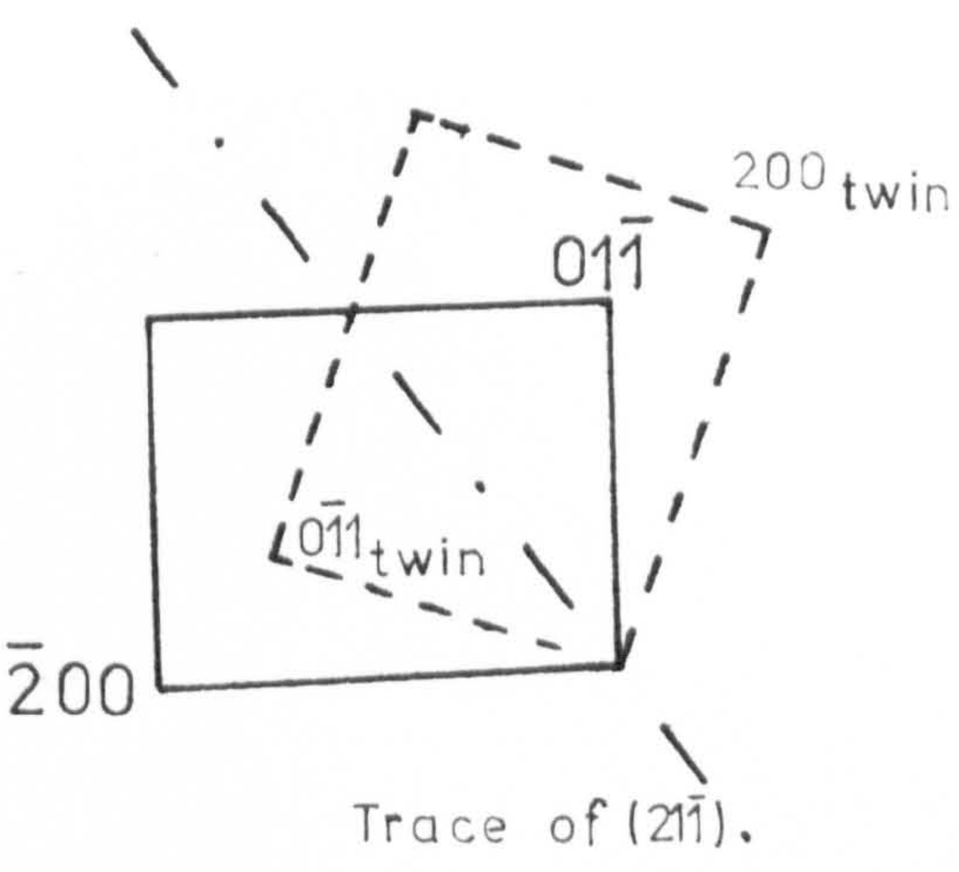

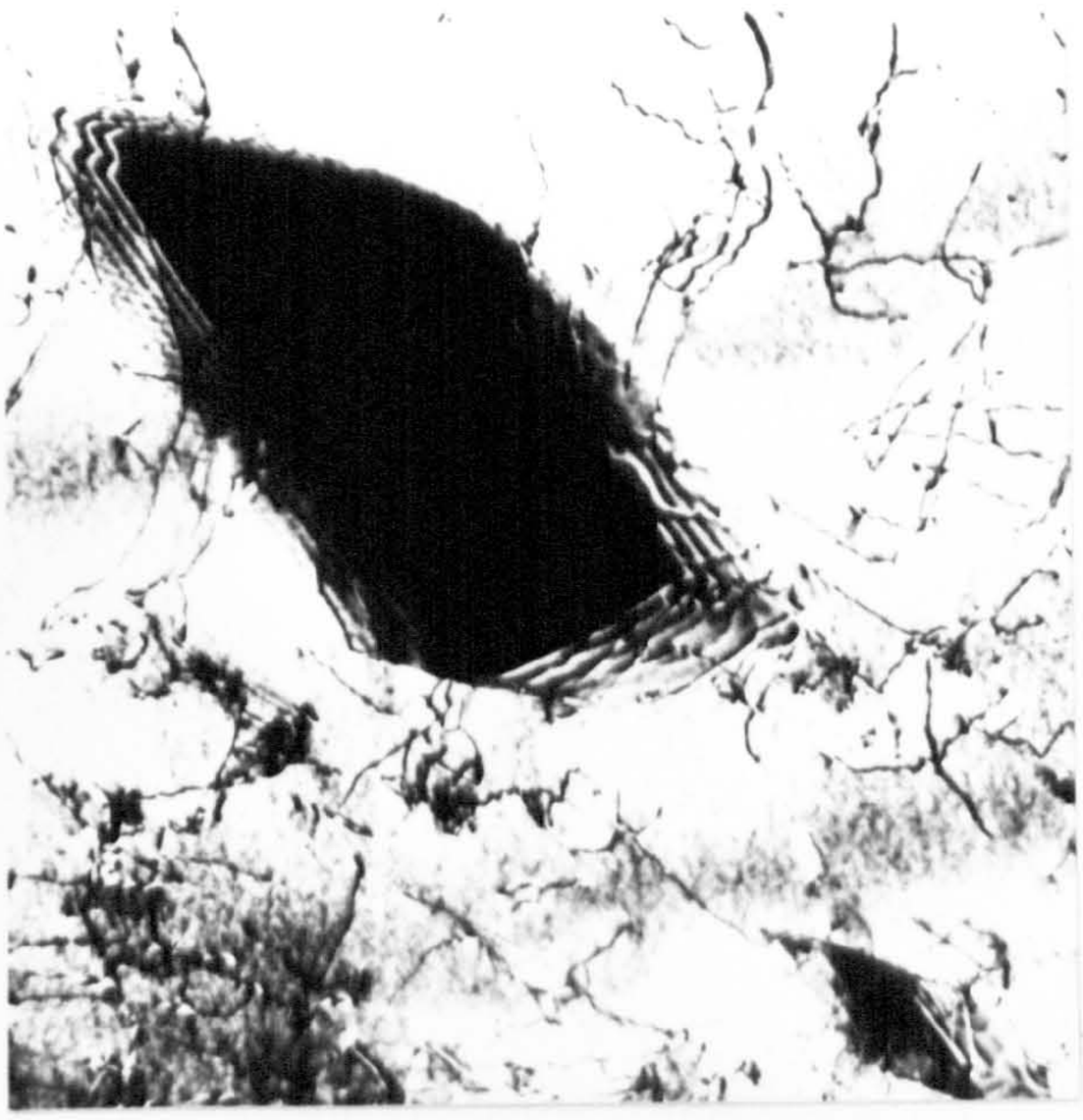

0.5μm D.F. $\bar{g}=[200]_{Fe}$

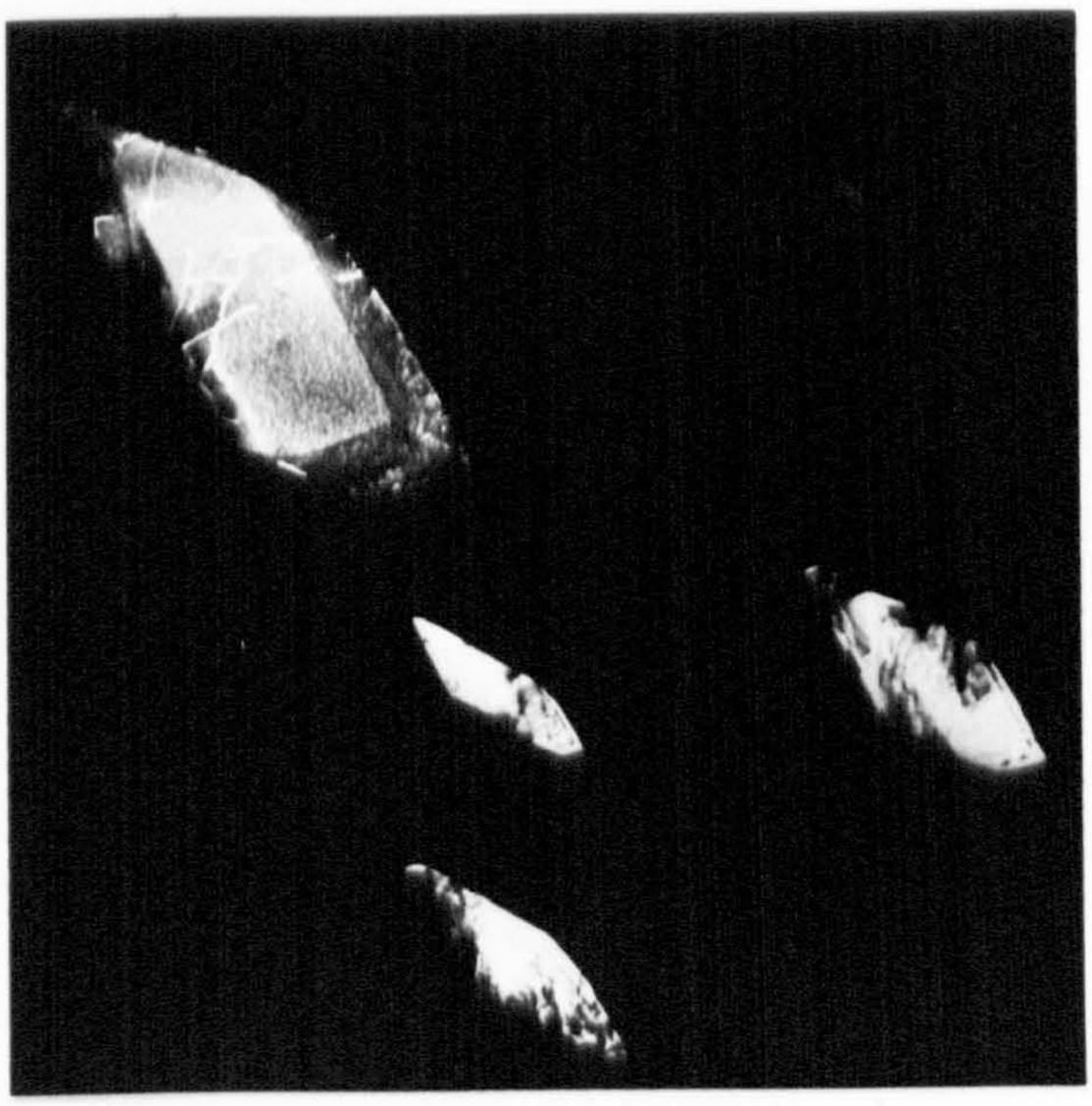

1.0 μm D.F. $\bar{g}=[0\bar{1}1]_{twin}$

Fig. 5.17 Twinning in Fe - 0.04 C - 0.06 Nb - 0.72 Mn at peak hardening.

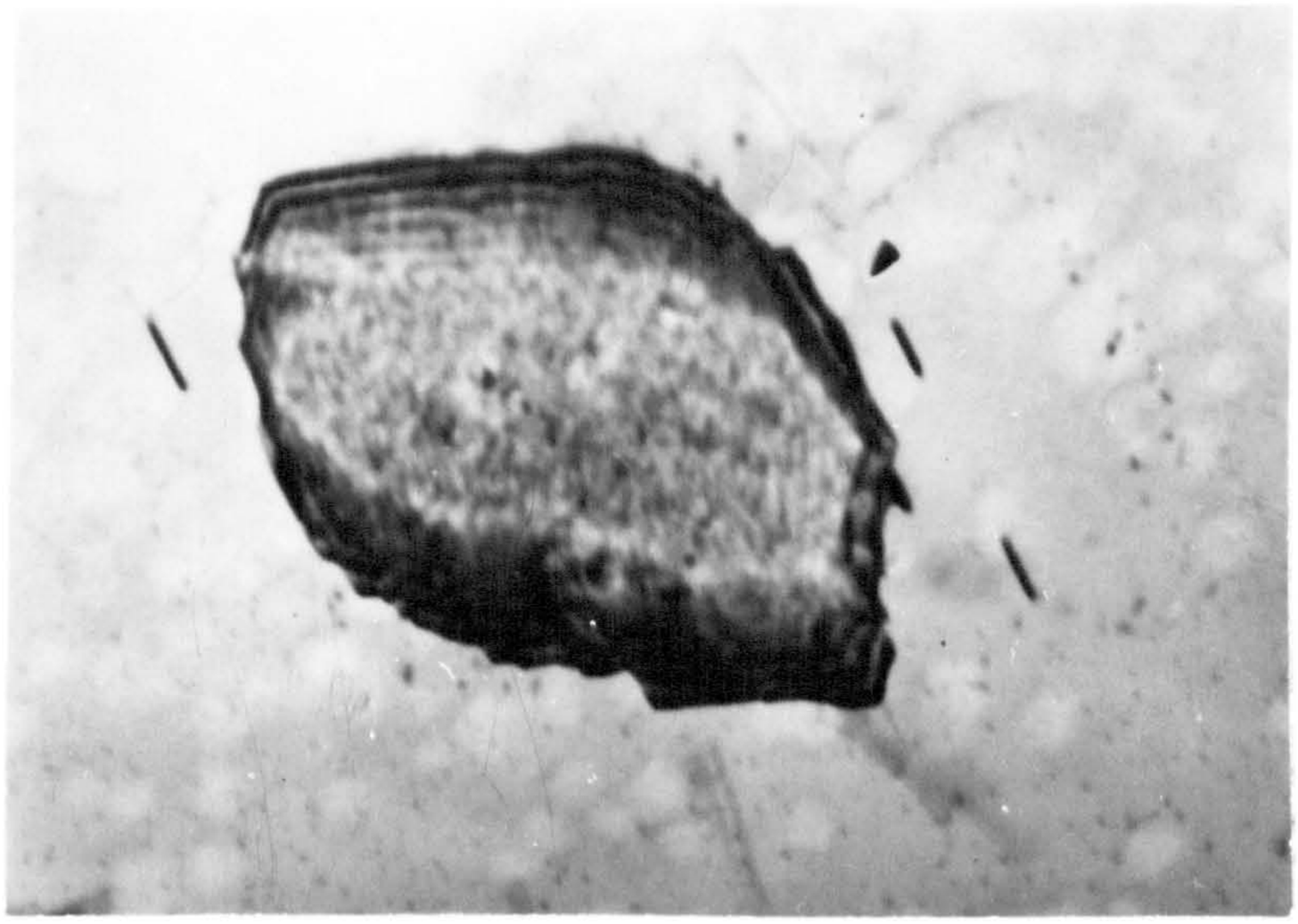

$(\bar{1}\bar{1}\bar{3})$

0.2 μm

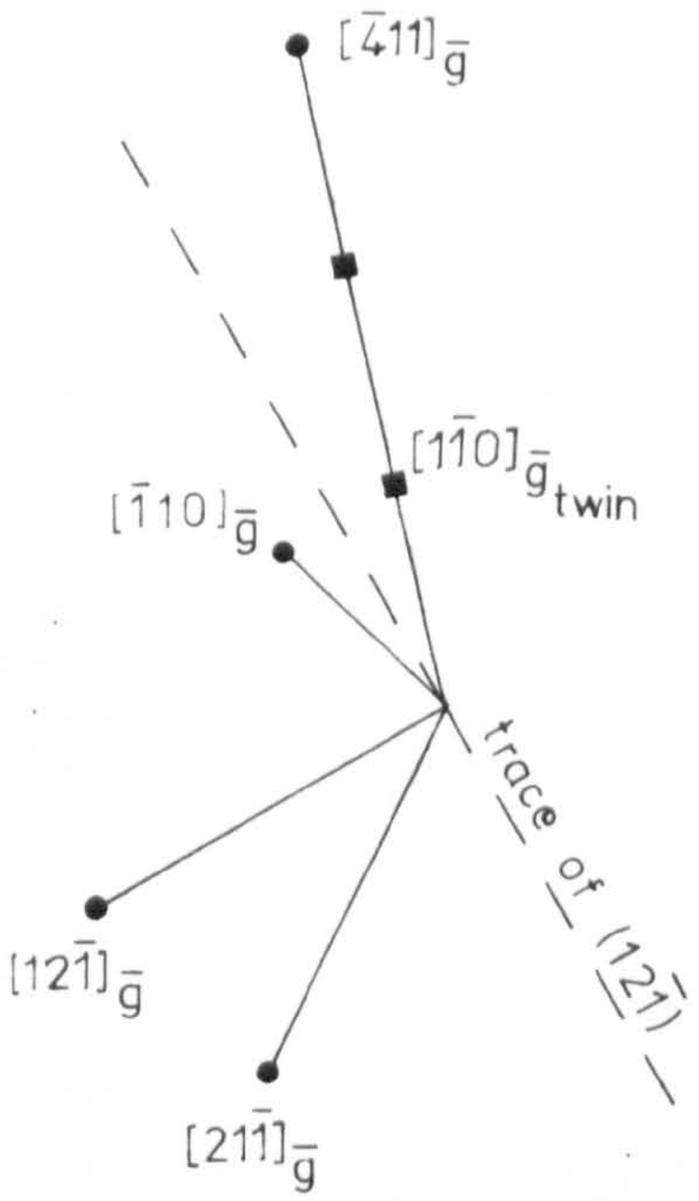

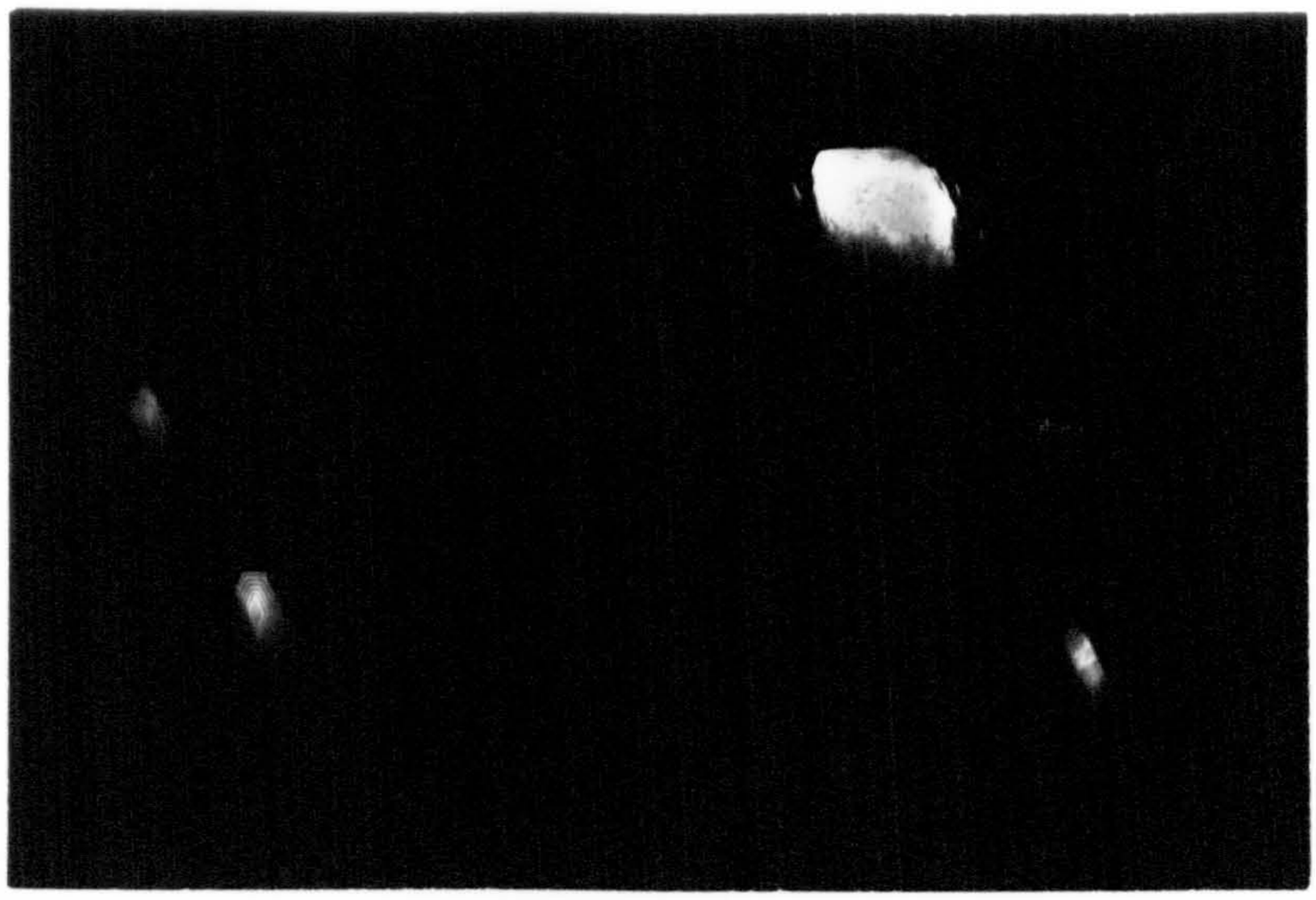

$\bar{g}_{twin} = [1\bar{1}0]$

1 μm

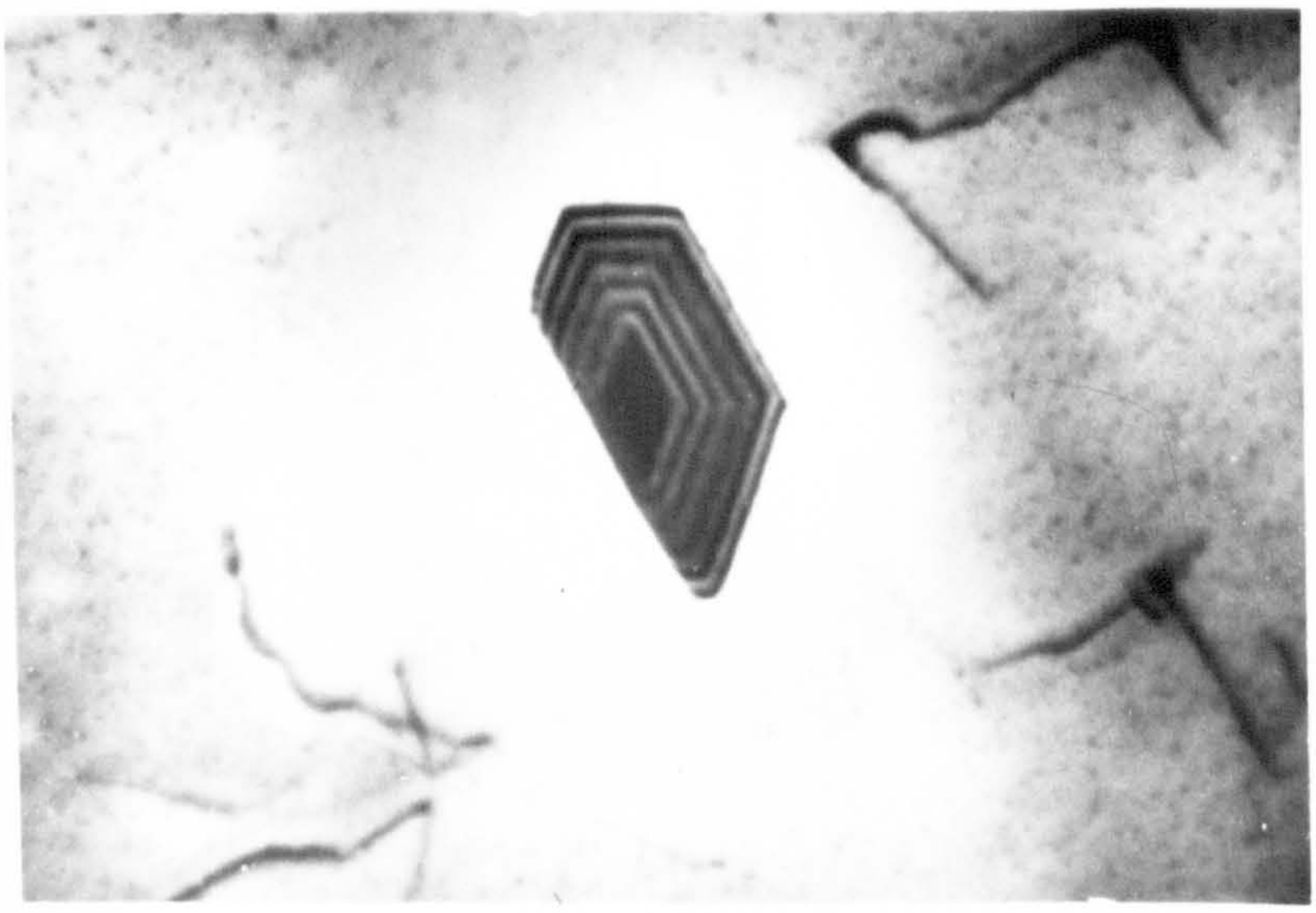

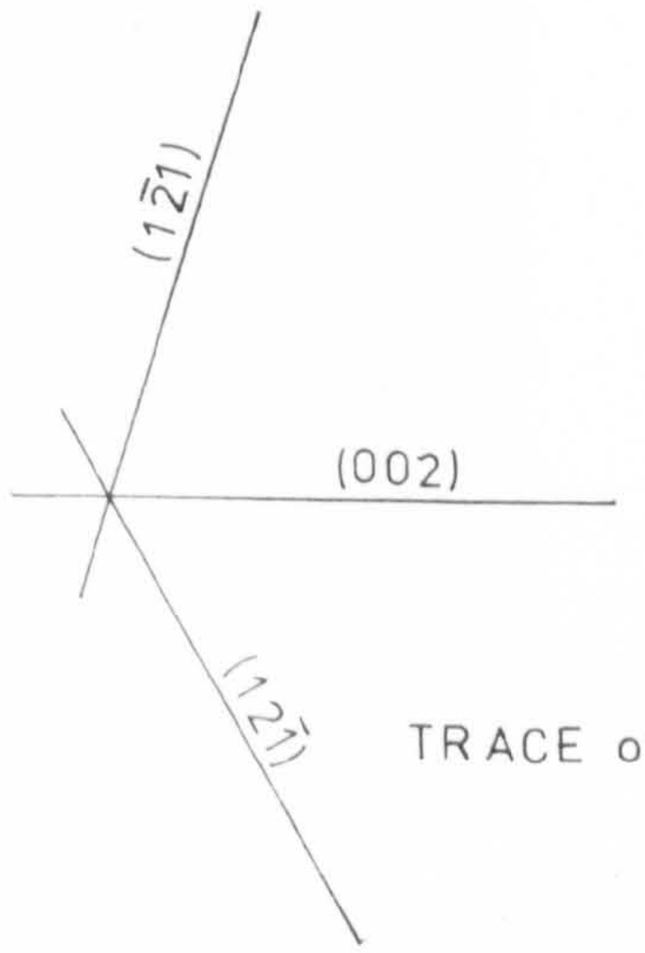

0.2 μm

Fig. 5.18 Twinning in Fe-0.04C-0.06Nb-0.72Mn CR=0.5K.s^{-1}

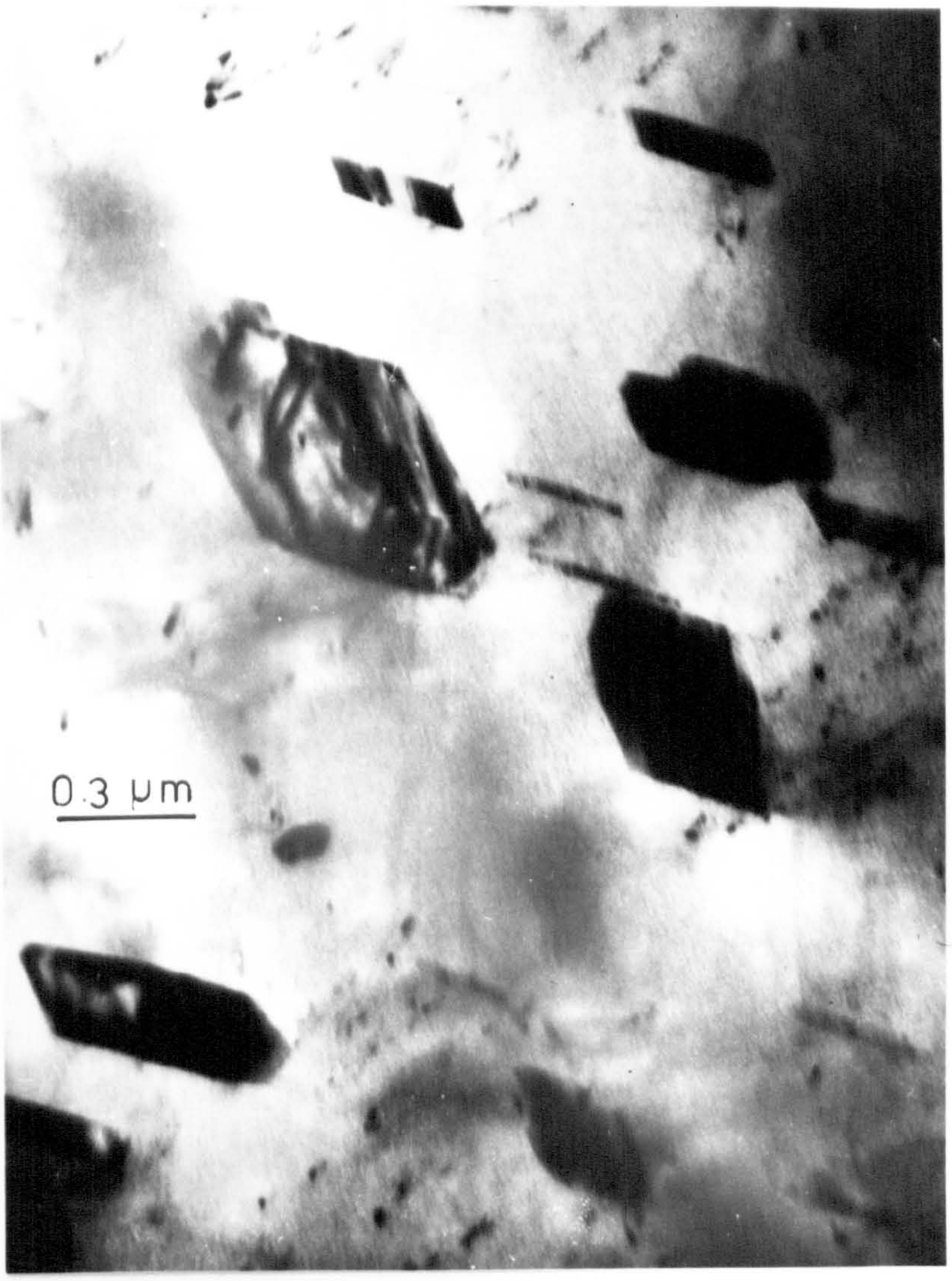

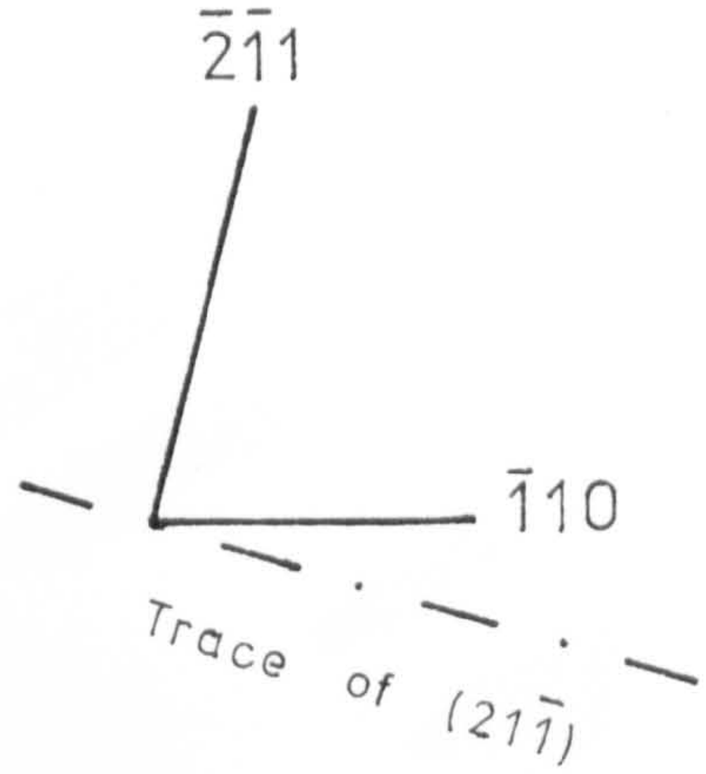

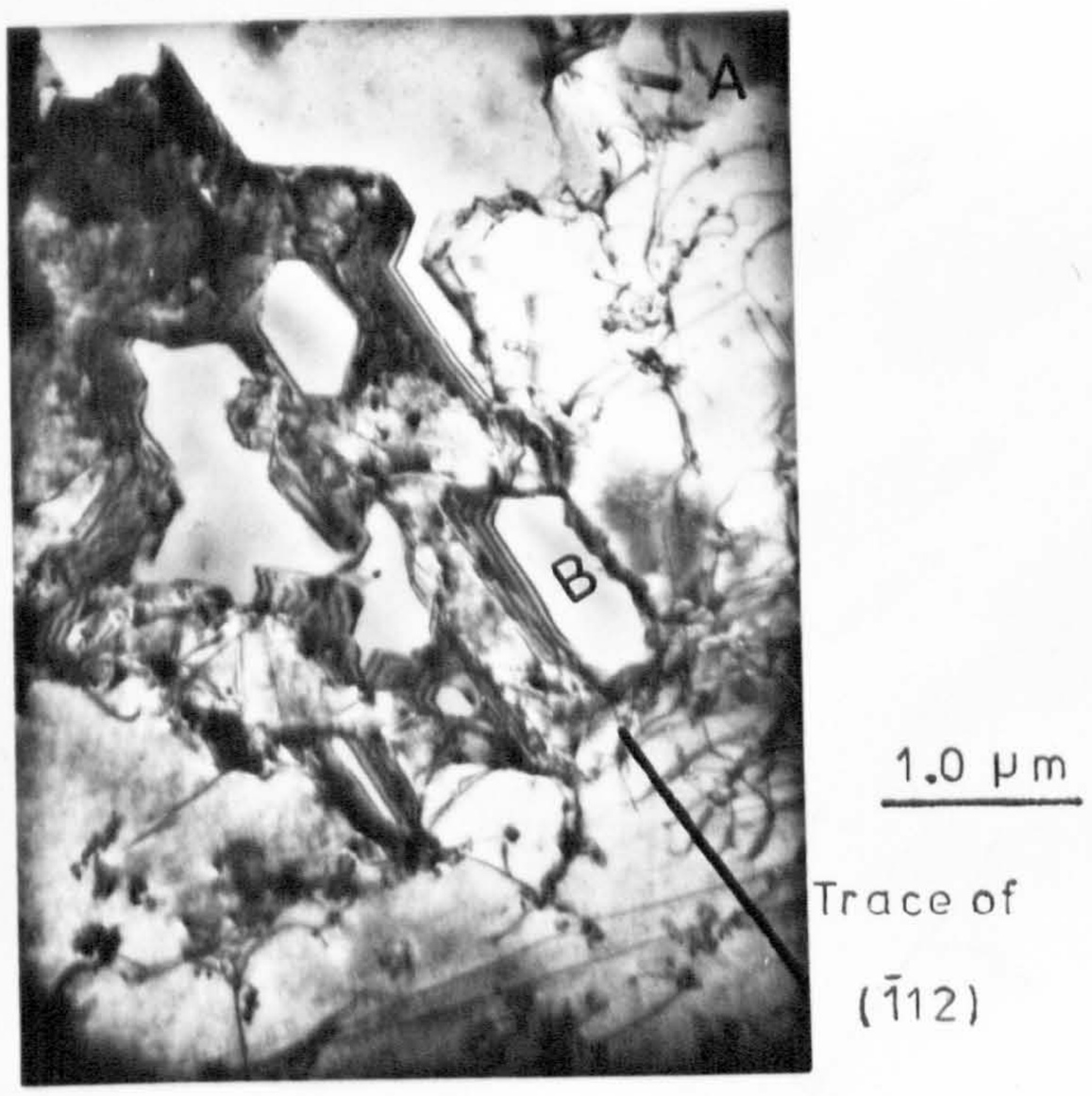

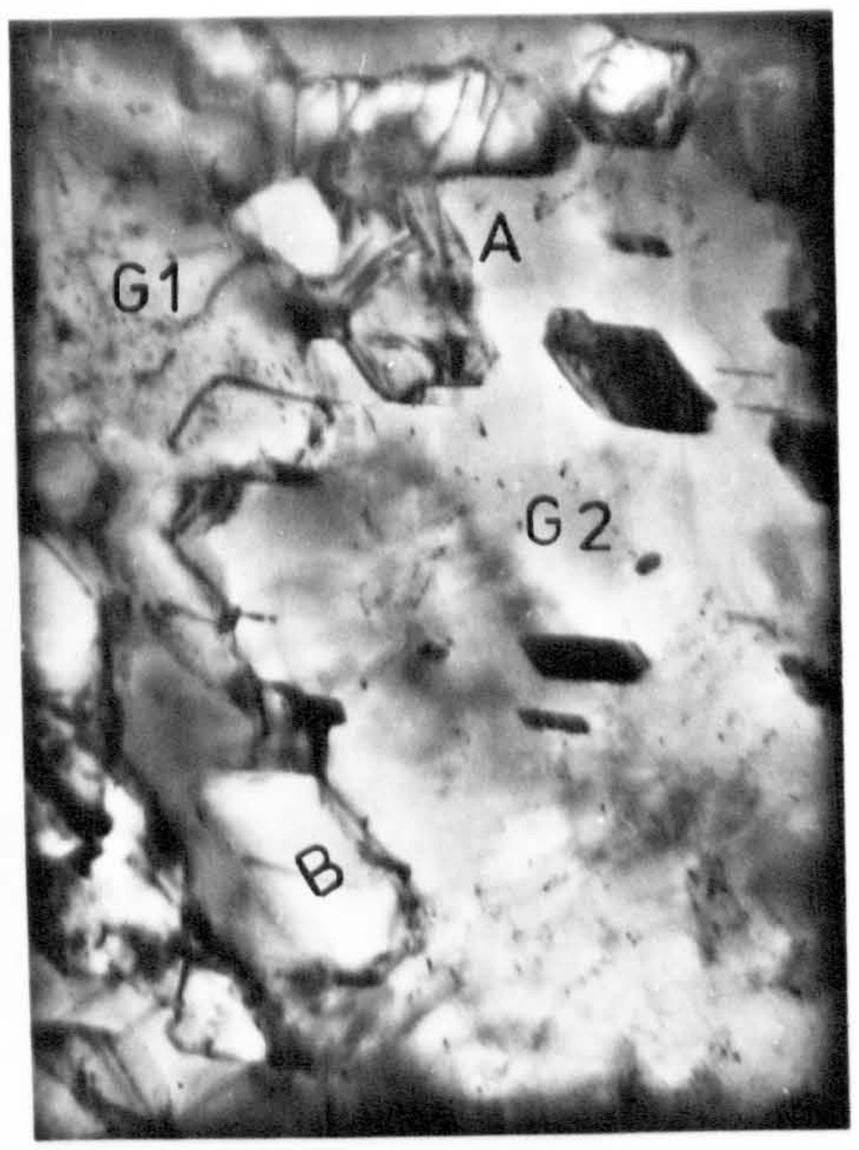

Fig. 5.19 HVEM of twinning in Fe-0.04C-0.06Nb-0.72Mn

CR= 0.06 $K.s^{-1}$

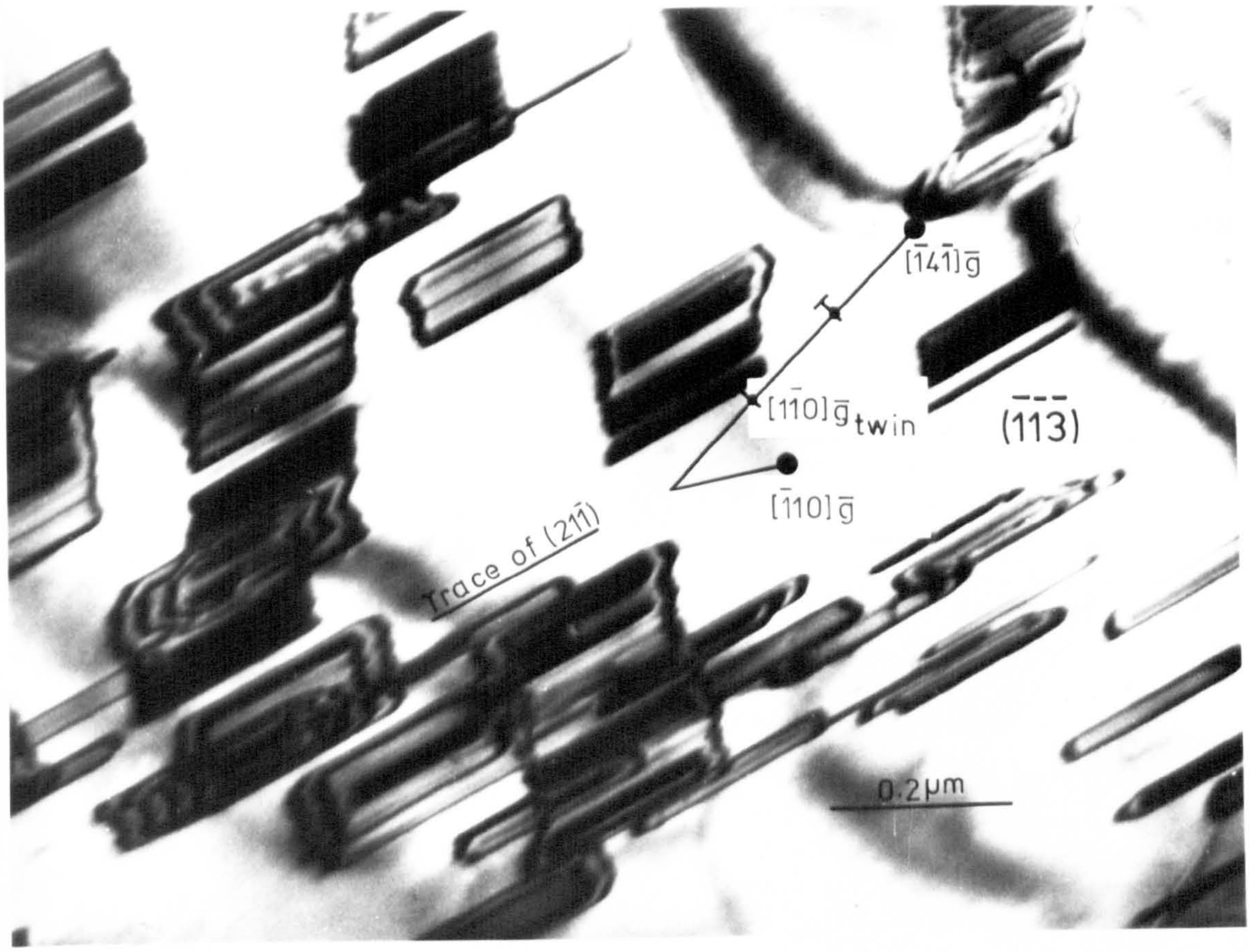

CR= PEAK HARDENING

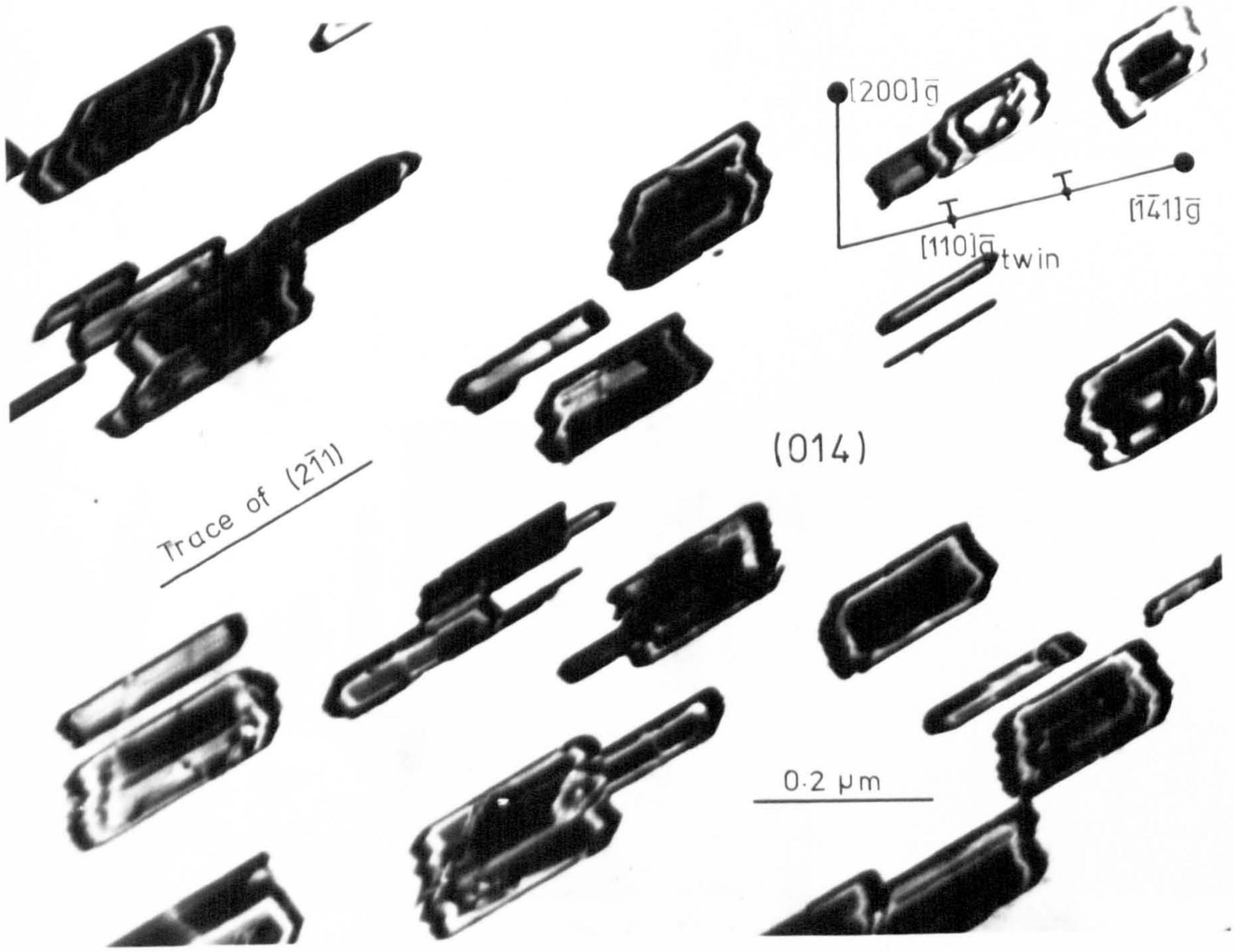

CR=0.06 K.s^{-1}

Fig. 5.20 Twinning in 0.1C-0.13V-1.5Mn steel.

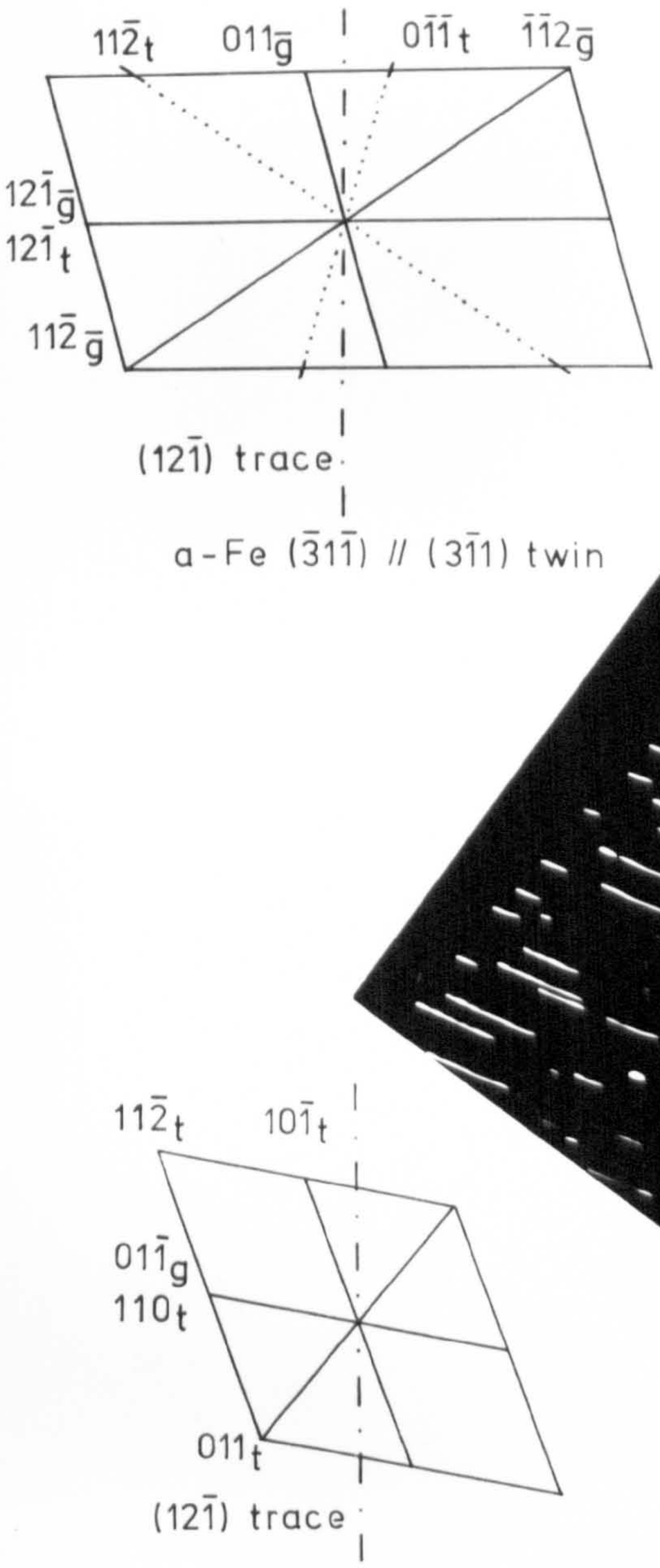

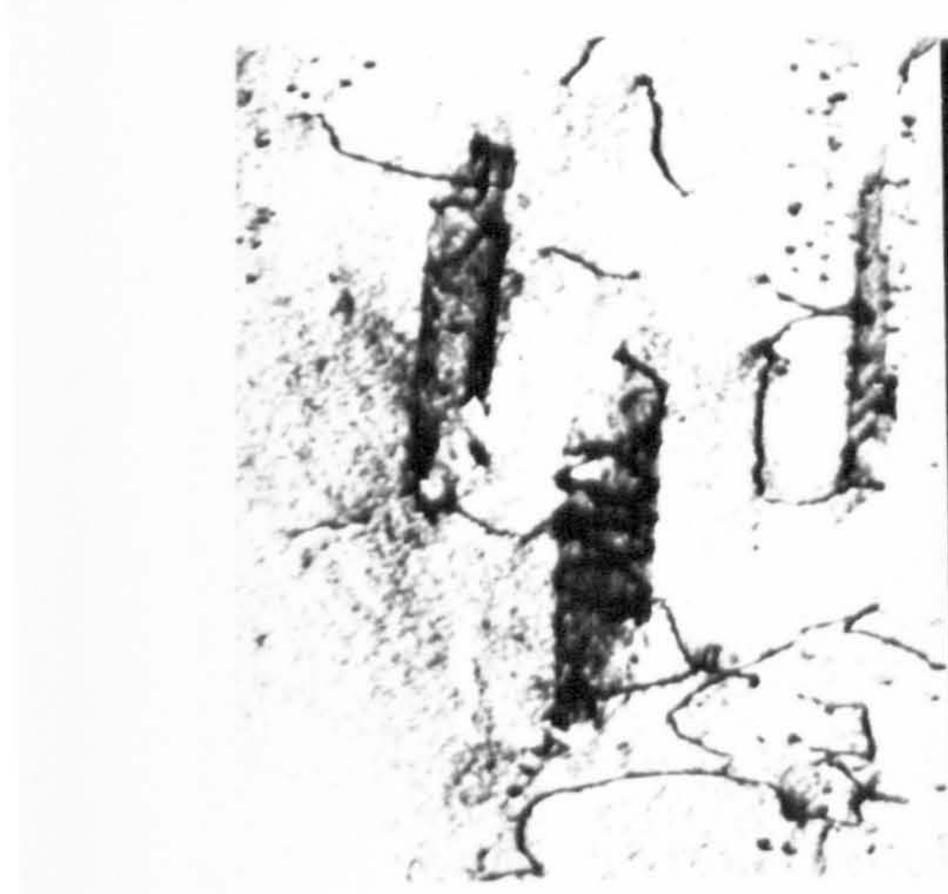
$(\bar{5}\bar{1}\bar{1})$ a-Fe BF

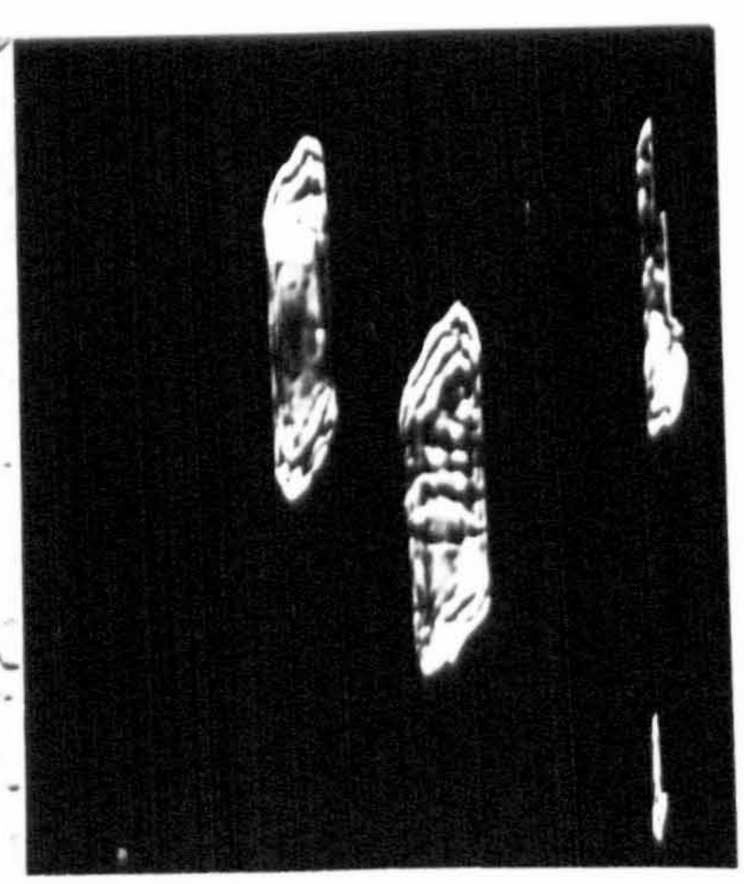
$(1\bar{1}1)$ twin $\bar{g} = [10\bar{1}]$

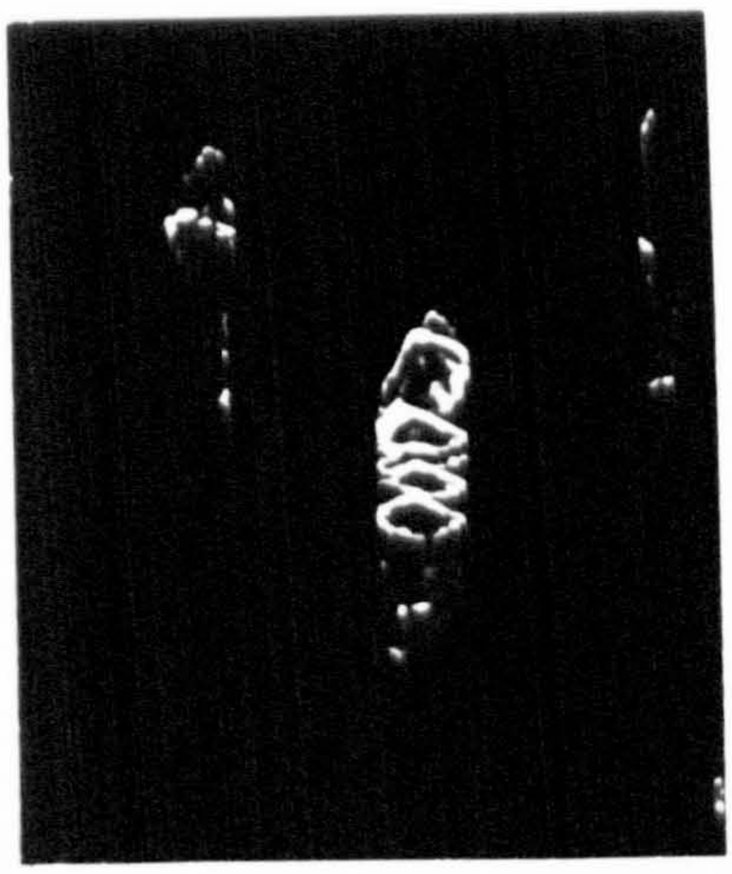
$(3\bar{1}1)$ twin $\bar{g} = [11\bar{2}]$

Fig. 5.21: Twinning in neighbouring aligned precipitates.

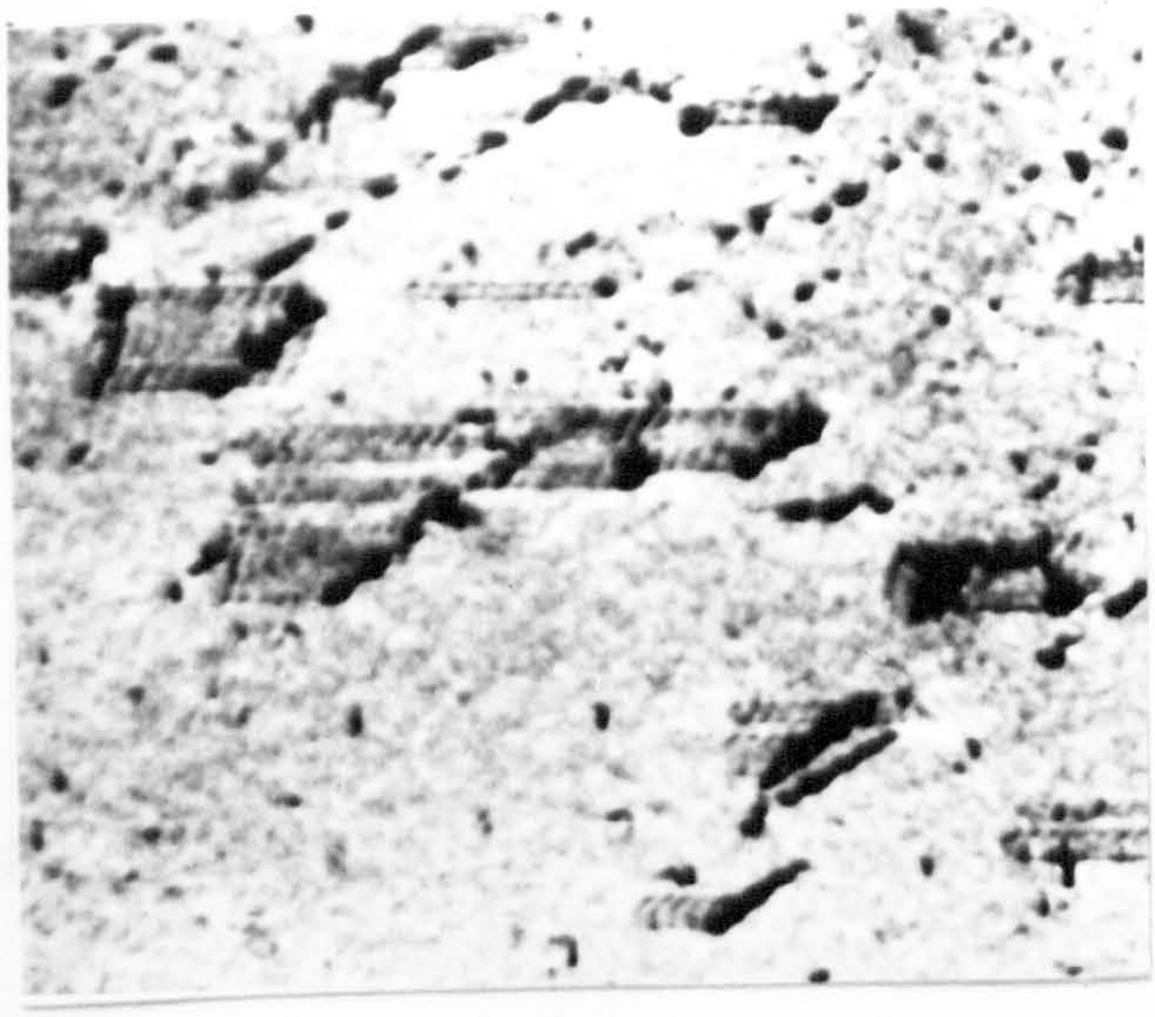

BRIGHT-FIELD

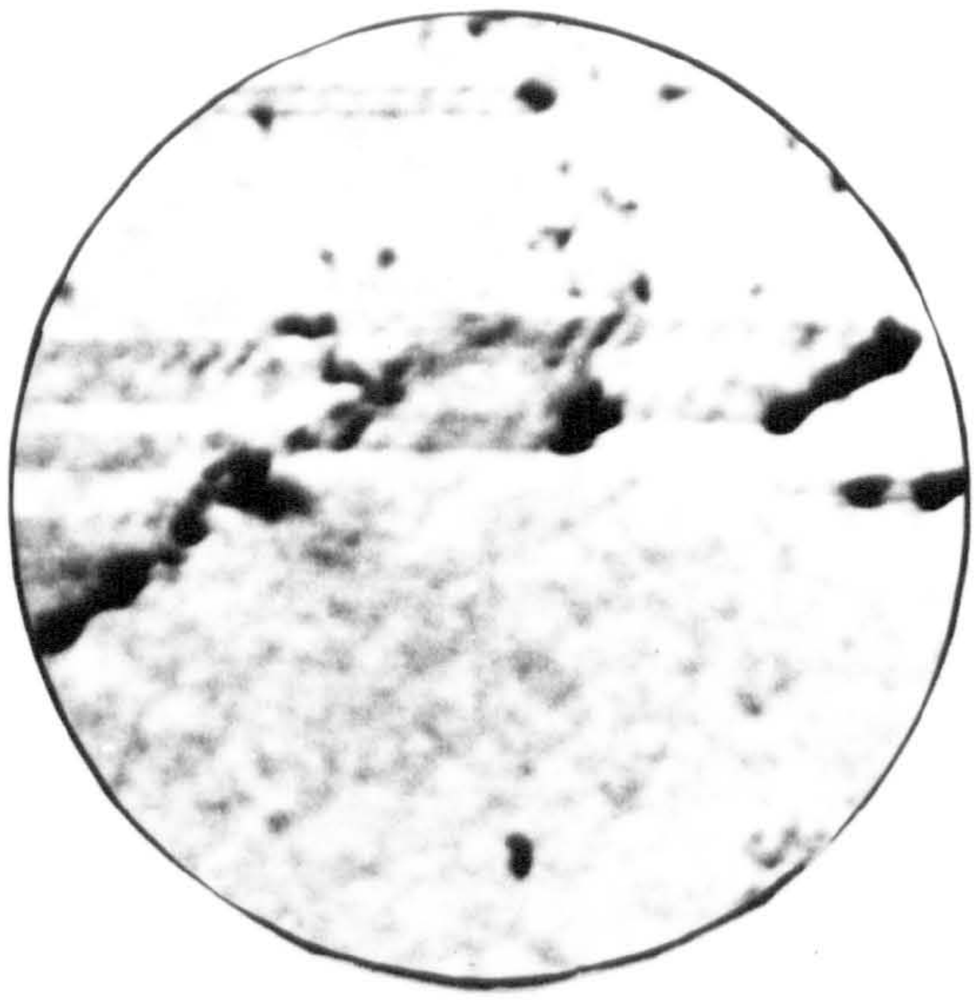

1.5 X

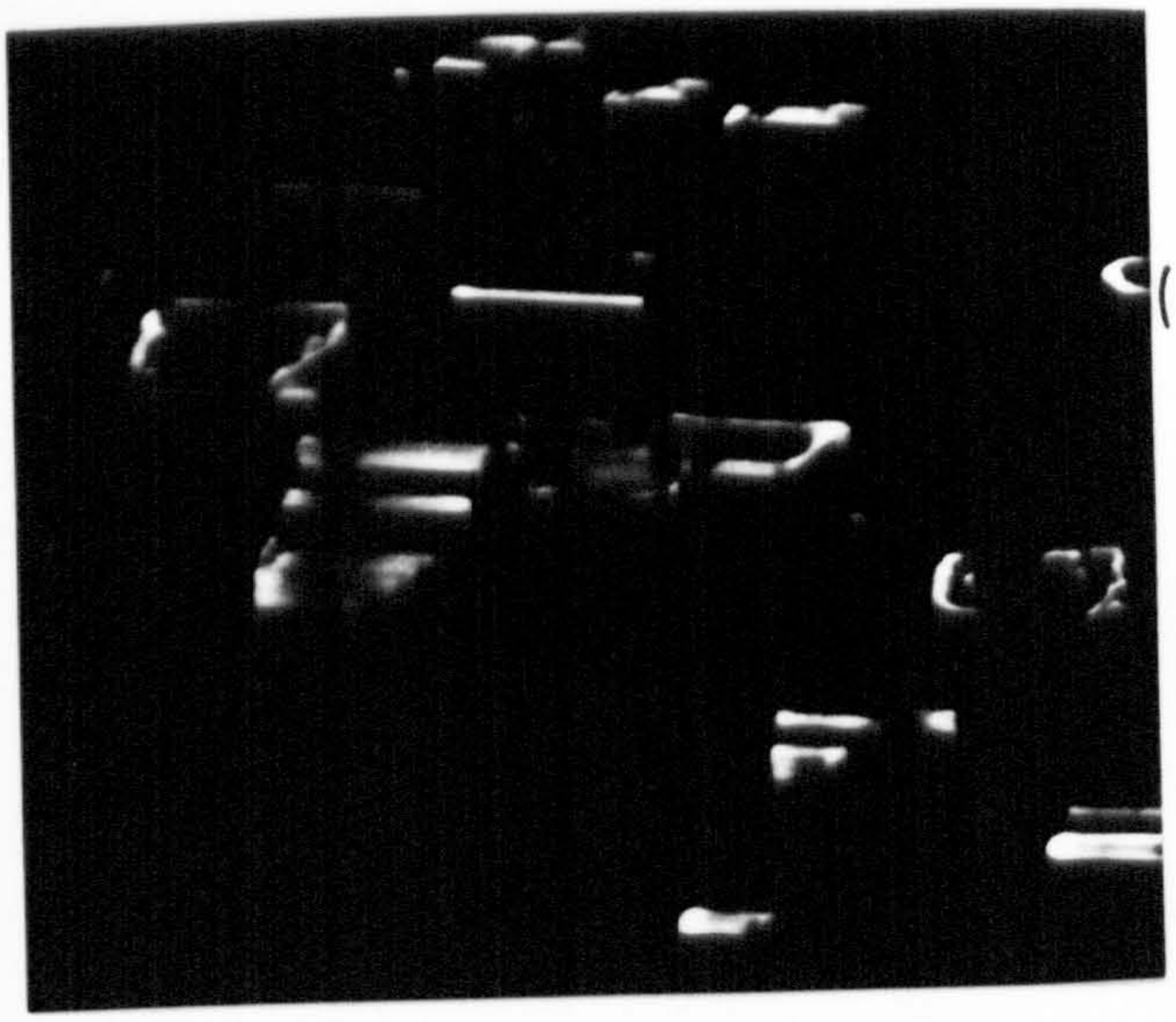

DARK-FIELD $01\bar{1}\ \bar{g}_{twin}$

$(011)_{Fe} // (0\bar{1}\bar{1})_{twin} // (001)_{VCN}$

0.2 μm

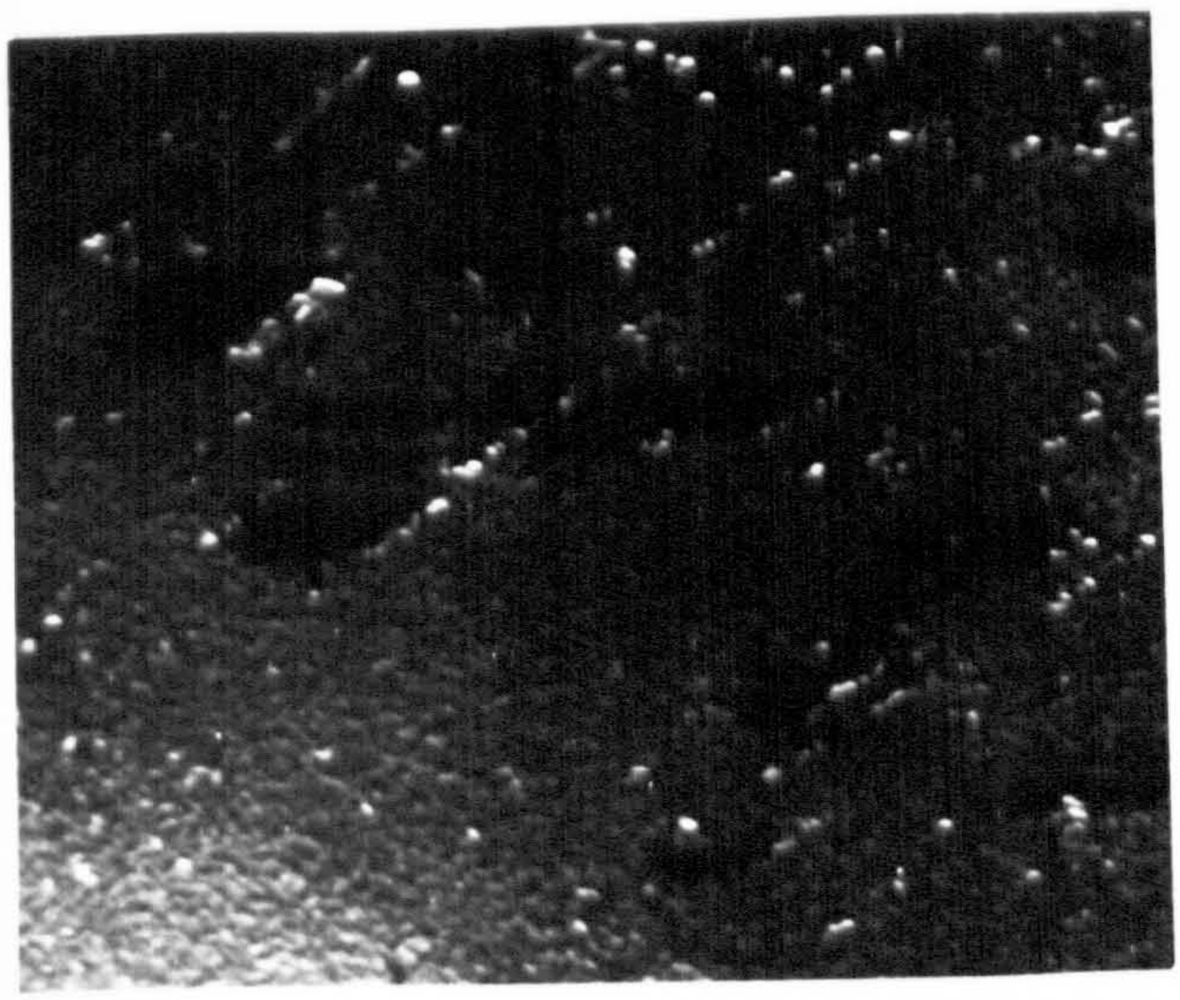

DARK-FIELD $020\bar{g}_{VCN}$

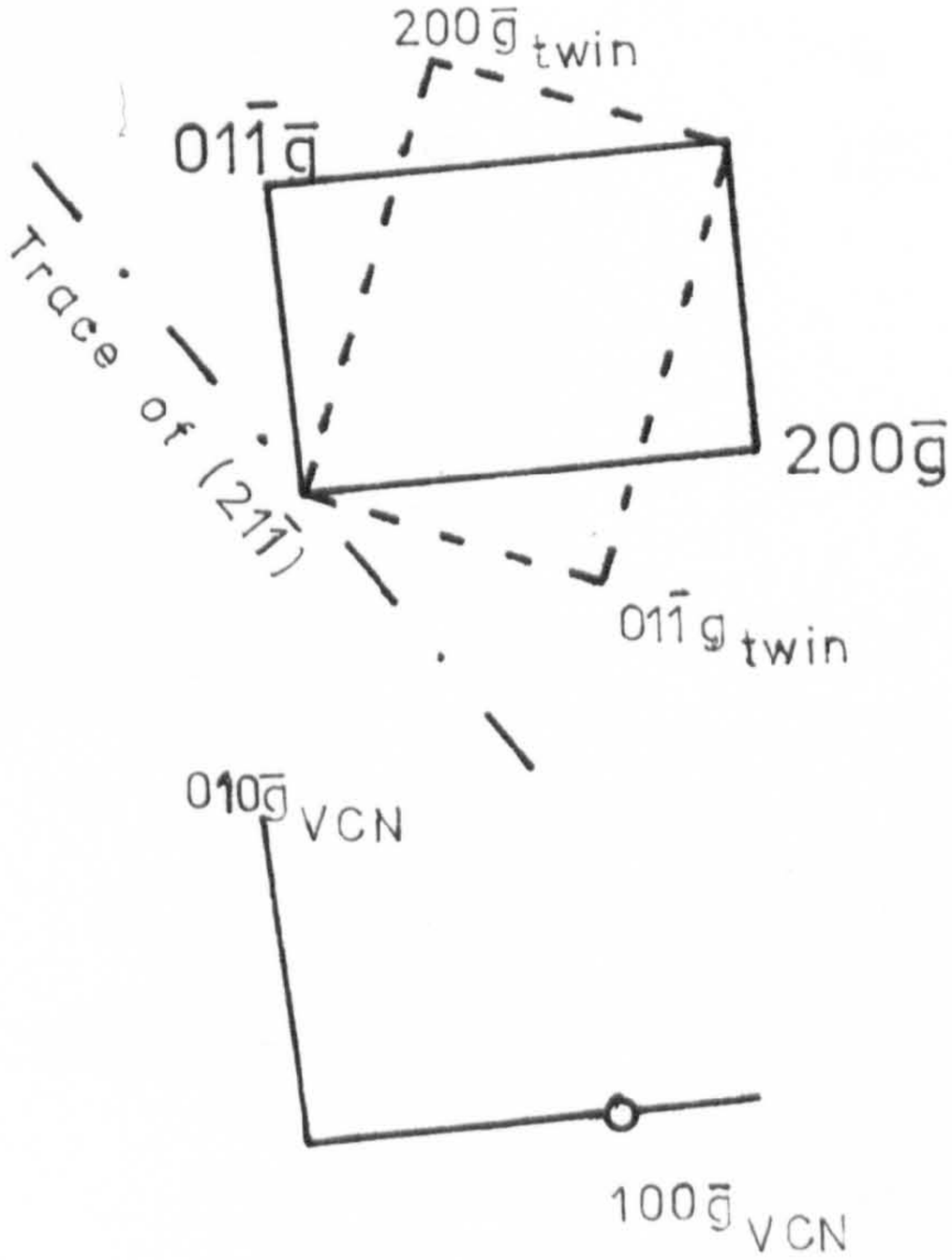

Fig.5.22 Twinning associated with particles and dipoles.

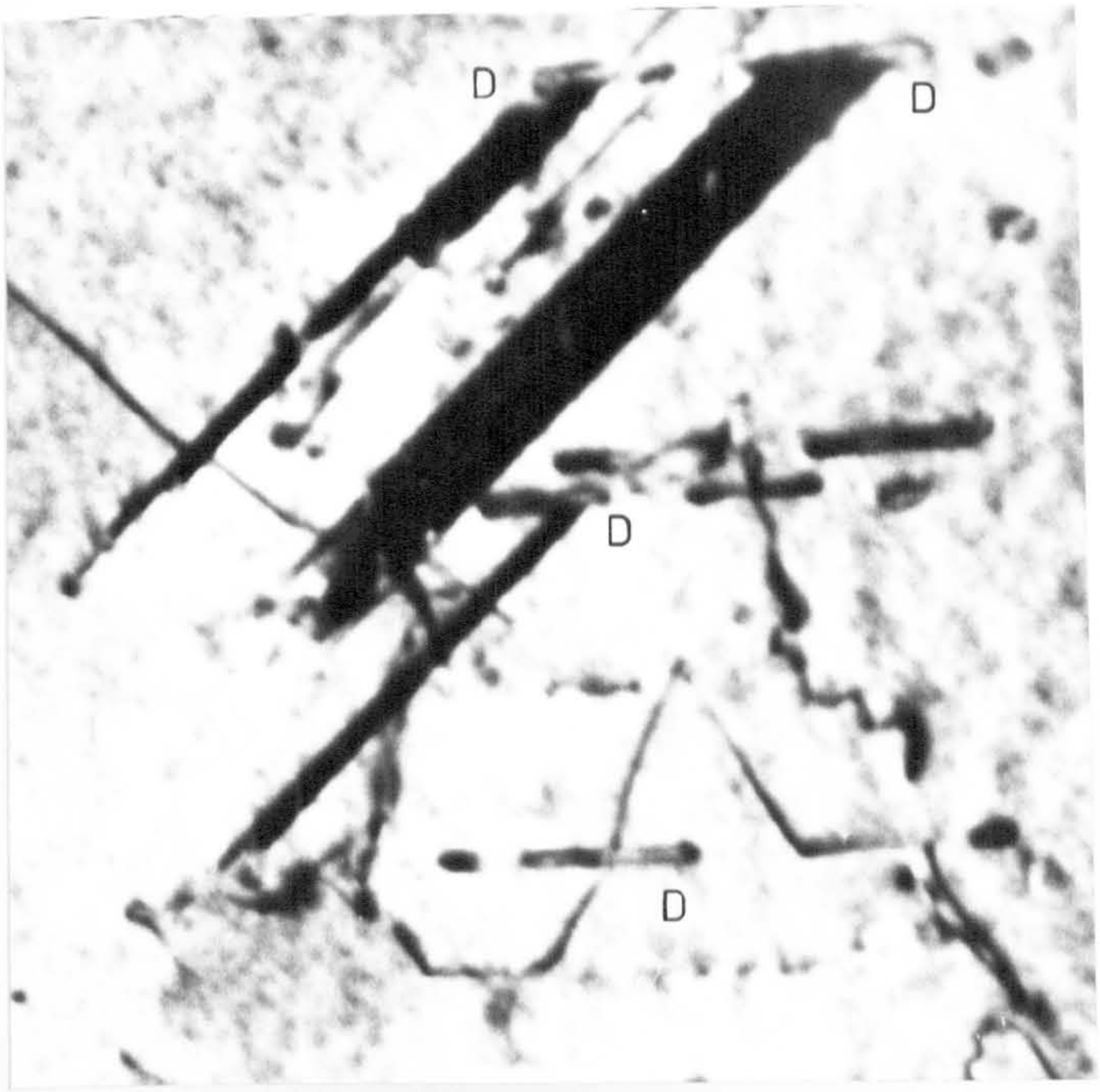

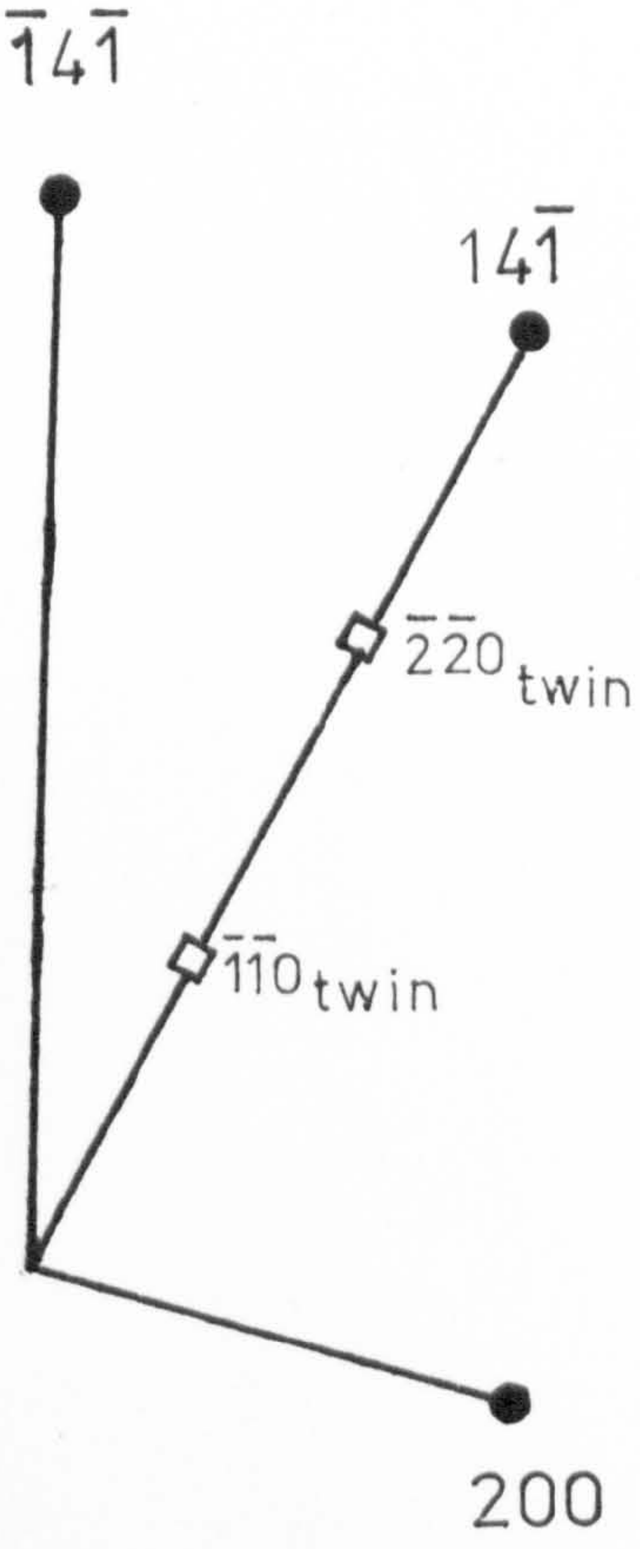

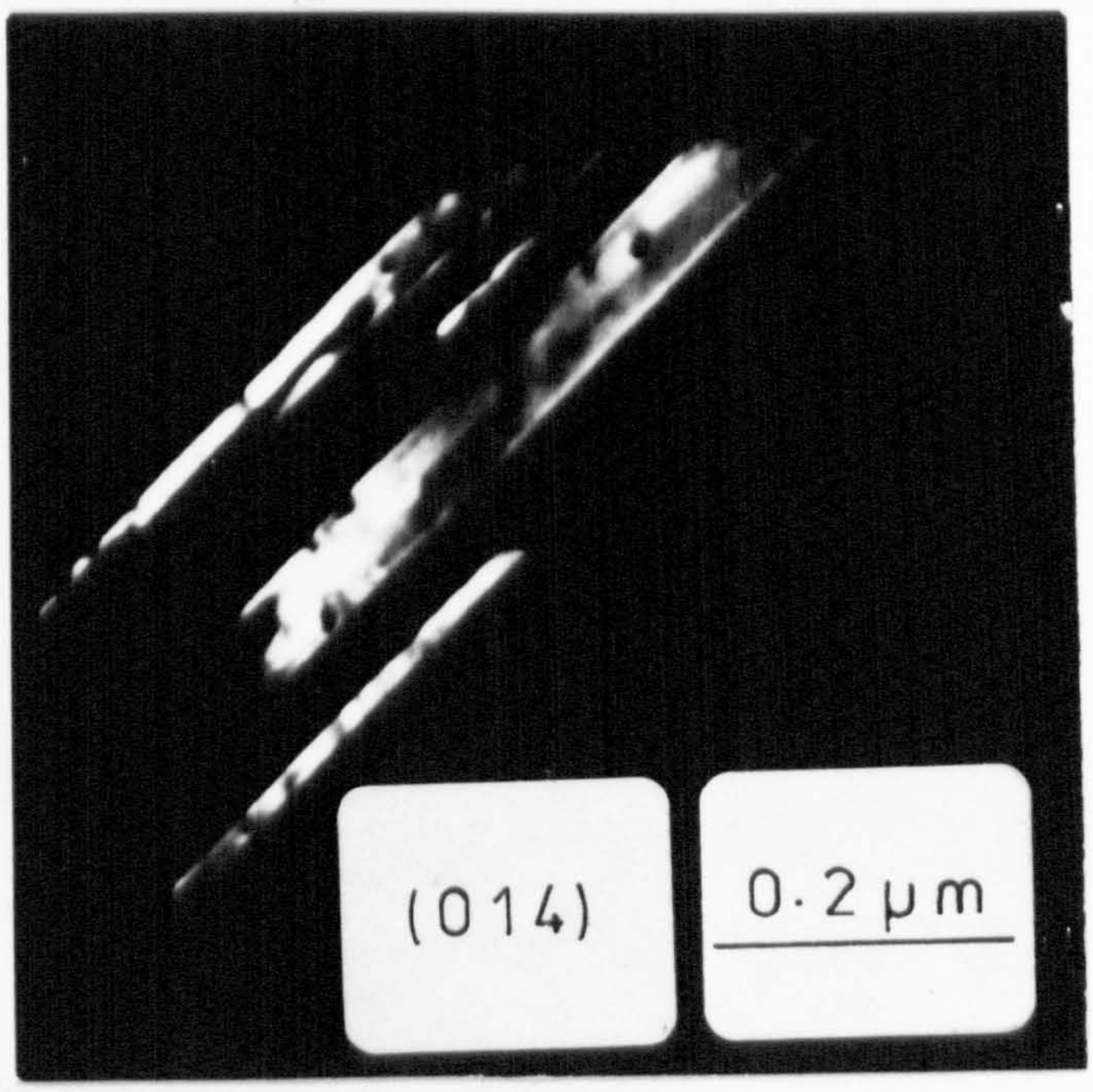

Fig.5.23 Twinning associated with dipoles.

Chapter six: INTERPRETATION AND DISCUSSION OF RESULTS.

The present chapter discusses further the strengthening mechanisms observed in the steels investigated. In chapter four, it was shown that a peak hardening was obtained at a critical cooling rate. Also, an attempt was made to quantify the strength obtained in terms of the various strengthening mechanisms. These aspects were reviewed in detail in section 1.3. To complement these findings, the microstructures obtained in these materials were illustrated in chapter five.

A means of conversion from hardness to yield strength is proposed in the first section, whereas the effect of alloying additions with respect to the hardness increase and the cooling rate at which the peak was obtained, is examined in the second section. An attempt to correlate the different strengthening mechanisms is made in the third section, in order to study the causality for the peak hardening. Finally, a brief comment is included about the contribution to strength from twinning.

6.1 Hardness and strength correlation in low alloy vanadium and niobium steels.

A relationship between the yield strength and the steel hardness was sought for comparison and analysis purposes. The reader is referred to section 2.6 and 4.3 for details about the experimental procedures and results of the mechanical testing.

In the present study, a plot of the yield strength against the hardness of steels is shown in Fig.6.1.1 (see also Table 4.3.1 and text). These steels were all continuously cooled and contained low alloy additions. It can be seen that a linear relationship exists between the tensile stress (UTS) and the Diamond pyramid (HV). A similar relationship was also obeyed between the yield strength (σ_y) and the hardness. The relationships are represented in the following equations:

$$UTS = 3.3\ HV \qquad 6.1.1$$

$$\sigma_y = 2.1\ HV \qquad 6.1.2$$

The UTS and σ_y are in MPa with the HV expressed in $Kg.mm^{-2}$.

More than twenty years ago, a proportional relationship was proposed between the Diamond pyramid hardness (HV) and the tensile stress (UTS) of metals [152]:

$$UTS = \frac{HV}{C}\ (1-n)\ \frac{(12.5n)^n}{1-n} \qquad 6.1.3$$

In this equation, the HV and UTS adopt the units of $Kg.mm^{-2}$; n is the strain hardening coefficient and

n = m - 2, where m is the Meyer's hardness coefficient. The constant of proportionality "C" was empirical and equal to 2.9 for steel. This constant was approximately equivalent to the stress at a strain of eight percent [152]. The representative deformation itself corresponded to eight or ten percent.

More recently, Cahoon produced an alternative equation [153],

$$UTS = \frac{HV}{2.9}\left(\frac{n}{0.217}\right)^{n} \qquad 6.1.4$$

When an average value of the Meyer's hardness coefficient for steel is taken into consideration, i.e. $m \simeq 2.2$ (from Tabor [152]), the equations 6.1.3 and 6.1.4 become:

$$UTS \simeq \frac{HV}{2.9} \qquad 6.1.5$$

A linear relationship between the yield strength (σ_y, 0.2% offset) and the Diamond pyramid hardness of metals was also proposed in the literature [155]. The relationship varied for different materials and should be determined by comparison with the material investigated [154]. The Cahoon et al. relationship between the yield strength (σ_y) and the hardness (HV) of a metal was [155],

$$\sigma_y = \frac{HV}{3.0}(0.1)^{n} \qquad 6.1.6$$

The average Meyer's hardness coefficient for steel [152] can again be substituted in equation 6.1.6, and a direct relationship obtained between the yield strength (σ_y)

and the hardness (HV) of steels:

$$\sigma_y = \frac{H}{4.75} \qquad 6.1.7$$

The dimensionless ratios HV/UTS and HV/σ_y of equations 6.1.2 and 6.1.1 can be compared with the ratios of equations 6.1.5 (3.0 against 2.9) and 6.1.7 (4.7 against 4.75).

It can thus be inferred that a correlation exists between the tensile stress (UTS), the yield strength (σ_y) and the Diamond pyramid hardness (HV) in the materials investigated. These relationships were shown to agree reasonably well with others proposed in the literature. Thus, the Diamond pyramid hardness provided a simple technique to obtain σ_y in the present study. The technique was particularly suitable for testing end quench specimens, whereas tensile testing would have been very complicated, if not impossible to use (tensile specimens would require to be very thin).

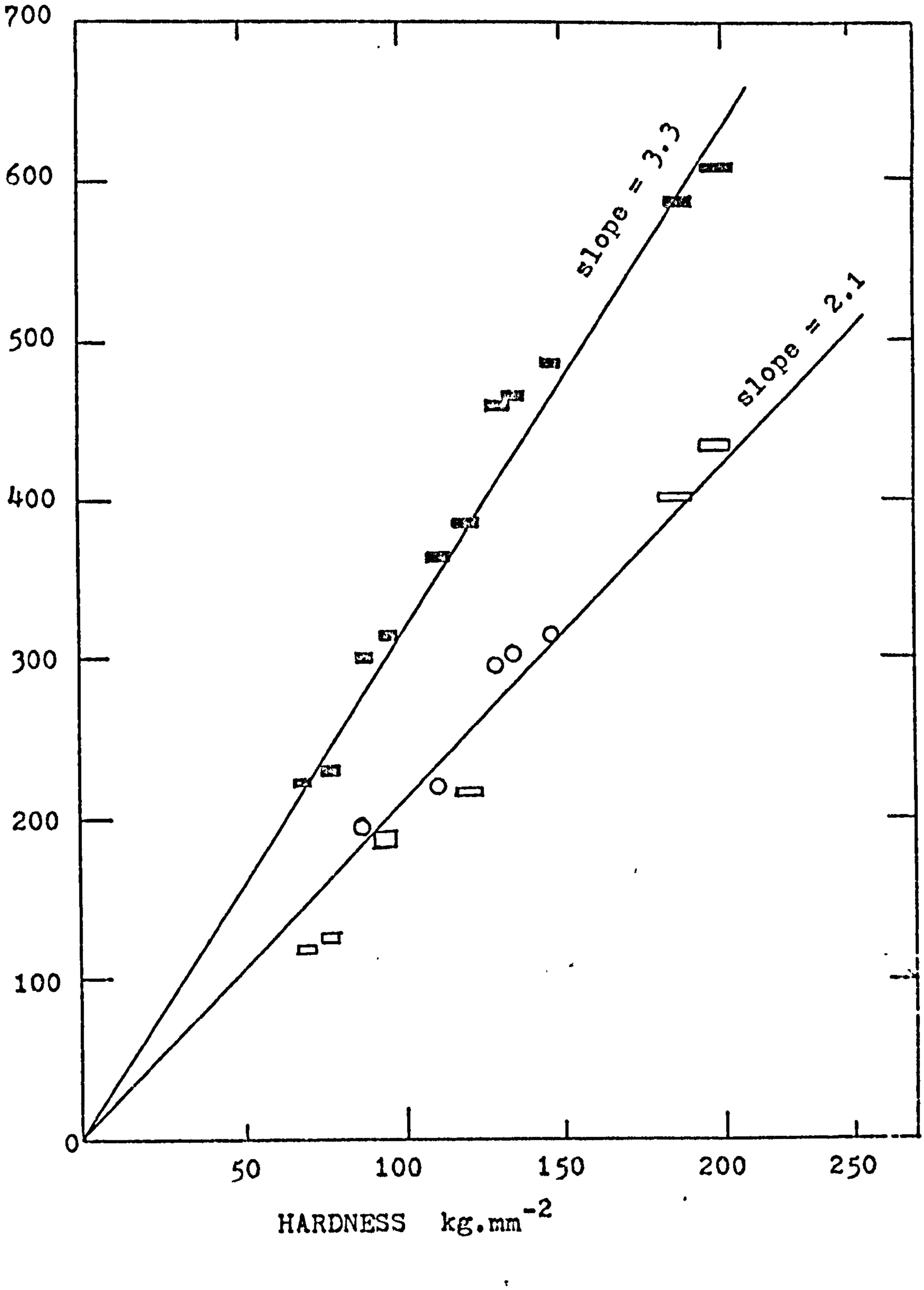

Fig.6.1.1 Strength against Diamond pyramid hardness.

6.2 Peak hardening in continuously cooled vanadium and niobium steels.

This section compares the peak hardening obtained at critical cooling rates in continuously cooled vanadium and niobium steels. The effect of alloying elements is also discussed.

The cooling curves of Fe - 0.1C - 0.46V steel (B) and Fe - 0.1C - 0.13V - 1,5Mn steel (V) are reproduced together with a Fe - 0.2C - 0.53V steel (T) of Tanino et al. [23] in Fig.6.2.1. It can be seen that the total height of the peak hardness and the total increase in hardness are equivalent for both steels B and T. The percentage of increase ($\triangleq$60%) is defined as the ratio of the total peak height on the lowest hardness value obtained at a higher cooling rate than the peak. The cooling curves of the three vanadium and vanadium-manganese steels of the present study are reproduced in Fig.6.2.2. The addition of manganese displaced the peak to a lower cooling rate and decreased the importance of the peak vis-à-vis the curve itself. The cooling rate and the height increase values of the peak are shown in Table 6.2.3.

At the time of writing, it appears that the Tanino et al. [23] study is the only one reported in the literature concerning the effect of cooling rates on the hardness of vanadium and niobium steels. In brief, the microstructure of the vanadium steels investigated by Tanino et al. [23] consisted of ferrite and pearlite between 0.1K.s^{-1} and

2.0K.s^{-1} with a grain size of about 50 μm. The peak hardening was reported to be located between 1.0K.s^{-1} to 1.4K.s^{-1}. However, the exact values taken from the graph of Tanino et al. [23] are reproduced in Table 6.2.3. The heat-treatment was carried out on 0.3 - 1.0 mm thick specimens and the strengthening effect of vanadium was ascribed to the formation of substructures and to precipitation of fine carbides (≲ 5nm) on both dislocation loops and dislocation dipoles. Substructures were classified in three categories: (1) dispersed dislocation loops and elongated dislocation dipoles, (2) dispersed and lined-up carbide particles, and (3) microtwins. Similar "substructures" were also observed in the present study. Tanino et al. [23] found that the substructures changed with vanadium content and cooling rates, although most of their investigation was carried out at 0.67K.s^{-1}. All the substructures were said to be present at this cooling rate. In the present study, it was easier to study structures at lower cooling rates than at the peak hardening; there was more ferrite present in the steel and the "substructures" were better developed.

It can be expected that an increase in vanadium content would produce a higher peak hardening (see Fig. 6.2.1). However, the 0.53% vanadium steel produced the same value of hardness at the peak as the 0.46% vanadium steel. The Fe - 0.12C - 0.46V steel had a quasi stoichiometric composition of VC whereas the Fe - 0.18C - 0.53V steel was rich in carbon. However, the 0.53% vanadium steel

should have produced a volume fraction of VC 15% higher than the 0.46% vanadium steel. Three explanations should be considered: (1) the increase in hardness is not a linear function of vanadium content, (2) the γ-α transformation temperature is influential on precipitation (if the peak is due to precipitation hardening), (3) because vanadium has an affinity for carbon and nitrogen atoms, it slows down their diffusion similarly to manganese.

On the other hand, a large increase in the percentage height of the peak was found, when the addition of vanadium was doubled and tripled from 0.21%V to 0.53%V and 0.13%V to 0.45%V respectively (see Fig.6.2.3). The first explanation suggested above is therefore unlikely, unless the effect produced by the vanadium additions ceased after 0.46 weight percent. The most suitable moment for precipitation in steel is at the allotropic transformation [18-22]. However, vanadium carbonitride was also found to precipitate in austenite [4]. A decrease in the temperature of the γ-α transformation could lead to: (1) more precipitation in γ, (2) a lower volume fraction of the interphase precipitation, and (3) a lower diffusivity of the elements (C,V,N) in alpha iron.

The percentage of the volume fraction of vanadium carbide in solution at particular equilibrium temperatures is shown in Fig.6.2.4, for the 0.53% and 0.46% vanadium steels. If precipitation of vanadium carbide (VC) occurs in γ-iron at a specific level of supersaturation

of VC, the feasibility of this occurring will be greater in the Fe - 0.18C - 0.53V steel. Manganese was reported to slow down the diffusion of nitrogen [156]. Vanadium which has a greater affinity than manganese for carbon and nitrcgen should have a similar effect as manganese on the rate of diffusion of these two elements in iron.

Low γ-α transformation temperatures of the 0.53% vanadium steel also decrease the diffusivity of the vanadium, nitrogen and carbon elements in α iron. This can account for the lowering of the peak and for the shift of the peak to a lower cooling rate in Fe - 0.18C - 0.53V steel compared to the Fe - 0.13C - 0.46V steel. Although Taninò et al. [23] may have calculated the cooling rate in a different manner than the present study, the broadening of the peak and the general hardness enhancement of the 0.53% vanadium, suggest that the above (2) and (3) explanations are acceptable.

Similar considerations can be inferred for the three vanadium steels presented in Fig.6.2.2. The manganese reduced the γ-α transformation temperatures and it may interferealso with the carbon diffusion. In the Fe - 0.45V - 0.12C - 1.5Mn steel, the peak percentage was reduced: there was a general enhancement of the curve (leaving aside the effect of solid solution) and a shift of the peak to lower cooling rates.

The effect of niobium additions in steels is similar to the effect produced by vanadium additions, as can be seen in Fig.6.2.5. The Fe - 0.02C - 0.14Nb steel contains

a stoichiometric composition of NbC. A greater change in the shape of the curve was noticed, compared with the two other niobium steels. This can be related to the steep change of the curve of 0.46% vanadium steel (see Fig.6.2.2). The effects of an excess of carbon or an addition of manganese in niobium steels were similar to those produced in vanadium steels. However, contrary to the vanadium, the niobium cannot be added to produce the same volume fraction of carbonitride; the NbC is less soluble than the VC (see Fig.1.1.1.1) in γ-iron. This can account for the less marked "peak" effect of niobium additions compared to vanadium.

In résumé, a peak hardening was obtained at a critical cooling rate in niobium and vanadium steels. The steepest peaks were produced for steels of a stoichiometric composition of (Nb, V)C. In those steels, a successive addition of carbon or manganese produced a spread of the peak with its consequent decrease, and caused the peak to appear at lower cooling rates. This observation was ascribed mainly to the effect of a lower γ-α transformation on the diffusivity of the V or Nb, C and N. The reduced effect in niobium steels resulted from the lower volume fraction of niobium carbide present in those steels.

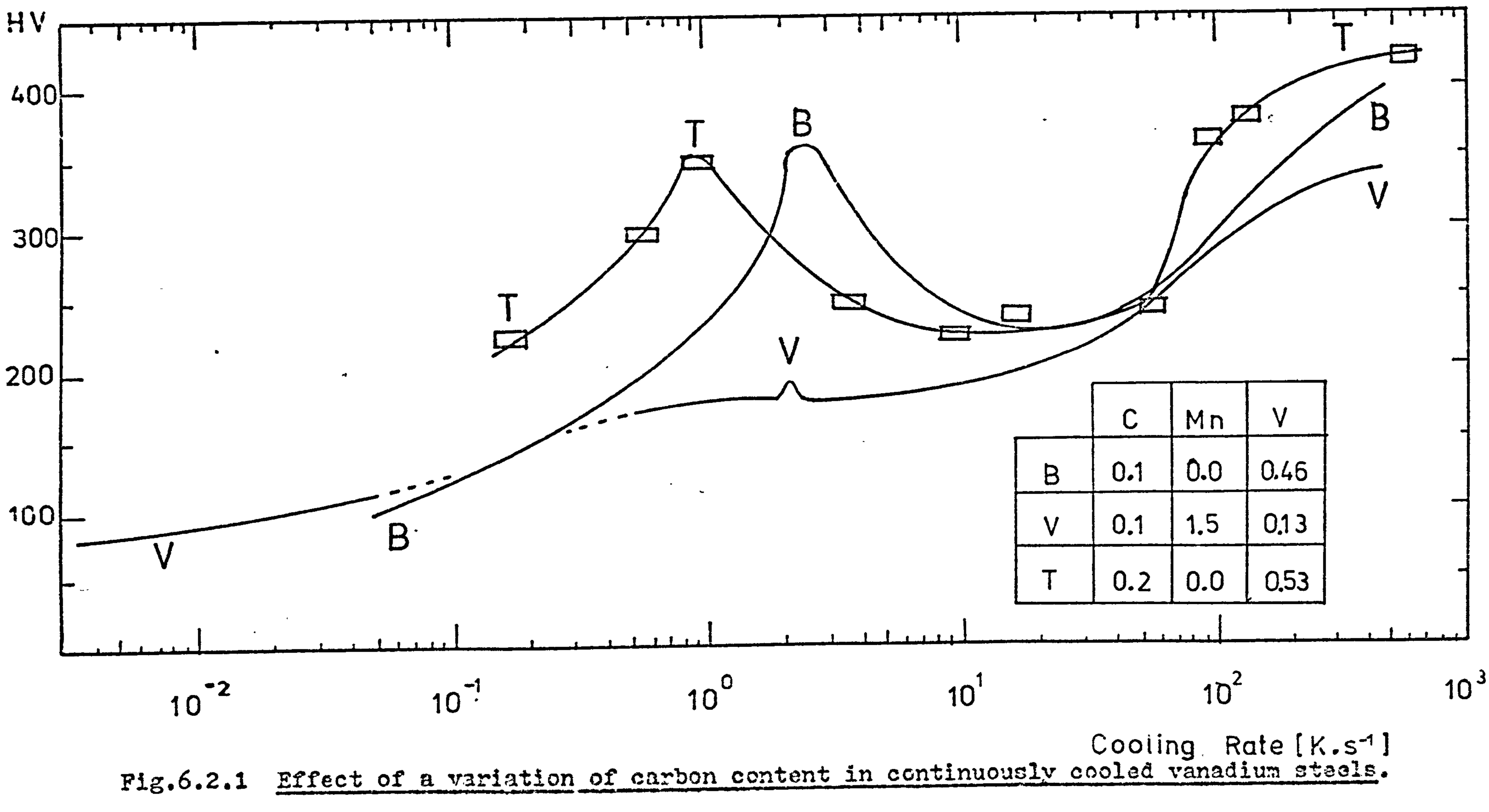

	C	Mn	V
B	0.1	0.0	0.46
V	0.1	1.5	0.13
T	0.2	0.0	0.53

Fig.6.2.1 Effect of a variation of carbon content in continuously cooled vanadium steels.

fig

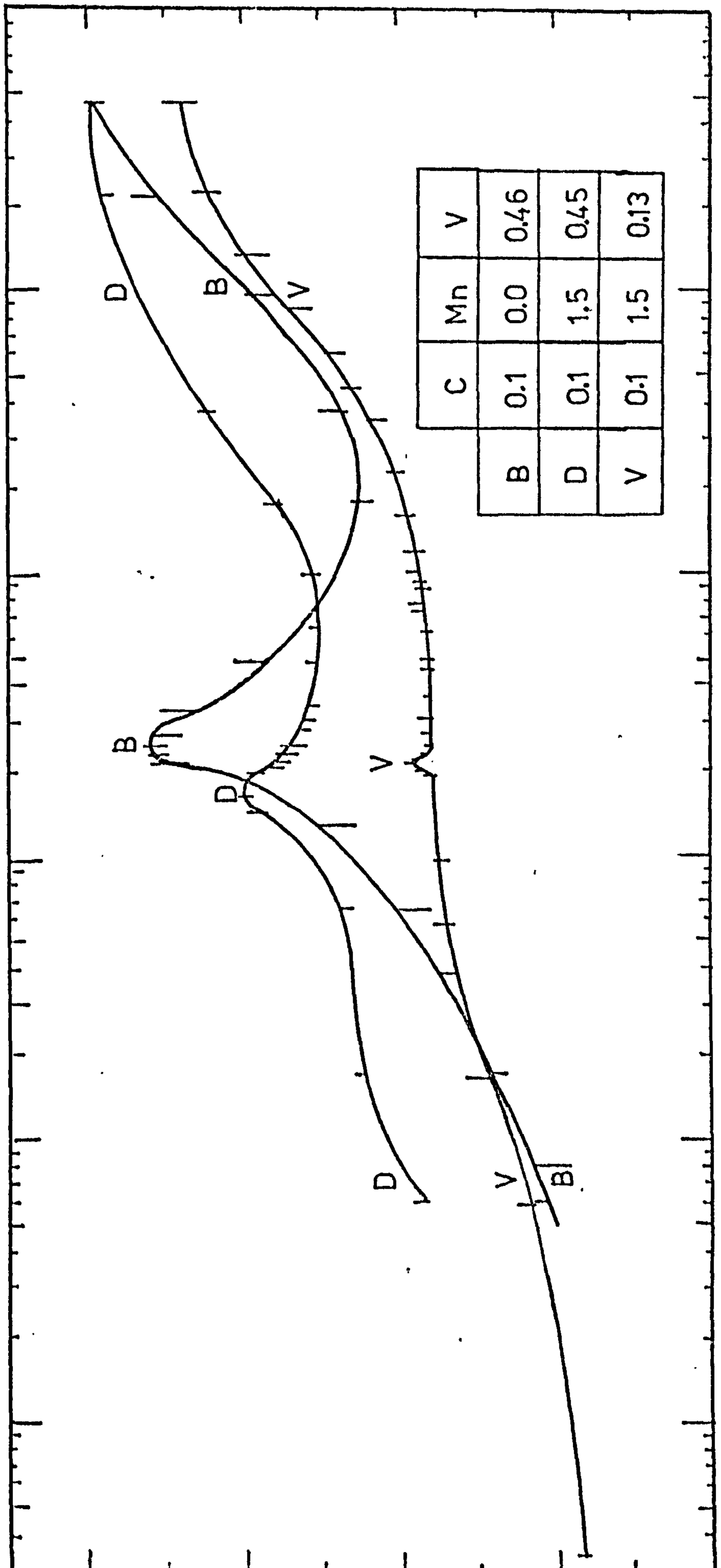

C	Mn	V
0.1	0.0	0.46
0.1	1.5	0.45
0.1	1.5	0.13

B	D	V

Fig.6.2.2 Effect of manganese addition in continuously cooled vanadium steels.

STEEL COMPOSITION		PEAK HARDENING	
		Cooling rate $K.s^{-1}$	Percentage increase
T' 0.21V - 0.17C	Ref [23]	1.4	10.0
T 0.53V - 0.18C	Ref [23]	0.90	59.0
B 0.46V - 0.12C		2.5	60.0
D 0.45V - 0.13C - 1.5Mn		1.7	20.0
V 0.13V - 0.10C - 1.5Mn		2.1	5.5

Table 6.2.3 Cooling rate and percentage increase at the peak hardening in vanadium steels.

TEMPERATURE		% Volume fraction in solution at equilibrium	
Remarks	(K)	0.18C-0.53V steel	0.12C-0.46V steel
Solution	1320	100%	100%
	1270	55%	100%
Intermediate	1200	15%	27%
γ to α starts	1163	8%	14%
	1138	4.6%	-

Table 6.2.4 Volume fraction of vanadium carbide in solution as a function of temperature.

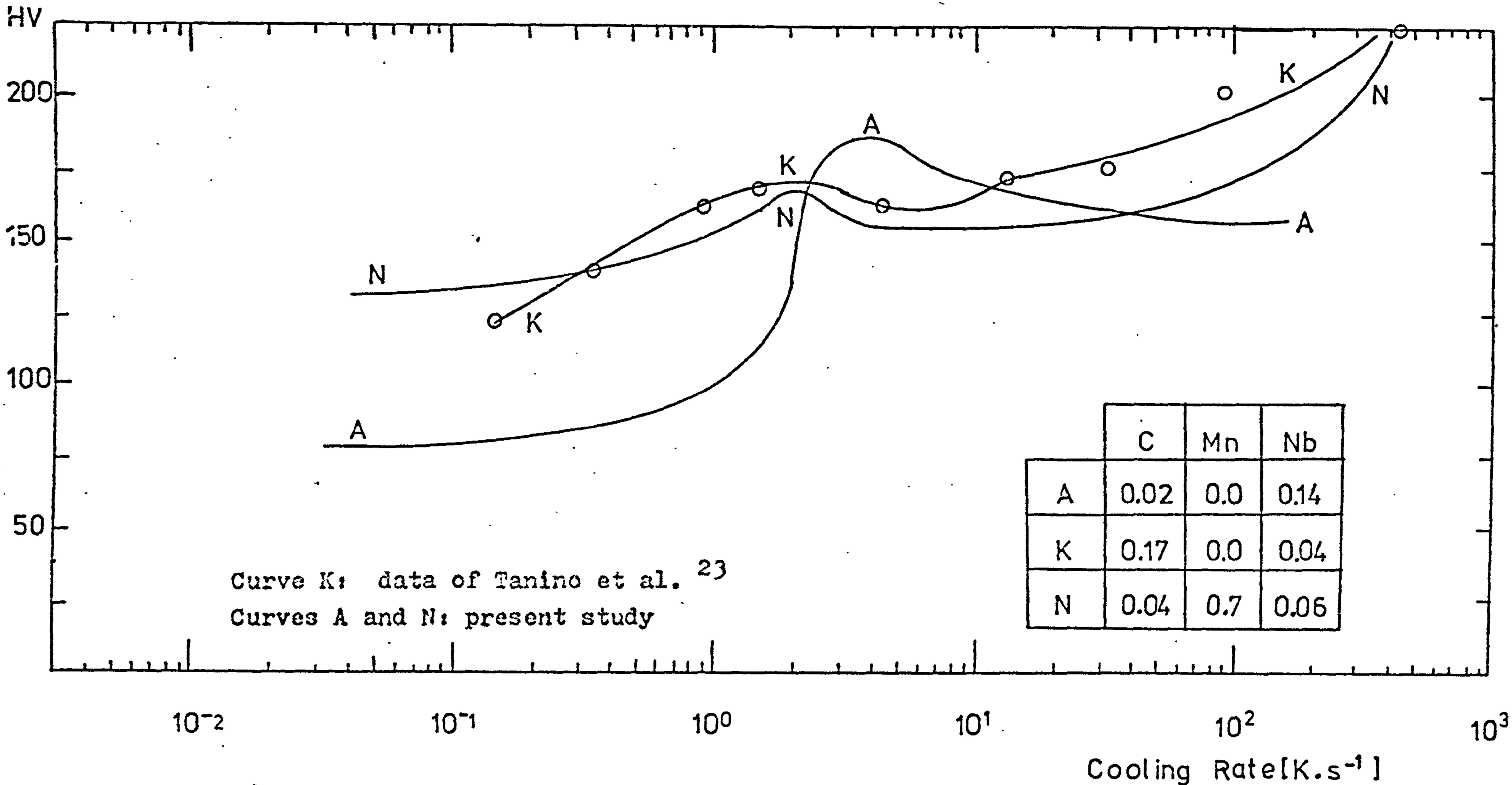

	C	Mn	Nb
A	0.02	0.0	0.14
K	0.17	0.0	0.04
N	0.04	0.7	0.06

Curve K: data of Tanino et al. [23]
Curves A and N: present study

Fig.6.2.5 Effect of cooling rates on the hardness of niobium steels.

6.3 Study of causality for peak hardening.

This section tries to explain how the peak hardening observed in vanadium and niobium steels has occurred (see Fig.6.2.2 and Fig.6.2.5). The Hall-Petch equation is used to correlate the different strengthening mechanisms in steel and to find out if precipitation hardening makes a major contribution to strength.

6.3.1 Identification of the strengthening mechanisms causing the peak hardening observed.

There are four main hardening mechanisms in steel (see section 1.3): (1) grain size hardening, (2) solid solution hardening, (3) dislocation density hardening and (4) precipitation hardening. The steels were continuously cooled and a texture hardening is thus not considered in the present study. In this sub-section, each hardening mechanism is studied successively with respect to its contribution to the hardness observed.(see Fig. 4.1.1 to 4.1.5).

First, the Hall-Petch equation [80,81] was used as a means to calculate the grain size hardening:

$$\sigma_y = \sigma_o + ky\ d^{-\frac{1}{2}} \qquad 6.3.1.1$$

where: σ_y is the lower yield stress

σ_o is the lattice friction stress

ky is a stress intensity factor

d is the grain size.

Some Hall-Petch constants (σ_o, ky) for low carbon

steels are listed in Table 6.3.1.1. It can be seen that the σ_o and k_y values are dependent upon the composition but also they depend upon the thermal history of the materials (e.g. Imai and Shino's values). It was also shown, in a carefully written paper [159], that the "k_y" value in quenched low-carbon steels returned to its saturation value in subsequent ageing, $k_y \simeq 0.675$ MN $m^{-3/2}$. Consequently, the values of σ_o and k_y selected, were those of materials and conditions closely related to the experimental conditions and the materials used in the present study. The values of Cracknell and Petch [170] (σ_o=71 MPa, k_y = 0.716 MN $m^{-3/2}$) were found applicable to the vanadium steels of the present study. Values [170] of σ_o = 47 MPa, k_y = 0.708 MN $m^{-3/2}$ from the same authors were also adopted for the niobium steels. The contribution to strength from the grain size was thus calculated, but could not account for the peak hardening observed.

Second, the hardening from solid solution of vanadium and niobium is very small [94], (see also Fig.1.3.2.1) and can be neglected. It was also expected that niobium or vanadium would combine with the intertitials of carbon and nitrogen. This therefore cannot explain the peak hardening observed.

Third, the strengthening effect of dislocation density was also investigated. In the present study, it was shown that the number of dislocations in niobium and vanadium steels was about 10^{10} dislocations. cm/cm^3 from the cooling rate of $2K.s^{-1}$ down to $0.06K.s^{-1}$ (see Fig.4.6.1). Thus,

once more, this strengthening mechanism cannot account for the peak hardening observed.

Finally, the contribution to strength from precipitation was sought. The Hall-Petch equation [80,81] (equation 6.3.1.1) was used as a means of isolating the contribution to strength from precipitation hardening. One of the problems is whether precipitation hardening influenced the σ_o and ky terms separately or whether both of them were affected simultaneously in the Hall-Petch equation.

A recent study [135], carried out on vanadium steels, related the grain size and precipitation to the lower yield strength through the Hall-Petch equation. The σ_o and ky components for the vanadium steels were compared with plain carbon steels of similar composition. A variation in the "σ_o" value was observed whilst the "ky" term remained approximately constant in the steels with or without vanadium additions.

Also, there has been a tendency in the literature to express the Hall-Petch equation [80,81] as a succession of additive components [94,160-162]; "ky" is taken as a constant. A similar interpretation was adopted in the section 1.3 of the present study. The precipitation hardening component can thus be isolated from the equation 1.3.4.1:

$$\sigma_p = \sigma_y - (\sigma'_o + \sigma_{dd} + \sigma_{ss} + ky\ d^{-\frac{1}{2}}) \qquad 6.3.1.2$$

where: σ_p is the contribution from precipitation hardening to the lattice friction stress

σ_y is the yield stress

σ'_o is the inherent lattice friction stress

σ_{dd} is the contribution from dislocations to the lattice friction stress

σ_{ss} is the contribution from solid solution to the lattice friction stress

$ky\ d^{-\frac{1}{2}}$ is the grain size hardening component.

The preceding discussion was related to the validity of the additive terms in the Hall-Petch equation. In plain carbon steels, the σ_o component of equation 6.3.1.1 contains three terms of the equation 6.3.1.2:

$$\sigma_o = \sigma'_o + \sigma_{dd} + \sigma_{ss} \qquad 6.3.1.3$$

The symbol "σ_o" is the lattice friction stress and represents the resistance of the lattice crystal to the movement of dislocations [81]. It can be foreseen that an increase of dislocation densities increases σ_o from a higher intensity of events of interactions crystal-dislocation interaction with reduced effect on grain boundaries and on ky.

The effect of substitutional solid solution may present some controversy. The drag of interstitials atmospheres on moving dislocations (edges) is well known. It is possible that a similar effect exists for substitutional atoms. However, Takeuchi [172] studied six Fe - alloy systems in order to elucidate the mechanisms of the substitutional solid solution of iron. In his study, the author pointed out that the strengthening effect cannot be fully explained by the atomic size effect of the solute atoms. It was proposed that the elastic interaction

of the screw dislocations with the solute atoms was the dominant cause of the solid solution in iron at 300K. Although the elastic theory predicts a stronger interaction with edge dislocations, one may regard the effect of these interactions dislocation-substitutional atoms as increasing also the lattice friction stress "σ_o".

Usually, in the literature reviewed, σ_o was determined for a specific material with a specific heat-treatment (see Table 6.3.1.1). It was thus necessary to estimate the values of σ_{dd} and σ_{ss} in order to obtain the inherent "σ_o" in equation 6.3.1.3. As mentioned early on, the values of Cracknell and Petch [170] were adopted for vanadium and niobium steels of the present study. The Fe - 0.12C - 0.5Mn steel of Cracknell and Petch [170] was slowly cooled from austenite to room temperature. It is estimated that the dislocation density should be similar to those of an annealed material, which is in the order of 10^8 dislocations. cm/cm^3. This value was substituted in equation 6.3.1.3 to obtain σ_{dd}. The contribution of manganese to solid solution was estimated from data presented in Fig.1.3.2.1: hence,

(1) for vanadium steels:

$$\sigma'_o(48MPa) = \sigma_o(71MPa) - \sigma_{dd}(7.6MPa) - \sigma_{ss}(16MPa) \qquad 6.3.1.4$$

(2) for niobium steels:

$$\sigma'_o(34MPa) = \sigma_o(47MPa) - \sigma_{dd}(7.6MPa) - \sigma_{ss}(5MPa) \qquad 6.3.1.5$$

The term σ'_o thus takes into account the strengthening

effect of interstitials of carbon and nitrogen, which is very small at equilibrium and at room temperature (from 996K to 300K, the solubility of carbon in ferrite is 0.02% and $2X10^{-7}$% respectively [163]).

Finally, the equation 6.1.2, which related the hardness (HV) to the yield stress (σ_y), can be substituted in equations 6.3.1.2:

$$\sigma_p = 2.1\ HV - (\sigma_o + \sigma_{dd} + \sigma_{ss} + ky\ d^{-\frac{1}{2}}) \qquad 6.3.1.6$$

The contribution from precipitation hardening can thus be isolated in Fig.6.3.1.2 to Fig.6.3.1.6 (lower yield stress against cooling rate), and the results are shown in Fig.6.3.1.7 and Fig.6.3.1.8. The values of σ_{dd} measured for low vanadium and niobium steels (data of Fig. 4.6.1) were also adopted for high vanadium and niobium steels (using equation 1.3.3.2). It can be seen that the peak hardening observed in the Diamond pyramid hardness in Fig.6.2.2 and Fig.6.2.5 were caused by precipitation hardening. A greater contribution was obtained from the materials having a stoichiometric composition of VC or NbC, but without manganese addition. The cooling rate at which the peak occurred coincided with the presence of small ferrite grains (see section 5.1).

These findings can be compared to the study of Bucher and Grozier [164]. They reported data for precipitation hardening against cooling rate in vanadium steels. The authors used aluminium to remove the nitrogen from the metal and to obtain only vanadium carbide precipitates (hot rolled steel fully killed with aluminium).

The exchange effect of aluminium, vanadium and nitrogen is well known [165].

However, some criticisms of the study of Bucher and Grozier can be formulated. These criticisms raise doubts about the value of their findings. For instance: (1) the composition of the steels investigated is not mentioned, (2) it is possible that AlN may have contributed to precipitation hardening, but this aspect is not discussed in the study, (3) the method of measuring the contribution from precipitation hardening is not presented and (4) the solution temperature is not included, which makes it impossible to convert their cooling rate. Consequently, their results should be considered with much scepticism. Despite this criticism, it should be noted that their results are in good agreement with the cooling rate at which a peak hardening was observed in vanadium steels (see Fig.6.3.1.3).

It can therefore be concluded that the peak hardening observed in continuously cooled vanadium and niobium steels was due to precipitation hardening. The highest increase at peak hardening was found in materials which had a stoichiometric composition of VC or NbC, but having no manganese additions.

σ_o MPa	K_y (MN $m^{-3/2}$)	Composition (wt %)	Heat-treatment	Reference
24	0.695	Zone refined iron, 0.002(C+N)	Heat-treated between 873K and 1173K, then furnace cooled to room temperature in 12-14 hr	Christ and Smith (158)
63	0.747	Electrolytic iron 0.014C-0.003N-0.005O	Heat-treated between 993K and 1173K, furnace cooled to 993K, then air cooled (1.3mm diameter ⇒ fast cooling rate) aged 24 hr at 423K to obtain a stable precipitate structure	Conrad and Schoeck (156)
45	0.712	0.038C-0.4Mn-0.004N	Heated 2 hr at 973K, then cooled to 473K in 18 hr. Tensile specimens were made (13mm X 1.8mm), heat-treated at 473K for 2000 min and rapidly cooled	Wilson and Russell (169)
47	0.708	0.02C- 0.14Mn-0.003N	Austenitic heat-treatment: up to 1323K, then cooled to room temperature in 15 hr.	Cracknell and Petch (170)
71	0.716	0.12C-0.5Mn-0.0085N	Austenitic heat-treatment : up to 1323K, then cooled to room temperature in 15 hr	Cracknell and Petch (170)

Table 6.3.1.1 Hall-Petch constants

(/...)

σ_o MPa	K_y (MN $m^{-3/2}$)	Composition (wt %)	Heat-treatment	Reference
111	0.716	0.12C-0.05Mn-0.0085N	Austenitic heat-treatment : up to 1325K, then quenched from 923K	Cracknell and Petch (170)
71	0.75	0.12C-0.5Mn-0.008N	Annealed in the 1173-1473K range, (cooling rate?). Specimens were machined, 8mm diameter bars, and annealed again (cooling rate?)	Armstrong et al. (171)
52	0.776	Low carbon steels (0.005 to 0.21C)	Austenitic heat-treatment, cooled at 17K.s^{-1} near the A_3	Imai and Shino (135)
18	0.839	Low carbon steels (0.005 to 0.21C)	Austenitic heat-treatment, cooled at 1.7K.s^{-1} near the A_3	Imai and Shino (135)
81	0.630	various carbon-manganese steels (0.007-0.29C, 0.32-2.1Mn)	As rolled (finishing temperature: 1323K - 1073K, cooled at 0.02-1K.s^{-1}), as normalized, as annealed)	Iranio et al. (157)

Table 6.3.1.1 Hall-Petch constants

.../)

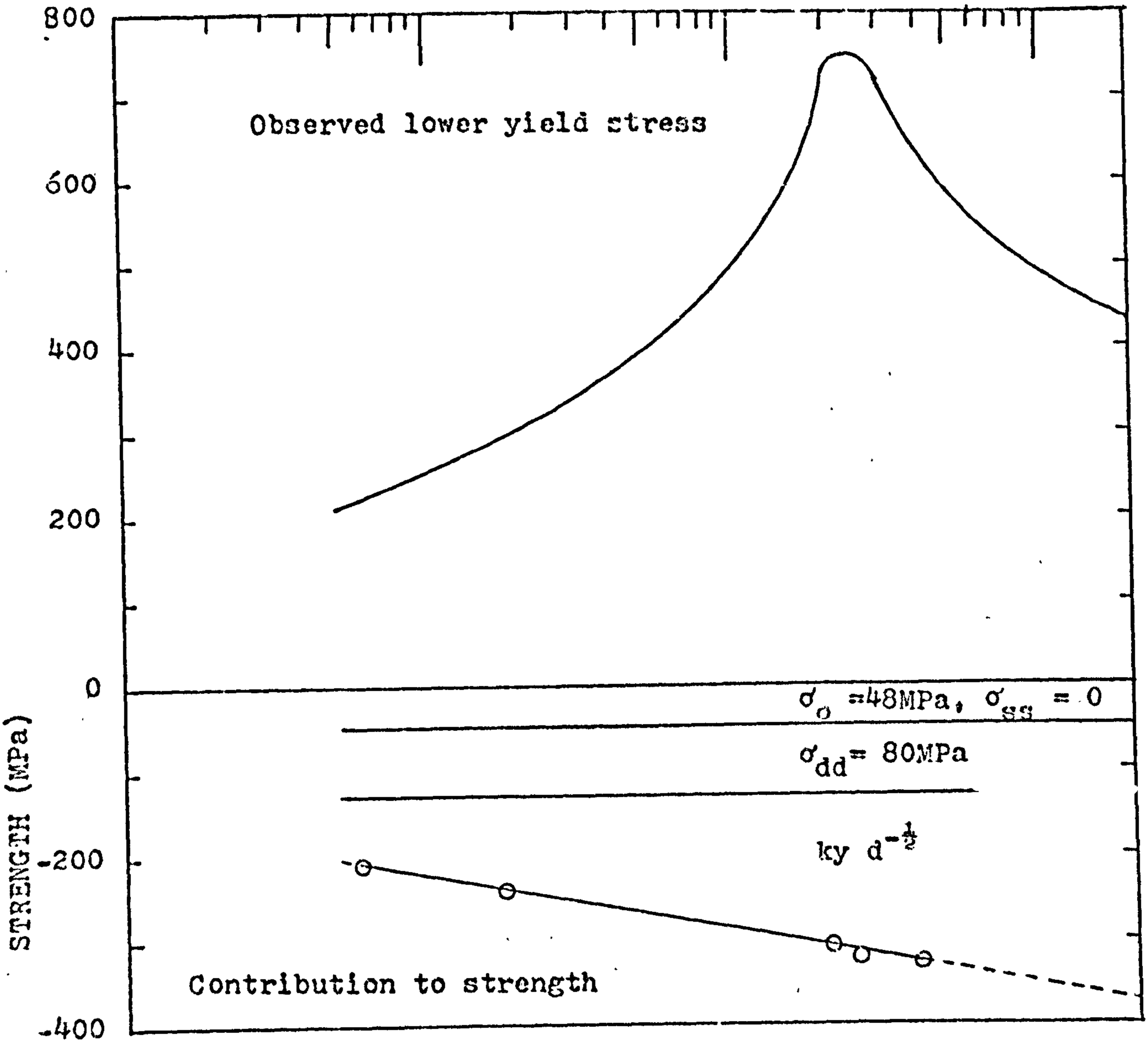

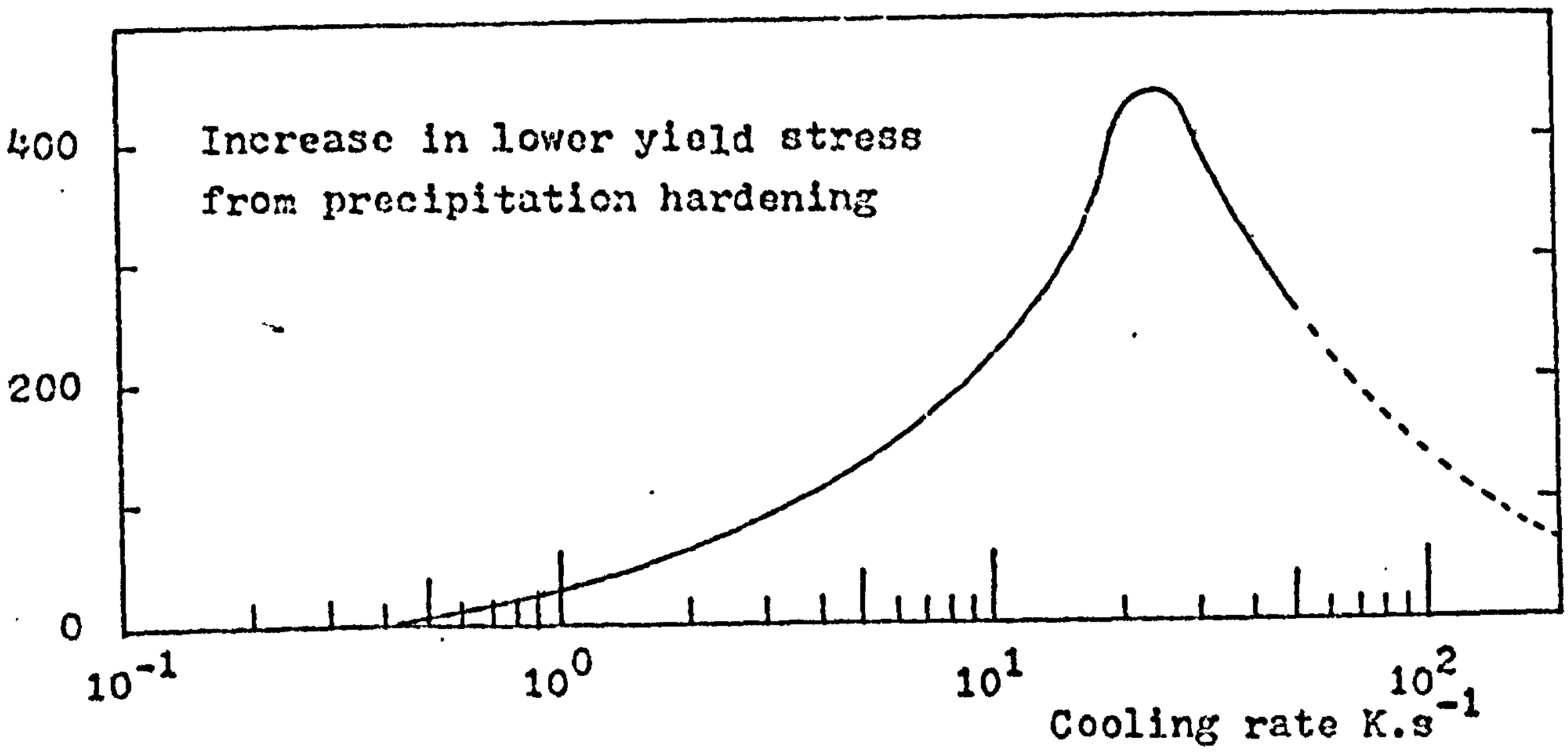

Fig.6.3.1.2 Contribution to strength from precipitation hardening in Fe - 0.1C - 0.46V steel.

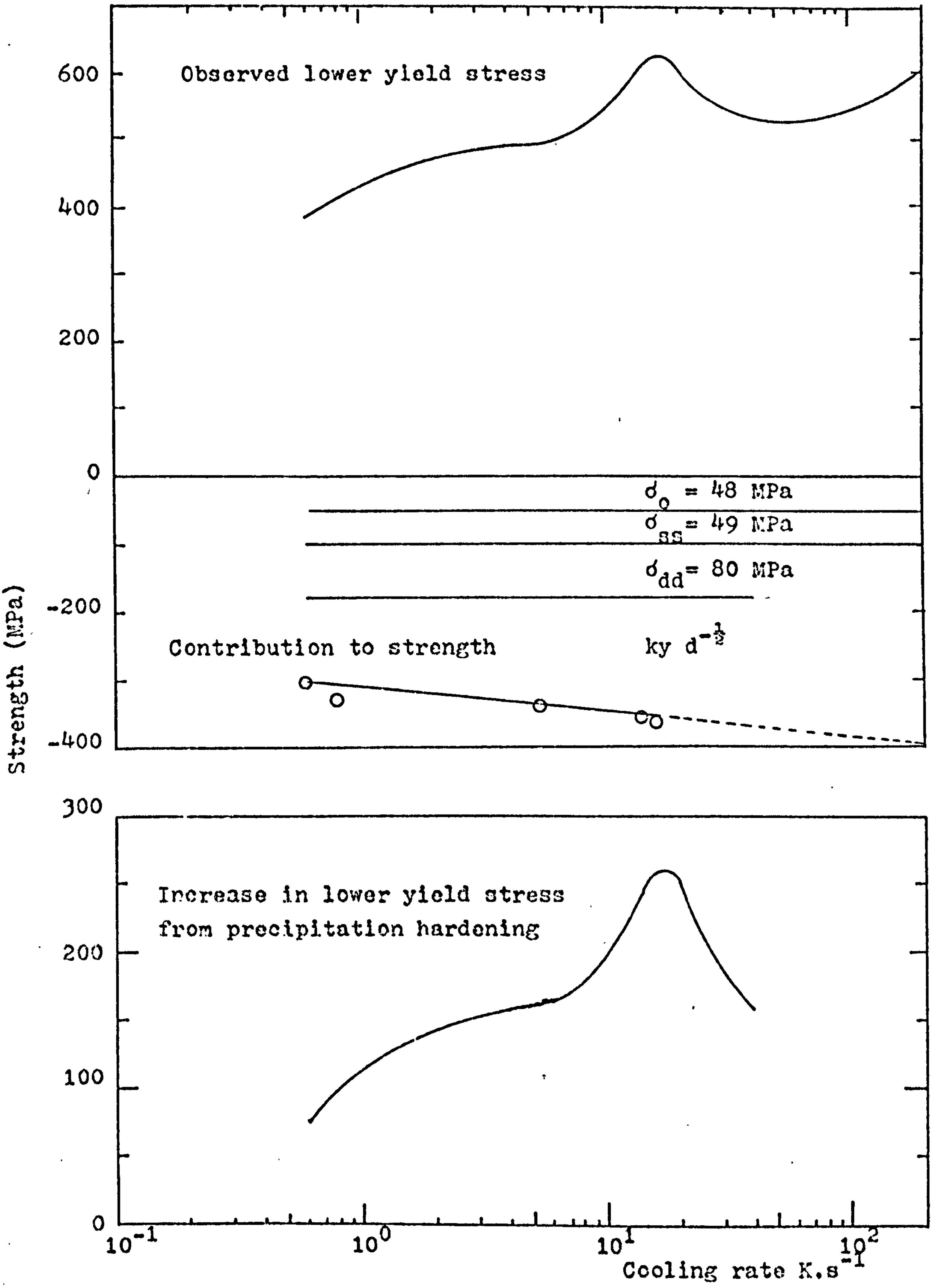

Fig.6.3.1.3 Contribution to strength from precipitation hardening in Fe - 0.1C - 0.45V - 1.5Mn steel.

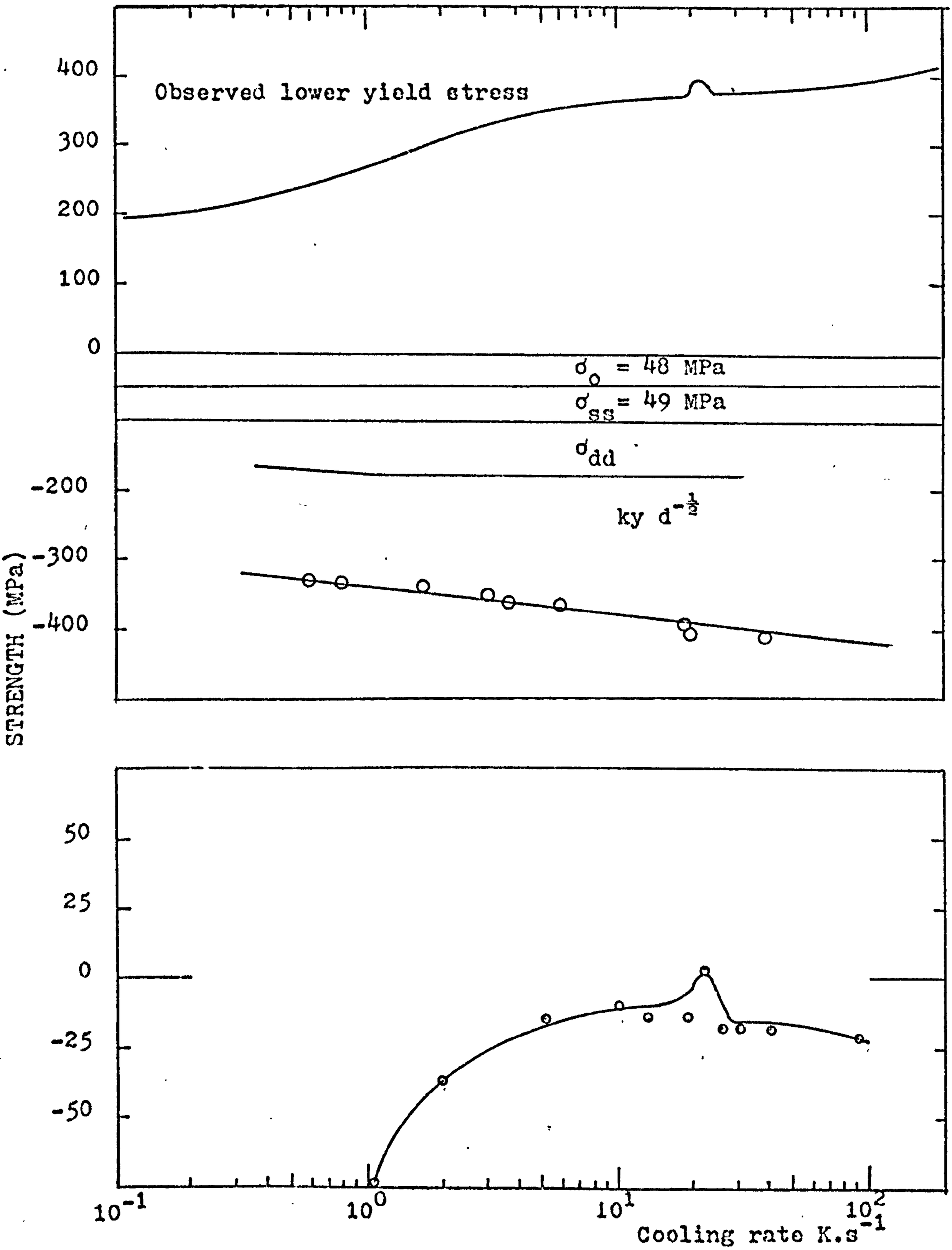

Fig.6.3.1.4 Contribution to strength from precipitation hardening in Fe - 0.1C - 0.13V - 1.5Mn steel.

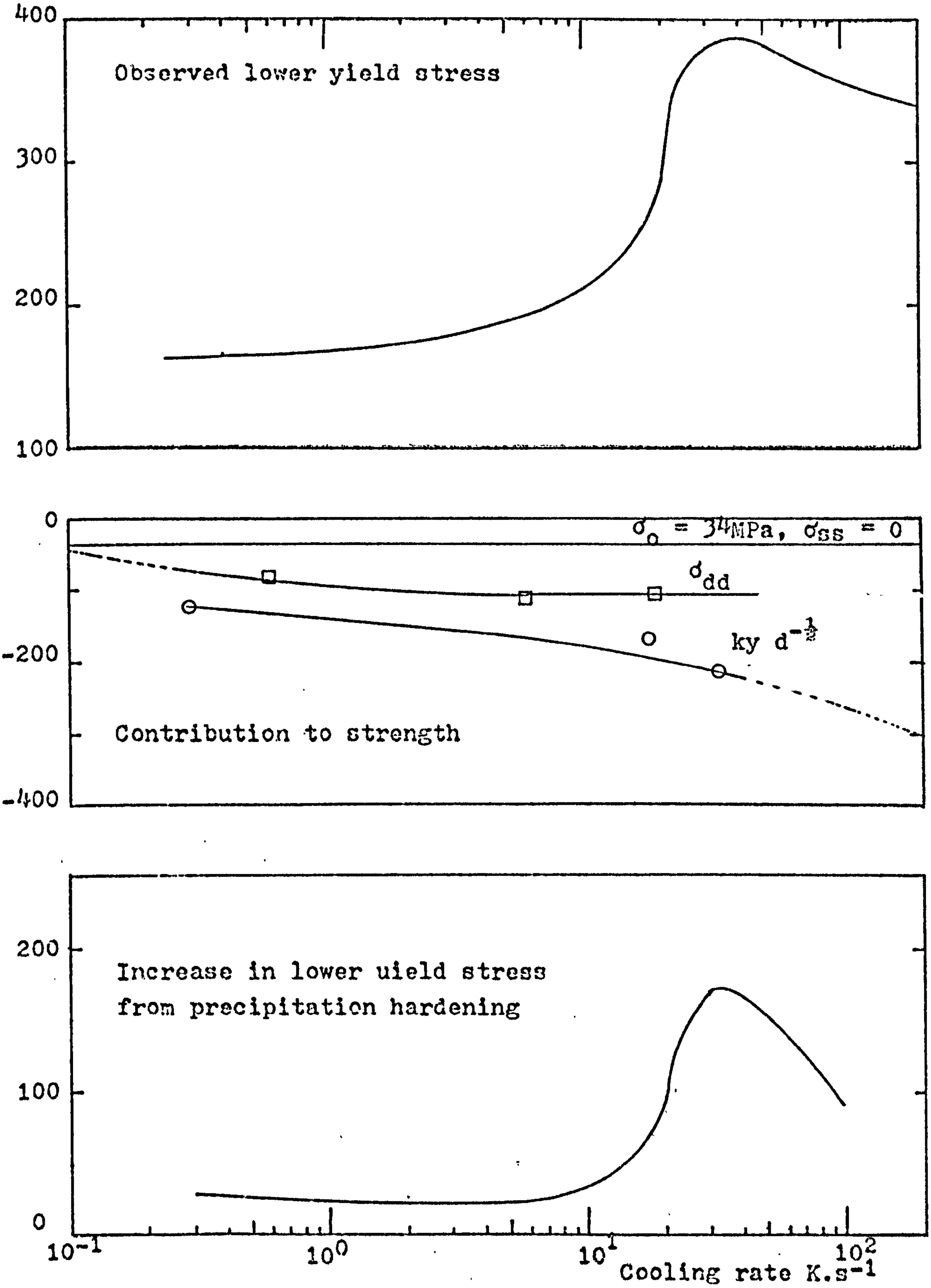

Fig.6.3.1.5 Contribution to strength from precipitation hardening in Fe - 0.02C - 0.14Nb steel.

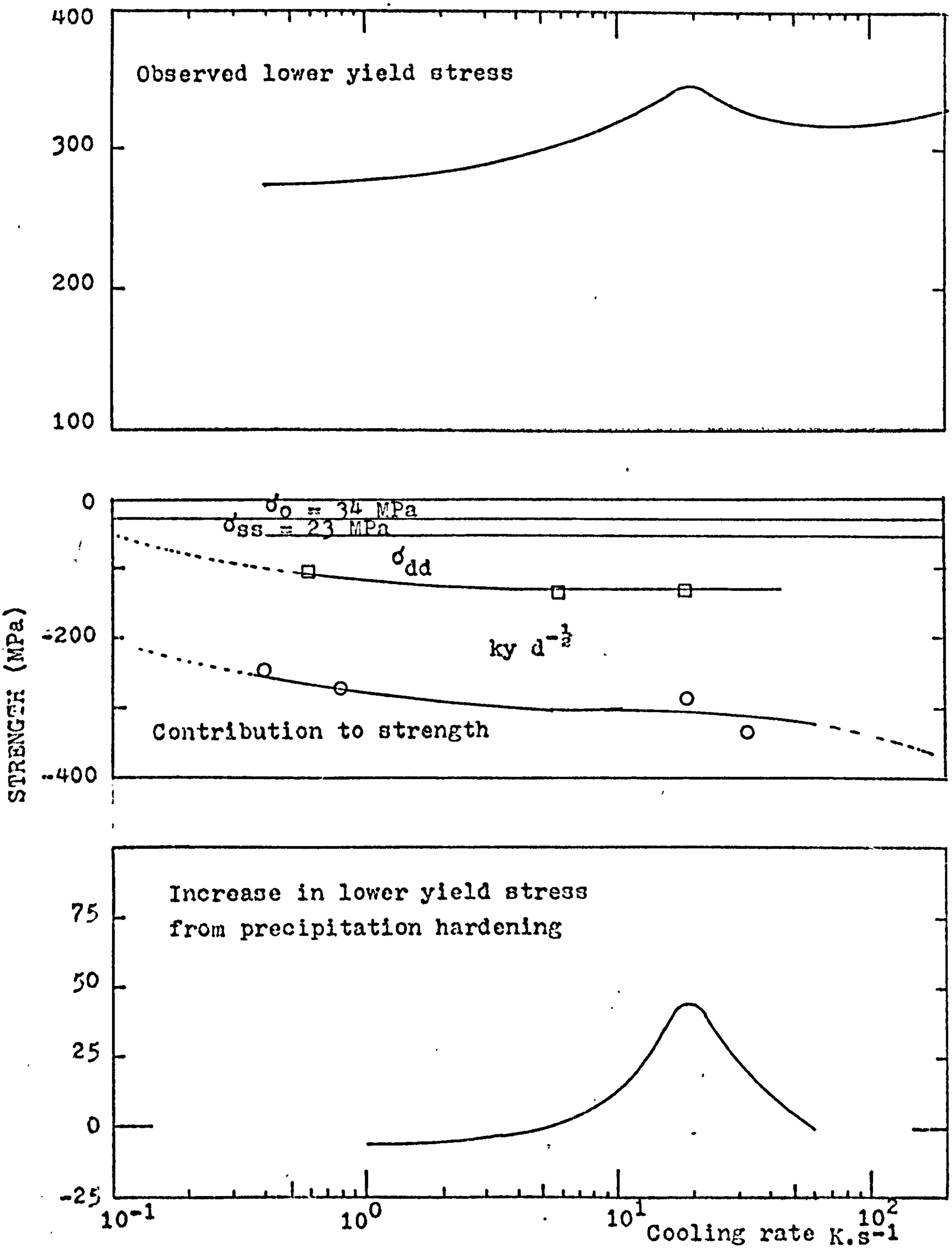

Fig.6.3.1.6 Contribution to strength from precipitation hardening in Fe - 0.04C - 0.06Nb - 0.7Mn steel.

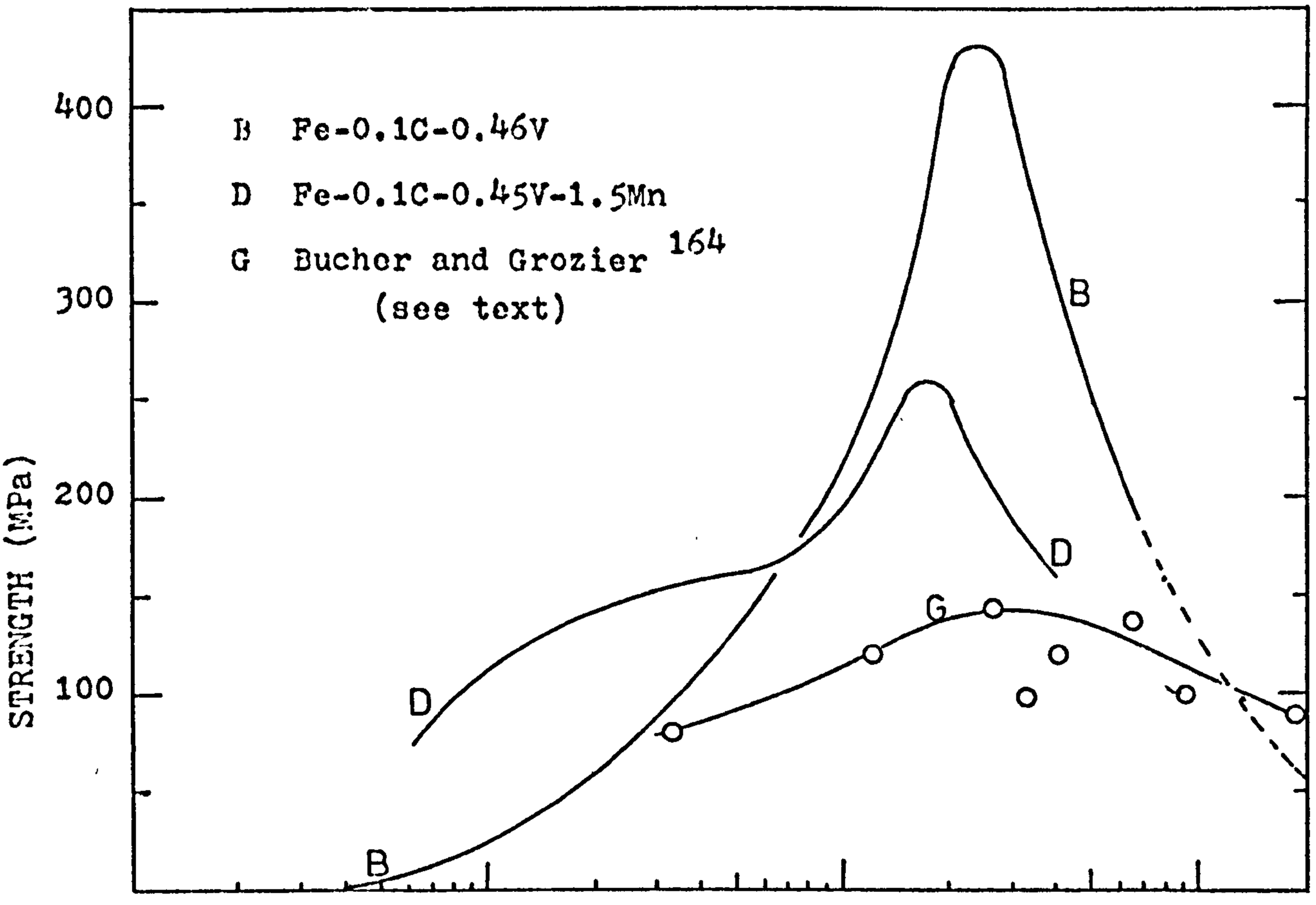

Fig.6.3.1.7 Precipitation hardening in vanadium steels.

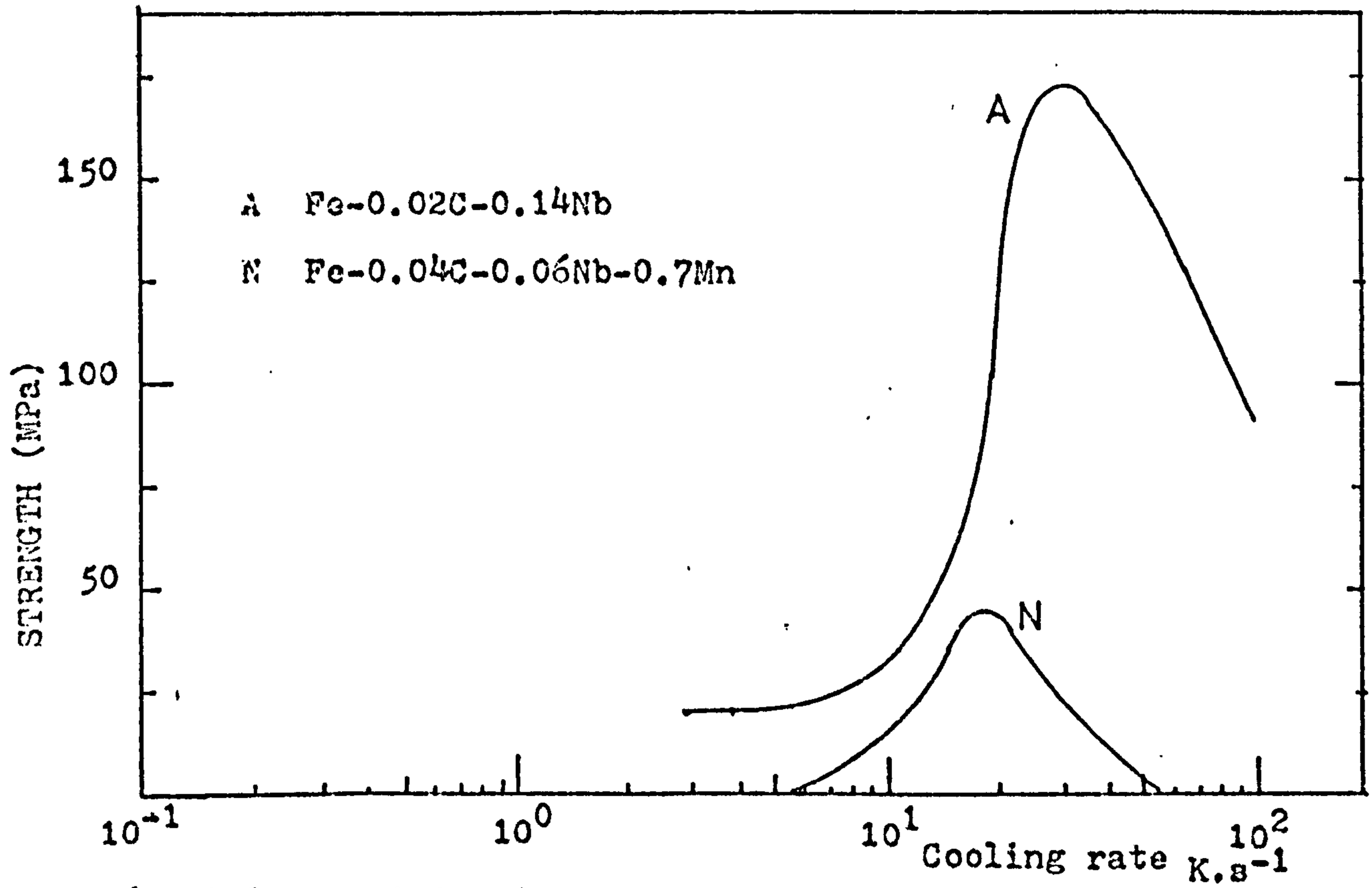

Fig.6.3.1.8 Precipitation hardening in niobium steels.

6.3.2 Precipitation hardening in high vanadium steels.

In this sub-section, an attempt is made to correlate the peak hardening arising from precipitation hardening with the particle size and volume fraction measured. The discussion will be concentrated on high vanadium steels which presented the highest volume fraction of carbides in the alloy steels investigated.

The particle size and volume fraction were measured in the two vanadium steels (see Fig.4.5.7 and 4.5.8). Some of these results are shown in Fig.6.3.2.1. It can be seen that the change in the diameters of small particle sizes with cooling rate is approximately the same for both steels. There is no abrupt change in particle size near the peak hardening. ($\simeq 2K.s^{-1}$). The group of small particle sizes contribute largely to precipitation hardening (see Appendix C), and consequently, the peak hardening (see Fig.6.3.1.7) cannot be explained by a variation of particle size alone at constant volume fraction. The size of the particle and the volume fraction of precipitates must be taken into consideration. Unfortunately, carbon replicas appear unable to measure the exact volume fraction of precipitates (see section 4.5). However, the volume fraction of small particle sizes is higher in the 0.46% vanadium steel than in the 0.45% vanadium - 1.5% manganese steel. This corresponds to a higher precipitation hardening value in the former than in the latter. The volume fraction should be regarded

as a trend, and is possibly only applicable to material of similar composition and producing approximately the same volume fraction of carbonitrides. The error on magnification may be worth considering in particle size determinations. However, the magnification of the elcctron microscope was calibrated prior the the particle size determination. The results of the calibration agreed well with a previous calibration (within 5% error limit). The main source of error arose when the specimen was not positioned at the correct tilt axis of the goniometer of the electron microscope.

On the other hand, it can be postulated that the contribution to strength from large particle sizes is significant when their size is only marginally different from the group of small precipitate sizes, while having at the same time a meaningful volume fraction. It can be seen in Fig.4.5.7, 4.5.9 and 4.5.11 that the diameters of the group of large particle sizes are decreasing considerably near the peak hardening. Bearing in mind the uncertainty of the volume fraction measurements, the interparticle spacing was calculated for the high vanadium steels, taking into consideration the two groups of particle sizes (see Appendix C). The results are presented in Table 6.3.2.2 together with the predicted increase from Gladman et al. [105] and Hirsch and Humphreys [104] derivations of the Orowan [99] equation.

Gladman et al. [105] used the Orowan-Ashby [103] equation to predict the increase in tensile strength from precipitation hardening:

$$\tau = \frac{1.2\ G.b}{2.36\ L} \ln \frac{\bar{X}}{2b} \qquad 6.3.2.1$$

where: τ is the resolved shear stress

L is the centre to centre interparticle spacing in the slip plane

$\bar{X}$ is the average diameter of the circle of intersection between the particle and the slip plane: ($\bar{X} = \sqrt{\frac{2}{3}} \cdot D$, where D is the measured particle diameter, see Appendix C)

$\bar{b}$ is the Burgers vector *

The equation thus becomes:

$$\sigma_p \text{ (MPa)} = \frac{5.7 \times 10^{-6}}{L_D} \ln \frac{D}{0.685} \qquad 6.3.2.2$$

where: σ_p is the contribution to the yield strength from precipitation hardening ($\sigma_p = 1.27\,\tau$)

L_D is the centre to centre interparticle spacing calculated from the measured particle (D).

The observed contributions from precipitation hardening were plotted against those predicted by equation 6.3.2.2 and this is shown in Fig.6.3.2.3. As can be seen, prediction and experiment disagree considerably.

---

* An error appears to be present in the Burgers vector value of Gladman et al.'s equation. They also reported the increase in strength in a vanadium steel as a function of cooling rate in Bucher and Grozier [164]. The cooling rate should be divided by $(1.8)^2$ to obtain the original data of Bucher and Grozier.

Although the method used to determine the volume fraction had unsatisfactory characteristics, perhaps it is not the unique explanation. For instance, it should be said that Gladman et al. [105] verified experimentally the equation 6.3.2.2 by assuming a complete precipitation and a constant average particle size (three nanometers) in the steels investigated. Their steels also contained very little alloying additions (0.04 weight percent of niobium maximum). Thus, the concept of complete precipitation cannot be used for the high vanadium steels of the present study. It would have been necessary to observe a similar contribution to strength from precipitation hardening in both steels; however, a large discrepancy was observed between the two steels (see Fig.6.3.1.7). Similarly, a higher peak hardening should have been observed in the Fe - 0.2C - 0.53V steel compared to the Fe - 0.1C - 0.46V steel (see Fig.6.2.1). Although the MCN precipitation in steel appears at the moment complex, the particle sizes measured experimentally and the contributions from precipitation hardening tended to disapprove the assumptions of Gladman et al. [105].

In Fig.6.3.2.4, the observed yield stress increases are plotted against the measured surface to surface interparticle spacing (L-2R). A straight line can be fitted to the data in order to obtain a simple version of the Orowan equation: i.e. $\sigma_p \propto \frac{Gb}{(L-2R)}$

$$\underset{(MPa)}{\sigma_p} = \frac{2.15 \times 10^{-5}}{(L-2R)} \qquad 6.3.2.3$$

The observed yield stress increases are plotted against the σ_p of equation 6.3.2.3. It can be seen that a reasonable agreement is obtained. The logarithmic term in equation 6.3.2.1 can be considered as a constant according to Hirsch and Humphreys [104]. The energy at the unpinning depends upon the width (X) of the dipole rather than upon the interparticle spacing. The flow stress (σ_p) is thus [104]:

$$\sigma_p = \frac{0.4}{\pi} \frac{G.b}{(L-2R)_T} \frac{\ln (X/b)}{(1-v)^{\frac{1}{2}}} \qquad 6.3.2.4$$

where: v is the Poisson ratio (Iron = 0.28)

$(L-2R)_T$ is the surface to surface interparticle spacing in the slip plane, i.e.

$$(L-2R)_T = \sqrt{\frac{2}{3}} (L-2R) \text{ measured.}$$

The VCN particles present the shape of a thin disc. Assuming that particles conserve the same disc shape as they grow and that the ratio disc diameter to thickness is constant ($D/t \simeq 16$ in a Baker-Nutting orientation relationship [33]), a value of X = 10b (2.5 nm) was found in the equation 6.3.2.4 to fit the data of the Fig.6.3.2.5. It is interesting to note that the value X = 10b (2.5nm) in the logarithmic term coincides with the assumption of a constant particle size of 3 nm of Gladman et al. [105].

Therefore, there is little doubt that precipitation hardening is responsible for the peak hardening in vanadium and niobium steels. The observed precipitation hardening was found to agree reasonably well with the Hirsch

and Humphreys [104] version of the Orowan [99] equation, but a large discrepancy was noted with the Ashby-Gladman [103,105] version of the Orowan equation. Both these findings agree with Brown and Ham [109] who pointed out that the replacement of X by the interparticle spacing in equation 6.3.2.4 represented too large a correction in the Orowan equation. It is also believed that the volume fraction is too small ($f < 10\%$ [109]) for Ansell's theory [173] to apply.

However, the origins of the two groups of precipitates appear difficult to clarify. The following discussion is based on assumptions and most certainly, further studies are required to gain understanding on the origins of precipitates.

In Fig.6.3.2.1, it can be seen that the diameters of the group of small particle sizes were approximately the same for both vanadium steels except their volume fraction was different. If one assumes that they may have precipitated at or after the $\gamma - \alpha$ allotropic transformation, their size should be approximately the same. This is verified in the present study.

However, the diameters of the group of large particle sizes were different near the peak hardening ($\simeq 2K.s^{-1}$). In the manganese steel, their size was even larger. Precipitation of VC in austenite has been reported previously [4]. However, when larger particles are assumed to precipitate in austenite, at a fast cooling rate, they should be bigger in the manganese steel considering that manganese

decreases the $\gamma - \alpha$ transformation temperatures. This increases the possible supersaturation of VC in austenite and increases also the time available for precipitation to occur before the allotropic change. At lower cooling rates, the effect should be reverse: that is, the growing of the large particles will be faster in the steel without manganese compared to the steel with manganese addition (if Mn slows down the diffusivity of the interstitials in α iron).

In résumé, the peak hardening observed in vanadium and niobium steels was ascribed to precipitation hardening. The dimensions of the particles alone could not explain the precipitation hardening effect, and the volume fraction of precipitates had to be considered.

The volume fractions measured by carbon replicas were not sufficiently accurate to be useful in accounting for the peak observed. However, in materials of similar composition, the precipitation hardening component appeared to follow a simple version of the Orowan [99,104] equation rather than the Orowan-Ashby equation.

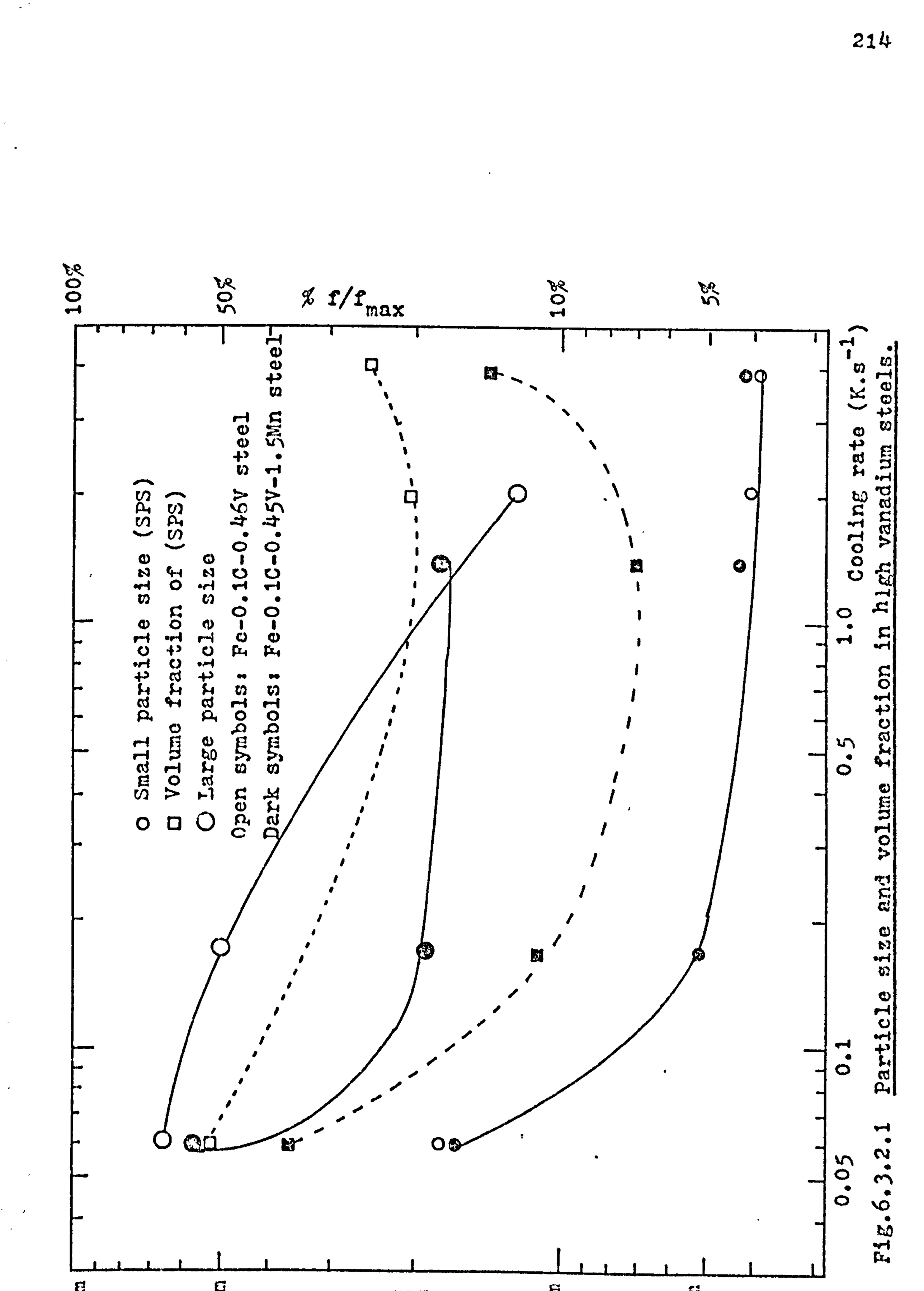

Fig.6.3.2.1 Particle size and volume fraction in high vanadium steels.

Steel	CR	(L)	$(\overline{X})$	$(L-\overline{X})$	σP_{obs}	σP_{A-G}	σP_{exp}
	$K.s^{-1}$	nm	nm	nm	MPa	MPa	MPa
B	0.06	234	21	213	10	84	100
D	0.06	264	38	226	75	87	95
B	0.17	207	18	189	50	90	114
D	0.17	145	6.4	139	135	88	155
D	1.4	125	10.0	115	240	125	187
B	2.0	93	4.7	88	410	118	245
D	4.0	118	4.2	114	160	88	188
B	4.0	79	3.9	75	300	125	290

List of symbols:

B Fe - 0.1C - 0.46V steel

D Fe - 0.1C - 0.45V - 1.5Mn steel

CR Cooling rate

L Measured centre to centre interparticle spacing

$\overline{X}$ Average diameter measured

$(L-\overline{X})$ Measured surface to surface interparticle spacing

σ_p Contribution to the strength from precipitation hardening

obs: observed values

A-G: predicted value from the Orowan-Ashby-Gladman equation 6.3.2.2

exp: predicted from the equation 6.3.2.3

Table 6.3.2.2 Correlation between observed and predicted precipitation hardening in high vanadium steels.

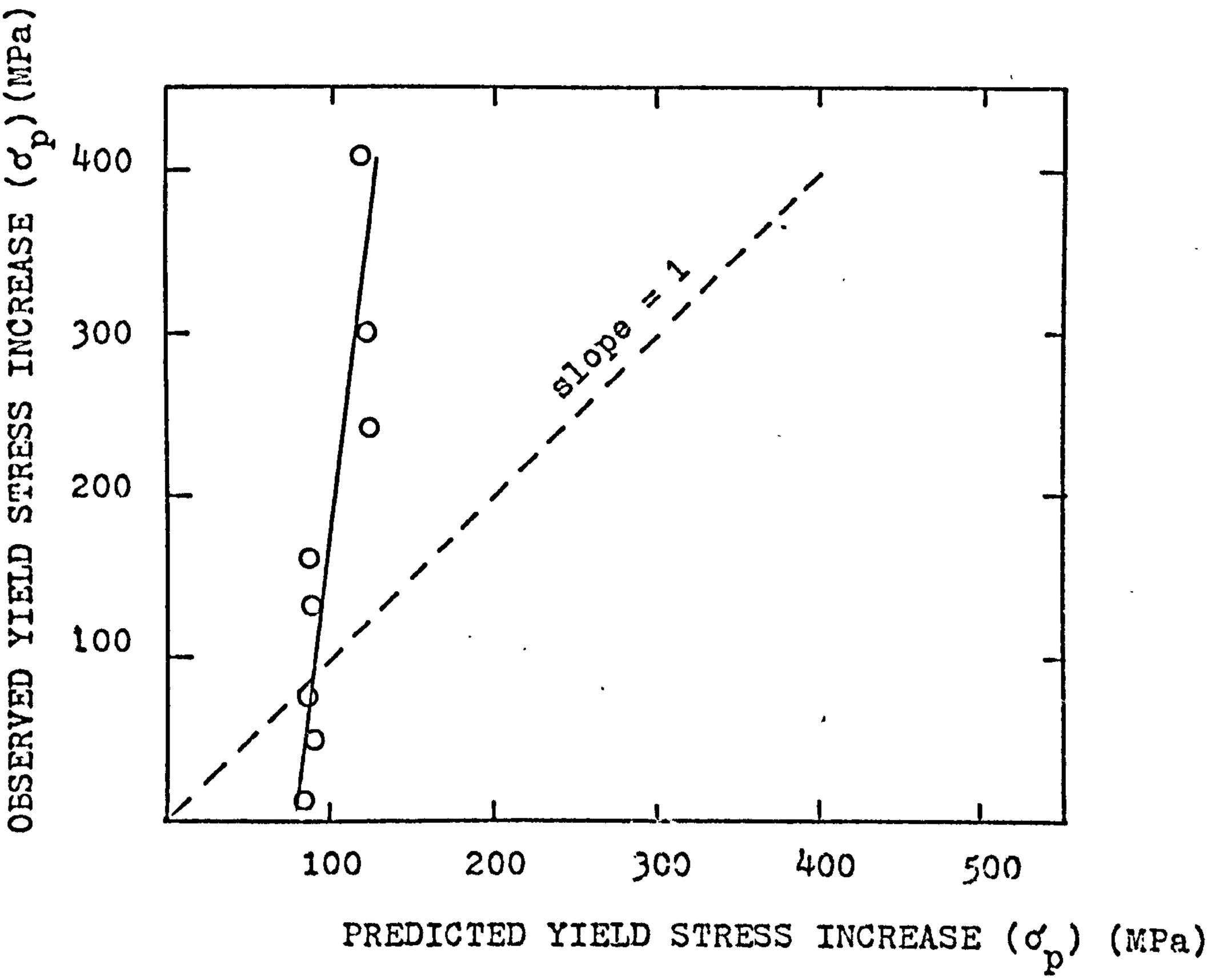

Fig.6.3.2.3 Predicted yield stress from equation 6.3.2.2 (Orowan-Ashby [103] from Gladman [105]).

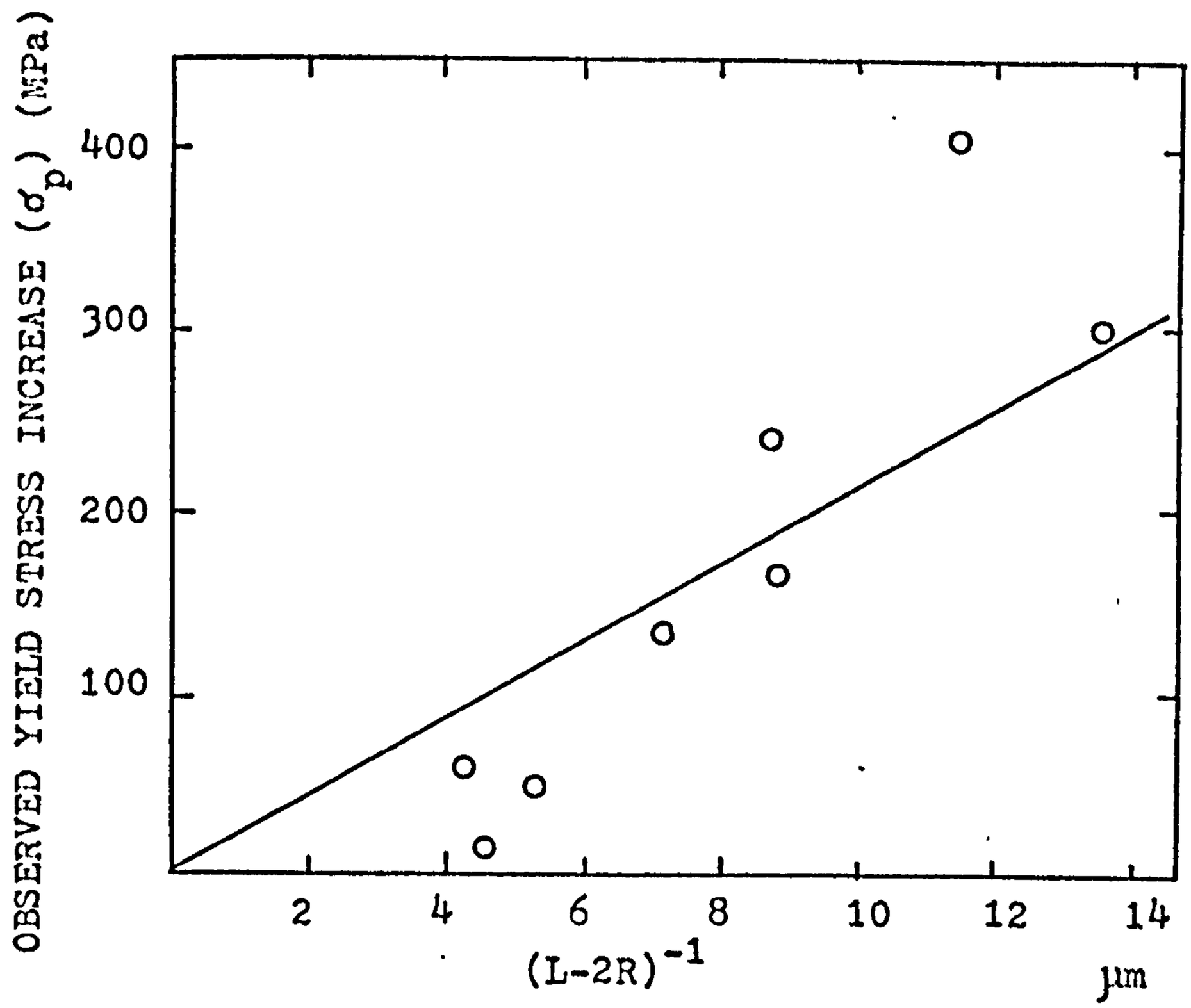

Fig.6.3.2.4 Observed yield stress increase against the surface to surface interparticle spacing.

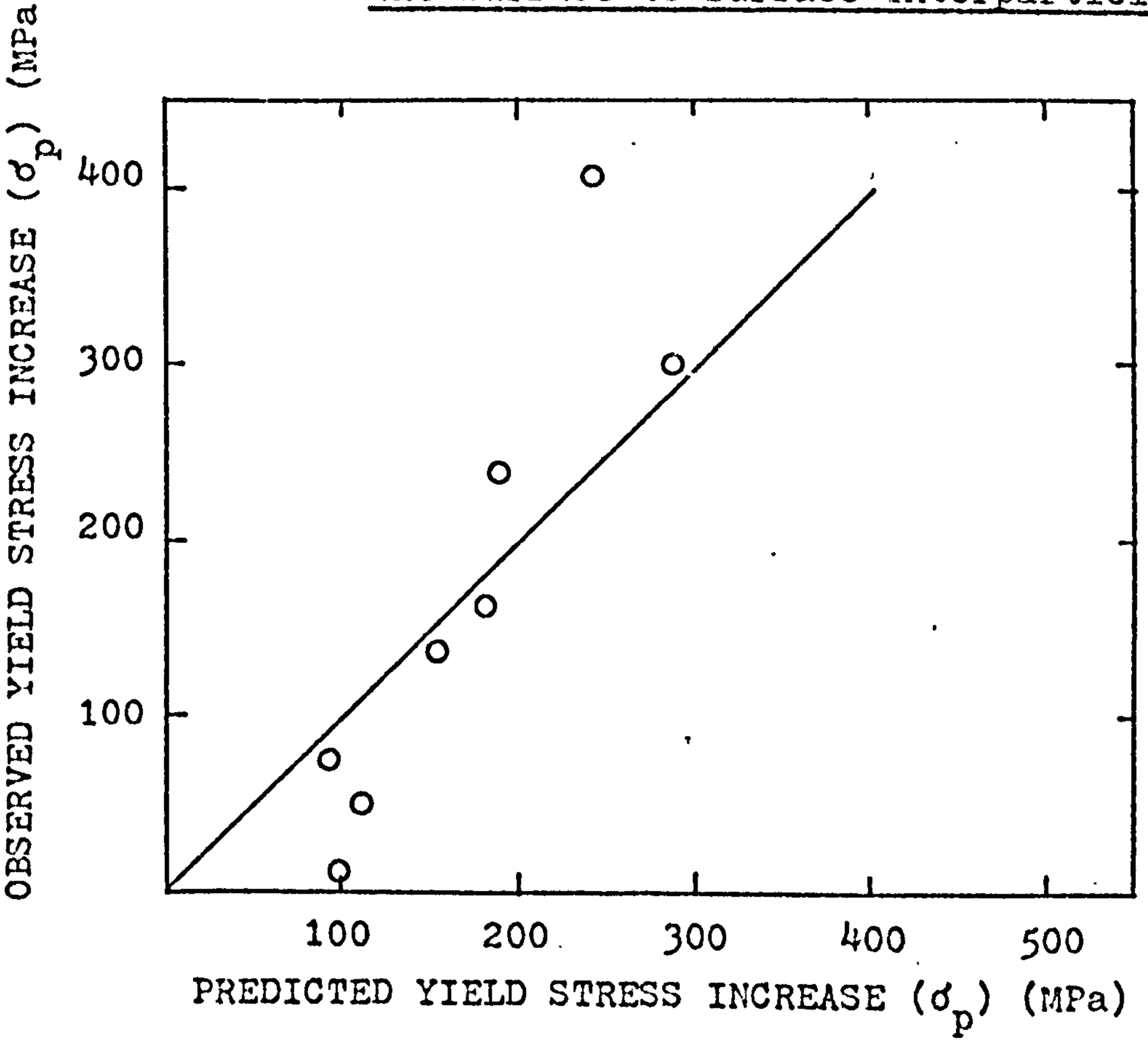

Fig.6.3.2.5 Predicted yield stress from equation 6.3.2.3.

6.4 Twinning as a contribution to strength.

It is proposed in this section, to review the possible contribution to strength from twinning. The scarcity of the studies on continuously cooled vanadium and niobium steels was mentioned earlier. When the subject is restricted further to the twins obtained in continuously cooled steels, the present study can be seen as a preliminary report.

A twin can be considered as (1) a hard particle or (2) a small grain (or subgrain). An attempt was made in the present study to calculate the number of twins present in 0.13% vanadium steel. When a twin is considered to behave like a particle, the strengthening effect should be approximately proportional to the inverse of the intertwin (interparticle) spacing following the Orowan mechanism. However, the intertwin spacing was too large ($\simeq 100$ μm) (see Fig.5.4.1) for significance when it was compared to an interparticle spacing of 0.2 μm from MCN particles present in the steel (e.g. Table 6.3.2.2). Consequently, it can be inferred that if microtwins behaved like hard particles, their contribution to strength would be negligible.

However, the twins can also be considered as small grains or subgrains which contribute to strength by increasing the effective grain size diameter. It has been suggested in the past [166], that the subgrain size can occasionally be substituted to the grain size in

the Hall-Petch [80,81] equation. In the Fe - 0.13V - 1.5Mn steel, the walls of the microtwins were coherent with the alpha iron matrix and the twins were very small compared to the grain size. The only exception arose in the vanadium and niobium steels without manganese addition (see Fig.5.16 to Fig.5.19).

Related to this subject, a recent study was carried out by Heikkinen and Soininen [167] to evaluate the contribution to strength from twinning. Two of the steels investigated are compared below:

Fe - 0.13% C - 0.15% V - 1.0% Mn, σ_y = 410 MPa

Fe - 0.13% C - 0.046%Nb- 1.1% Mn, σ_y = 342 MPa.

These steels were heat-treated 30 min at 1373K and continuously cooled at approximately 0.06K.s^{-1}. The grain size was 7½ (ASTM) for both steels. Some of the findings include: (1) no twin was found in the niobium steel but some were observed in the vanadium steel, (2) the increase in strength in the vanadium steel was ascribed to the refining effect of twinning on the grain size (although in Fig.4 of their paper, a mechanical twin can be seen to cross the walls of the transformation twins without hindrance), (3) "the order of magnitude of the increase" in the above steels was "difficult to evaluate, because of the parallel effect of the dispersion hardening", and (4) the transition brittle to ductile fracture was higher in the steel containing vanadium addition, where twins were also present. The authors [167] explained the last finding by the masking

effect of precipitation hardening rather than due to twinning.

It is therefore possible to summarize the above findings by the observation that the positive effect on strength was attributed to twinning and the detrimental effect on the transition temperature was conferred to precipitation hardening in the vanadium steel. When Heikkinen and Soininen's work [167] is compared to the present study, it should be mentioned that the dimensions of their twins appeared to be similar to those observed in the 0.13% vanadium steel of this investigation.

On the other hand, the increase in strength might be explained without involving twinning. For instance, it should be noted that in the 0.46% niobium steel of Heikkinen and Soininen's study, only half of the niobium was dissolved in the γiron at 1373K. Thus, probably coarsening of the NbC occurred. Also, in the same steel, the authors attributed the yield stress observed solely to the grain size. Two methods can be used to argue the increase in the strength observed:

(1) a change in the constants of the Hall-Petch equation [80,81]

(2) a variation in the dislocation densities.

Constants of the Hall-Petch equation [80,81] (see equation 1.3.1.1 and text) have been determined for plain carbon steels and for vanadium steels [135],

(a) $\sigma_y = 18.6 + 27\ d^{-\frac{1}{2}}$

(MPa)

Low carbon steels cooled at 1.67 $K.s^{-1}$ from austenite,

(b) $\sigma_y = 81.5 + 27\ d^{-\frac{1}{2}}$

(MPa)

Fe-(0.12+0.15%)C - (0.19 to 0.20%)V steels cooled at 0.17K.s^{-1} from austenite.

These conditions were approximately equivalent to the niobium and vanadium steel of Heikkinen and Soininen [167]. At a constant grain size of 7½ (ASTM), the $\Delta\sigma$ in the vanadium steels was in the order of 63 MPa against a value of 68 MPa observed by the authors [167]. The contribution to strength from twins is thus negligible.

In the present study, a higher dislocation density was found in the 0.13% vanadium steel compared to the 0.06% niobium steel (see Fig.4.6.1). The vanadium steel examined by Heikkinen and Soininen [167] contained similar alloying additions, and perhaps, it can be assumed that a similar number of dislocations was present in their vanadium steel cooled at 0.06K.s^{-1} (1.4X 10^{10} dislocations.cm/cm^3). According to the authors, the niobium steel they studied should be typical of a steel in an annealed state. Therefore, a typical number of dislocations for such a steel can be stated at 10^8 dislocations.cm/cm^3 [168]. It can also be predicted from the equation 1.3.3.3 that the contribution to strength from dislocation hardening would be:

$$\sigma_{dd}(68\text{MPa}) = \sigma_{10^{10}}(76\text{MPa}) - \sigma_{10^8}(7.6\text{MPa}).$$

Therefore, the contribution from dislocation hardening can account for the increase in strength observed by Heikkinen and Soininen [167].

In the present study, the contribution from precipitation hardening to strength was isolated by means of a modified Hall-Petch equation (eq.6.3.1.6). Doubts have been raised about the contribution of twinning to strength. It can therefore be concluded that if twinning contributes to strength, it would be included in the precipitation hardening component. It can be seen in Fig.6.3.1.4, that such a contribution is approximately zero for the 0.13% vanadium steel.

Therefore, thc microtwins observed in Fe - 0.13V - 1.5Mn steel of this study do not appear to have any significant contribution to the strength. However, macrotwins (i.e. twins such as those observed in vanadium and niobium steels without manganese addition) might develop from coherent twins and become subgrains or small grains. At this latter stage, they can thus contribute to the grain size component of the Hall-Petch equation [80,81].

In résumé, in this chapter a discussion of the various strengthening mechanisms was provided in relation to the peak hardening observed at a critical cooling rate, in continuously cooled vanadium and niobium steels. The peak was ascribed to precipitation hardening.

It was also found that the percentage increase at the peak was very much related to the alloying additions in the steel. The maximum increase was found in the steel with stoichiometric composition of niobium and vanadium carbide. Furthermore, an addition of manganese decreased the peak and seemed to spread the strengthening effect of precipitates over a larger range of cooling rates compared to the steels without manganese. The measured contribution to strength from precipitates was found to obey a calculated contribution from a simplified Orowan [99] equation such as the equation proposed by Hirsch and Humphreys[104]. However, the contribution to strength from twinning was believed to be negligible.

CONCLUSION

In respect of the objectives outlined at the beginning of this study, a peak hardening was found at a critical cooling rate in vanadium and niobium steels, and it was ascribed to precipitation hardening. The cooling rate at which the peak appeared and the height of the peak were found to be very dependent upon alloying additions. These are some of the definite conclusions of the present study.

The microtwins observed in both vanadium and niobium steels appeared to have little effect on the strength of the steels, although large twins may develop to subgrains or to small grains and thus might contribute to strength. However, the nucleation of these fascinating features remains unresolved; if one can draw a parallel with dislocations, twins are probably stress induced by the indirect effect of the one percent volume change when the γ iron transforms to α iron.

Two distinct groups of precipitate sizes were found in niobium and vanadium steels and were attributed to precipitation occurring in γ iron and at the γ/α transformation. Therefore, the orientation relationship with the alpha iron matrix should be different between the two groups of precipitates, and some knowledge could be gained from electron microscopy.

Some of the experimental methods and procedures used in the present study are worth considerations. Although the direct carbon extraction replica is a fairly standard

technique in Physical Metallurgy, it contains uncontrollable limitations. The present study demonstrated the unsatisfactory measurements obtained for the volume fraction of particles. Other alternative methods to evaluate the volume fraction (such as chemical analysis, electrical resistance measurements) do not appear at the moment to be very accurate. It is also difficult to measure the true distribution of particle sizes and volume fractions by transmission electron microscopy of thin foils. This situation might explain the absence of a valid model to predict precipitation hardening applicable to niobium and vanadium carbonitride precipitates in steels. For example, a model predicting a maximum contribution to strength from precipitation hardening, based on the assumptions of a constant particle size and complete precipitation, cannot explain the decrease in precipitation hardening in alloys when manganese is added. This was one of the findings of the present study.

A general comment can also be made about the literature relevant to the present investigation. Although an abundance of literature was available on the subject of niobium and vanadium steels, only a few papers were specifically dealing with the effect of the cooling rate on these steels. One remark may also be added: there was insufficient data in some of the papers making comparisons very difficult.

Finally, as a commercial application, the peak hardening observed in steels was at its maximum value

for a stoichiometric composition of Nb/V carbonitrides. An addition of manganese to such a steel decreased the maximum height, but spreaded also the hardening effect over a range of cooling rates. These findings are important in commercial heat-treatments. For example, the "peak hardening" cooling rate is approximately equivalent to an air cooled bar of twenty five millimeters diameter. However, since many materials of this dimension are rolled, in order to gain the maximum contribution to strength from niobium and vanadium additions, a good understanding of the characteristics of precipitation and of the thermal and mechanical treatments is essential. This aspect associated with the grain refinement by mechanical treatments remains a challenging field of research.

LIST OF REFERENCES

1.1 Precipitation of NaCl - type carbonitride in steel.

1 Aronsson B., The Microstructure and Mechanical Properties of some Martensitic Steels with special references to the Influence of Niobium and Molybdenum, in "Steel-Strengthening mechanisms", Climax Molybdenum Co., 1969, p. 77-87.

2 Gray J.M., Yeo R.B.G., Columbium carbonitride precipitation in low-alloy steels with particular emphasis on "precipitate-row" formation, in "Trans. of A.S.M."; vol. 61, no.2, 1968, p. 255-269.

3 Gray J.M., Webster D., Woodhead J.H., Precipitation in mild steels containing small addition of Niobium, "JISI", vol 203, no. 8, 1965, p. 812-818.

4 Meyzaud Y., Murry G., Durcissement d'aciers au nickel et au manganèse par précipitation de carbures de molybdène et vanadium, in "Mem. Scient. Rev. Mét.", vol 68, no.9, 1971, p. 545-563.

5 Le Bon A., Rofes-Vernis J., Rossard C., Recristallisation et précipitation provoquées par la déformation à chaud: cas d'un acier de construction soudable au niobium, in "Mém. Scient. Rev. Mét.", vol 70, no. 7-8, 1973, p.577-588.

6 Le Bon A., Rofes-Vernis J., Rossard C., Recrystallization and Precipitation during Hot working in a Nb-Beaving HSLA Steel, in "MES.", vol 9, no.1, 1975, p. 36-40.

7 Le Bon A., Rofes-Vernis J., Rossard C., High Temperature Thermomechanical treatments of H.S.L.A. steels, paper presented to the International Symposium on the "Hot Formality of Steels", organised by the S.V.T.S., 10-12 Sept. 1974, Strbské Pleso, Czechoslovakia.

8 Silcock J.M., Precipitation in Austenite Steels containing Vanadium, in "JISI", vol 211, no. 11, 1973, p. 792-800.

9 Silcock J.M., Denham A.W., Precipitation of NaCl-type and their behaviour in the Neighbourhood of Grain Boundaries, in "The Mechanism of phase transformation in crystalline solids", Institut of Metals, mono no. 33, 1969, p. 59-64.

10 Silcock J.M., Precipitation of NbC in niobium stabilized austenitic steels observed by thin foil electron microscopy, in "JISI", vol 201, no. 5, 1963, p. 409-421.

11 Silcock J.M., Partial Dislocations associated with NbC Precipitation in Austenitic Stainless Steels, in "Phil Mag." vol.10, no. 105, 1964, p. 361-389.

12 Baker T.N., unpublished work.

13 Roberts W., Grieveson P., On the prediction of the Composition of f.c.c. Interstitial Phases when precipitation in Steel, in "Script. Met.", vol 8, 1974, p. 451-458.

14 Hollox G.E., Microstructure and mechanical behaviour of carbides, in "Met. Science. Eng.", vol 3, 1968/69, p. 121-137.

15 Meyzaud Y., Some comments about "On the prediction of the composition of FCC interstitial phases when precipitated in steel", in "Scrip. Met.", vol 9, 1975, p. 171-172.

16 Narito K., Koyama S., Lecture in the Kubuaka Meeting of JIM, quoted by Sekine H. et al., Solubility of V_4C_3 in α-iron, in "Trans. ISIJ", vol 8, 1968, p. 101-102.

17 Baker T.N., Effect of vanadium on the properties and structure of controlled-rolled iron alloys, Ph.D. dissertation, University of Strathclyde, 1970.

18 Davenport A.T., Honeycombe R.W.K., Precipitation of Carbides at γ-α boundaries in alloy steels, in "Preceed. of Roy. Soc.", A322, no. 1549, 1971, p. 191-205.

19 Davenport A.T., Berry F.G., Honeycombe R.W.K., Inter-phase precipitation in iron alloys, in "M.S.J.", vol 2, 1968, p. 104-106.

20 Batte A.D. Honeycombe R.W.K., Precipitation of vanadium carbide in ferrite, in"JISI", vol 211, no. 4, 1973, p. 284-289.

21 Batte A.D., Edmonds D.V., Honeycombe R.W.K., The strengthening of Iron-Base Alloys by carbide precipitation at the Austenite Ferrite phase boundaries, in "Second Int. Conf. on The Strength of Metals and alloys,"A.S.M. 1970, p. 585-594.

22 Morrison W.B., Woodhead J.H., The Influence of small niobium additions on the mechanical properties of commercial mild steels, "JISI", vol 201, no.1, 1963, p. 43-46.

23 Tanino M., Nishida T., Ooka T., Yoshikawa K., The effect of a small amount of vanadium and niobium on the microstructures and the strength of proeutectoid ferrite of iron-carbon alloys, in "Proc. Symp. on Micrometallurgy", Jamshedpur, India, 1965, p. 77-88.

24 Suzuki H.G., Tanino M., Mechanism of formation of lined-up V_4C_3 precipitates in low carbon vanadium steels, in "Trans. of ISIJ", vol 12, 1972, p. 217-222.

25 Tanino M., Aoki K., The precipitation behaviour and the strenghtening effect of NbC during tempering and during continuous cooling, in"Trans. of ISIJ", vol 8, no. 5, 1968, p. 337-345.

26 Heikkinen V.K., Formation of two-Dimensional Granular colonies in Vanadium fine Grained Steels, in "Scand. J. of Met.", vol 2, 1973, p. 109-112.

27 Baker T.N., Structure of controlled-rolled and continuously cooled low-carbon vanadium steels, in JISI, vol 211, 1973, p. 502-510.

28 Baker T.N., Effect of second-phase particle on the mechanical properties of steel, in "I.S.I.", London, 1971, p. 204.

29 Kinsman K.R., Eichen E.,Aaronson H.I.,quoted in Phase Transformations, "Amer. Soc. for Metals", Ohio, 1970, p. 375.

30 Tanino M., Nishida T., On the Secondary Hardening on Tempering in Vanadium Steels, in"Trans. JIM", vol 9, 1968, p. 103-110.

31 Tekin E., Kelly P.M., Secondary Hardening of vanadium steels, in "JISI", vol 203, no.7, 1965, p. 715-720.

32 Bain E.C., in "Trans. A.I.M.E.", 70, 1924, p. 25.

33 Baker R.G., Nutting J., The tempering of a Cr - Mo - V - W and a Mo - V steel, in Precipitation processes in steels, in "ISI", no. 64, 1959, p. 1-22.

34 Hall M.G., Kinsman K.R., Aaronson H.I., Mechanism of formation of Mo_2C needles in an Fe - C - Mo alloy, in "Met. Trans.", vol 3, no. 5, 1972, p. 1320-1322.

35 Hall M.G., Kinsman K.R., Aaronson H.I., Carbon content of small regions of austenite and transformation mechanisms of Mo_2C fibres, in "JISI", vol 210, 1972, p. 541-542.

36 Berry F.G., Davenport A.T., Honeycombe R.W.K., The Isothermal decomposition of alloy austenite, in "The Mechanism of phase transformation in crystalline solids"; Inst. of Metals, mono no. 33, 1969, p. 288-292.

37 Edmonds D.V., Occurence of fibrous vanadium carbide during transformation of an Fe - V - C steel, in "JISI", vol 210, no. 5, 1972, p. 363-365.

38 Edmonds D.V., Honeycombe R.W.K., Structure and properties of an isothermally transformed Fe - 4Mo - 0.2C alloy, in"JISI", vol 211, 1973, p. 209-216.

39 Mannerkoski M., The Mechanism of formation of a periodic eutectoid structure at low temperatures in plain chromium steel, in"MSJ"; vol 3, 1969, p. 54-55.

40 Heikkinen V., On the decomposition of austenite in vanadium - treated fine grain steels, doctoral dissertation, Helsinki University of Technology, (publication) 1972, p. 67.

41 Jack H.K , The Effect of Substitutional Alloying Elements on the behaviour of Interstitial Solutes in Iron, in "Scand. J. of Met.", vol 1, no. 5, 1972, p. 195-202.

42 Mascanzoni A., Buzzichelli G., Homogeneous precipitation of niobium nitride in alpha-iron during isothermal treatment, in"Phil Mag.", vol 30, no. 1, 1974, p. 207-212.

1.2 Twinning in alpha iron and other b.c.c. metals.

43 Mahajan S., Williams D.F., Deformation Twinning in Metals and Alloys, in "Int. Met. Rev.", vol 18, no. 173, 1973, p. 43-61. (207 references).

44 Fullman R.L., Fisher J.C., Formation of annealing twins during grain growth, in "J. Appl. Phys.", vol 22, no. 11, 1951, p. 1350-1355.

45 Fullman R.L., Crystallography and Interfacial Free Energy of Noncoherent Twin Boundaries in Copper, in "J. Appl. Phys.", vol 22, no. 4, 1951, p. 456-460.

46 Fullman R.L., Interfacial Free Energy of Coherent Twin Boundaries in Copper, in "J. Appl. Phys.", vol 22, no. 4, 1951, p. 448-455.

47 Baker T.N., Twins in Iron alloys containing vanadium, In "Acta Met.", vol 21, 1973, p. 261-266.

48 Cahn R.W., Twinned Crystals, in"Adv. in Phys.", vol 3, no. 12, 1954, p. 364-445.

49 Hall E.O., Twinning and diffusionless transformations in metals, London, Butterworths, 1954, p. 181.

50 Reid C.N., A review of mechanical twinning in body-centered cubic metals and its relation to brittle fracture, in "J. Less-Common Metals", vol 9, 1965, p. 105-122.

51 Reed-Hill R.E., Hirth J.P., Rogers H.C., Deformation twinning, New York, Gordon and Breach, 1964, p. 464.

52 Hull D., Growth of Twins and associated dislocation phenomenon, New York,Gordon and Breach, 1964, p. 121-155.

53 Bevis M., Crocker A.G., Twinning modes in lattices, in "Proc. Roy. Soc. Lond.", A.313, 1969, p. 509-529.

54 Paxton H.W., Experimental verification of the twin system in alpha-iron, in "Acta Met.", vol 1, 1953, p. 141-143.

55 Kelly A., Neumann bands in pure iron, in "Proc. Roy. Soc. Lond.", A.66, 1953, p. 403-405.

56 Schmid E., Boas W., Plasticity of Crystals, (translation), London, Hughes and Co., 1950, p. 72.

57 Johari O., Thomas G., The Stereographic Projection and its applications, New York, John Wiley and Sons, 1969, p. 79-83.

58 Bullough R., Wayman C.M., Twinning and some Associated Diffraction Effect in Cubic and Hexagonal Metals, Part I, in "Trans. Met. Soc. Aime", vol 236, 1966, p. 1704-1710.

59 Crocker A.G., The Calculation of electron diffraction patterns containing twin reflections, in "Trans. Met. Soc. Aime", vol 233, 1965, p. 1917-1919.

60 Johari O., Thomas G., A General Method for calculating electron-diffraction patterns containing twin reflections in Isometric crystals,

61 Meieran E.S., Richman M.H., An Analytical Method for calculating electron diffraction patterns containing twin reflections, in "Trans. Met. Soc. Aime", vol 227, 1963, p. 1944-1946.

62 Tamura S., "J.I.S.I.", vol 115, 1927, p. 747.

63 Hutton D.S., Coleman G.L., Leslie W.C., Transformation twins in alpha iron, in"Trans. Met. Soc. Aime", vol. 215, p. 681.

64 Venables J.A., Deformation twinning in F.C.C. metals, Ref (9), p. 77-116.

65 Hobson D.O., McHargue C.J., "J. Metals", vol 15, 1963, p. 91.

66 Moiseev V.F., Trefilov V.I., Change of the deformation mechanism (Slip-twinning) in polycrystalline α-iron, in "Phys. stat. sol.", vol 18, 1966, p. 881-895.

67 Hirsch P.B., Otte H.M., X-ray diffraction from body-centered cubic crystals containing stacking faults, in "Acta Cryst.", vol 10, 1957, p. 447-453.

68 Vitek V., Intrinsic stacking faults in body-centered cubic crystals, in"Phil Mag.", vol 18, 1968, p. 773-786.

69 Vitek V., Multilayer stacking faults and twins on [211] planes in b.c.c. metals, in "Scrip. Met.", vol 4, 1970, p. 725-732.

70 Steigler J.O., McHargue C.J., The Effect of Impurities on mechanical twinning and dislocation behaviour in b.c.c., ref (9), p. 209-236.

71 Magee C.L., Hoffman D.W., Davies R.G., The Effect of Interstitial solutes on the twinning stress of B.C.C. metals, in "Phil. Mag.", vol 23, 1971, p. 1531-1540.

72 Cottrell A.H., Bilby B.A., A mechanism for the growth of deformation twins in crystals, in "Phil. Mag.", vol 42, 1951, p. 573-581.

73 Sleeswyk A.W., ½<111>Screw dislocation and the nucleation of [112] <111> twins in the b.c.c. lattice, in "Phil. Mag.", vol 8, 1963, p. 1467-1486.

74 Ogawa K., Edge dislocations dissociated in [112] planes and twinning mechanism of b.c.c. metals, in "Phil. Mag." vol 11, 1965, p. 217-233.

75 Mahajan S., Nucleation and growth of deformation twins in Mo - 35 at.% Re alloy, in "Phil. Mag.", vol 26, 1972, p. 161-171.

76 Sleeswyk A.W., Perfect dislocation pole models for twinning in the F.C.C. and B.C.C. lattices, in "Phil. Mag." vol 29, 1974, p. 407-421.

77 Mahajan S., Interrelationship between slip and twinning in b.c.c. crystals, in "Acta Met.", vol 23, 1975, p. 671-684.

78 Heikkinen V.K., Transformation twins in vanadium- bearing mild steels, in "Second. J. Met.", vol 3, 1974, p. 41-45.

79 Orowan E., Dislocations in Metals, New York, "Aime", 1954, p. 116.

80 Hall E.O., The deformation and ageing of mild steel, III, in "Proc. Phys. Soc.", B64, 1951, p. 747-753.

1.3 Strengthening mechanisms in steel.

81 Petch N.J., The Cleavage Strength of Polycrystals, in "J.I.S.I.", 174, 1953, p. 25-28.

82 Kouwenhoven H.J., The influence of ferrite grain size and volume fraction of pearlite on the lower yield stress and Lüders strain of carbon steel, in "Trans.ASM," vol 62, 1969, p. 437-446.

83 Petch N.J., The ductile-cleavage transition in alpha-iron, in Fracture, in "Proc. of the Swampscott Conference," by Averbach B.L., et al., (ed.) John Wiley, 1959, p. 54-67.

84 Baker T.N., Structure of controlled-rolled and continuously cooled low-carbon vanadium steels, in "JISI", vol 211, 1973, p. 502-511.

85 McPherson N.A., Thermomechanical treatment of low carbon steels, Ph.D dissertation, University of Strathclyde, 1974.

86 Haynes E.J., Heat treatment of low alloy steels containing titanium, Ph.D dissertation, University of Strathclyde, 1973.

87 Reed-Hill R.E., Physical Metallurgy principles, 2nd edition, D.Van Nostrand Co., New York, 1973,.

88 Gladman T., On the theory of the effect of precipitate particles on grain growth in metals, in "Proc. Roy. Soc." (London), A294, 1966, p. 298-309.

89 Gladman T., Dulieu D., Grain-size Control in steels, in "Metal Sci.", vol 8, 1974, p. 167-176.

90 Quoted by Smith C.S., in "Trans. Met. Soc., Aime", vol 175, 1948, p. 15.

91 Lücke K., Detert K., A Quantitative theory of grain-boundary motion and recrystallisation in metals in the presence of impurities, in "Acta Met.", vol 5, 1957, p.628-37.

92 Lücke K., Stüwe H.P., On the theory of grain boundary motion, in "Recovery and Recrystallization of metals", edited by L. Himmel, New York, 1963, p. 171-210.

93 Higgins G.T., Grain - boundary migration and grain growth, in "Metal Sci.", vol 8, 1974, p. 143-150.

94 Pickering F.B., Gladman T., An investigation into some factors which control the strength of carbon steels, in "Metallurgical developments in carbon steels", ISI, 1963, p. 19-29.

95 Leslie W.C., Iron and its dilute substitutional solid solution, in "Met. Trans.", vol 3, 1972, p. 5-26.

96 Keh A.S., Weissmann, Electron microscopy and strength of crystals, New York, Interscience, 1963, p. 231.

97 Keh A.S., Work hardening and deformation sub-structure in iron single crystals deformed in tension at 298K, in "Phil. Mag.", vol 12, 1965, p. 9-30.

98 Batte A.D., Honeycombe R.W.K., Strengthening of ferrite by vanadium carbide precipitation, in "MSJ", vol 7, 1973, p. 160-168.

99 Orowan E., Effects associated with internal stresses, discussion in "Symposium on Internal Stresses in Metals and alloys", London, Inst. Metals, 1948, p. 451-453.

100 Nicholson R.B., Strengthening of steels by second-phase particles, in "Effect of second-phase particles on the mechanical properties of steel", London, publ no. 145, ISI, 1971, p. 1-8.

101 Kelly P.M., The quantitative relationship between microstructure and properties in two-phase alloys, in "Int. Met. Rev.", vol 18, 1973, p. 31-36.

102 Papaleo R., Whiteman J.A., Deformation mechanism in ferritic Fe - Si - Ti alloys containing ordered misfit-free intermetallic particles, in "Effect of second-phase particles on the mechanical properties of steel", London, publ no. 145, ISI, 1971, p. 22-27.

103 Ashby M.F., On the Orowan stress, in "Physics of Strength and Plasticity", by Argon A.S., (ed.), M.J.T. Press, Cambrige, 1969, p. 113-131.

104 Hirsch P.B., Humphreys F.J., Plastic deformation of two-phase alloys containing small nondeformable particles, in "Physics of Strength and Plasticity", by Argon A.S. (ed.), M.J.T. Press, Cambridge, 1969, p. 189-216.

105 Gladman T., Holmes B., McIvor I.D., Effects of second-phase particles on strength, toughness, and ductility, in "Effect of second-phase particles on the mechanical properties of steel", London, Publ no. 145, ISI, 1971, p. 68-78.

106 Corti C.W., Cotterill P., Fitzpatrick G.A., The evaluation of the interparticle spacing in dispersion alloys, in "Int. Met. Rev.", vol 19, no. 182, 1974, p. 77-88.

107 Kocks U.F., Statistical treatment of penetrable obstacles, in "Canad. J. Physics.", vol 45, 1967, p. 739-755.

108 Foreman J.E., Makin M.J., Dislocation movement through random arrays of obstacles, in "Canad. J. Physics.", vol 45, 1967, p. 511-517.

109 Brown L.M., Ham R.K., Dislocation-particle interactions, in "Strengthening methods in crystals", Kelly A. (ed.) London, Elsevier, 1971, p. 12-135.

110 Norberg H., Aronsson B., Solubility of niobium carbide in austenite, in "JISI", vol 206, 1968, p. 1263-1266.

111 Irvine K.J. Pickering F.B., Gladman T., Grain-refined C - Mn steels, in "JISI", vol 205, 1967, p. 161-181.

112 Iron and Steel Industry Standards Committee, The End Quench Hardenability Test for Steel, in "British Standard 4437, 1969.

113 Carslow H.S., Jaeger J.C., Conduction of Heat in Solids, 2nd edition, Clarendon Press, 1959, p. 99-101.

114 A.S.M., Metal Handbook, 8th edition, vol 1, 1967, p. 1206-1212.

115 Russell T.F., Williamson B.A., Surface Temperature Measurement during the Cooling of a Jominy Test-Piece, in "ISI", "Symposium on the Hardenability of Steel," 1946, p. 34-46.

116 ASTM Committe A1 on Steel, End-Quench test for Hardenability of Steel, in "ASTM", A255, 1967.

117 Atkins M., Andrews K.W., Continuous Cooling Transformation Diagrams, I - Cooling Curve Analysis for transformation Diagrams and Heat Treatment, in "British Steel Corporation Research Report", SP/QTM/6036/1971/C.

3.2 Determination of dislocation densities.

118 Hirsch P.B., Howie A., Nicholson R.B., Pashley D.W., Whelan M.J., Electron microscopy of thin crystal, London, Butterworths, 1965, p. 416-424.

119 Ham R.K., The determination of dislocation densities in thin films, in "Phil. Mag.", no 69, 1961, p. 1183-84.

120 Underwood E.E., Quantitative Stereology, California, Addison Wesley, 1970, p. 7-9.

121 Staker M.R., Holt D.L., The dislocation cell size and dislocation density in copper deformed at temperatures between 25 and 700°C, in "Acta Met.", vol 20, 1972, p. 569-579.

122 Spiegel M.R., Statistics, New York, Shaum Publ.Co., 1961, p. 142.

123 Hale K.H., Brown A.H., Experimental determination of Burgers vectors of dislocation, in "Proc. Roy. Soc." (London), A310, 1969, p. 479-491.

124 France L.K., Loretto M.H., The influence of the size of diffracting vectors on the visibility of dislocation in α-iron, in "Proc. Roy. Soc." (London),A307, 1968, p. 83-96.

125 Vingsbo O., On stereoscopic foil thickness determination in transmission electron microscopy, in "Jernkont.Ann.," no. 155, 1971, p. 465-467.

126 Cosslett V.E., High voltage electron microscopy, in "Quart. Rev. of Biophysics", vol 2, 1969, p. 95-133.

127 Dingley D.J., Hale K.F., Burgers vectors of dislocations in deformed iron and iron alloys, in "Proc. Roy. Soc." (London), A295, 1966, p. 55-71.

3.3 Analysis of MCN particle size distributions in metallic materials using carbon replica.

128 Ashby M.F., Ebeling R., On the determination of the number, size, spacing, and volume fraction of spherical second-phase particles from extraction replica, in "Trans. Met. Soc. of Aime", vol 236, 1966, p. 1396-1404.

129 Mukherjee T., Stumpf W.E., Sellars C.M., Quantitative assessment of extraction replicas for particle analysis, in "Journ. of Mat. Sc.", vol 3, 1968, p. 127-135.

130 Exner H.E., Analysis of grain and particle-size distributions in metallic materials, in "Int. Met. Rev.", vol 17, 1972, p. 111-128.

131 Cosslett V.E., Specimen thickness and image resolution in electron microscopy, in "Brit. J. App. Phys.", vol 7, 1956, p. 10-13.

132 Smith E., Nutting J., Direct carbon replicas from metal surfaces, in "Brit. J. App. Phys.", vol 7, 1956, p. 214-217.

133 Kay D.H., (editor), Techniques for electron microscopy, 2nd edition, Blackwell. Sr. Publ., Oxford, 1965, p. 109 and p. 146.

3.4 Estimation of the error on grain size measured by linear intercept method.

134 Farrell K., Loh B.T.M., Hardness-flow-stress-grain-size relationships in iron, in "JISI", vol 209, 1971, p. 915-917.

135 Imai Y., Shino Y., The Effect of grain size and precipitate on lower yield strength of vanadium steel, in "Second International Conference on the Strength of Metals and Alloys", Conference Proceedings, ASM, vol 2, 1970, p. 595-599.

136 Thompson A.W., Calculation of true volume grain diameter, in "Metallography", vol 5, 1972, p. 366- 369.

137 Underwood E.E., Quantitative Stereology, Addison-Wesby Publishing Co., 1970, p. 81.

4. Results.

138 Met. Soc. of AIME, ASM, Essential of SI System, in "Met. Trans.", vol 3, 1972, p. 355-358.

139 ASTM Committee on Metric Practice, Metric Practice Guide (a guide to the use of SI), (included Editorial corrections made in June 1973), in "ASTM Standard no E 380-72".

5. Study of microstructure.

140 Alexander W., Street A., Metals in the Service of Man, Penguin Books Ltd., Fifth edition, 1972, p. 20.

141 Greaves R.H., Wrighton H.M. Practical Microscopical Metallography, Science Paperback - 1971, Fourth edition, 1957, Chapman and Hall Ltd., p. 1.

142 Roberts C.S., in "Trans. AIME", vol 197, 1953, p. 203.

143 Reed-Hill R.E., Physical Metallurgy Principles, in "D.Van Nostrand Company", Second edition, 1973, p. 722.

144 Humphreys C.J., Thomas L.E., Lally J.S., Fisher R.M., Maximazing the penetration in high voltage electron microscopy, in "Phil. Mag.", vol 23, 1971, p. 87-114.

145 Stuart H., Ridley N., Thermal expansion of some carbides and tessalated stresses in steels, in "JISI", vol 208, 1970, p. 1087-1092.

146 Hirsch P.B., Howie A., Nicholson R.B., Pashley D.W., Whelan M.J., Electron Microscopy of thin crystals, London, Butterworths, 1965, p. 327-336. a) p. 256.

147 Cahn R.W., Physical Metallurgy, North-Holland Publ. Second edition, 1970, p. 506.

148 Davenport A.T., Occurence of "arced" reflections in diffraction patterns from a vanadium steel, "JISI", vol 206, 1968, p. 499-501.

149 Kelly P.M., Blake G., The characterization of dislocation loops in neutron irradiated zerconium, in "Phil. Mag.", vol 28, 1973, p. 415-426.

150 Fulman R.L., Measurement of particle sizes in opaque bodies, in "Trans. AIME", vol 197, 1953, p. 447-452.

151 Lapointe A.J., Baker T.N., Microtwins in low alloy steels, Proceedings of Conference, Bristol, September 1975.

6. Interpretation and discussion of results.

152 Tabor D., The Hardness of Metals, Clarendon Press, Oxford, 1951, p. 102-108.

153 Cahoon J.R., An improved equation relating hardness to ultimate strength, in "Met. Trans.", vol 3, 1972, p.3040.

154 Abson D.J., Gurney F.J., Hardness, strength, and elongation correlations for some titanium-base alloys, in "Metals Technology", 1974, p. 483-489.

155 Cahoon J.R., Broughton W.H., Kutzak A.R., The determination of yield strength from hardness measurements, in "Met. Trans.", vol 2, 1971, p.1979-1983.

156 Conrad H., Schoeck G., Cottrell locking and the flow stress in iron, in "Acta Met.", vol 8, 1960, p.791-796.

157 Irani J.J., Burton D., Jones J.D., Rothwell A.B., Beneficial effects of controlled rolling in the processing of structural steels, in "Strong tough structural steels", Scarborough, ISI publication no 104, 1967, p. 110-122.

158 Christ B.W., Smith G.V., Comparison of the Hall-Petch parameters of zone-refined iron determined by the grain size and extrapolation methods, in "Acta Met.", vol 15, 1967, p. 809-816.

159 Wilson D.V., Role of grain boundaries in the discontinuous yielding of low-carbon steels, in"MSJ", vol 1, 1967, p. 40-47.

160 Petch N.J., In fracture, Edition Averback et al., Wiley, 1959, p. 54-64.

161 Little J.H., Chapman J.A., Morrison W.B., Mintz B., The production of high strength plate steels by controlled rolling, in "The microstructure and design of alloys", Proc. 3rd International Conference on Strength of Metals and Alloys, Cambridge, 1973, p. 80-84.

162 Morrison W.B., Chapman J.A., Controlled rolling, in "The contribution of physical metallurgy to engineering practice", (Rosentrain centenary conference), London 1975, p. 193-207.

163 Reed-Hill R.E., Physical Metallurgy principles, 2nd edition, D. Van Nostrand Company, 1973, p. 332.

164 Bucher J.H. Grozier J.D., Toughness of high-strength hot rolled steels, in "Met. Eng. Quartely", ASM, 1965, Nov., p. 1-6.

165 König P., Scholz W., Ulmer H., Wechselwirkung von Aluminium, vanadin und stickstoff in aluminiumberuhigten, mit vanadin und stickstoff legierten, SchweiBaren Baustählen mit rd. 0,2%C und 1,5%Mn, Archiv für das Eisenhüttenwersen, J.Heft8, Augst, 1971, p. 541-556.

166 Warrington D.H., The flow-stress-subgrain size relationship in iron, "JISI", vol 201, 1963, p. 610-613.

167 Heikkinen V.K., Soininen R., Effect of transformation twins on the strength and ductility of vanadium-bearing mild steels, in "Scand. J. Metallurgy", vol 3, 1974, p. 245-248.

168 Smallman R.E., Modern Physical Metallurgy, 3rd edition, London, Butterworths, 1970, p. 387.

169 Wilson D.V., Russell B., The contribution of atmosphere locking to the strain ageing of low carbon steels, in "Acta Met.", vol 8, 1960, p. 36-45.

170 Cracknell A., Petch N.J., Frictional forces on dislocation arrays at the lower yield point in iron, in "Acta Met.", vol 3, 1955, p. 186-189.

171 Armstrong R., Codd I., Douthwaite R.M., Petch N.J., Plastic deformation of polycrystalline aggregates, in "Phil. Mag.", vol 7, 1962, p. 45-58.

172 Takeuchi S., Solid solution strengthening in single Crystals of Iron alloys, in "J. Phys. Soc. Japan", vol 27, no. 4, 1969, p. 929-940.

173 Ansell G.S., Mechanical properties of two phase alloys, in "Physical Metallurgy", edited by R.W. Cahn, North-Holland Publishing Co., 1970, p. 1083-1128.

Appendix A: Position of a b.c.c. twin reflection with respect to a matrix reciprocal lattice vector.

Matrix reflection	Twinning planes											
$h_m k_m l_m$	211	$21\bar{1}$	$2\bar{1}1$	$\bar{2}11$	121	$12\bar{1}$	$1\bar{2}1$	$\bar{1}21$	112	$11\bar{2}$	$1\bar{1}2$	$\bar{1}12$
110	$\bar{3}0\bar{3}$*	$\bar{3}03$*	$14\bar{1}$	141	$0\bar{3}\bar{3}$*	$0\bar{3}3$*	411	$41\bar{1}$	$11\bar{4}$	114	330*	330*
$1\bar{1}0$	$1\bar{4}\bar{1}$	$1\bar{4}1$	$\bar{3}0\bar{3}$*	$\bar{3}03$*	$4\bar{1}1$	$4\bar{1}\bar{1}$	$03\bar{3}$*	033*	$3\bar{3}0$*	$3\bar{3}0$*	$1\bar{1}4$	$1\bar{1}4$
101	330*	114	330*	114	141	303*	141	303*	$0\bar{3}\bar{3}$*	411	$03\bar{3}$*	$4\bar{1}1$
$10\bar{1}$	$1\bar{1}\bar{4}$	$\bar{3}\bar{3}0$*	$11\bar{4}$	$\bar{3}30$*	$30\bar{3}$*	$1\bar{4}\bar{1}$	$30\bar{3}$*	$14\bar{1}$	$41\bar{1}$	$0\bar{3}3$*	$4\bar{1}\bar{1}$	033*
011	$\bar{4}11$	033*	033*	411	$\bar{3}\bar{3}0$*	$\bar{1}14$	114	$3\bar{3}0$*	$\bar{3}0\bar{3}$*	141	$\bar{1}41$	$30\bar{3}$*
$01\bar{1}$	$03\bar{3}$*	$\bar{4}1\bar{1}$	$41\bar{1}$	$03\bar{3}$*	$\bar{1}1\bar{4}$	$\bar{3}\bar{3}0$	$3\bar{3}0$*	$11\bar{4}$	$14\bar{1}$	$\bar{3}03$*	303*	$\bar{1}4\bar{1}$
200	$\bar{2}\bar{4}\bar{4}$	$\bar{2}\bar{4}4$	$\bar{2}4\bar{4}$	$\bar{2}44$	$4\bar{4}\bar{2}$	$4\bar{4}2$	$44\bar{2}$	442	$4\bar{2}\bar{4}$	$4\bar{2}4$	$42\bar{4}$	424
020	$\bar{4}4\bar{2}$	$\bar{4}42$	442	$44\bar{2}$	$\bar{4}\bar{2}\bar{4}$	$\bar{4}\bar{2}4$	$4\bar{2}4$	$4\bar{2}\bar{4}$	$\bar{2}4\bar{4}$	$\bar{2}44$	244	$24\bar{4}$
002	$\bar{4}\bar{2}4$	424	$\bar{4}24$	$4\bar{2}4$	$\bar{2}\bar{4}4$	244	$\bar{2}44$	$2\bar{4}4$	$\bar{4}\bar{4}\bar{2}$	$44\bar{2}$	$\bar{4}4\bar{2}$	$4\bar{4}\bar{2}$
211	$\bar{6}\bar{3}\bar{3}$*	$\bar{2}\bar{1}7$	$\bar{2}7\bar{1}$	255	$1\bar{7}\bar{2}$	$3\bar{3}6$*	552	712	$1\bar{2}\bar{7}$	525	$36\bar{3}$*	721
$21\bar{1}$	$\bar{2}1\bar{7}$	$\bar{6}\bar{3}3$*	$25\bar{5}$	$\bar{2}71$	$3\bar{3}\bar{6}$*	$1\bar{7}2$	$71\bar{2}$	$55\bar{2}$	$52\bar{5}$	$1\bar{2}7$	$72\bar{1}$	363*
$2\bar{1}1$	$\bar{2}7\bar{1}$	$2\bar{5}5$	$\bar{6}\bar{3}\bar{3}$*	$\bar{2}17$	$5\bar{5}2$	$7\bar{1}2$	$17\bar{2}$	336*	$3\bar{6}\bar{3}$*	$7\bar{2}1$	$12\bar{7}$	$5\bar{2}5$
$\bar{2}11$	$\bar{2}55$	$27\bar{1}$	$2\bar{1}7$	$6\bar{3}\bar{3}$*	$\bar{7}12$	$\bar{5}52$	$\bar{3}\bar{3}6$*	$\bar{1}\bar{7}\bar{2}$	$\bar{7}21$	$\bar{3}6\bar{3}$*	$\bar{5}25$	$\bar{1}\bar{2}\bar{7}$
121	$\bar{7}1\bar{2}$	$\bar{3}36$*	172	552	$\bar{3}\bar{6}\bar{3}$*	$\bar{1}27$	525	$72\bar{1}$	$\bar{2}1\bar{7}$	255	271	$6\bar{3}\bar{3}$*
$12\bar{1}$	$\bar{3}3\bar{6}$*	$\bar{7}12$	$55\bar{2}$	$17\bar{2}$	$\bar{1}\bar{2}\bar{7}$	$\bar{3}\bar{6}3$*	$72\bar{1}$	$52\bar{5}$	$25\bar{5}$	$\bar{2}17$	633*	$27\bar{1}$
$1\bar{2}1$	$1\bar{7}2$	$5\bar{5}2$	$\bar{7}1\bar{2}$	$\bar{3}36$*	$5\bar{2}5$	$72\bar{1}$	$\bar{3}6\bar{3}$*	$\bar{1}27$	$27\bar{1}$	$6\bar{3}\bar{3}$*	$\bar{2}1\bar{7}$	$25\bar{5}$
$\bar{1}21$	$\bar{5}52$	$\bar{1}72$	336*	$71\bar{2}$	$\bar{7}\bar{2}\bar{1}$	$\bar{5}25$	$12\bar{7}$	$36\bar{3}$*	$\bar{6}\bar{3}\bar{3}$*	$\bar{2}71$	$\bar{2}55$	$21\bar{7}$
112	$\bar{7}\bar{2}1$	127	$\bar{3}63$*	525	$\bar{2}\bar{7}1$	217	255	$6\bar{3}3$*	$\bar{3}\bar{3}\bar{6}$*	552	$\bar{1}7\bar{2}$	$7\bar{1}\bar{2}$
$11\bar{2}$	$12\bar{7}$	$\bar{7}2\bar{1}$	$52\bar{5}$	$\bar{3}6\bar{3}$*	$21\bar{7}$	$\bar{2}7\bar{1}$	$6\bar{3}\bar{3}$*	$25\bar{5}$	$55\bar{2}$	$\bar{3}3\bar{6}$*	$7\bar{1}2$	$\bar{1}72$
$1\bar{1}2$	$\bar{3}6\bar{3}$*	$5\bar{2}5$	$\bar{7}21$	$12\bar{7}$	$25\bar{5}$	633*	$\bar{2}71$	$21\bar{7}$	$\bar{1}\bar{7}\bar{2}$	$71\bar{2}$	$\bar{3}\bar{3}6$*	552
$\bar{1}12$	$\bar{5}25$	363*	$\bar{1}27$	$72\bar{1}$	$6\bar{3}3$*	$\bar{2}55$	$\bar{2}17$	$27\bar{1}$	$\bar{7}1\bar{2}$	172	$\bar{5}52$	$3\bar{3}\bar{6}$*

The twin reflection is on the direction and at one third of the matrix reciprocal lattice vector. The twin reflection has the indices of the matrix reflection, plus a π radian rotation:

$$h_t k_t l_t = h_m k_m l_m .$$

The symbol (*) indicates that the twin reflection is superposed to a matrix reflection.

Appendix B: Determination of the volume of a twin.

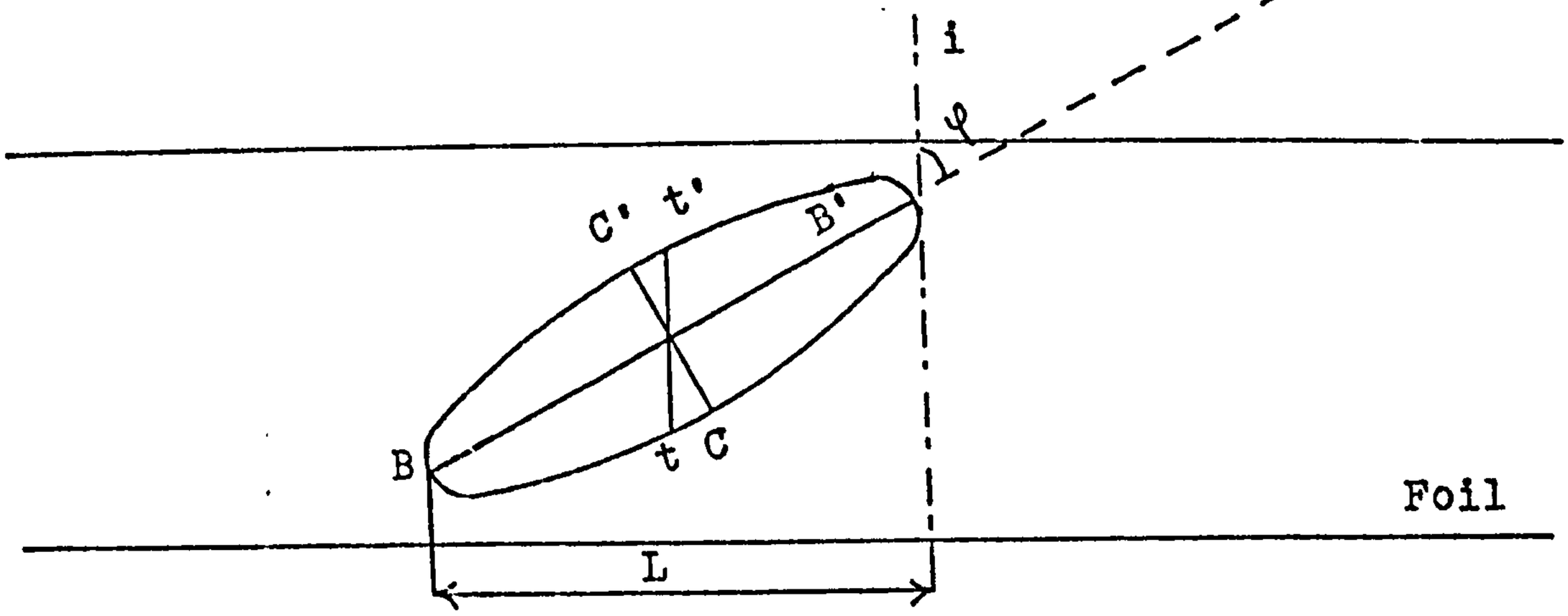

where: i : incident beam (zone axis)

φ : angle between $\langle i \rangle$ and a $\langle 111 \rangle$ direction related to the composite plane [112]

A'A: width of the twin (not shown)

B'B: the $\langle 111 \rangle$ direction related to the composition plane [112]

C'C: true thickness of the twins (i.e. layers of [112])

t't: thickness of the twin in the $\langle i \rangle$ direction (determined by displacement fringes)

L : projected length in the twin direction $\langle 111 \rangle$.

Thus, the volume occupied by a twin can be calculated:

Volume of a twin: $4/3\,\pi abc$,
where: a,b,c are the semi-axis of the ellipsoid.

$$a = A'A/2$$

$$b = \frac{B'B}{2} = \frac{L}{2 \sin \varphi}$$

$$c = \frac{C'C}{2} = b \cdot \frac{t't}{2} \cdot \frac{\cos \varphi}{\sqrt{b^2 - \frac{(t't)^2}{2} \cdot \sin^2 \varphi}}$$

Appendix C: Expression of the interparticle spacing for two different groups of particle size.

1) The particles are assumed to conserve the same shape as they grow,
2) The following is restricted to particles having the same shear modulus (i.e. same material).

The surface to surface interparticle spacing is:

$$L = \frac{1}{\sqrt{N_s}} - \bar{X} \qquad (C1)$$

where: N_s is the total number of particles,

$\bar{X}$ is the average area of a sphere in the slip plane.

With two groups of particle size, the total number of particles is:

$$N_s = N_1 + N_2 \qquad (C2)$$

The volume fraction (f) is related to N_s and X through:

$$f = n_s \cdot \frac{\pi X^2 s}{4} \qquad (C3)$$

Hence, the equation (C2) becomes:

$$N_s = \frac{4}{\pi}\left[\frac{f_1}{X_1^2} + \frac{f_2}{X_2^2}\right] \qquad (C4)$$

The average particle size in the slip plane is:

$$\bar{X} = \frac{N_1X_1 + N_2X_2}{N_1 + N_2} \qquad (C5)$$

The average particle size ($\bar{X}$) can also be expressed in terms of volume fractions (C3→C5):

$$\bar{X} = \frac{X_1 X_2 (f_1 X_2 + f_2 X_1)}{f_1 X_2^2 + f_1 X_1^2} \qquad (C6)$$

when the two different groups of particles have different dimensions and different volume fraction,

$$f_2 < f_1 \quad \text{and} \quad X_2 >> X_1 ,$$

then in equation (C4):

$$\frac{f_1}{X_1^2} >> \frac{f_2}{X_2^2} \qquad (C7)$$

and in equation (C6):

$$f_1 X_2^2 >> f_2 X_1^2 . \qquad (C8)$$

It should be remembered that the measured particle diameters are not the mean intercept diameters with the slip plane. A factor of $\sqrt{2/3}$ converts the measured diameter (D) to the mean intercept [150]:

$$\bar{X} = \sqrt{2/3}\ D, \qquad (C9)$$

Hence, if the equations (C7) and (C8) are found to apply, the effect of large particle size to strength is negligible. The surface to surface interparticle spacing thus becomes:

$$L = 0.817\ D\ , \left(\frac{8.87}{\sqrt{f_1}} - Z\right)$$

where: D_1 is the average measured diameter of the small group of particle size of volume fraction (f_1),

$$Z = \frac{f_1 D_2 + f_2 D_1}{f_1 D_2} \ ; \qquad Z \simeq 1 \text{ usually.}$$